

Andreas Wittek

Mechanical and pathophysiological in vivo characterization of the individual aortic wall based on 4D ultrasound imaging

Schriftenreihe der Arbeitsgruppe
für Technische Mechanik
im Institut für Mechanik und Regelungs-
technik - Mechatronik

Herausgeber: Claus-Peter Fritzen

Band 17

Impressum

Prof. Dr.-Ing. Claus Peter Fritzen

Arbeitsgruppe für Technische Mechanik

Institut für Mechanik und Regelungstechnik - Mechatronik

Universität Siegen

57068 Siegen

ISSN 2191-5601

URN urn:nbn:de:hbz:467-21221

DOI: 10.25819/ubsi/10045

Zugl.: Siegen, Univ., Diss., 2020

Mechanical and pathophysiological in vivo
characterization of the individual aortic wall based on
4D ultrasound imaging

genehmigte
DISSERTATION
zur Erlangung des Grades eines Doktors
der Ingenieurwissenschaften

vorgelegt von
Dipl.-Ing. (FH) Andreas Wittek
geb. in Ansbach (Mittelfranken)

eingereicht bei der Naturwissenschaftlich-Technischen Fakultät
der Universität Siegen
Siegen 2020

Betreuer und erster Gutachter
Prof. Dr.-Ing. Claus-Peter Fritzen
Universität Siegen

Zweiter Gutachter
Prof. em. Dr. Jürgen Bereiter-Hahn
Johann Wolfgang Goethe-Universität Frankfurt am Main

Tag der mündlichen Prüfung
11. Dezember 2020

Preface

This work was conducted in an ongoing project that aims at the establishment of novel non-invasive in vivo predictors for pathological changes of the aortic wall and for immediate rupture risk of abdominal aortic aneurysms. A particular feature of this project is that the development of numerical analysis and modeling methods was based on available non-invasive in vivo data, exclusively. This was only possible in close interdisciplinary cooperation between mechanical engineers, heart and vascular surgeons and biologists. I would like to thank everyone who has supported me in this work.

I would especially like to thank Prof. Fritzen for the opportunity to write this dissertation in his working group as well as for the pleasant and fruitful discussions and the stimulating feedback on my work.

Very special thanks go to Dr. Christopher Blase, head of the Cell and Vascular Mechanics Group at the Faculty of Biological Sciences of the Goethe University Frankfurt, where the work that is presented in this thesis was conducted. The intensive interdisciplinary discussion of the biomechanical research topic and the critical questioning of modeling approaches and simulation results have significantly contributed to the success of this work.

Moreover, I would like to thank Prof. Bereiter-Hahn very much for fruitful discussion of the topics of this thesis and the support of the project.

My sincere thanks for excellent cooperation go to the clinical partners, who established the jointly developed 4D ultrasound measurement of aortic wall motion clinically. Without the in vivo patient data provided by Wojciech Derwich, MD and Prof. Thomas Schmitz-Rixen, MD, PhD (Department of Vascular and Endovascular Surgery of the Goethe University Hospital, Frankfurt am Main) and by Konstantinos Karatolios, MD, (Department of Cardiology, Universitätsklinikum Marburg und Gießen) and Prof. Sebastian Vogt, MD, PhD (Department of Heart Surgery, Universitätsklinikum Marburg und Gießen), the work presented in this thesis would not have been possible in its current form.

Proofreading of parts of the thesis by Prof. Dr-Ing. Inka Müller and Dr. techn. Justyna Niestrawska is gratefully acknowledged.

My wife has played a major role in the success of the present work. From all my heart, I would like to thank her for her manifold support throughout the period of the doctorate.

Most of the methods and results presented in this thesis have been published previously in peer-reviewed research articles or peer-reviewed contributions to conference proceedings where the author of this thesis was either sole or shared first author. These publications are listed in appendix D of this thesis. Images, tables and text passages from these original works by the author are used in this thesis. Images and tables are referenced separately, phrases, sentences and text passages are referenced here only in general. The author gratefully acknowledges the editors' permissions to use content, figures and tables of the listed articles in this thesis.

Karben, February 2020

Andreas Wittek

Summary

This work focuses on the development of new non-invasive methods for the *in vivo* characterization of the individual elastic behavior of the human aortic wall. Due to the physiological function of the elastic properties within the cardiovascular system and its change with degenerative processes, this knowledge is of direct diagnostic relevance. In addition, the individual material properties are an important, prior to the work presented here unknown, determinant of patient-specific finite element models, which have been developed to calculate the maximum wall stress and to estimate the rupture risk of abdominal aortic aneurysms.

Using a modified device that provides time resolved 3D echocardiography with speckle tracking (4D ultrasound), a non-invasive *in vivo* full field measurement of human aortic wall motion was established in cooperation with industrial and clinical partners. It provided highly resolved motion functions of discrete material points and derived in-plane strain tensors for wall surface segments with a sizes between 1 and about 20 mm². This new measurement of displacement and strain was validated in an *in vitro* experiment with respect to its agreement with optical full field measurements and to its reproducibility under identical conditions (test-retest reliability).

Two different methods for the analysis of aortic wall motion were developed and applied to different patient cohorts in clinical studies. A comparison of the cyclic three-dimensional deformation of the proximal ascending and the abdominal aorta in terms of length and diameter change and twist provided deepened insight in the physiological “Windkessel” function of the ascending aorta. Statistical analysis of the distributions of local in-plane strains was used to obtain measures for size and heterogeneity of elastic aortic wall deformation (‘strain distribution indices’). A comparative clinical study in young volunteers and two groups of aged cardiovascular patients without and with abdominal aortic aneurysm showed that aortic walls reliably can be classified according to their cardiovascular health state by use of the obtained strain distribution indices and that these, therefore, are suited as new biomarker for cardiovascular health.

Two approaches were developed to characterize and model the individual elastic properties of the aortic wall. Firstly, a local distensibility coefficient has been introduced to linearly approximate and identify the heterogeneous local functional elastic properties in the physiological range *in vivo*. Secondly, an iterative Finite Element Model Updating approach to the inverse identification of the individual orthotropic and hyperelastic constitutive behavior of geometrically irregular aneurysmal walls was developed. It could be shown that constitutive parameter identification based on heterogeneous full field

strain data is feasible even though only two load cases are accessible non-invasively in vivo. The approach was verified numerically and the effect of the measurement uncertainty on the constitutive parameter identification was examined. Finally, the approach was applied exemplarily to in vivo data of three patients of different age and cardiovascular health state.

Zusammenfassung

Ziel dieser Arbeit war die Entwicklung neuer nicht-invasiver Methoden zur Charakterisierung des individuellen elastischen Verhaltens der menschlichen Aortenwand. Aufgrund der physiologischen Funktion der elastischen Eigenschaften im Herz-Kreislauf-System und deren Änderung bei degenerativen Prozessen und Erkrankungen hat die Kenntnis des individuellen elastischen Verhaltens zum einen unmittelbar diagnostische Relevanz. Zum anderen sind die individuellen Materialeigenschaften eine wichtige, bislang unbekannte, Bestimmungsgröße Patienten-spezifischer Finite Elemente Modelle, die zur Berechnung der maximalen Wandspannung und zur Abschätzung des Rupturrisikos von Bauchaaortenaneurysmen entwickelt wurden.

Unter Verwendung eines modifizierten kommerziellen Echtzeit-3D-Echokardiographiegeräts, dessen Software über einen Speckle-Tracking-Algorithmus verfügt (4D-Ultraschall), wurde in Zusammenarbeit mit industriellen und klinischen Partnern eine neuartige Vollfeldmessung der Verformung der Aortenwand etabliert. Die Messung liefert die räumliche Bewegungsfunktion diskreter materieller Punkte im Sinne der Kontinuumsmechanik über den Herzzyklus. Diese Daten ermöglichen die Bestimmung aller Komponenten des ebenen Dehnungszustandes für Gefäßwandsegmente mit einer Größe zwischen ca. 1 mm^2 und 20 mm^2 . Die etablierte Messung der Wandbewegung wurde in einem *in vitro*-Experiment hinsichtlich ihrer Messunsicherheit und ihrer Reproduzierbarkeit validiert.

Zwei Methoden zur Analyse der Wandbewegung wurden entwickelt und in klinischen Studien exemplarisch auf Patientengruppen angewendet. Ein Vergleich der dreidimensionalen Verformung der herznahen aufsteigenden Aorta und der Bauchaaorta führte zu einem verbesserten Verständnis der physiologischen Windkessel-Funktion der herznahen Aorta. Durch statistische Analyse der aus den Vollfeldmessungen erhaltenen Verteilungen lokaler Dehnungen wurden neue Maße für Größe und Heterogenität der elastischen Verformung der Wand gewonnen, sog. Dehnungs-Verteilungs- oder Wandbewegungs-Kennwerte. In einer vergleichenden klinischen Studie konnte gezeigt werden, dass diese Kennwerte zuverlässige Kriterien für die Klassifikation des pathologischen Zustands von Aortenwänden sind und sich daher als zusätzliche Biomarker für Erkrankungen der Aortenwand eignen.

Zur Identifikation der individuellen elastischen Eigenschaften der Aortenwand wurden im Rahmen dieser Arbeit zwei Ansätze entwickelt. Zum einen wurde ein lokaler Distensibilitätskoeffizient eingeführt. Er kann ohne Modellannahmen auf Basis der 4D Ultraschalldaten und nichtinvasiver Blutdruckmessungen bestimmt werden und ist proportional zur Inversen des Sekantenmoduls des lokalen nichtlinear elastischen Materialverhaltens im Bereich physiologischer Belastung durch den Blutdruck. Zum

anderen wurde ein iteratives Finite-Element-Model-Updating-Verfahren zur inversen Identifikation des individuellen orthotropen und hyperelastischen konstitutiven Verhaltens entwickelt, das auch auf Aorten und Aneurysmen mit geometrisch unregelmäßigen Konfigurationen angewendet werden kann. In einem numerischen Verifikationsexperiment konnte gezeigt werden, dass die Identifikation des Materialverhaltens auf Basis der mit 4D Ultraschall gemessenen Dehnungsfelder reproduzierbar möglich ist, obwohl nur zwei Lastfälle nichtinvasiv messbar sind. Die Auswirkung der in der Validierungsstudie bestimmten Messunsicherheit auf die Parameteridentifikation wurde untersucht. Schließlich wurden exemplarisch die elastischen Eigenschaften von drei Patienten identifiziert, die sich nach Alter und Herz-Kreislaufferkrankungen charakteristisch unterschieden.

Contents

Preface.....	I
Summary	III
Zusammenfassung.....	V
Contents.....	IX
Nomenclature	XV
1 Introduction	1
1.1 Motivation by the abdominal aortic aneurysm rupture risk estimation.....	1
1.2 Organization of the thesis.....	4
1.3 The heart and the physiological function of the arteries' elastic properties.....	5
1.3.1 Left ventricle and systemic circulation.....	5
1.3.2 Elastic and muscular arteries.....	11
1.4 Microstructural elements and composition of the aortic wall	12
1.4.1 Microstructural elements of aortic walls	12
1.4.2 Structural composition of the healthy aorta.....	15
1.5 Mechanical properties of the aortic wall	18
1.5.1 Stress-strain path I: reversible deformation.....	18
1.5.2 Stress-strain path II: irreversible deformation	19
1.5.3 Stress-strain path III: reversible deformation after irreversible, plastic deformation....	19
1.5.4 Pseudoelasticity	19
1.5.5 Anisotropy	19
1.5.6 Incompressibility	21
1.6 Axial prestretch and residual stresses.....	21

1.7	Degenerative changes of the aorta's elastic properties with age and pathology	23
1.7.1	Aging	23
1.7.2	Abdominal aortic aneurysm (AAA)	25
2	Continuum mechanical framework	29
2.1	Kinematics of finite deformations	29
2.2	Stress tensors	36
2.3	Elastic material properties	38
2.3.1	Cauchy elasticity	38
2.3.2	Hyperelasticity	39
2.3.3	Objectivity	42
2.3.4	Material symmetry	43
3	A method for non-invasive full field strain measurement	53
3.1	Ultrasound measurement of aortic wall deformation	53
3.2	Clinical data acquisition and post-processing	58
3.2.1	4D ultrasound examination and blood pressure measurement	58
3.2.2	Clinical post-processing: wall motion tracking	60
3.3	Deformation metrics based on customized 4D ultrasound wall motion data	62
3.3.1	Customized data interface	62
3.3.2	Motion function	63
3.3.3	Quantification of the size and global deformation of aortic wall segments	64
3.3.4	Highly resolved fields of local in-plane strains	68
3.4	Effects of increased spatial resolution on in vivo strain measurement	72
3.4.1	Study collective and in vivo data acquisition	73
3.4.2	Computation of circumferential in-plane wall strain with different spatial resolutions	73
3.4.3	Dependency of the strain values and distributions on the spatial resolution	74
3.4.4	Results	75
3.4.5	Discussion	77

3.5	Characteristic size of aortic wall motion in vivo.....	77
3.5.1	Study group	78
3.5.2	Data acquisition and customized post-processing.....	78
3.5.3	Wall displacement in young, elderly and AAA patients	79
4	In vitro validation of full-field wall motion measurement	81
4.1	Introduction	81
4.2	Methods of the in vitro validation study.....	83
4.2.1	Design of the study.....	83
4.2.2	Sample and experimental set up	85
4.2.3	Quantification of the agreement of 4D ultrasound and optical measurements.....	91
4.2.4	Methods for the quantification of the test-retest reliability	104
4.3	Results of the validation study	106
4.3.1	Agreement of 4D ultrasound and optical measurements.....	106
4.3.2	Reproducibility of 4D ultrasound measurements	112
4.4	Discussion of the validation results.....	115
4.4.1	Comparison of the validation results with literature values	118
4.5	Limitations of the validation study.....	121
5	Comparative Analysis of ascending and abdominal aortic wall motion	123
5.1	Introduction	123
5.2	Study collective and in vivo data acquisition	125
5.3	Statistics	126
5.4	Multiaxial deformation of the ascending and the abdominal aorta	128
5.5	Relations between deformation patterns and physiological function.....	132
5.5.1	Comparison with literature	134
5.5.2	Physiological function of longitudinal strain in the ascending aorta.....	134
5.5.3	Conclusions and limitations	138

6	Locally varying elastic behavior of human aortae in vivo	139
6.1	In vivo measures of aortic elasticity in the physiological range.....	139
6.2	The local distensibility coefficient	143
6.3	Indices for the characterization of the spatial distribution of the local elastic behavior	144
6.4	Distributions of local elasticity in young, aged and aneurysmal aortic walls	145
6.4.1	Study group and data acquisition	145
6.4.2	Statistics.....	146
6.4.3	Comparison of strain distribution indices.....	148
6.4.4	Comparison of distensibility distribution indices between patient groups.....	151
6.4.5	Correlation of distensibility distribution indices with age and diameter.....	153
6.4.6	Correlation of strain and distensibility distribution indices.....	155
6.5	Discussion and limitations.....	156
7	Identification of the orthotropic and hyperelastic constitutive behavior of aortic walls in vivo .	165
7.1	Introduction	165
7.1.1	State of research	165
7.1.2	Overview of the main steps of the inverse approach.....	168
7.1.3	Organization of the chapter	169
7.2	Assumptions for the patient-specific modeling	170
7.3	Theoretical basis for constitutive parameter identification in vivo	172
7.4	Constitutive equation.....	178
7.5	Non-invasive in vivo data.....	180
7.5.1	Patient data	180
7.5.2	Diastolic-systolic in-plane strain fields from 4D ultrasound measurements	181
7.6	Model-based estimation of systolic in-plane strains.....	182
7.6.1	Displacement and strain field as a function of the chosen constitutive model.....	182
7.6.2	Reference configuration, FE discretization and boundary conditions.....	182
7.6.3	In-plane strains as a function of the chosen constitutive behavior	183

7.7	Constitutive parameter identification strategy.....	186
7.7.1	Finite Element Model Updating workflow.....	186
7.7.2	Error function	188
7.7.3	Optimization algorithm	189
7.8	Numerical verification experiment.....	190
7.9	Results of the verification experiment.....	193
7.10	Individual constitutive behavior identified based on in vivo data.....	197
7.10.1	Constitutive parameters and stress-stretch curves	197
7.10.2	Estimated load-free configurations and recovery of in vivo in-plane strain states.....	200
7.11	Discussion and conclusions	203
8	Summary and outlook	211
9	References	213
	Appendix	229
A.	Derivatives of the pseudoinvariants	229
a.	4 th pseudoinvariant	229
b.	5 th Pseudoinvariant	230
c.	Pseudoinvariant for the coupling of two preferred directions	231
B.	Convergence study for the FE discretization of pressurized aortic segments	232
C.	First approach to a Finite Element Model Updating workflow	238
D.	List of first author publications that were used in this thesis	240
a.	Peer reviewed journal articles	240
b.	Peer reviewed contributions to conference proceedings	240

Nomenclature

Latin symbols

a	scalar $a \in \mathbf{R}$
\mathbf{a}	vector $\mathbf{a} \in \mathbf{R}^3$: $\mathbf{a} = a_i \mathbf{e}_i$
\mathbf{A}	second order tensor $\mathbf{A} \in \mathbf{R}^{3 \times 3}$: $\mathbf{A} = A_{ij} \mathbf{e}_i \otimes \mathbf{e}_j$
\mathcal{B}_0	load and deformation free natural configuration of a continuum body
\mathcal{B}_r	chosen reference configuration for description of the deformation of a continuum body
\mathcal{B}_t	any loaded and deformed current configuration of a continuum body
\mathbf{C}	right CAUCHY-GREEN strain tensor; $\mathbf{C} \in \mathbf{R}^{3 \times 3}$ is a rotation-free deformation measure for finite deformations
\mathbf{E}	right GREEN-LAGRANGE strain tensor
\mathbf{F}	deformation gradient, second order tensor; $\mathbf{F} \in \mathbf{R}^{3 \times 3}$
\mathbf{I}	second order unity tensor; $\mathbf{I} \in \mathbf{R}^{3 \times 3}$
\mathbf{P}^I	1 st PIOLA-KIRCHHOFF stress tensor
\mathbf{P}^{II}	2 nd PIOLA-KIRCHHOFF stress tensor
\mathbf{R}, \mathbf{Q}	rotation tensors
Q_1, Q_3	1 st and 3 rd quartile, respectively. The interval $[Q_1, Q_3]$ is the interquartile range.
$Q_{0.025}, Q_{0.975}$	2.5 % and 97.5 % quantile, respectively. The interval $[Q_{0.025}, Q_{0.975}]$ is the 95 % confidence interval.
\mathbf{S}	nominal stress tensor
\mathbf{U}, \mathbf{V}	right and left stretch tensor, respectively; $\mathbf{U}, \mathbf{V} \in \mathbf{R}^{3 \times 3}$
X	material point, regardless of its reference or current position in space
\mathbf{X}_0	position vector of a material point in its load and deformation free natural configuration \mathcal{B}_0 ; $\mathbf{X}_0 \in \mathbf{R}^3$
\mathbf{X}	position vector of a material point in its (chosen) reference configuration; $\mathbf{X} \in \mathbf{R}^3$
$\mathbf{X}_{i,j}$	discrete position vector of a material point X in its reference configuration \mathcal{B}_r
\mathbf{x}	position vector of a material point in a loaded and deformed current configuration; $\mathbf{x} \in \mathbf{R}^3$

$\mathbf{x}_{i,j,k}$ discrete current position vector of a material point X as obtained from 4D ultrasound measurements at time point k of the cardiac cycle; indices i and j refer to placement of the discrete material point into subsets the wall motion data as exported from the Toshiba ACP; i indicates the “height” and j the “degree” of the material point.

Greek symbols

$\boldsymbol{\varepsilon}$ nominal or BIOT’s strain tensor; $\boldsymbol{\varepsilon} \in \mathbf{R}^{3 \times 3}$ is a rotation-free deformation measure for finite deformations

λ_i principal stretch in direction of basis vector \mathbf{e}_i , $i = 1, 2, 3$, $\lambda_i \in \mathbf{R}$; eigenvalue of \mathbf{F}

$\chi: \mathcal{B}_a \rightarrow \mathcal{B}_b$ motion function that maps one configuration of a continuum body onto another configuration

Mathematical operators

\cdot scalar or inner product of two tensors

$:$ double scalar product or double contraction of two second order tensors. For $\mathbf{A} = A_{ij}\mathbf{e}_i \otimes \mathbf{e}_j$ and $\mathbf{B} = B_{kl}\mathbf{e}_k \otimes \mathbf{e}_l$ it is defined as
 $\mathbf{A}:\mathbf{B} = A_{ij}\mathbf{e}_i \otimes \mathbf{e}_j : B_{kl}\mathbf{e}_k \otimes \mathbf{e}_l := A_{ij}B_{kl}(\mathbf{e}_i \cdot \mathbf{e}_k)(\mathbf{e}_j \cdot \mathbf{e}_l) = A_{ij}B_{ij} \in \mathbf{R}$.

\otimes dyadic or outer product of the vectors \mathbf{a} and \mathbf{b} : $\mathbf{a} \otimes \mathbf{b} = a_i b_j \mathbf{e}_i \otimes \mathbf{e}_j$

\circ coupling of two mappings

$\langle \mathbf{e}_i \otimes \mathbf{e}_j \rangle$, $i, j = 1, 2, 3$ gives the basis system of a tensor in matrix representation

Abbreviations

2D-/3D-STE time resolved two-dimensional/three-dimensional ultrasound imaging of the heart combined with speckle tracking

3D ultrasound time resolved three-dimensional ultrasound without speckle tracking

4D ultrasound time resolved three-dimensional ultrasound combined with speckle tracking

AAA abdominal aortic aneurysm

A. abd. abdominal aorta

A. asc. ascending aorta

ACP Advanced Cardiac Package

AV atrioventricular

BMI body mass index

BP blood pressure

BC boundary condition

bpm beats per minute

cct, ct	counterclockwise twist, clockwise twist, respectively
cfPWV	carotid-femoral pulse wave velocity
circ.	circumferential
CS	circumferential strain
CT	computed tomography
CV	cardio-vascular
CVD	cardio-vascular disease
cyclic strain	peak-to-peak amplitude of the strain that is observed throughout the cardiac cycle
DC	distensibility coefficient
DDI	distensibility distribution index
ECG	electrocardiogram
ECM	extracellular matrix
EVAR	endovascular repair
FE	finite element
FEA	finite element analysis
FEM	finite element method
FEMU	Finite Element Model Updating
fps	frames per second
HI	heterogeneity index \equiv coefficient of variation of the distribution of systolic local wall strains
HV	healthy volunteer
ICC	intraclass correlation coefficient
ILT	intra-luminal thrombus
IQR	interquartile range
LSR	local strain ratio \equiv ratio of the local peak and the mean of the distribution of local systolic wall strains
LV	left ventricle (of the human heart)
MDCT	cardiac multi-detector computed tomography
mmHg	millimeter mercury column; 1 mmHg = 1 torr = 133.32 Pa
MRI	magnetic resonance imaging
PAOD	peripheral aortic occlusive disease
PWV	pulse wave velocity
ref.	reference
RF	radio frequency
ROI	region of interest
sd	standard deviation

s.e.m.	standard error of the mean
SMC	smooth muscle cell
STE	speckle tracking echocardiography
wt	wall thickness
y.o.	years old

Anatomical direction designations

caudal	towards the tail or buttock
cranial	towards the skull
ventral	towards the abdomen, at the front of the body
dorsal	towards/at the back
proximal	towards or at the center of the body or towards the heart
distal	towards or at the periphery of the body

1 Introduction

1.1 Motivation by the abdominal aortic aneurysm rupture risk estimation

An abdominal aortic aneurysm (AAA) is a degenerative disease of the human aorta, which is characterized by its permanent local dilatation to a diameter of ≥ 30 mm, compared to 15 to 20 mm of the healthy adult abdominal aorta [Figure 1-1]. Men younger than 55-60 years and women are rarely affected. Main risk factors for developing an AAA are age > 60 years, male sex, atherosclerosis, hypertension, ethnicity, family history and smoking [Wanhainen et al. 2019]. AAAs occur with a rate between 1.3% and 8.9% in men over 60 years and 2.2% in women [Vorp 2007; Nichols et al. 2011]. The main danger of this mostly asymptomatic disease is the rupture of the aneurysmal wall [Frömke 2006; Kühnl et al. 2017; Wanhainen et al. 2019] with severe bleeding into neighboring tissue and the abdomen. The consequence of acute bleeding from the high pressure system is hypovolemic shock and cardiovascular instability, which can lead to the death of the patient within minutes. Therefore, AAA rupture still is associated with mortality rates $\geq 80\%$ [Debus and Gross-Fengels 2012; Reimerink et al. 2013b; Reimerink et al. 2013a; LeFevre 2014; Scaife et al. 2016; Kühnl et al. 2017].

There is no drug therapy available to slow down disease progression or even heal an AAA. Also exercise has not proven to stop or reduce AAA growth. The only available therapy is elective repair: Open surgical repair and increasingly minimally invasive endovascular repair (EVAR) are available as treatment options for non-ruptured AAA [Wanhainen et al. 2019]. In both cases, the treatment consists of placing an implant in the abdominal aorta which, instead of the weakened aneurysm wall, absorbs the mechanical load of the pulsatile blood pressure and thus prevents its rupture. Several randomized controlled trials have compared the outcome of open surgical repair and EVAR [Greenhalgh et al. 2004; Blankensteijn 2005; Becquemin et al. 2011; Lederle et al. 2016]: Consistently, these studies report lower perioperative mortality after EVAR (0.5-1.7% vs. 3.0-4.7% for open repair). However, this early survival benefit is lost after 1-3 years due to the necessity of secondary interventions resulting in comparable long-term survival. In a clinical study (EVAR 1 trial), Greenhalgh et al. [2004] observed increased aneurysm related mortality in the EVAR group beyond 8 years after surgery, mostly due to secondary

aneurysm sac rupture (7% vs. 1%, Wanhainen et al. 2019). These findings necessitate life-long imaging surveillance after EVAR. Some studies even state that, because of perioperative and long-term complications, short-term survival of AAA patients is decreased and long-term survival is not increased by surgical or endovascular treatment compared to pure surveillance [UK Small Aneurysm Trial Participants 2002; Karthikesalingam et al. 2013]. The “immediate decision about the size at which an aneurysm should be repaired is framed by the balance between the risk of aneurysm rupture [...] and the risk of operative mortality for aneurysm repair.” [Wanhainen et al. 2019]

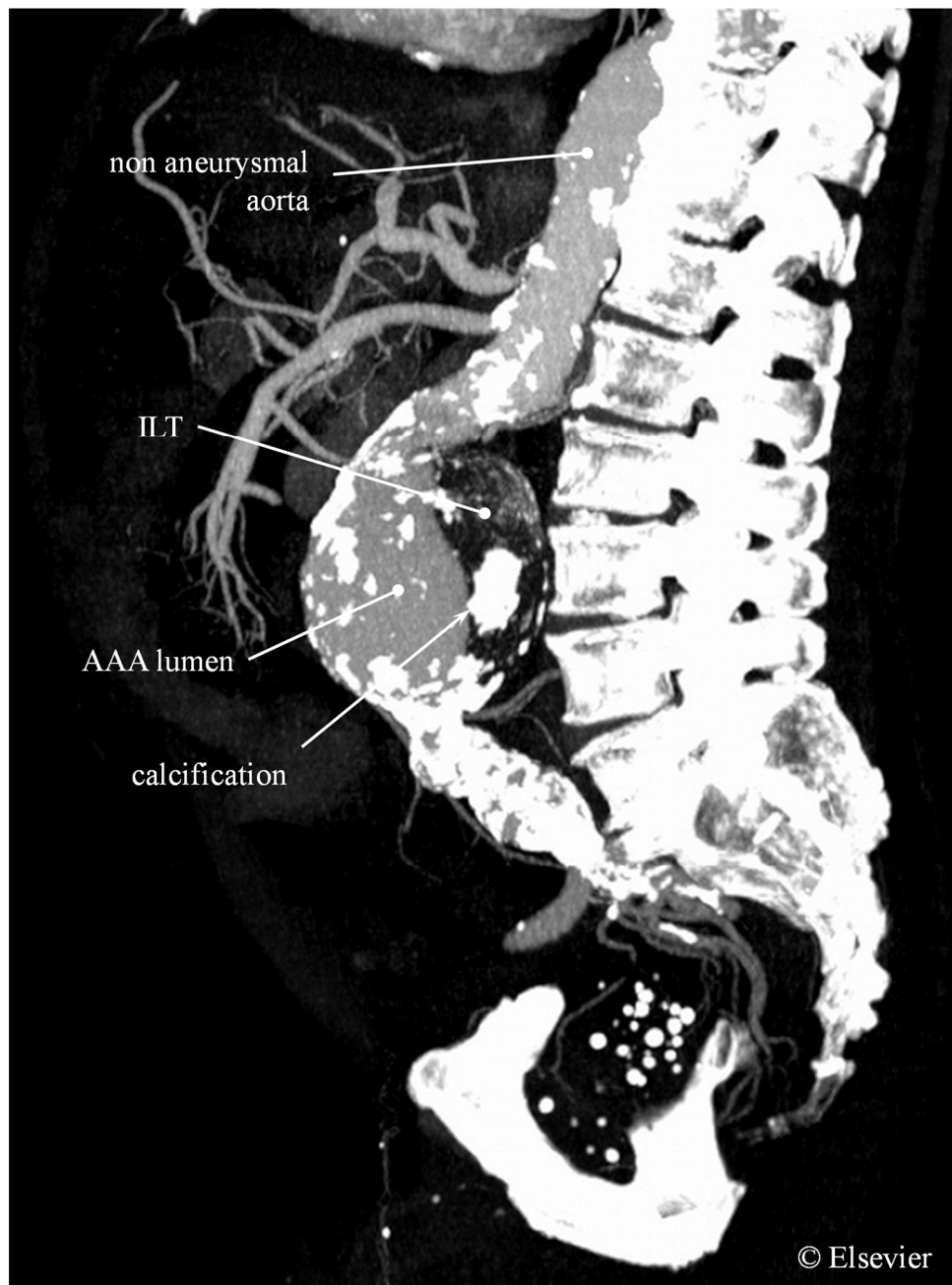


Figure 1-1 Sagittal cross-sectional view of an abdominal aortic aneurysm (AAA) with intra-luminal thrombus (ILT) obtained from a CT scan. [Figure reprinted from Buijs et al. 2013 with permission from Elsevier; captions in the image were added by A. Wittek]

Therefore, the assessment of the individual immediate rupture risk, on which alone the decision on a therapeutic intervention is based, is of particular importance. The statistical correlation of the rupture risk with the maximum diameter of the AAA and its growth rate has been demonstrated in a number of studies [see e.g. Lederle et al. 2002, UK Small Aneurysm Trial Participants 1998, 2002]. The risk doubles in AAA with a diameter between 3.0 and 5.4 cm per 0.5 cm growth [Thompson et al. 2013]. Based on these findings, the clinical standard is to monitor "small" AAA with diameters between 3.0 and 5.4 cm at regular intervals and to treat AAA with diameters ≥ 5.5 cm or a growth rate > 1 cm/year either by open surgical or by endovascular repair. However, up to 13% of small AAA ($d < 5$ cm) rupture [Cronenwett et al. 1985] and 54% of untreated large AAA with diameters between 7.1 and 10 cm remain stable [Darling et al. 1977]. Thus, the need for additional patient-individual biomarkers for short-term AAA rupture risk as basis for improved clinical decision making is widely acknowledged [Vorp 2007; Humphrey and Holzapfel 2012; Kontopodis et al. 2015].

Because the rupture of the AAA wall represents its mechanical failure, the engineering concept of mechanical strength verification has been adopted during the past two decades in order to obtain additional patient-individual rupture risk predictors [Vande Geest et al. 2006; Vorp 2007; Maier et al. 2010; Humphrey and Holzapfel 2012; Martufi and Christian Gasser 2013; Farotto et al. 2018]. Mostly, the individual wall stress that results from the loading of the wall by pulsatile blood pressure and residual stresses is estimated by nonlinear Finite Element (FE) analyses whereas statistical models have been proposed to estimate the tensile strength of the individual wall non-invasively [Vande Geest et al. 2006]. In order to be able to solve the direct solid mechanical boundary value problem, i.e. calculate resulting stress, displacement and strain fields in the aortic wall with the required accuracy and reliability, the computational models have to be determined with regard to geometry, material properties and applied loads and boundary conditions [Fung 1993; Avril et al. 2008; Humphrey and Holzapfel 2012]. Because of the great inter-individual variance of these biomechanical parameters, *patient specific* computational models have to be developed if clinical diagnostic use is intended [Taylor and Figueroa, 2009]. This is still a challenge because all in vivo data on which the models are based have to be acquired non-invasively and radiation free for ethical reasons. Thus, most of the proposed FE models are patient-specific only with regard to the geometrical configuration which is obtained from medical imaging data and with regard to blood pressure as the most relevant load. In contrast, neither the wall thickness, nor the individual nonlinear elastic and orthotropic constitutive behavior of the AAA wall are known, cf. e.g. Humphrey and Holzapfel [2012], Martufi and Christian Gasser [2013] and Gasser [2016]. Population averaged values obtained from post-mortem studies of intraoperatively excised tissue samples are used instead. Joldes et al. [2015a] have shown that AAA walls are statically determinate structures and that, therefore, the computation of AAA wall stress is independent of the individual elastic properties if the deformed current configuration of the wall is known that corresponds to the current pressure load. In either approach, the fact that the individual material properties are unknown limits the predictive value of the FE analyses for AAA rupture risk: Typically, rupture does not occur when blood pressure of

hypertensive patients is well regulated by drugs at rest as is mostly the case during follow up examinations in the clinics, but under strongly elevated pressures. These conditions, however, cannot be assessed using the ‘material-free’ approach proposed by Joldes et al. [2015a]. Using population averaged instead of individual constitutive parameters, the results of the wall stress analyses will be the more inaccurate the further the simulated conditions are from the observed physiological conditions. This deficiency of most clinically applied FE analyses makes it understandable that – despite continuous research on this topic since about 20 years – “none of the proposed [wall stress based] biomechanical [...] markers are conclusively associated with AAA rupture or growth” [Indrakusuma et al. 2016].

This work focuses on the development of new non-invasive in vivo methods to assess the locally varying, heterogeneous cyclic deformation and the anisotropic and nonlinear elastic properties of the individual human aortic and aneurysmal wall. One motivation for this was to provide a tool to overcome the described shortcoming of previous AAA wall stress analyses and to contribute to the improvement of their accuracy and predictive value. In addition to this, the mechanical environment and the elastic properties of arteries, besides biochemical or genetic factors, play an important role in the origin and progression of vascular diseases [cf. e.g. Kassab 2006; Thubrikar 2007; Nichols et al. 2011]. It has been shown that changes in the individual elastic properties are independent predictors of cardiovascular disease [Boutouyrie et al. 2002] and, if observed in AAAs, may be related to imminent rupture [Wilson et al. 2003]. This opens the perspective to use the more detailed information on the elastic properties of the individual AAA wall that is available through the methods developed in this work as indicative biomarkers for the pathophysiological state of the aneurysmal wall.

1.2 Organization of the thesis

Chapter 1 gives an introduction to the pathophysiological background: first, the physiological function of the arteries’ elastic properties within the systemic circulation is briefly described. In a second step, the microstructural composition and corresponding elastic behavior of the healthy aortic wall are addressed. Finally, a brief view on the major degenerative changes of the aortic wall with age and development of an AAA is taken.

Chapter 2 outlines the theory of finite nonlinear elastic deformations as the continuum mechanical framework of the methods that were developed within this thesis. Particular attention is paid to different types of material symmetries.

Chapter 3 is dedicated to full field deformation and strain measurement of aortic wall motion by real-time three-dimensional ultrasound with speckle tracking (4D ultrasound): First, the clinical measurement and the modified data interface are described that provides motion functions of discrete material points on the imaged aortic wall. Then, the methods for computation and analysis of the aorta’s cyclic deformation are presented that were implemented in this thesis.

Chapter 4 is dedicated to the methods and results of the validation of 4D ultrasound measurement uncertainty and repeatability.

Chapter 5 presents the results of a clinical study, in which the developed methods were applied: the cyclic 3D deformations of the proximal ascending and of the suprarenal abdominal aortic segments were compared. The identified distinct deformation patterns are discussed with regard to the specific aortic segment's physiological function.

In chapter 6, a local distensibility coefficient is introduced as a novel in vivo measure for the aortic wall's local functional elastic properties in the physiological range. Statistical indices of strain and distensibility fields are proposed as biomechanical biomarkers that contain condensed information about the cyclic elastic behavior and the heterogeneity of the material. The results of a clinical study are reported and discussed in which these methods were applied to different patient collectives, exemplarily, in order to test the pathophysiological meaningfulness of the developed methods and biomechanical biomarkers.

Finally, chapter 7 presents a Finite Element Model Updating approach to the in vivo identification of the individual orthotropic hyperelastic constitutive behavior of the aortic and aneurysmal wall. The uniqueness of the results and the effects of the determined measurement uncertainty on identified parameters was investigated by means of a numerical verification experiment. Exemplarily, the approach was applied to in vivo data.

Chapters 4 to 7 are concluded by a discussion of the presented results, each.

In chapter 8 the major results of the work are briefly summarized and discussed.

1.3 The heart and the physiological function of the arteries' elastic properties

Because of its relevance for the understanding of the cyclic elastic deformation and the function of the elastic properties of the aortic wall, a brief sketch of some mechanical aspects of the physiology of the cardio-vascular (CV) system is given in this section. Particular attention is paid to the left ventricle (LV) of the heart from which the ascending aorta originates.

1.3.1 Left ventricle and systemic circulation

The CV system consists of the heart and the blood vessels. It can be subdivided into the *pulmonary circulation*, that includes the right heart and the lung, and the *systemic circulation*, which, amongst others, includes the left heart and the aortic tree and supplies oxygenated and nutrient-rich blood to the systemic organs, e.g. the heart itself, skeletal muscle, brain, bone, kidney and others. The left and the

right heart [cf. Figure 1-2] consist of an atrium at which blood arrives from the circulation and a ventricle from which blood is ejected into circulation. Atria and ventricles are separated by the atrioventricular (AV) plane, a fibrous, semi-rigid structure that serves as the “skeleton” of the heart, at which the musculature (myocardium) is fixed that is a principal constituent of the heart wall [Maksuti et al. 2015]. The AV plane marks the bases of the conical left and right ventricles, whereas the (lower) caudal endings of the ventricles that are attached to the diaphragm are called the apices. The whole heart and the roots of the great vessels arriving at and originating from the heart are enclosed by the pericardium, a two layered sac that contains the pericardial fluid. The pericardium is fixed to tissues surrounding the heart, in particular it is fixed at the lower or apical ending to the diaphragm that separates the thorax from the abdomen. On the one hand, the pericardium constrains the volume change of the total heart by this fixation [Maksuti et al. 2015 and citations therein: Watkins and LeWinter 1993; Fritz et al. 2014]. On the other hand, the pericardial fluid provides lubrication and enables the relative sliding motion between the contracting and relaxing myocardium and surrounding structures.

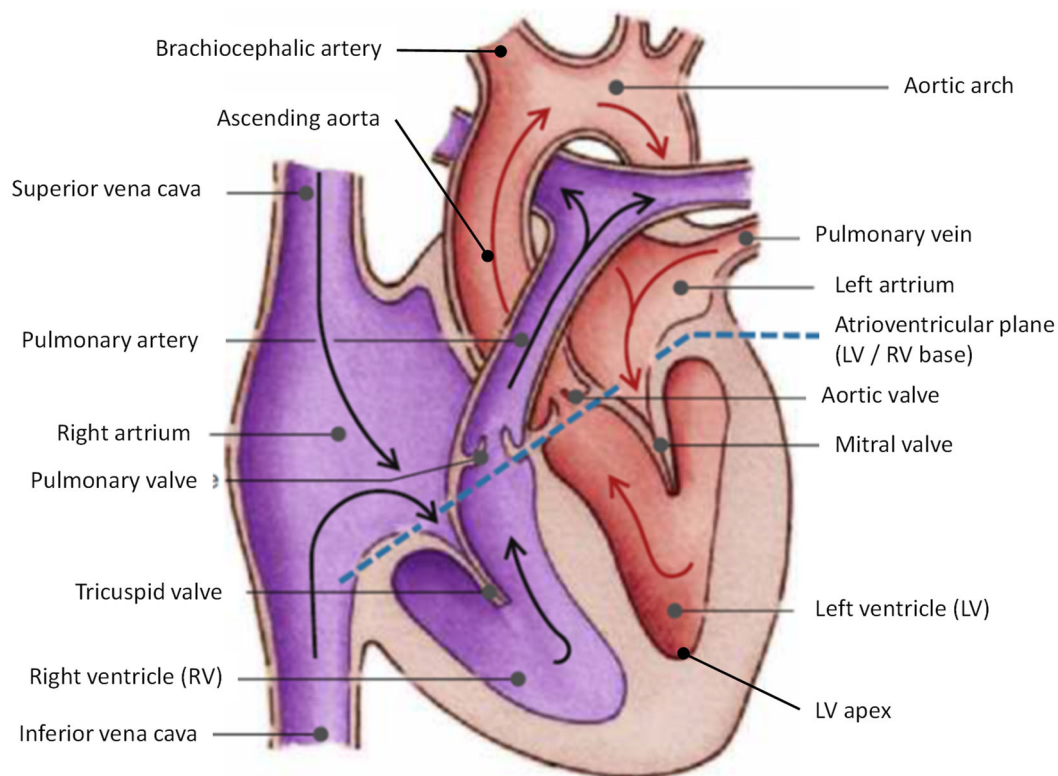


Figure 1-2 Cross sectional scheme of the four chambers of the right (violet) and left (red) heart. Atria and ventricles are separated by the atrioventricular (AV) plane (blue dashed line) in which the tricuspid valve and the mitral valve are situated that prevent backflow of blood from the ventricles to the atria during ventricular systole. Additionally, the origins of the pulmonary artery and of the aorta are located in the atrioventricular plane. Black and red arrows indicate the direction of the blood flow. In each cardiac cycle, the left ventricle ejects a blood volume into the ascending aorta and thereby supplies the systemic circulation with oxygenated blood. [Figure reprinted from Pape et al. 2019 with permission from Thieme, captions in the image were translated by A. Wittek]

Within the circulation, the heart functions as a pulsatile pump: its pumping effect results from the rhythmical succession of (active) contraction and (passive) relaxation of the myocardium, predominantly of the by far stronger ventricular musculature. The flow direction within the heart is regulated by the heart valves between the atria and the ventricles (tricuspid and mitral valve), the pulmonary valve and the aortic valve. All valves are located in the AV plane. [Klinke and Silbernagl 2010]

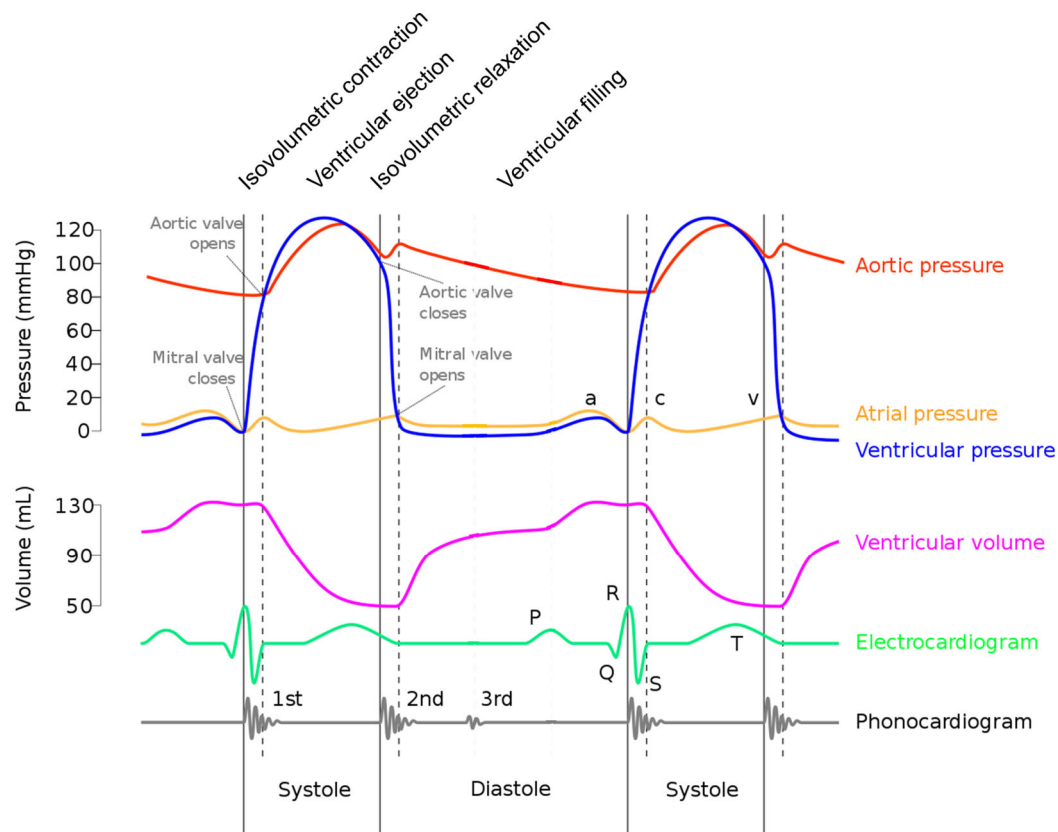


Figure 1-3 Wiggers diagram of pressure, volume curves and electrocardiogram (ECG) throughout the cardiac cycle. [Image: adh30 revised work by Daniel Chang MD who revised original work of DestinyQx; Redrawn as SVG by xavax (https://commons.wikimedia.org/wiki/File:Wiggers_Diagram_2.svg), modified by A. Wittek, <https://creativecommons.org/licenses/by-sa/4.0/legalcode>]

Because of its relevance for deformation, loading and function of the ascending aorta that originates from the LV and is the subject of chapter 5 of this thesis, the phases of the cardiac cycle [cf. Figure 1-3] are described here for the LV of a population average young and healthy subject according to Pape et al. [2018]:

Ventricular systole

- (i) Isovolumetric contraction: The LV has arrived at its maximum volume and is fully filled with oxygenated blood from the pulmonary circulation whereas the left atrium has its minimum volume. The LV myocardium starts to contract actively. Because the mitral valve and the aortic valve are closed, the LV pressure increases rapidly without volume change. The starting point of ventricular systole is marked in the electrocardiogram (ECG) by the peak ('R') of the QRS complex.

(ii) **Ventricular ejection:** As soon as the ventricular pressure exceeds the aortic pressure, the aortic valve opens and blood is ejected into the ascending aorta while the myocardium continues to contract and the ventricular and aortic pressure increases to its maximum of 120 mmHg (systolic blood pressure).

Ventricular diastole

(iii) **Isovolumetric relaxation:** Having reached its maximum contraction, the myocardium starts to relax passively. This leads to a rapid drop to zero pressure in the LV and, consequently, a reversal of the pressure gradient between the LV and the aorta, resulting in the closure of the aortic valve that is marked in the aortic pressure curve by the so-called incisura. The closed aortic valve prevents back-flow of ejected blood and guarantees the maintenance of a non-zero blood pressure of about 80 mmHg in the systemic arteries during diastole.

(iv) **Ventricular filling:** During ventricular systole, the left atrium has been refilled by oxygenated blood arriving from the pulmonary circulation. Due to the pressure drop in the LV the mitral valve opens and the LV refills. In this phase, the myocardium is expanded passively by elastic recoil and blood pressure.

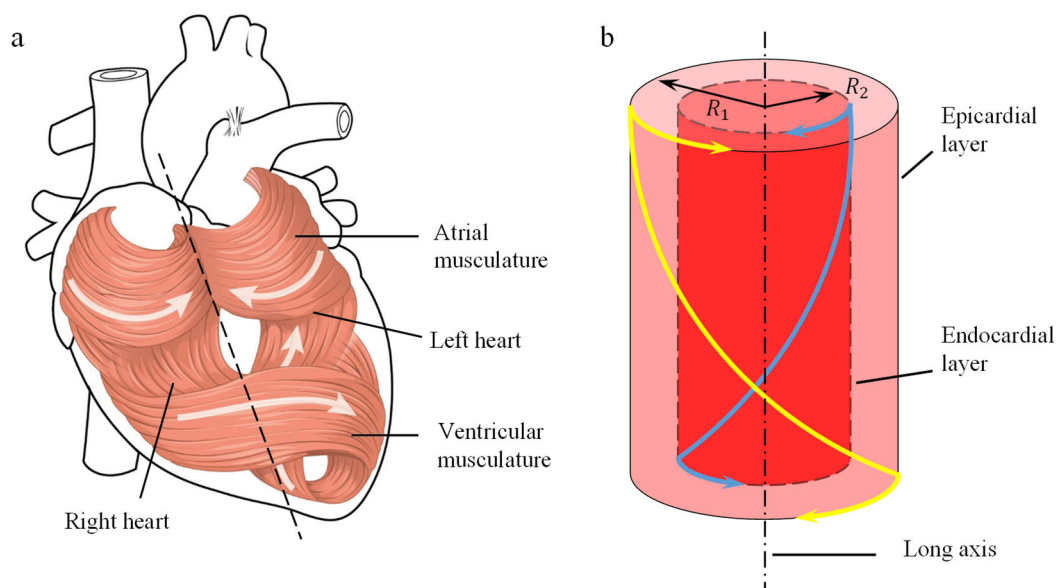


Figure 1-4 (a) Illustration of the helical ventricular myocardial band (HVMB) model of the atrial and ventricular musculature (myocardium) according to Torrent-Guasp [1957] and Buckberg et al. [2015]. [Image: OpenStax College (https://commons.wikimedia.org/wiki/File:2006_Heart_Musculature.jpg), „2006 Heart Musculature“, modified by A. Wittek, <https://creativecommons.org/licenses/by/3.0/legalcode>] (b) The schematic representation of the helical arrangement of the left ventricular myocardium illustrates that contraction of the fibers of the epicardial (outer) and endocardial (inner) layer create opposite twisting moments with a resulting nonzero moment due to the larger distance R_1 of the epicardial layer from the long axis of the ventricle compared to the distance R_2 of the endocardial layer. The yellow and blue solid lines indicate the epicardial and endocardial fiber directions, respectively. The arrows show the corresponding twist resulting from fiber contraction [Figure reprinted after Buckberg et al. 2015 with permission from Oxford University Press]

Neglecting differentiation into individual fiber tracts, Torrent-Guasp [1957] showed by manual dissection that the myocardium of the left and right atria and ventricles can be unfolded into a single flattened

rope-like band with muscle fibers aligned to its longitudinal direction. Refolding of this band into interconnected loops constitutes the four chambers of the heart [Figure 1-4 a]. The weaker atrial musculature forms the 'basal loop' that exhibits circumferential or horizontal fiber orientation. In contrast, the stronger myocardium of the left and right ventricle is formed by the conical 'apical loop', the fibers of which are arranged helically. In particular, the LV myocardium, which is the strongest section of the heart musculature, is formed by an inner (endocardial) helix with a fiber direction of $+60^\circ$ measured counterclockwise with respect to the horizontal direction that is covered by an outer (epicardial) helix that shows a fiber direction of -60° [Figure 1-4 b, Buckberg et al. 2015]. Because of this helical arrangement of the ventricular musculature that drives the ejection of blood volume against the arterial blood pressure, systolic contraction predominantly results long axis contraction that is coupled with twisting of the LV and rotation of the AV plane.

Based on previous findings by Hoffman and Ritman [1985], Lundbäck [1986] and Carlsson et al. [2004; 2007], Maksuti et al. [2015] have modeled the heart as a displacement pump with the AV plane as piston unit: "Throughout the cardiac cycle, the AV plane moves back and forth in the [long axis] base-apex direction, creating reciprocal volume changes between atria and ventricles while keeping almost constant total heart volume. During ventricular systole, the AV plane is pulled towards the apex by the shortening of cardiac muscle, generating a volume displacement in the direction of the arteries (the stroke volume of the heart). At the same time, this downward movement produces atrial expansion, allowing for inflow from the veins to the atria, which results in the quantitatively most important contribution to atrial filling [Steding-Ehrenborg et al. 2013]. During ventricular diastole, the AV plane moves back to its initial position, redistributing blood from the atria to the ventricles (the ventricular filling volume)."

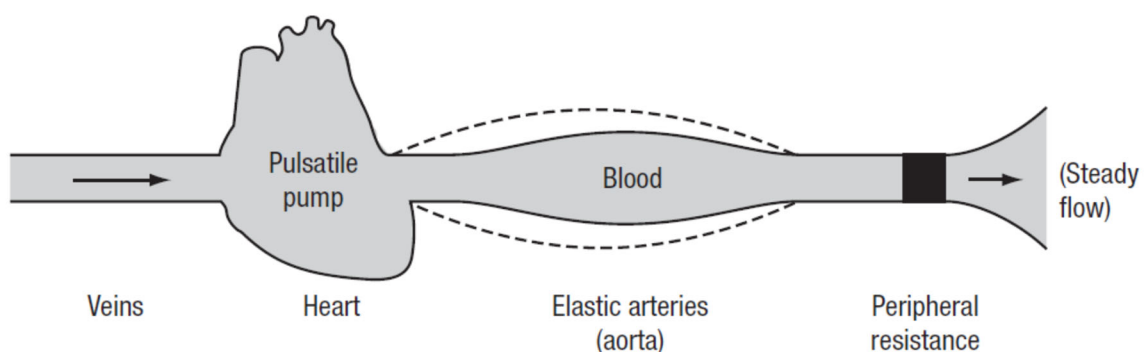


Figure 1-5 Schematic representation of the Windkessel model of the aorta. [Reprinted from Nichols et al. 2011 with permission from CRC after Westerhof et al. 2009]

Only during the ventricular ejection phase, i.e. about $1/3^{\text{rd}}$ of the cardiac cycle, blood is ejected from the heart into the systemic circulation and a pressure gradient between the LV and the systemic arteries is built up that drives blood flow towards the peripheral vessels and the organs. Because of its

elastic properties, the aortic wall is expanded in this phase by the increasing blood pressure and the LV contraction [cf. chapter 5, Wittek et al. 2016b] and portions of blood volume and elastic energy are stored in the deformed wall. During isovolumetric relaxation, ventricular filling and isovolumetric contraction, the aortic valve prevents the backflow of blood from the aorta into the LV. The pressure gradient towards the periphery and, consequently, blood flow in the systemic circulation are maintained during these phases by the elastic energy stored in the aortic wall: the aortic wall contracts due to elastic recoil and the stored blood volume is forwarded to the systemic circulation. This essential contribution of the aorta's and the systemic arteries' elastic properties to the maintenance of the circulation during diastole is called 'Windkessel' effect (Figure 1-5). [Westerhof et al. 2009; Pape et al. 2018; Nichols et al. 2011; Caro 2012]

A second important function of arterial elasticity is to prevent constructive interference of initial and reflected pressure waves and consequent hypertension as well as the increase of pressure load on the left ventricle: The pulse pressure wave that originates from the LV propagates with finite *pulse wave velocity* (PWV) in the elastic arterial tree [Figure 1-6].

According to the MOENS-KORTEWEG equation [Nichols et al. 2011], that holds for a NEWTONIAN fluid in a thin-walled cylindrical tube, the PWV depends on the elastic properties of the systemic arteries:

$$PWV = \sqrt{\frac{Eh}{\rho d_i}}, \quad \text{eq. 1-1}$$

where

- E is the YOUNG's modulus in circumferential direction,
- h is the wall thickness,
- d_i is the inner (or mean) diameter of the tube and
- ρ is the density of blood.

Since the elastic properties of arterial walls are not linear, E is not a proper YOUNG's modulus that describes the constitutive behavior, but a secant modulus that linearly approximates the elastic response of the whole arterial tree in the physiological pulsatile loading range.

The propagating pulse pressure wave is reflected in part at every discontinuity in the arterial tree [Figure 1-6], e.g. at every bifurcation where the vessel diameter changes. Major sites of reflection are the branching of the abdominal aorta into the iliac arteries and the transition from the large arteries into arterioles and capillaries. In a young and healthy CV system, heart rate and elastic properties (and resulting PWV) are harmonized to one another so that the initial pressure wave is not amplified by constructive interference with the reflected wave(s). Moreover, PWV is such that the reflected wave reaches the LV again only in early diastole when the aortic valve is already closed. In this way, the elastic properties of the arterial walls ensure that the reflected pressure wave does not increase the load against which the myocardium of the LV has to work. [O'Rourke et al. 2018]

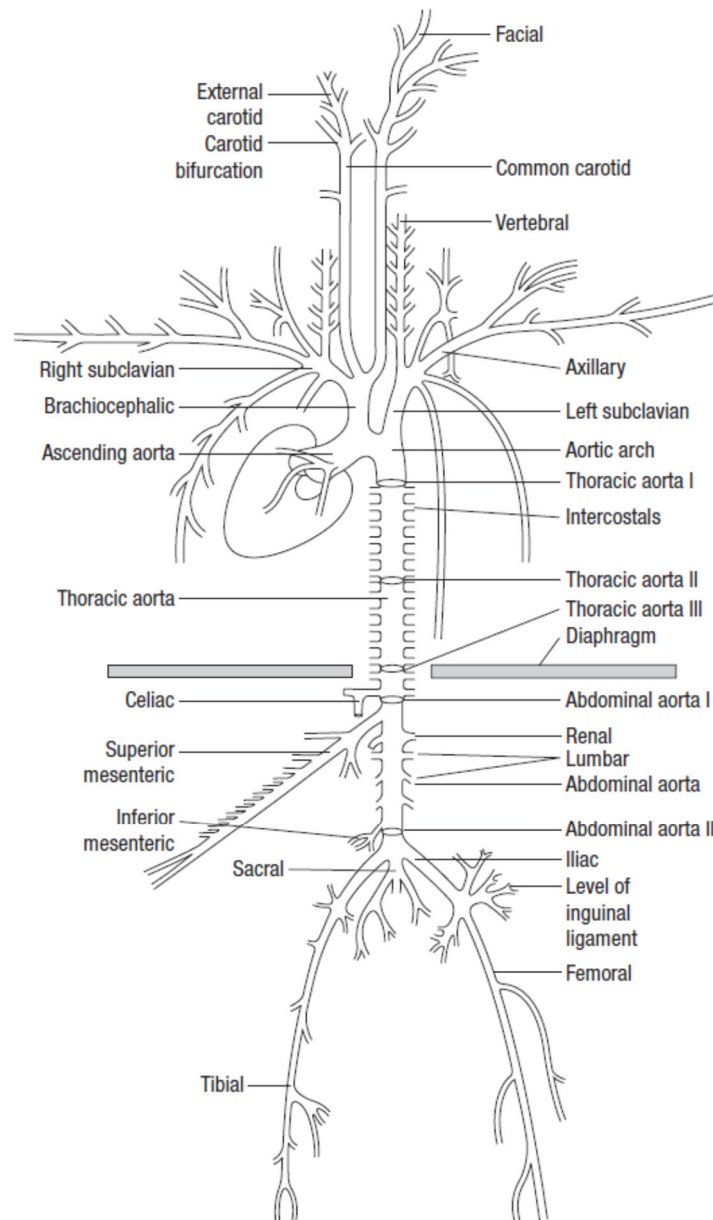


Figure 1-6 Schematic view of the “arterial tree”, i.e. the (elastic) aorta and (muscular) branching arteries. With every parting branch, volume flow rate is reduced in each of the branches. Consequently, diameter and wall thickness are reduced continuously along the arterial tree with increasing distance from the heart. [Figure reprinted from Nichols et al. 2011 with permission from CRC Press.]

1.3.2 Elastic and muscular arteries

The systemic arteries can be subdivided into elastic and muscular vessels. The *elastic arteries* are large conduit vessels that are found close to the heart, e.g. the aorta that is the main subject of this work and the common carotid artery. In contrast, the smaller arteries and arterioles that are situated more distally to the heart in the limbs and in general in the periphery of the body (e.g. the femoral arteries) are of the muscular type. The main difference between both types is the proportion and function of smooth muscle cells (SMCs) in the media. Only a smaller amount of smooth muscle cells is found in the media of elastic

arteries compared to muscular arteries. Their primary function is the remodeling of the wall by synthesizing and organizing extracellular matrix components such as collagen. Elastic arteries respond passively to external loads and their mechanical behavior is determined by the main load bearing components, elastin and collagen, and the composition of the extracellular matrix.

In contrast, the media of *muscular arteries* and arterioles mainly consists of helically arranged smooth muscle cells. These are able to actively change the cross-section of the vessel in response to wall shear stress due to blood flow. Thereby, muscular arteries regulate blood pressure and prevent hypertension. [Fung 1993; Nichols et al. 2011; Caro 2012]

1.4 Microstructural elements and composition of the aortic wall

1.4.1 Microstructural elements of aortic walls

Aortic walls are composed of different types of living cells and non-living extracellular matrix (ECM) elements. One primary function of the cells that are embedded in the wall (smooth muscle cells and fibroblasts) is the production and reproduction of the extracellular matrix, which is the load-bearing part of the wall. Two phenotypes of smooth muscle cells exist: one of these has an active contractile mechanism that is comparable to skeletal muscle, but cannot be controlled consciously. This phenotype is found predominantly in arteries of the muscular type. Besides this, a synthetic phenotype of smooth muscle cells exists that plays an important part in the remodeling of the aortic wall: it produces growth factors, protein degrading enzymes (proteases) and ECM components and organizes the ECM microstructure by depositing newly synthesized components, in particular collagen. This synthetic phenotype is dominant in elastic arteries such as the aorta. [Lesauskaite et al. 2003; Nichols et al. 2011; Niestrawska 2019]

The *extracellular matrix* consists of structural, fiber-like proteins, elastin and collagen, and of the unstructured ground substance that, together with smooth muscle cells, fills the interstices of the structural elements [Wolinsky and Glagov 1967b]. Due to their high content of elastin, young and healthy aortic walls are very distensible under physiological loading. Collagen, in turn provides the passive strength of the tissue, sets a limit to the physiological range of deformation and maintains the shape of organs and tissues. Moreover, it serves as a scaffold, on which cells can adhere. [Humphrey 2002]

The *ground substance* is a hydrophilic gel in which the structural elements of the extracellular matrix are embedded. It contains different saccharides (mucopolysaccharides or glycosaminoglycans) and tissue fluid. The amount of bonded water varies depending on various factors and influences the mechanical properties of the tissue. [Fung 1993]

Elastin is a protein. In the load-free state, these strand-like macromolecules that are loosely cross-linked by covalent bridges are arranged in an unstructured, crimped manner. Therefore, elastin behaves like an isotropic elastic solid despite its composition of fibers. Under external loading, the rubbery meshwork is stretched and the fibers get oriented in loading direction [Alberts et al. 2002, Figure 1-7]. This reversible reorganization of elastin under loading provides the high distensibility of elastic biological tissues, in particular at low stresses in the physiological domain. Biological tissues with a dominant elastin content behave almost linearly elastic in uniaxial tensile tests, even for large deformations. Loading and relief path are not identical, but form a hysteresis indicating the viscoelasticity of the material [Fung 1993]. Unlike most other microstructural components, elastin is not subject to continuous remodeling but „available data indicate that elastin is very inert and exists [chemically] unchanged in the body for decades, if not the whole human life span.“ [Nichols et al. 2011]

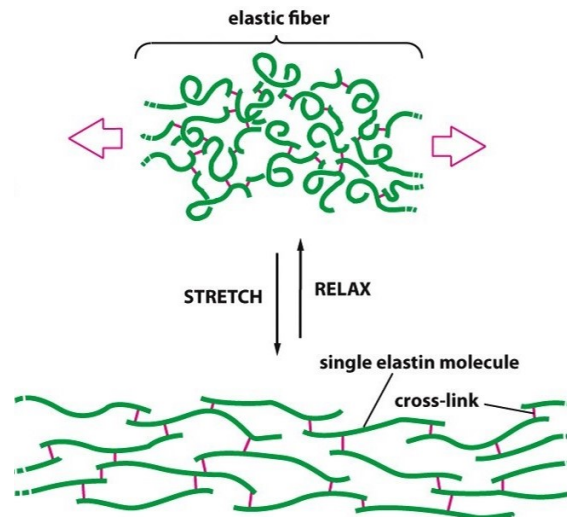


Figure 1-7 Arrangement of elastin fibers in the unloaded (relaxed) state and under uniaxial tension (stretched). [Image reprinted from Alberts et al. 2007 with permission from Taylor & Francis Group]

Like elastin, *collagen* is a protein. In contrast to elastin, the strand-like macromolecules are continuously synthesized by cells in the arterial wall, so that fractured collagen fibers can be replaced. Moreover, collagen molecules are organized in hierarchical order structures at different length scales [cf. Heim et al. 2010, Figure 1-8]. In addition to the properties of the macromolecules themselves, the way of their hierarchical arrangement into fibrils and fibers strongly determines the elastic properties of collagenous tissues: The individual macromolecules are left-handed helices. Three of these chains together form a right-handed triple helix, which is the characteristic building unit of collagen [van der Rest and Bruckner 1993]. The triple helices, in turn, are organized in fibrils: they are arranged in parallel and show an offset in longitudinal direction, one against another, so that they overlap. This highly ordered microstructure provides the high stiffness, characterized by a YOUNG's modulus of about 1 GPa and

high tensile strength (50-100 MPa) of collagenous tissues. Bundles of fibrils form collagen fibers showing diameters between $0.2\ \mu\text{m}$ and $12\ \mu\text{m}$. These, in turn, are embedded in fasciae in a wavy configuration [Figure 1-9]. [Fung 1993; Kassab 2006; Holzapfel 2008]

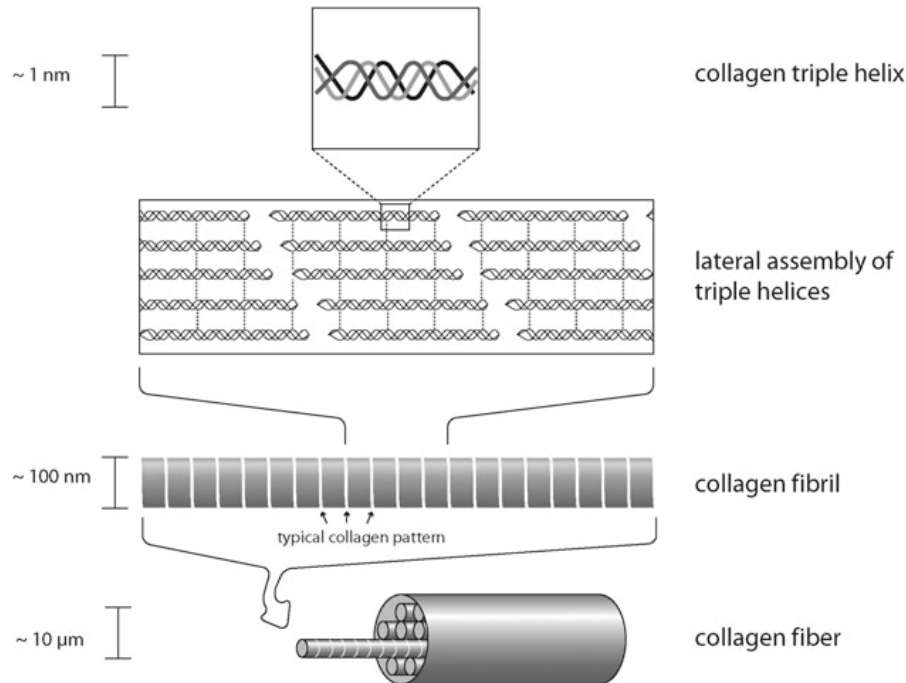


Figure 1-8 Scheme of the hierarchical organization of collagen at different length scales. [Figure reprinted from Heim et al. 2010 with permission]

According to variations in their hierarchical organization, 28 types of collagen are distinguished to date [Díez 2007] that show markedly different mechanical properties. However, there are important mechanical characteristics that are shared by all collagenous tissues:

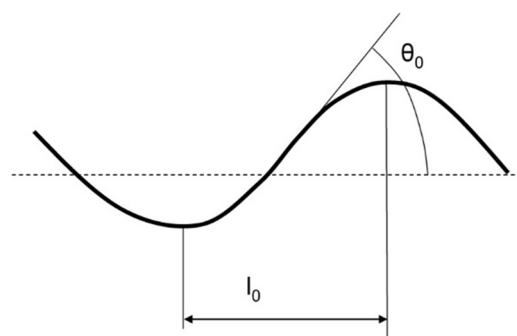


Figure 1-9 Wavy configuration of a collagen fiber shown with the characteristic length l_0 and angle θ_0 in the unloaded state. [Reproduced after Fung 1993 with permission from Springer Nature]

- (i) Because of its composition of highly ordered fibers and fasciae, most collagenous tissues show strongly anisotropic elastic properties. According to the way how the fibers are arranged, these may

be two- or three-dimensional, transversally isotropic (ligaments and tendons) or orthotropic (arterial walls).

- (ii) Collagen fibers are able to withstand high tensile stresses, but buckle immediately under compressive stresses like a rope.
- (iii) The characteristic high tensile strength (50-100 MPa) and stiffness (≈ 1 GPa) of collagenous tissues do not come into effect at low physiological loads because of the wavy configuration of the collagen fibers in the load-free state [Figure 1-9]. Only with rising loading, collagen fibers are straightened by and by and contribute increasingly to the mechanical response of the tissue which is governed by other constituents of the composite tissues, mainly elastin, at lower loading. This results in the typical, exponential force-extension (and correspondingly: stress-strain) curves of collagenous tissues under uniaxial loading [Figure 1-10]. Once smoothed, collagen fibers do allow only small additional deformation.

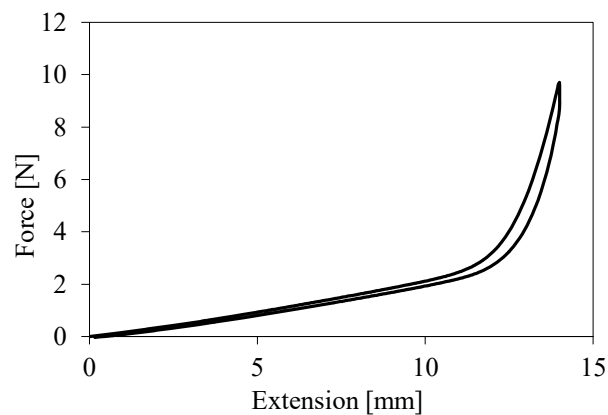


Figure 1-10 Force-extension data recorded from an uniaxial tensile test on a porcine aortic specimen. [Image with permission: Cell and Vascular Mechanics Group, Goethe University Frankfurt]

Usually, their recruitment marks the upper boundary of physiological loading and deformation. Collagen fibers prevent tissues against super physiological loading. [Fung 1993]

Proteoglycans, i.e. a type of macromolecules that consist of a protein to which several carbohydrates are covalently bound, are able to regulate residual stresses [cf. 0] in the wall and, thus, influence stress distribution inside the wall [Azeloglu et al. 2008; Niestrawska 2019].

1.4.2 Structural composition of the healthy aorta

The walls of young and healthy aortae are composed of three layers: intima, media and adventitia [Figure 1-11, cf. Fung 1993; Holzapfel et al. 2000; Humphrey 2002; Kassab 2006; Caro 2012 as general references for the paragraphs of this section].

1.4.2.1 Intima

The intima constitutes the luminal surface of the arterial wall. In young and healthy arteries, it consists of a single layer of endothelial cells. These rest on a basal membrane and a thin subendothelial layer of collagen fiber bundles, elastic fibers and some smooth muscle cells. The intima provides an interface to the blood flow: mechanically it reduces shear stress between blood flow and the wall. The intima does not contribute to the mechanical strength and properties of the wall in young and healthy aortae.

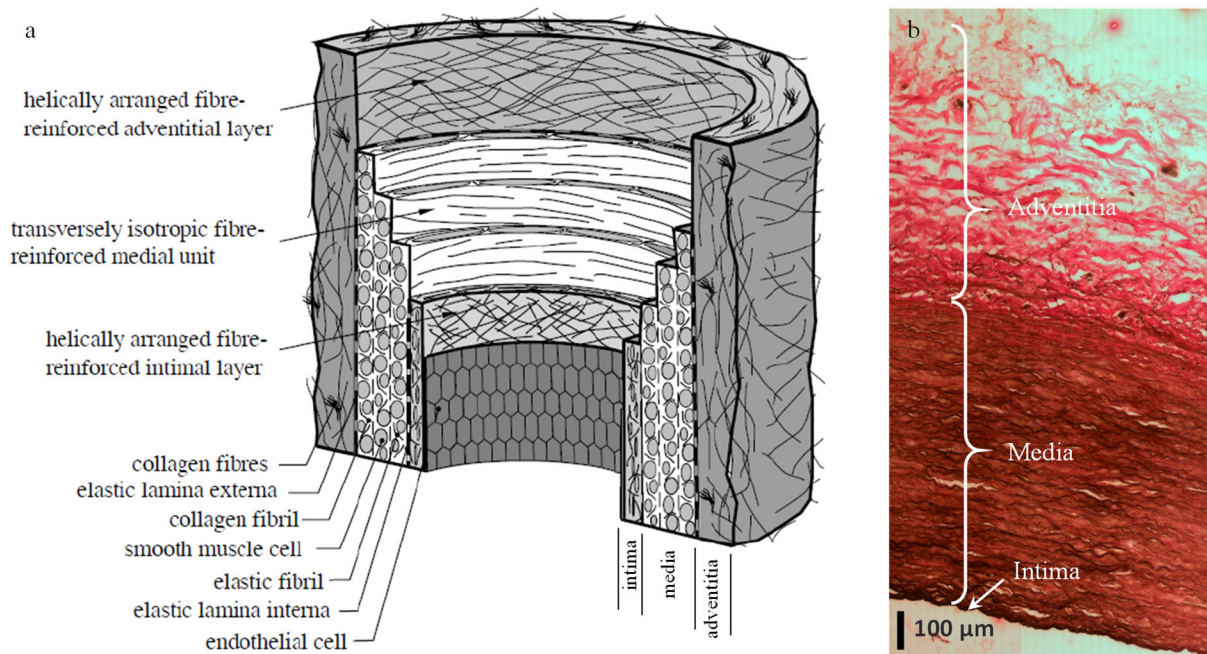


Figure 1-11 a) Schematic view of the layered structure of arterial walls indicating the layers' dominant structural components [Image reprinted from Holzapfel et al. 2000 with permission from Springer Nature]. b) Histological micrograph showing a transversal cross section of a healthy porcine aortic wall with Elastica van Gieson staining: elastin and collagen fibers appear in dark and light red, respectively. [Image with permission: Cell and Vascular Mechanics Group, Goethe University Frankfurt, Germany].

1.4.2.2 Media

The media is the middle layer of the aorta. It is separated from and connected to the intima and the adventitia by the internal and external elastic laminae. The media consists of a three-dimensional network of smooth muscle cells and elastin and collagen fibers that is organized in concentric elastic layers. Wolinsky and Glagov [1967b] have first identified these layers as building units of the aortic wall that can be found in all mammalian species: Each layer is composed of relatively thick elastin bands, whereas a network of elastin fibers connects the layers. Collagen fibrils are situated in the interstices in a wavy configuration. They are arranged helically in several, layer-specific preferred fiber directions which are oriented predominantly in circumferential direction of the vessel: Niestrawska et al. [2016] determined two symmetrically arranged fiber directions (given as median [IQR]) of $\varphi_1 = 24.46^\circ [22.45^\circ - 30.18^\circ]$ and $\varphi_2 = 180^\circ - \varphi_1$ with respect to the circumferential direction of the vessel in 17 human abdominal

aortae from aged donors (mean \pm SD = 63 ± 11 years). Smooth muscle cells are present between adjacent elastic layers. Wolinsky and Glagov [1967b] showed that size and structure of these elastic lamellar units is almost uniform in different mammalian species with body weights ranging from 28 g to approximately 200 kg. According to the different loading conditions that are connected with size and body weight, the aortic wall is composed of a different number of lamellar units: Corresponding to the well-known linear dependency of the circumferential wall stress σ_φ of a thin-walled pressurized (p) cylinder on the ratio of radius r and wall thickness h : $\sigma_\varphi = p \cdot r/h$, the number of lamellar units, and consequently wall thickness h , is nearly proportional to the diameter of the aorta in different species. As a consequence, r/h and tension per lamellar unit are almost constant for a wide range of species. In the human aorta, the media consists of 40 to 70 lamellar units. The number of lamellar units decreases proportional to the vessel diameter with increasing distance from the heart.

1.4.2.3 Adventitia

The outermost layer of the wall is less organized than the media. It predominantly consists of ground substance and thicker bundles of collagen fibers, which are oriented more to the axial direction of the vessel (Niestrawska et al. [2016]: median [IQR] = 77.53° [67.04° , 84.02°] with respect to the circumferential vessel direction), and to a smaller extend of elastin. Mechanically, it has a twofold function as a protective ‘shell’ of the aortic wall, preventing it against overload under super-physiological conditions, and as a connection and an interface to the surrounding connective and perivascular adipose tissue. Extracellular matrix producing cells (fibroblasts) are embedded in the collagen network as well as nerves and blood vessels that provide nutrients and remove waste products from the outer aortic wall. [Niestrawska 2019]

1.5 Mechanical properties of the aortic wall

Uniaxial quasistatic tensile tests in axial and circumferential directions of the vessel as well as biaxial tests show the strongly nonlinear and anisotropic elastic properties and the low degree of viscoelasticity of the aortic wall in a cyclically loaded physiological state. According to Holzapfel et al. [2000], three different characteristic types of mechanical response to external loading can be distinguished [Figure 1-12].

1.5.1 Stress-strain path I: reversible deformation

An almost isotropic and linear stress response to small strain is followed by an anisotropic exponential increase of stress at larger strains. Loading and unloading path are not identical, but form a closed hysteresis indicating the time dependent relaxation of the stress response, i.e. viscoelastic behavior. Cyclic loading and unloading of excised tissue in the reversible range at first results in a softening of the stress response: the stress-strain hysteresis is shifted to the right in the diagram that is shown in Figure 1-12. In addition to this, the hysteresis becomes narrower, the loading and unloading paths are closer together. After 5 to 10 loading cycles a cyclically stable state with a narrow hysteresis is reached. This corresponds to the typical physiological loading condition.

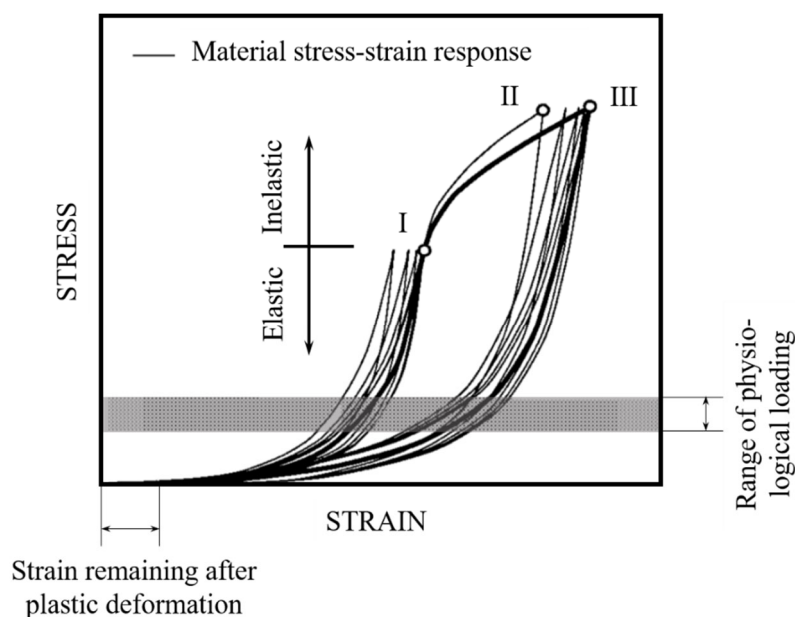


Figure 1-12 Three characteristic types of the aortic wall's mechanical response to uniaxial loading: (I) reversible deformation at low loading, (II) irreversible deformation and (III) reversible deformation after previous irreversible deformation. [Figure reprinted from Holzapfel et al. 2000 with permission from Springer Nature]

1.5.2 Stress-strain path II: irreversible deformation

Loading beyond point I in Figure 1-12 results in irreversible plastic deformation of the tested tissue sample. The transition from reversible deformation to irreversible damage of the tissue is marked by a turning point of the stress-strain curve. Compared to viscoelastic deformations, plastic deformations are characterized by a considerably enlarged and not closed hysteresis: after complete unloading, the sample does not return to its original length, but a residual elongation remains.

1.5.3 Stress-strain path III: reversible deformation after irreversible, plastic deformation.

If samples that underwent plastic deformation are not exposed to loads beyond the maximum load that was reached during plastic deformation, the material will show again viscoelastic behavior under cyclic loading like in case I: during the first load cycles a considerable softening of the material is observed that is associated with a narrowing of the viscoelastic hysteresis. Eventually, a cyclically stable, stationary state with almost identical loading and unloading paths, i.e. almost elastic behavior is reached. However, compared to case I, the material will exhibit an irreversibly changed, considerably softened elastic behavior

1.5.4 Pseudoelasticity

The *viscoelastic properties* of the aortic wall have considerable effects only at the transition from the load-free to the loaded state, but become more and more negligible under stationary cyclic loading which corresponds to the physiological loading condition. The hypothesis of almost elastic material properties under cyclic physiological loading is supported by simultaneous in vivo recordings of the aortic diameter and pressure during a single cardiac cycle that were performed by Barnett et al. [1961]: both curves do not show any remarkable phase shift [reported in Caro 2012]. Therefore, it is widely accepted to neglect the viscoelastic properties of arterial walls in biomechanical modeling since Fung et al. [1979] have proposed the concept of *pseudoelasticity*, i.e. the approximation of the aortic wall's constitutive behavior in the reversible domain by time-independent hyperelastic models.

1.5.5 Anisotropy

The experimentally observed two preferred collagen fiber directions that lie in the wall plane and are arranged symmetrically to the longitudinal and circumferential directions of the aorta render the elastic behavior of the material locally *orthotropic* [cf. Figure 1-13, cf. chapters 2.3.3 and 6.4 and for more

detailed information e.g. Holzapfel 2009; Holzapfel and Ogden 2017; Niestrawska 2019]. These preferred directions vary layer-specifically [Holzapfel 2009; Badel et al. 2012]. However, it has been shown that arterial walls can be adequately modeled continuum mechanically as a single-layered thin shell [Marra et al. 2006; Avril et al. 2010]. Then, however, the two directions may model the anisotropy of the composite phenomenologically rather than having a physical meaning as preferred fiber directions. In some collagenous materials like ligaments and tendons, the collagen fibers and fasciae are almost perfectly aligned in parallel so that these tissues show strongly anisotropic behavior. In the aortic wall, however, the collagen fibers are not perfectly aligned but dispersed about the preferred directions [Canham et al. 1989; Finlay et al. 1995; Horny et al. 2010; Schriefl et al. 2012]. In contrast to the preferred directions, the orientation of single collagen fibers is not restricted to the wall plane so that collagen fibers form a three-dimensional network in aortic walls [Fung 1993; Niestrawska 2019]. Depending on the degree of fiber dispersion, the degree of anisotropy of the aortic wall may vary. For a completely random distribution of the collagen fibers about a preferred direction – as was observed e.g. by Niestrawska et al. [2019] in the remodeled neo-adventitia in some abdominal aortic aneurysms – the elastic properties are purely isotropic.

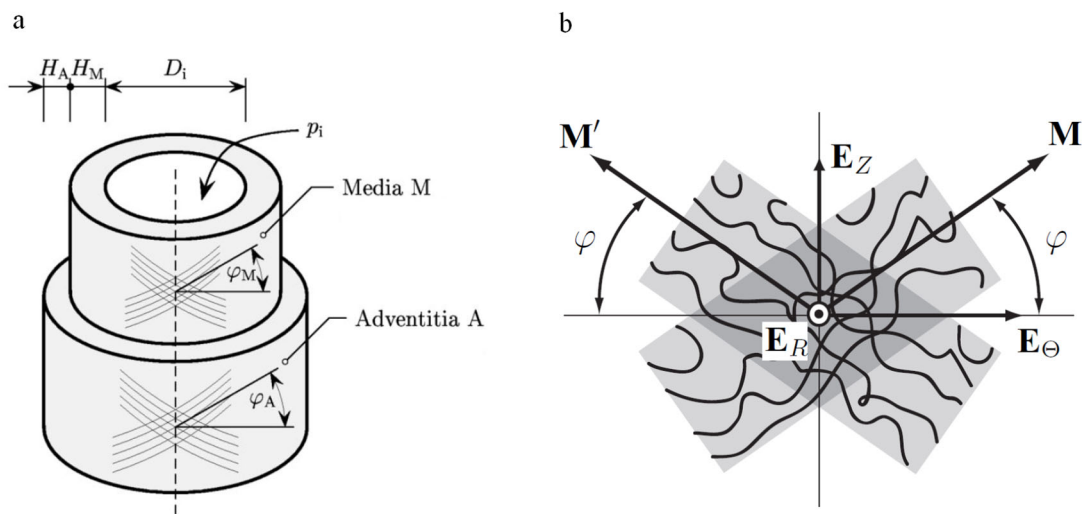


Figure 1-13 Schematic illustration of material symmetries and the arrangement of collagen fibers in the aortic wall. (a) The preferred in-plane directions of collagen fibers in the medial and the adventitial layer of the wall, φ_M and φ_A , are arranged symmetrically to the longitudinal and circumferential directions of the vessel. H_M and H_A refer to the thickness of the medial and the adventitial layers and D_i is the inner diameter of the vessel [Image reprinted from Holzapfel et al. 2004 with permission from the ASME]. (b) illustrates the dispersion of the collagen fibers about the preferred in-plane fiber directions \mathbf{M}' and \mathbf{M} in each layer of which is determined by their angle φ with respect to the unit normal vector \mathbf{E}_θ indicating the circumferential or tangential direction of the vessel wall. \mathbf{E}_R and \mathbf{E}_Z indicate the radial and the axial direction, respectively [Image reprinted from Holzapfel 2009 with permission from Springer Nature].

1.5.6 Incompressibility

Like other biological soft tissues, aortic wall tissue is characterized by a 70% volume fraction of water and behaves slightly compressible. As it is impossible to date to exactly quantify the volume change under loading *in vivo*, the *incompressibility* assumption is widely accepted as a good approximation for the purpose of modeling the elastic behavior of the aortic wall [cf. Holzapfel and Weizäcker 1998; Holzapfel et al. 2004; Humphrey and Holzapfel 2012; Farotto et al. 2018 and citations therein].

The elastic properties are not homogeneous, but change along the aortic tree [Figure 1-6]. Evidently, there will be a difference between elastic and muscular arteries due to the differences in the microstructural composition of both types of arteries. But also the stiffness of the aortic wall increases with growing distance of the aortic segment from the heart.

1.6 Axial prestretch and residual stresses

In vivo, the aortic wall is exposed to *prestresses* as well as to *residual stresses*, i.e. stresses that are present even in the unloaded configuration. Firstly, the aortic wall is loaded by cyclic pulsatile blood pressure. The minimum value that is assumed throughout the pulse cycle is about 80 mmHg in healthy subjects corresponding to 10.7 kPa so that the wall is inflated permanently in the living organism. Moreover, the aorta is exposed to a constant axial prestress and -stretch *in situ*, i.e. as long as it is situated in the body, even when not loaded by blood pressure [Fung 1993; Kassab 2006; Horný 2015]. Han and Fung 1995 have observed in *in vitro* experiments using canine and porcine aortae that axial *in situ* prestretch increases along the aortic tree with growing distance from the heart from about

$$\lambda = \frac{\text{in situ length}}{\text{excised length}} = 1.2 \quad \text{eq. 1-2}$$

in the proximal ascending aorta to 1.4 to 1.5 in the infrarenal aorta. Schulze-Bauer et al. [2003] and Sommer et al. [2010] have shown that the axial stretch remains almost constant in iliac and carotid arteries under pulsatile loading by pulse pressure. They have hypothesized that this is a principle of energetic optimization of arterial function, thereby avoiding cyclic motion of the arterial wall that does not contribute to its physiological function of guiding continuous blood flow from the heart to the smaller and the peripheral vessels. Horný et al. [2011; 2012; 2013; 2017] extensively have investigated the age dependency of axial prestretch and prestress in the human abdominal aorta. They observed that population average prestretch decreases exponentially from between 1.2 and 1.4 in 20 y.o. subjects to 1.0, i.e. no prestretch, in 80 to 90 y.o. subjects. Correspondingly, the reduced axial pretension force F_{red} that acts on the wall in longitudinal direction independently of the pulse pressure, decreases on average from about 2 N at the age of 20 y. to 0 N beyond 80 years of age.

Compared to the wall stresses due to blood pressure and axial prestretch, the wall shear stresses due to blood flow are very small and mechanically negligible: Caro [2012] reports a shear stress of 0.53 Pa for the abdominal aorta compared to wall stresses in the kPa range due to physiological hydrostatic pressure in the same artery. However, wall shear stresses are sensed by the endothelial cells of the intima and play an important role in regulation of the systemic blood pressure by active adaptation of peripheral arterial diameter through smooth muscle contraction and relaxation [cf. chapter 1.3.2] and as a trigger for the remodeling of arterial walls.

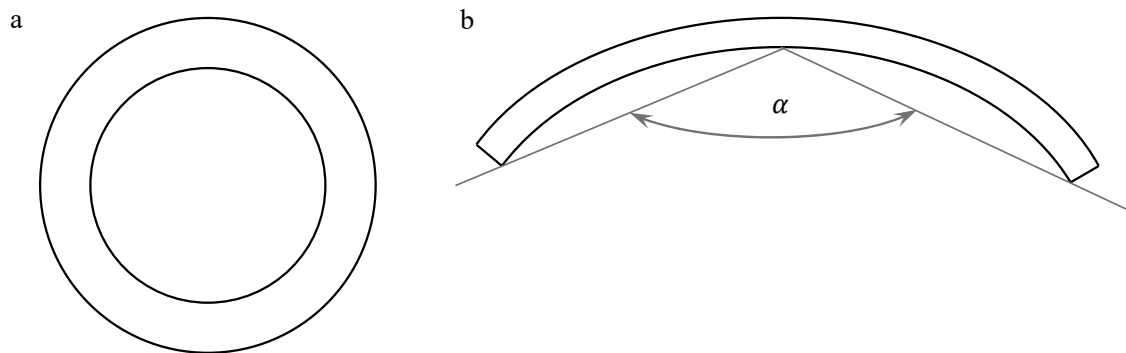


Figure 1-14 Schematic view of (a) the load-free and (b) the stress-free configuration of an excised aortic wall's cross section. The stress-free configuration is characterized by the opening angle α . [Reproduced after Fung 1993 with permission from Springer Nature]

Only when excised from the body, the aorta is in a load-free state. However, in arterial and aortic walls, this load-free state is not the stress-free state. Fung [1984] and Vaishnav and Vossoughi [1983] have observed independently that an excised ring segment of the aortic wall opens up when cut radially and its cross section becomes a circle segment with a characteristic opening angle α [cf. Figure 1-14b].

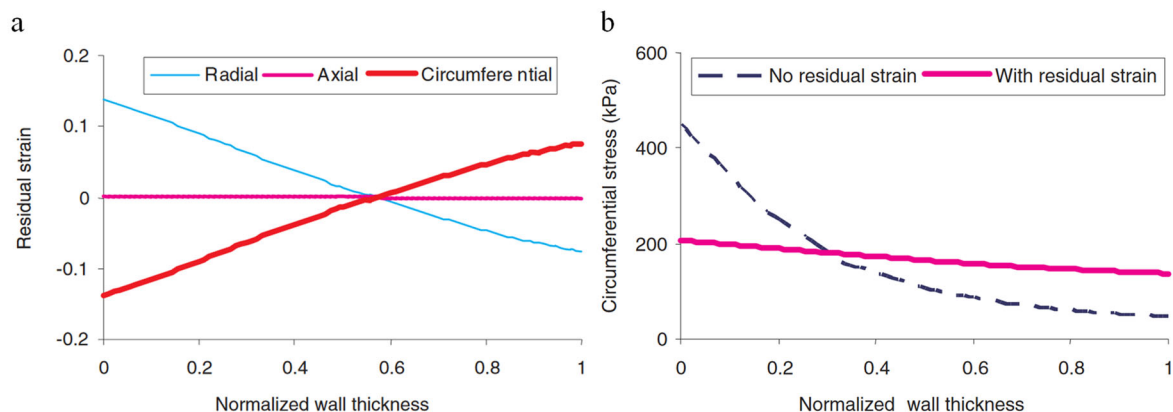


Figure 1-15 (a) Distribution of residual strains across the wall thickness of a porcine left anterior descending artery. (b) Comparison of the resulting distributions of circumferential wall stresses across the wall thickness under physiological loading by axial prestretch and blood pressure with and without consideration of residual strain. [Figure reprinted from Zhang et al. 2005 with permission from Tech Science Press]

This behavior indicates the presence of residual bending stresses in tangential or circumferential direction of the vessel in the load-free (intact) configuration [Figure 1-14a], i.e. compressive and tensile stresses at the luminal (inner) and abluminal (outer) border of the wall and a steady, almost linear progression and a neutral surface in between [cf. Chuong and Fung 1986, Zhang et al. 2005, Figure 1-15a]. Chuong and Fung [1986], Zhang et al. [2005] and Cardamone et al. [2009] have shown that these prestresses prevent peaks of circumferential stress that are observed usually at the luminal border of pressurized cylinders [cf. e.g. Ogden 1997; Silber and Steinwender 2005]. The superposition of bending stresses and wall stresses due to pressurization result in an almost homogeneous distribution of circumferential stresses across the wall thickness under physiological loading [Figure 1-15b].

Holzapfel et al. [2007] have shown that the three layers of human aortic walls exhibit characteristically diverging configurations when separated from each other experimentally. I.e. even the open ring segment does not represent a configuration of the wall that is free of residual stresses, but the three layers are tensed together in this common configuration.

1.7 Degenerative changes of the aorta's elastic properties with age and pathology

1.7.1 Aging

Degenerative age-related changes in the large elastic, but not in the muscular arteries are progressive throughout life, starting from early adulthood. With age, stiffening, i.e. the increase of the circumferential secant modulus in the physiological loading domain, and dilation of elastic arteries are observed. Both macroscopic changes are effects of changes in the load-bearing media: Elastin fibers and elastic laminae, the building units of the media [cf. 1.4.1, 1.4.2], are progressively degenerated and lose their orderly arrangement. The elastic laminae undergo thinning, splitting, fraying and fragmentation. [Nichols et al. 2011]

Concomitant remodeling results in the increase in – by far stiffer – collagenous material and in thickening of the intima due to hyperplasia: Elastin fibers decrease from 32.14% to 20.26% dry weight of the thoracic aortic wall between 20 and 80 years of age while collagen fibers increase from 21.44% to 32.41% dry weight [Faber and Møller-Hou 1952; Nichols et al. 2011]. For the abdominal aorta, Schulze-Bauer and Holzapfel [2003] report a thickness ratio of intima/media/adventitia of about 13/56/31 in the elderly and a thickness ratio of 20/49/31 was observed for a same age group by Niestrawska et al. [2019]. Calcium is deposited in degenerate elastic laminae, contributing to further stiffening, and a decrease in SMC content is observed. In addition to this, there are indications for (chronic) in-

inflammation of arterial walls with age. The mentioned changes can be summarized under the term *arteriosclerosis*. This diffuse, not localized, degeneration affects the media of all arteries of the elastic, but not the muscular type. [Cf. Nichols et al. 2011, Teixeira et al. 2015 and citations therein.]

Nichols et al. [2011] hypothesize that fatigue and fracture of elastin fibers due to cyclic mechanical loading by pulsatile pressure and resulting deformation are the principal cause of these age-related changes. The by far larger cyclic deformation to which the elastic conduit arteries are exposed compared to muscular arteries then could explain the fact that only these are affected by medial degeneration. Following early works by Byrom and Dodson [1948] and Byrom [1969], Nichols et al. [2011] consider the observed inflammation as a consequence of the destruction of elastin fibers and laminae due to mechanical overload (hypertension) or fatigue: inflammatory cells such as macrophages invade the arterial wall to clean up fractured elastin and repair the wall by collagen remodeling. Other groups argue that inflammation is not a consequence, but the reason for elastin degradation and draw attention to proteolytic (i.e. elastin and collagen degrading) enzymes such as matrix metalloproteinases (MMPs) that are produced by inflammatory cells [cf. Niestrawska 2019 for a brief overview of inflammation related processes that degrade ECM and inhibit its remodeling]. Regardless of the undecided debate of the origin of elastin degradation in elastic arteries, it results in a persistent medial degeneration, since – in contrast to other non-living molecular components of cells and ECM – elastin is synthesized only prenatally and cannot be remodeled [cf. 1.4.1].

Arterial stiffening, in turn, triggers a cascade of adverse changes that have been described as the “cardio-vascular (ageing) continuum” in order to emphasize their mutual dependency [Dzau et al. 2006b, 2006a; O'Rourke 2007; O'Rourke et al. 2010]: Depending on arterial stiffness, PWV is increased [cf. 1.3, eq. 1-1]. As a consequence, the phase shift between the initial pressure wave that propagates towards the periphery and the reflected wave is diminished and both waves interfere constructively resulting in increased systolic and pulse pressure at constant diastolic pressure, i.e. in systolic hypertension [Nichols et al. 2011; Caro 2012; O'Rourke et al. 2018]. This increased cyclic pressure load extends further downstream along the arterial tree and causes damages in the capillary vessels of brain and kidneys, which may lead to dementia and renal failure [Nichols et al. 2011]. Moreover, with increased PWV, the reflected pressure wave returns to the heart before the aortic valve is closed, so that the LV has to work against this additional load [Avolio et al. 1983]. It was shown that this hypertensive load increases the risk of cardiovascular events, leads to LV hypertrophy and, eventually, cardiac failure [Boutouyrie et al. 2002; Nichols et al. 2011]. Though the described ageing changes have universal validity and have been observed in various populations independent of life style and ethnicity, a large variability of individual arterial stiffness is observed at any age [Nichols et al. 2011].

In contrast to arteriosclerosis and arterial stiffening, *atherosclerosis* is not an ageing effect in itself: it is ubiquitous among adults in western societies and the most common cause of cardiovascular death in the West, but so far it is rarely observed in studies on e.g. aged Chinese population. Atherosclerosis affects all large and medium arteries regardless of the difference between elastic and muscular arteries.

It refers to the localized presence of lipids in the *intima* that causes local intimal thickening by inflammation, fibrous remodeling and hyperplasia of the endothelium. These changes predominantly extend into the arterial lumen, causing its narrowing (stenosis), reduction of blood flow and, thus, ischemia downstream. If the coronary arteries are affected, it may cause coronary heart disease and heart attack. The localized spreading of atherosclerotic changes into the media is discussed as a cause of local dilatation of the abdominal aorta, i.e. of abdominal aortic aneurysms. [Nichols et al. 2011; Teixeira et al. 2015]

1.7.2 Abdominal aortic aneurysm (AAA)

The development and propagation of an AAA is associated with significant changes in the microstructural composition and the mechanical behavior of the aortic wall: Tavares Monteiro et al. [2014] observed correlations of aneurysmal maximum diameter [cf. 1] with elastin, collagen and SMC content and the infiltration of inflammatory cells into the media [cf. 1.4.2]. Failure stress of the wall was increased [1] with maximum diameter, but no correlation was found between maximum diameter and failure strain. Niestrawska et al. [2016] determined micro-calcifications in the intima and media of AAAs. Based on histological analysis, Tanaka et al. [2015a], Tanaka et al. [2015b], Kugo et al. [2016], Ollikainen et al. [2016], Niestrawska et al. [2016] and Niestrawska et al. [2019] identified increased accumulations of lipids and adipocytes (fat cells) in the load-bearing media of AAAs, i.e. sections that consisted of components with negligible mechanical strength and extended up to the mm range. Investigating the reorganization of collagen in AAA walls, Lindeman et al. [2010] were able to show that remodeled collagen in some AAAs does not behave as a network any more: The tissue loses its ability to distribute mechanical forces resulting in stress concentration in single fibers, potential overload and rupture. In most AAAs, intraluminal thrombus (ILT) is present. ILT is a pseudo-tissue with low tensile strength that forms mostly from coagulated blood in backwater areas of the AAA lumen [Figure 1-1]. Thrombus covered parts of the wall generally show lower structural integrity and strength compared to thrombus free parts: walls are thinner and contain significantly less elastin, remaining elastin bands are broken and elastic laminae are disorganized to a higher degree [cf. Niestrawska 2019 and citations therein]. Moreover, Raghavan et al. [2006] demonstrated that wall thickness may vary locally between 0.23 mm close to a rupture site and 4.26 mm in a highly calcified area in the same aneurysm. Several studies report increased circumferential stiffness and a decreased degree of anisotropy of AAA walls [Thubrikar et al. 2001; Pierce et al. 2015; Sassani et al. 2015].

Combining microstructural analysis by histology and second harmonic generation imaging with macroscopic mechanical characterization by biaxial tensile testing of intraoperatively excised AAA tissue, Niestrawska et al. [2019] have recently proposed a systematic classification of AAAs according to three stages of disease progression. The three stages were defined by the size of the ‘inflection stretch’, i.e. the stretch [cf. chapter 2.1, eq. 2-10] at which the maximum change of slope of the nonlinear

stress-stretch curve under equi-biaxial loading was observed [cf. Figure 1-10, Figure 1-12]. It was shown that the three stages are distinctly different with regard to the degree of degeneration of elastic components, inflammation and collagenous remodeling:

AAAs that showed an inflection stretch λ comparable to healthy, non-aneurysmal aortae in the range of $1.10 \leq \lambda < 1.15$ were classified as stage 1. Stage 1 AAAs showed significantly reduced contents of elastin and SMCs compared to the healthy control (3% vs. 20% and 3.5% vs. 35%, respectively), disorganization of the media as well as the three-layered structure of the wall [cf. 1.4.2]: internal and external elastic laminae that separate the media from intima and adventitia, respectively, were not distinguishable any more. The characteristics of the anisotropic behavior changed from orthotropy with two symmetrical preferred directions of collagen fibers to transversal isotropy with collagen fibers almost aligned to the circumferential direction [cf. chapter 2.3.4].

AAAs that showed increased inflection stretches $\lambda \geq 1.15$ were classified as stage 2. In this sample group, elastin and SMC content were further decreased to only 1%, each. The original layers of the wall (intima, media, adventitia) were not distinguishable any more. The remains of the original wall showed transversely isotropic behavior comparable to stage 1. Abluminally, i.e. outside the original wall, remodeling of a new collagenous layer, the so-called ‘neo-adventitia’, was observed that extended over 9-50% of the total wall thickness with a median value of 18%. Collagenous remodeling correlated with the occurrence of (in part disrupted) adipocytes and of inflammatory cells inside the wall that were neither found in the healthy control, nor in stage 1 AAAs.

Stage 3 AAA walls were defined by inflection stretches $\lambda < 1.10$ that were smaller compared to the healthy control. The original walls were almost completely degraded, only remains of the former adventitia were found. The remodeled collagenous neo-adventitia span over about 66% of the total wall thickness and exhibited almost isotropic behavior. Compared to stage 2, elastin and SMC content decreased even further to 0%. However, two significantly different subtypes of stage 3 walls could be identified: A ‘vulnerable’ type showed significant contents of adipocytes and co-localized inflammatory cells inside the wall. In contrast, in the walls of a ‘stable remodeled’ type neither of both was found. They were characterized by a dense, multilayered collagen network. No difference in maximum diameter was seen between the ‘vulnerable’ and the ‘stable’ type. These findings are in accordance with Cohen et al. [1988], who showed experimentally that the degradation of elastin (‘elastase’) leads to dilatation, but not rupture, of aortic walls, whereas the degradation of collagen (‘collagenase’) results in rupture without dilatation.

The described microstructural changes are reflected by correlations between disease progression and parameters of constitutive equations that model the nonlinear elastic anisotropic biomechanical behavior of the AAA wall [cf. Holzapfel et al. 2015]. Evidently, the mentioned changes of the preferred collagen fiber directions and of the degree of anisotropy are reflected by the corresponding constitutive parameters. Moreover, Niestrawska et al. [2019] found significant correlations with parameters that determine the stiffness of the material.

Alongside with inflammatory processes, increased expression of diverse proteases (e.g. matrix metalloproteases 2 and 9 [Freestone et al. 1995; Petersen et al. 2002]) and of cytokines was observed in aneurysmal walls. Proteases are enzymes that degrade components of the load bearing ECM such as elastin and collagen and contribute directly to the weakening of the wall. In contrast, cytokines such as TNF (tumor necrosis factor) and IFN- γ (interferon-gamma) are proteins that may cause the death (apoptosis) of collagen synthesizing SMCs or inhibit collagen synthesis by SMCs and fibroblasts. In this way, they indirectly promote the weakening of the wall by preventing its repair. Both, proteases and cytokines, are produced by inflammatory cells. [Cf. Niestrawska 2019 for a more complete representation of these processes and further references to original literature.]

As already discussed in the context of aging, it is still unclear what is first and initiates AAA development: increased fracture and fatigue of load bearing ECM components as a consequence of local mechanical overload (e.g. due to locally excessive constructive interference of initial and reflected pressure waves or due to turbulent flow) that entails inflammatory processes [He and Roach 1994; Niestrawska et al. 2019], or, vice versa, inflammation that originates e.g. from intimal atherosclerotic plaque, expands into the media and promotes ECM degradation through the mentioned chemical processes.

2 Continuum mechanical framework

The continuum mechanical framework is developed in this section as far as it is necessary for the understanding of the research that is presented in the subsequent chapters of this thesis. The deformation of the aortic wall and its passive elastic properties, i.e. the functional connection of the deformation of a continuum body and its stress response, are described based on the theory of finite non-linear elastic deformations. The representation in this chapter is limited to homogenous deformations and quasistatic processes.

The chapter is based on the more complete representations in Holzapfel [2010], Ogden [1997], Parisch [2003], Silber and Steinwender [2005] and Ogden [2009], which are given here as global references for the whole chapter. Unless otherwise stated, the EINSTEIN summation convention is used in this chapter.

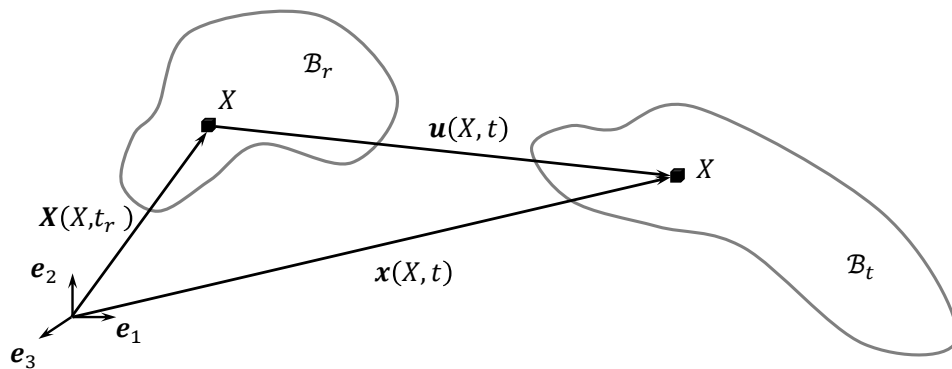


Figure 2-1 Basic kinematics of a continuum body: The identical material point X is shown in its reference configuration \mathcal{B}_r and a current configuration \mathcal{B}_t . \mathbf{X} and \mathbf{x} denote the position vectors of X in \mathcal{B}_r and \mathcal{B}_t , respectively. \mathbf{u} is the displacement of X from \mathcal{B}_r to \mathcal{B}_t .

2.1 Kinematics of finite deformations

A continuum body B is regarded as a coherent subset of the EUCLIDEAN vector space \mathbf{R}^3 that consists of densely packed *material points* X . These are neither mathematical points without extension, nor point masses in a physical sense. In contrast, each material point X is carrier of physical properties, it has an

infinitesimally small volume dV and mass dm . In its arbitrarily chosen *reference configuration* \mathcal{B}_r at a time point $t_r \in \mathbf{R}$, B can be described with regard to a LAGRANGIAN or *material* reference frame by a field of material position vectors $\mathbf{X} \in \mathbf{R}^3$:

$$\mathbf{X} = \mathbf{X}(X, t_r) = X_i(X, t_r)\mathbf{e}_i, \quad \text{eq. 2-1}$$

where $\mathbf{e}_i, i = 1, 2, 3$ is a right-handed set of orthonormal basis vectors and $X_i \in \mathbf{R}$ [cf. Figure 2-1]. In principle, any observed configuration of B can be chosen as reference configuration \mathcal{B}_r for the description of its deformation. Often however, the stress and deformation free *natural configuration* \mathcal{B}_0 of a body is chosen. Any deformed or *current configuration* \mathcal{B}_t of B is described by the vector field

$$\mathbf{x}(X, t) = x_i(X, t)\mathbf{e}_i \quad \text{eq. 2-2}$$

marking the current spatial position of a material point X at a time point $t \in \mathbf{R}$. Without loss of generality, the position vector $\mathbf{X}(X, t_r)$ and $\mathbf{x}(X, t)$ are given with regard to the same basis in this work. The *motion*

$$\mathbf{x}(X, t) = \boldsymbol{\chi}(\mathbf{X}(X, t_r), t) \quad \text{eq. 2-3}$$

is a – potentially nonlinear – one-to-one mapping of the reference configuration \mathcal{B}_r onto the current configuration \mathcal{B}_t at time point t : $\boldsymbol{\chi}: \mathcal{B}_r \rightarrow \mathcal{B}_t$. $\boldsymbol{\chi}$ is a C^2 -diffeomorphism, i.e. the inverse mapping $\boldsymbol{\chi}^{-1}: \mathcal{B}_t \rightarrow \mathcal{B}_r$ exists and $\boldsymbol{\chi}$ and $\boldsymbol{\chi}^{-1}$ are twice continuously differentiable:

$$\mathbf{X}(X, t) = \boldsymbol{\chi}^{-1}(\mathbf{x}(X, t), t_r) \quad \text{eq. 2-4}$$

For practical purposes, the distinction between the material point X and its position vector \mathbf{X} in \mathcal{B}_r is neglected. As initially stated, arterial walls are regarded as purely elastic in this work, i.e. the time history between two different configurations of a continuum body B has no effect on the current configuration and \mathcal{B}_r and \mathcal{B}_t may be directly compared without regarding the intermediate configurations. Therefore eq. 2-3 and eq. 2-4 may be rewritten as

$$\mathbf{x} = \boldsymbol{\chi}(\mathbf{X}) \quad \text{eq. 2-5}$$

and

$$\mathbf{X} = \boldsymbol{\chi}^{-1}(\mathbf{x}). \quad \text{eq. 2-6}$$

In general, $\boldsymbol{\chi}$ can be formulated as

$$\boldsymbol{\chi}(\mathbf{X}) = \mathbf{X} + \mathbf{u}(\mathbf{X}), \quad \text{eq. 2-7}$$

where $\mathbf{u}(\mathbf{X}) = \mathbf{x} - \mathbf{X}$ is the displacement field that transforms the reference configuration of the material point field into its current configuration. Equations eq. 2-3 to eq. 2-7 provide a description of the deformation of a solid body according to the LAGRANGIAN method, i.e. the motion function follows the trajectory of the identical material point over time. In contrast, the EULERIAN description method provides functions of varying displacement and velocity vectors over time at a fixed location in space, which is passed by different material points X .

If one considers two neighboring material points located at \mathbf{X} and $\mathbf{X} + d\mathbf{X}$ in the chosen reference configuration \mathcal{B}_r , the infinitesimal line element $d\mathbf{x}$ that connects their positions in the current configuration \mathcal{B}_t can be approximated linearly using the total derivative

$$d\mathbf{x} = \frac{\partial \mathbf{x}}{\partial \mathbf{X}} \cdot d\mathbf{X} = \text{Grad } \mathbf{x} \cdot d\mathbf{X}, \quad \text{eq. 2-8}$$

where ' \cdot ' is the scalar or inner product and Grad is the gradient operator in \mathcal{B}_r . The non-singular second-order tensor

$$\mathbf{F} = \text{Grad } \mathbf{x} = \frac{\partial \mathbf{x}}{\partial \mathbf{X}} \quad \text{eq. 2-9}$$

is defined as the *deformation gradient*. According to eq. 2-8 it is a linear mapping of the infinitesimal line element $d\mathbf{X}$ in the reference configuration onto its current configuration $d\mathbf{x}$ and thus describes the deformation of the continuum body in the infinitesimal neighborhood of a material point X . A *homogeneous* deformation is characterized by the fact that \mathbf{F} is identical for all material points $X \in B$ or that \mathbf{F} is independent of the material position vectors \mathbf{X} .

Let $l_r = |d\mathbf{X}|$ be the length of the infinitesimal line element $d\mathbf{X}$ in the reference configuration, $l = |d\mathbf{x}|$ be the length of the same line element in its current configuration and $d\bar{\mathbf{X}} = d\mathbf{X}/|d\mathbf{X}|$ and $d\bar{\mathbf{x}} = d\mathbf{x}/|d\mathbf{x}|$ be the normalized direction vectors of the line element in its respective configuration. Then eq. 2-8 with eq. 2-9 may be formulated as

$$\frac{l}{l_r} d\bar{\mathbf{x}} = \mathbf{F} \cdot d\bar{\mathbf{X}}. \quad \text{eq. 2-10}$$

$$\lambda = \frac{l}{l_r} \quad \text{eq. 2-11}$$

is defined as the *stretch*. In addition to this, the deformation gradient \mathbf{F} provides linear mappings of infinitesimal area and volume elements from the arbitrarily chosen reference configurations $d\mathbf{a}_r = \mathbf{N}dA_r$ and dV_r onto their current configurations $d\mathbf{a}_t = \mathbf{n}dA_t$ and dV_t , where \mathbf{N} and \mathbf{n} are the normal unit vectors on the area element in its respective configuration:

$$d\mathbf{a}_t = \det(\mathbf{F})\mathbf{F}^{-T} \cdot d\mathbf{a}_r, \quad \text{eq. 2-12}$$

$$dV_t = \det(\mathbf{F})dV_r. \quad \text{eq. 2-13}$$

The scalar

$$J = \det(\mathbf{F}) = \frac{dV_t}{dV_r} \quad \text{eq. 2-14}$$

is defined as the *volume change*.

Since the reference configuration \mathcal{B}_r can be chosen arbitrarily, the effect of a *change of the reference configuration* on the deformation gradient has to be considered. Regard two mappings from different reference configurations \mathcal{B}_r and \mathcal{B}'_r onto the identical current configuration \mathcal{B}_t , $\chi: \mathcal{B}_r \rightarrow \mathcal{B}_t$ and $\chi': \mathcal{B}'_r \rightarrow \mathcal{B}_t$. The respective deformation gradients \mathbf{F} and \mathbf{F}' are given by

$$\mathbf{F} = \frac{\partial \mathbf{x}}{\partial \mathbf{X}} \quad \text{and} \quad \mathbf{F}' = \frac{\partial \mathbf{x}}{\partial \mathbf{X}'} \quad \text{eq. 2-15}$$

Using the chain rule, \mathbf{F}' can be expressed in terms of \mathbf{F}

$$\mathbf{F}' = \frac{\partial \mathbf{x}}{\partial \mathbf{X}} \cdot \frac{\partial \mathbf{X}}{\partial \mathbf{X}'} = \mathbf{F} \cdot \frac{\partial \mathbf{X}}{\partial \mathbf{X}'} = \mathbf{F} \cdot \mathbf{P}^{-1}, \quad \text{eq. 2-16}$$

where

$$\mathbf{P} = \frac{\partial \mathbf{X}'}{\partial \mathbf{X}} = \text{Grad } \mathbf{X}' \quad \text{eq. 2-17}$$

is the deformation gradient that transforms an infinitesimal line element $d\mathbf{X}$ in \mathcal{B}_r into the corresponding line element $d\mathbf{X}'$ in \mathcal{B}'_r and describes the mapping $\kappa: \mathcal{B}_r \rightarrow \mathcal{B}'_r$. The transformations of uniaxial stretch λ [eq. 2-11] and volume change J [eq. 2-14] under such a change of reference configuration are given by

$$\lambda' = \frac{l}{l_r} \frac{l_r}{l'_r}, \quad \text{and} \quad \text{eq. 2-18}$$

$$J' = \frac{dV_t}{dV_r} \frac{dV_r}{dV'_r}. \quad \text{eq. 2-19}$$

According to the polar decomposition theorem, any deformation gradient \mathbf{F} can be decomposed uniquely into positive definite symmetric second-order tensors \mathbf{U} and \mathbf{V} and a proper orthogonal or rotational second-order tensor \mathbf{R} such that

$$\mathbf{F} = \mathbf{R} \cdot \mathbf{U} = \mathbf{V} \cdot \mathbf{R} \quad \text{eq. 2-20}$$

with $\mathbf{R} \cdot \mathbf{R}^T = \mathbf{I}$ and $\det \mathbf{R} = 1$.

The *right* and *left stretch tensor* \mathbf{U} and \mathbf{V} are symmetric and positive definite second order tensors. Both tensors have the same eigenvalues as \mathbf{F} , the principal stretches λ_i , $i = 1, 2, 3$. With regard to the normalized principal stretch directions \mathbf{N}_i in the reference or material configuration and \mathbf{n}_i in the current or spatial configuration they are represented as follows:

$$\mathbf{U} = \sum_{i=1}^3 \lambda_i \mathbf{N}_i \otimes \mathbf{N}_i, \quad \text{eq. 2-21}$$

$$\mathbf{V} = \sum_{i=1}^3 \lambda_i \mathbf{n}_i \otimes \mathbf{n}_i. \quad \text{eq. 2-22}$$

Without loss of generality, the *nominal* or *BIOT's strain tensor* may be defined with regard to an orthonormal basis system constituted by the principal stretch directions in the reference configuration as

$$\boldsymbol{\varepsilon} = \mathbf{U} - \mathbf{I} = \sum_{i=1}^3 (\lambda_i - 1) \mathbf{N}_i \otimes \mathbf{N}_i, \quad \text{eq. 2-23}$$

and correspondingly the nominal strains are given by $\varepsilon_i = \lambda_i - 1 = \Delta l_i(t)/l_{i,r}$. Stretches as well as nominal strains are direct and intelligible measures of deformation.

The *right* and *left CAUCHY-GREEN strain tensors*, \mathbf{C} and \mathbf{B} , respectively, are defined by means of the deformation gradient as

$$\mathbf{C} = \mathbf{F}^T \cdot \mathbf{F} \quad \text{eq. 2-24}$$

$$\mathbf{B} = \mathbf{F} \cdot \mathbf{F}^T. \quad \text{eq. 2-25}$$

From this definition follows immediately that \mathbf{C} and \mathbf{B} are positive definite symmetric second order tensors:

$$\mathbf{C} = \mathbf{C}^T, \quad \text{eq. 2-26}$$

$$\mathbf{B} = \mathbf{B}^T. \quad \text{eq. 2-27}$$

The *principal invariants* of \mathbf{C} and \mathbf{B} are identical and given by

$$I_1 = \text{tr}(\mathbf{C}), \quad \text{eq. 2-28}$$

$$I_2 = \frac{1}{2}[I_1^2 - \text{tr}(\mathbf{C}^2)], \quad \text{eq. 2-29}$$

$$I_3 = \det \mathbf{C} = J^2. \quad \text{eq. 2-30}$$

Without loss of generality, the principal invariants may be given in terms of the principal stretches $\lambda_1, \lambda_2, \lambda_3$:

$$I_1 = \lambda_1^2 + \lambda_2^2 + \lambda_3^2, \quad \text{eq. 2-31}$$

$$I_2 = \lambda_1^2 \lambda_2^2 + \lambda_1^2 \lambda_3^2 + \lambda_2^2 \lambda_3^2, \quad \text{eq. 2-32}$$

$$I_3 = \lambda_1^2 \lambda_2^2 \lambda_3^2, \quad \text{eq. 2-33}$$

and using eq. 2-30 from eq. 2-33 follows

$$J = \lambda_1 \lambda_2 \lambda_3. \quad \text{eq. 2-34}$$

The case that a continuum body does not undergo any deformation or rigid body motion can be regarded as an identical mapping $\chi: \mathcal{B}_r \rightarrow \mathcal{B}_r$. Then

$$d\mathbf{X} = \mathbf{F} \cdot d\mathbf{X} \Leftrightarrow \mathbf{F} = \mathbf{I} \quad \text{eq. 2-35}$$

and consequently $\mathbf{U} = \mathbf{V} = \mathbf{C} = \mathbf{B} = \mathbf{I}$. The *GREEN-LAGRANGE* strain tensor

$$\mathbf{E} = \frac{1}{2}(\mathbf{C} - \mathbf{I}) \quad \text{eq. 2-36}$$

is defined as a deformation measure that returns the zero vector for the undeformed state. In the undeformed state, for any rigid body motion and for any isochoric deformation, the volume change J takes the value 1.

Regard an arbitrary motion \mathbf{x} and a motion $\hat{\mathbf{x}}$ with overlaid rigid body rotation \mathbf{Q} and rigid body translation \mathbf{c} :

$$\hat{\mathbf{x}}(\mathbf{X}) = \mathbf{Q} \cdot \mathbf{x}(\mathbf{X}) + \mathbf{c}, \quad \text{eq. 2-37}$$

where \mathbf{Q} is a proper orthogonal second order tensor [cf. eq. 2-20] and $\mathbf{c} \in \mathbf{R}^3$ is a vector. Note that both motion functions refer to the same reference configuration. According to eq. 2-9, for the motion \mathbf{x} , the deformation gradient is given by $\mathbf{F} = \partial \mathbf{x} / \partial \mathbf{X}$. In contrast, $\widehat{\mathbf{F}}$ corresponding to $\widehat{\mathbf{x}}$ reads as

$$\widehat{\mathbf{F}} = \frac{\partial \widehat{\mathbf{x}}}{\partial \mathbf{X}} = \frac{\partial}{\partial \mathbf{X}} (\mathbf{Q} \cdot \mathbf{x} + \mathbf{c}) = \mathbf{Q} \cdot \frac{\partial \mathbf{x}}{\partial \mathbf{X}} + \frac{\partial \mathbf{c}}{\partial \mathbf{X}} = \mathbf{Q} \cdot \mathbf{F}. \quad \text{eq. 2-38}$$

The latter equation shows that the representation of the deformation of a continuum body by the deformation gradient is free of translational rigid body motions but not free of rigid body rotations. Note that \mathbf{Q} and \mathbf{F} can be understood as two deformation gradients and that the scalar product indicates the sequential application of both to the reference configuration:

$$\mathbf{F}: \mathcal{B}_r \rightarrow \mathcal{B}_t, \quad \mathbf{Q}: \mathcal{B}_t \rightarrow \widehat{\mathcal{B}}_t, \quad \text{and}$$

$$\mathbf{Q} \cdot \mathbf{F} = \mathbf{Q} \circ \mathbf{F}: \mathcal{B}_r \rightarrow \widehat{\mathcal{B}}_t \quad \text{eq. 2-39}$$

In contrast, the right and left stretch tensor \mathbf{U} and \mathbf{V} , respectively, are free of any rotational elements by definition, including any rigid body rotations. That \mathbf{C} and \mathbf{B} are unaffected by rigid body rotations can be understood from their dependency on \mathbf{U} and \mathbf{V} , respectively:

$$\mathbf{C} = \mathbf{F}^T \cdot \mathbf{F} = (\mathbf{R} \cdot \mathbf{U})^T \cdot \mathbf{R} \cdot \mathbf{U} = \mathbf{U}^T \cdot \mathbf{R}^T \cdot \mathbf{R} \cdot \mathbf{U} = \mathbf{U} \cdot \mathbf{I} \cdot \mathbf{U} = \mathbf{U}^2, \quad \text{eq. 2-40}$$

$$\mathbf{B} = \mathbf{F} \cdot \mathbf{F}^T = \mathbf{V} \cdot \mathbf{R} \cdot (\mathbf{V} \cdot \mathbf{R})^T = \mathbf{V} \cdot \mathbf{R} \cdot \mathbf{R}^T \cdot \mathbf{V}^T = \mathbf{V} \cdot \mathbf{I} \cdot \mathbf{V} = \mathbf{V}^2. \quad \text{eq. 2-41}$$

Since \mathbf{U} describes the deformation state with respect to the normalized principal stretch directions \mathbf{N}_i in the reference configuration [eq. 2-21], $\mathbf{C} = \mathbf{U}^2$ is a material strain tensor, whereas $\mathbf{B} = \mathbf{V}^2$ is a spatial strain tensor [eq. 2-22].

These deformation tensors as well as the BIOT's strain tensor, that was defined by means of its relation to \mathbf{U} [eq. 2-23], are suited for the description of finite deformations that may include large rigid body rotations as they are commonly observed in aortic wall mechanics [cf. chapters 5 and 6 of this thesis].

2.2 Stress tensors

According to NEWTON's 2nd law of motion, the sum of all forces \mathbf{K} acting on a continuum body (in any current configuration \mathcal{B}_t) equals the temporal change of its linear momentum $\dot{\mathbf{p}} = m\dot{\mathbf{v}}$, where m is the mass, \mathbf{v} the velocity of a volume element and the operator $\dot{\mathbf{p}} = d\mathbf{p}/dt$:

$$\mathbf{K} = \dot{\mathbf{p}}. \quad \text{eq. 2-42}$$

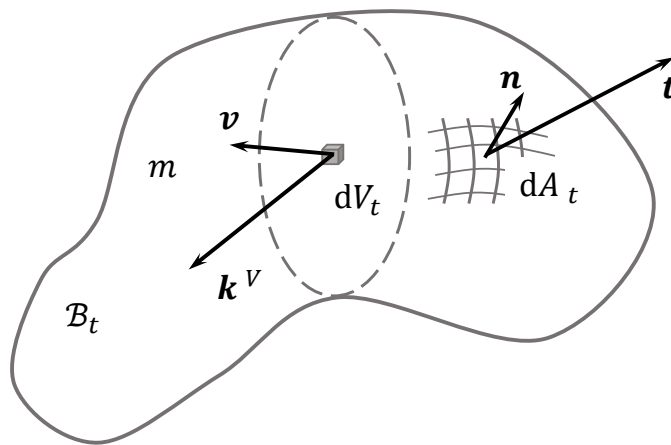


Figure 2-2 Kinetics of a continuum body: Velocity \mathbf{v} of an infinitesimal volume element dV_t , body forces \mathbf{k}^V per volume element dV_t and surface forces \mathbf{t} per area element $dA_t = \mathbf{n}dA_t$ acting on the current configuration of the body.

Distinguishing directed body forces \mathbf{k}^V that are defined per volume element dV_t and directed surface forces \mathbf{t} that are defined per area element dA_t , i.e. stress vectors, the impulse balance eq. 2-42 may be formulated without loss of generality for any current configuration \mathcal{B}_t of the continuum body [cf. Figure 2-2] as follows:

$$\int_{\partial V_t} \mathbf{k}^V dV_t + \int_{\partial A_t} \mathbf{t} dA_t = m\dot{\mathbf{v}}, \quad \text{eq. 2-43}$$

where ∂V_t is the volume and ∂A_t is the bounding surface of the whole continuum body.

In the absence of body forces and for the static or quasistatic case, eq. 2-43 reduces to the equilibrium equation

$$\int_{\partial A_t} \mathbf{t} \, dA_t = \mathbf{0}. \quad \text{eq. 2-44}$$

According to CAUCHY's stress theorem, the stress vector $\mathbf{t} \in \mathbf{R}$ is linearly related to the non-singular CAUCHY stress tensor $\boldsymbol{\sigma} \in \mathbf{R}^{3 \times 3}$ by means of the surface normal unit vector \mathbf{n} :

$$\mathbf{t} = \boldsymbol{\sigma}^T \cdot \mathbf{n}. \quad \text{eq. 2-45}$$

Using eq. 2-45 and the divergence or GAUSS's theorem, equilibrium eq. 2-44 may be formulated as

$$\int_{\partial A_t} \boldsymbol{\sigma}^T \cdot \mathbf{n} \, dA_t = \mathbf{0} \Leftrightarrow \int_{\partial V_t} \text{div } \boldsymbol{\sigma} \, dV_t = \mathbf{0}, \quad \text{eq. 2-46}$$

where div is the divergence operator on the current configuration. Equation eq. 2-46 must hold for arbitrary volumes ∂V_t and therefore the integrand itself must vanish. This provides the local form of the equilibrium equation for the current configuration \mathcal{B}_t :

$$\text{div } \boldsymbol{\sigma} = \mathbf{0}. \quad \text{eq. 2-47}$$

In order to fulfill the balance of moments, $\boldsymbol{\sigma}$ must be a symmetric tensor: $\boldsymbol{\sigma}^T = \boldsymbol{\sigma}$ [cf. e.g. Silber and Steinwender 2005 for a detailed description]. Using eq. 2-12 and eq. 2-14, eq. 2-46 can be transformed to the reference configuration \mathcal{B}_r :

$$\int_{\partial A_t} \boldsymbol{\sigma}^T \cdot \mathbf{n} \, dA_t = \mathbf{0} \Leftrightarrow \int_{\partial A_r} \boldsymbol{\sigma}^T \cdot J \mathbf{F}^{-T} \cdot \mathbf{N} \, dA_r = \mathbf{0} \Leftrightarrow \int_{\partial A_r} J \boldsymbol{\sigma}^T \cdot \mathbf{F}^{-T} \cdot \mathbf{N} \, dA_r = \mathbf{0} \quad \text{eq. 2-48}$$

Following Ogden [2009] the *1st PIOLA-KIRCHHOFF stress tensor*, which is denoted here as \mathbf{P}^I , and its transpose, the *nominal stress tensor* designated \mathbf{S} in this thesis, are defined as

$$\mathbf{P}^I = J \boldsymbol{\sigma}^T \cdot \mathbf{F}^{-T}, \quad \text{eq. 2-49}$$

$$\mathbf{S} = (\mathbf{P}^I)^T = J \mathbf{F}^{-1} \cdot \boldsymbol{\sigma}. \quad \text{eq. 2-50}$$

Consequently, from eq. 2-48 the local form of the equilibrium equation for the reference configuration \mathcal{B}_t is obtained:

$$\text{Div } \mathbf{S} = \mathbf{0}, \quad \text{eq. 2-51}$$

where Div is the divergence operator on the reference configuration. Finally, the 2nd *PIOLA-KIRCHHOFF stress tensor*, denoted in this thesis by \mathbf{P}^{II} , is introduced as

$$\mathbf{P}^{\text{II}} = J \mathbf{F}^{-1} \cdot \boldsymbol{\sigma} \cdot \mathbf{F}^{-\text{T}} = \mathbf{S} \cdot \mathbf{F}^{-\text{T}}. \quad \text{eq. 2-52}$$

2.3 Elastic material properties

The elastic material equation constitutes the relation between the two state variables of a continuum body that have been introduced in the previous sections 2.1 and 2.2: deformation and stress. Therefore, it is called *constitutive equation*. It can be determined experimentally, only.

2.3.1 Cauchy elasticity

For a CAUCHY elastic material, the stress response depends on the current deformation state, only, not on the deformation history [see Silber and Steinwender 2005 and Silber and Then 2013 for detailed discussion of this topic]. The constitutive equation is a symmetrical, tensor valued function of the deformation gradient \mathbf{F} :

$$\boldsymbol{\sigma} = \boldsymbol{\sigma}(\mathbf{F}), \quad \boldsymbol{\sigma} = \boldsymbol{\sigma}^{\text{T}}. \quad \text{eq. 2-53}$$

If \mathbf{F} describes a deformation with regard to an arbitrarily chosen reference configuration \mathcal{B}_r , $\boldsymbol{\sigma}(\mathbf{F})$ gives the stress difference between the current configuration \mathcal{B}_t and \mathcal{B}_r . In this case, \mathcal{B}_r may be loaded with prestresses that originate from boundary conditions. If, in contrast, the reference configuration is an undeformed and load-free *natural configuration* \mathcal{B}_0 , it is required that the stress vanishes for the undeformed state $\mathbf{F} = \mathbf{I}$:

$$\boldsymbol{\sigma}(\mathbf{I}) = \mathbf{0}. \quad \text{eq. 2-54}$$

Stresses that do not vanish in the load-free configuration are called *residual stresses* and the corresponding residually stressed configuration is distinguished from the natural configuration. Note that

residual stress and corresponding deformation states are necessarily inhomogeneous since the boundary region of the unloaded body must be stress free.

2.3.2 Hyperelasticity

From the first law of thermodynamics together with the law of the conservation of mass,

$$\rho_r = J\rho_t, \quad \text{eq. 2-55}$$

where ρ_r and ρ_t are the density of the body in its reference and current configuration, the mechanical law of power conservation in its local form can be derived [cf. Silber and Steinwender 2005 for detailed derivation]:

$$\rho_r \dot{u} = \mathbf{P}^{\text{II}} : \dot{\mathbf{E}}. \quad \text{eq. 2-56}$$

It balances the product of the time derivative of the inner energy of the body per mass unit $\dot{u} = du/dt$ and the density ρ_r of the body in the reference configuration, on the one hand, and the double contraction of the 2nd PIOLA-KIRCHHOFF stress tensor and the right GREEN strain rate tensor, on the other hand. Note that the density ρ_r in the reference configuration is time independent. Introducing the *strain energy potential*

$$w := \rho_r u \quad \text{eq. 2-57}$$

and regarding eq. 2-36, eq. 2-56 can be written as

$$\dot{w} = \frac{1}{2} \mathbf{P}^{\text{II}} : \dot{\mathbf{C}}. \quad \text{eq. 2-58}$$

Hyperelastic materials are characterized by the existence of such a strain energy potential w , that is a twofold steadily differentiable, scalar valued tensor function of the current deformation state. I.e. w depends only on the deformation gradient \mathbf{F} :

$$w = w(\mathbf{F}). \quad \text{eq. 2-59}$$

This includes that w may depend on \mathbf{F} through $\mathbf{C}(\mathbf{F})$, which is chosen here as representation [see e.g. Ogden 2009 for alternative formulations]:

$$w = w(\mathbf{C}). \quad \text{eq. 2-60}$$

Regarding the following relation for the time derivative of a scalar valued tensor function [cf. Silber and Steinwender 2005]

$$\dot{f}(\mathbf{A}) = \frac{\partial f(\mathbf{A})}{\partial \mathbf{A}} : \dot{\mathbf{A}}, \quad \text{eq. 2-61}$$

it follows immediately that for a hyperelastic material, the 2nd PIOLA-KIRCHHOFF stress tensor can be obtained as function of the partial derivative of the strain energy function with regard to the right CAUCHY-GREEN strain tensor:

$$\mathbf{P}^{\text{II}} = 2 \frac{\partial w(\mathbf{C})}{\partial \mathbf{C}}. \quad \text{eq. 2-62}$$

Using the relations given in eq. 2-52 the CAUCHY and the nominal stress tensors can be written as functions of $\partial w / \partial \mathbf{C}$, too:

$$\boldsymbol{\sigma} = 2J^{-1} \mathbf{F} \cdot \frac{\partial w(\mathbf{C})}{\partial \mathbf{C}} \cdot \mathbf{F}^{\text{T}}, \quad \text{eq. 2-63}$$

$$\mathbf{S} = 2 \frac{\partial w(\mathbf{C})}{\partial \mathbf{C}} \cdot \mathbf{F}^{\text{T}}. \quad \text{eq. 2-64}$$

Equations eq. 2-62 to eq. 2-64 hold for hyperelastic materials without any internal constraint such as incompressibility. For an incompressible material, the volume change J [eq. 2-14] equals 1 for all loading conditions, which is known as the *incompressibility condition*:

$$J = \det \mathbf{F} = 1. \quad \text{eq. 2-65}$$

With $J = \sqrt{\det \mathbf{C}} = \sqrt{\det \mathbf{B}}$ follows

$$\det \mathbf{C} = \det \mathbf{B} = 1 \quad \text{eq. 2-66}$$

in case of incompressibility. For such a material, hydrostatic pressures, that are represented by the tensor $-p\mathbf{I}$ with respect to the current configuration, do not induce any deformation of the body, but additional stress, which must be determined from the boundary conditions and loading of the body. This hydrostatic stress tensor has to be regarded in the CAUCHY stress tensor in addition to its dependency on the deformation through $w(\mathbf{C})$. In this case, the CAUCHY stress tensor, that gives the “true” stress with respect to the current configuration \mathcal{B}_t , reads as

$$\boldsymbol{\sigma} = 2J^{-1} \mathbf{F} \cdot \frac{\partial w(\mathbf{C})}{\partial \mathbf{C}} \cdot \mathbf{F}^{\text{T}} - p\mathbf{I}. \quad \text{eq. 2-67}$$

By application of the transformation rules that are given in eq. 2-49 and eq. 2-50 to the hydrostatic stress tensor $-p\mathbf{I}$, the following representations of the nominal and the 2nd PIOLA-KIRCHHOFF stress tensor are obtained that hold for incompressible materials:

$$\mathbf{S} = 2 \frac{\partial w(\mathbf{C})}{\partial \mathbf{C}} \cdot \mathbf{F}^T - p \mathbf{F}^{-1} \quad \text{eq. 2-68}$$

and

$$\mathbf{P}^{\text{II}} = 2 \frac{\partial w(\mathbf{C})}{\partial \mathbf{C}} - p \mathbf{C}^{-1} . \quad \text{eq. 2-69}$$

The total differential of the 2nd PIOLA-KIRCHHOFF stress tensor \mathbf{P}^{II} with respect to the right CAUCHY strain tensor \mathbf{C} gives the incremental change of stress for an incremental change of deformation [cf. Holzapfel 2010, 6.6 for the following]:

$$d\mathbf{P}^{\text{II}} = 2 \frac{\partial \mathbf{P}^{\text{II}}}{\partial \mathbf{C}} : \frac{1}{2} d\mathbf{C} . \quad \text{eq. 2-70}$$

The partial derivative

$$\mathbb{C} = 2 \frac{\partial \mathbf{P}^{\text{II}}}{\partial \mathbf{C}} = 2 \frac{\partial P_{ij}^{\text{II}}}{\partial C_{kl}} \mathbf{e}_i \otimes \mathbf{e}_j \otimes \mathbf{e}_k \otimes \mathbf{e}_l \quad \text{eq. 2-71}$$

is a 4th order tensor that characterizes the change of the directional components of stress depending on the change of the directional components of the deformation tensor. In general, the components C_{ijkl} of \mathbb{C} will be nonlinear functions of \mathbf{C} . If they are linearized for a specific multiaxial deformation state, they represent the tangent moduli of the nonlinear material in this deformation state. \mathbb{C} is called *elasticity tensor*.

Using eq. 2-62, it is evident that \mathbb{C} is the HESSIAN matrix of the strain energy function w in \mathbf{C} :

$$\mathbb{C} := 4 \frac{\partial^2 w(\mathbf{C})}{\partial \mathbf{C}^2} . \quad \text{eq. 2-72}$$

Because of the symmetry of the right CAUCHY strain tensor \mathbf{C} the elasticity tensor possesses the *minor symmetries*:

$$C_{ijkl} = C_{jilk} , \quad \text{eq. 2-73}$$

and according to the YOUNG's theorem, it enjoys the symmetry of second derivatives, the so-called *major symmetries*:

$$C_{ijkl} = 4 \frac{\partial^2 w}{\partial C_{ij} \partial C_{kl}} = 4 \frac{\partial^2 w}{\partial C_{kl} \partial C_{ij}} = C_{klij} . \quad \text{eq. 2-74}$$

It is required that the strain energy potential vanishes for a natural configuration \mathcal{B}_0 :

$$w(\mathbf{I}) = 0 \quad \text{eq. 2-75}$$

and that w has a global minimum for the undeformed state $\mathbf{C} = \mathbf{I}$:

$$w(\mathbf{C} \neq \mathbf{I}) > 0 . \quad \text{eq. 2-76}$$

In order to ensure that the norm of the stress response must be strictly increasing for increasing deformation, w has to be strictly convex. This is ensured if the elasticity tensor \mathbb{C} is positive definite.

2.3.3 Objectivity

Objectivity requires that the strain energy potential of a deformed hyperelastic solid is not changed by rigid body motions. In section 2.1 it was already shown that, for a motion \mathbf{x} with superimposed translation \mathbf{c} and rotation \mathbf{Q} : $\hat{\mathbf{x}}(\mathbf{X}) = \mathbf{Q} \cdot \mathbf{x}(\mathbf{X}) + \mathbf{c}$, the deformation gradient $\hat{\mathbf{F}} = \mathbf{Q} \cdot \mathbf{F}$ is independent of \mathbf{c} , but not of \mathbf{Q} . That means that the strain energy function $w(\mathbf{F})$ is not objective without additional conditions and it is demanded that

$$w(\mathbf{Q} \cdot \mathbf{F}) = w(\mathbf{F}) \quad \text{eq. 2-77}$$

holds for all proper orthogonal \mathbf{Q} [Ogden 2009].

In contrast, the right CAUCHY strain tensor \mathbf{C} is completely independent of rigid body motions and, therefore, is an objective deformation measure in itself. Bearing in mind that $\mathbf{Q}^T = \mathbf{Q}^{-1}$, it follows for \mathbf{C} that describes the deformation corresponding to an arbitrary motion \mathbf{x} and for $\hat{\mathbf{C}}$ and that corresponds to the motion $\hat{\mathbf{x}}$ with overlaid rigid body rotation:

$$\hat{\mathbf{C}} = \hat{\mathbf{F}}^T \cdot \hat{\mathbf{F}} = (\mathbf{Q} \cdot \mathbf{F})^T \cdot \mathbf{Q} \cdot \mathbf{F} = \mathbf{F}^T \cdot \underbrace{\mathbf{Q}^T \cdot \mathbf{Q}}_{\mathbf{I}} \cdot \mathbf{F} = \mathbf{C} . \quad \text{eq. 2-78}$$

Consequently, eq. 2-77 will hold automatically if w is formulated as a function of \mathbf{C} [eq. 2-60] or, equivalently, depends on \mathbf{C} through its principal invariants I_1, I_2, I_3 [cf. eq. 2-28, eq. 2-29, eq. 2-30]:

$$w = w(I_1, I_2, I_3) . \quad \text{eq. 2-79}$$

According to eq. 2-67 the CAUCHY stress tensor is then obtained by derivation of $w(I_1, I_2, I_3)$ with respect to the material strain tensor \mathbf{C} and the subsequent transformation of the obtained stress tensor to the current configuration \mathcal{B}_r :

$$\boldsymbol{\sigma} = 2J^{-1}\mathbf{F} \cdot \frac{\partial w(I_1, I_2, I_3)}{\partial \mathbf{C}} \cdot \mathbf{F}^T - p\mathbf{I} = 2J^{-1}\mathbf{F} \cdot \left[\frac{\partial w}{\partial I_1} \frac{\partial I_1}{\partial \mathbf{C}} + \frac{\partial w}{\partial I_2} \frac{\partial I_2}{\partial \mathbf{C}} + \frac{\partial w}{\partial I_3} \frac{\partial I_3}{\partial \mathbf{C}} \right] \cdot \mathbf{F}^T, \quad \text{eq. 2-80}$$

where

$$\frac{\partial I_1}{\partial \mathbf{C}} = \mathbf{I}, \quad \text{eq. 2-81}$$

$$\frac{\partial I_2}{\partial \mathbf{C}} = I_1\mathbf{I} - \mathbf{C}, \quad \text{and} \quad \text{eq. 2-82}$$

$$\frac{\partial I_3}{\partial \mathbf{C}} = I_3\mathbf{C}^{-1} = \mathbf{C}^2 - I_1\mathbf{C} + I_2\mathbf{I}. \quad \text{eq. 2-83}$$

See e.g. Silber and Steinwender [2005] for detailed derivation of eq. 2-81, eq. 2-82 and eq. 2-83. Since the three principal invariants represent three independent measures of deformation, the partial derivatives $\partial w/\partial I_1$, $\partial w/\partial I_2$ and $\partial w/\partial I_3$ represent the change of stored strain energy depending on three independent types of deformation. In other words, each of these partial derivatives of w represents the material response to a specific type of deformation and, therefore, can be regarded as an independent constitutive equation that describes the mechanical properties of the material [Ogden 2009].

2.3.4 Material symmetry

According to Ogden [2009], material symmetry, identified in the reference configuration \mathcal{B}_r , may be characterized by the fact that the strain energy w remains unchanged if the configuration is changed consistently with a symmetry. Regard two reference configurations \mathcal{B}_r and \mathcal{B}'_r of the identical body B that are related by a rigid body rotation, i.e. by the deformation gradient

$$\mathbf{Q} = \text{Grad}'\mathbf{X} = \frac{\partial \mathbf{X}}{\partial \mathbf{X}'}, \quad \text{eq. 2-84}$$

where \mathbf{Q} is a proper orthogonal second order tensor. According to eq. 2-9, the deformation gradient of any current configuration \mathbf{x} with respect to \mathcal{B}_r is given by $\mathbf{F} = \partial \mathbf{x} / \partial \mathbf{X}$ [eq. 2-9] and accordingly with respect to \mathcal{B}'_r

$$\mathbf{F}' = \frac{\partial \mathbf{x}}{\partial \mathbf{X}'} = \frac{\partial \mathbf{x}}{\partial \mathbf{X}} \cdot \frac{\partial \mathbf{X}}{\partial \mathbf{X}'} = \mathbf{F} \cdot \mathbf{Q}. \quad \text{eq. 2-85}$$

The resulting requirement for material symmetry

$$w(\mathbf{F}) = w(\mathbf{F} \cdot \mathbf{Q}) \quad \text{eq. 2-86}$$

is not fulfilled automatically by strain energy potentials that are formulated as function of \mathbf{C} :

$$w(\mathbf{C}') = w((\mathbf{F} \cdot \mathbf{Q})^T \cdot \mathbf{F} \cdot \mathbf{Q}) = w(\mathbf{Q}^T \cdot \mathbf{F}^T \cdot \mathbf{F} \cdot \mathbf{Q}) = w(\mathbf{Q}^T \cdot \mathbf{C} \cdot \mathbf{Q}). \quad \text{eq. 2-87}$$

In contrast to the objectivity condition eq. 2-77, the symmetry condition eq. 2-86 that may be formulated in terms of \mathbf{C} as

$$w(\mathbf{C}) = w(\mathbf{Q}^T \cdot \mathbf{C} \cdot \mathbf{Q}) \quad \text{eq. 2-88}$$

usually will not hold for all rotation tensors \mathbf{Q} , but only for a subset that constitutes the *symmetry group* of the material relative to \mathcal{B}_r .

2.3.4.1 Isotropy

An elastic material is called *isotropic* in the special case that eq. 2-88 holds for *all proper orthogonal tensors* \mathbf{Q} . Thus the strain energy function w is automatically isotropic if it depends on the three principal invariants I_1, I_2 and I_3 of \mathbf{C} and \mathbf{B} , [cf. eq. 2-28, eq. 2-29, eq. 2-30], which are defined by their property to remain constant for all rigid body motions or changes of basis. I.e. an isotropic material depends on three independent measures of deformation: I_1, I_2 and I_3 :

$$w = w(I_1, I_2, I_3) . \quad \text{eq. 2-89}$$

According to eq. 2-67 and using the derivatives of I_1, I_2 and I_3 with regard to the argument tensor \mathbf{C} [cf. eq. 2-81, eq. 2-82], the Cauchy stress tensor for an unconstrained isotropic material and a homogeneous deformation reads as

$$\begin{aligned} \boldsymbol{\sigma} &= 2J^{-1} \mathbf{F} \cdot \left[\frac{\partial w}{\partial I_1} \mathbf{I} + \frac{\partial w}{\partial I_2} (I_1 \mathbf{I} - \mathbf{C}) + \frac{\partial w}{\partial I_3} I_3 \mathbf{C}^{-1} \right] \cdot \mathbf{F}^T \\ \Leftrightarrow \boldsymbol{\sigma} &= 2J^{-1} \left[\frac{\partial w}{\partial I_1} \mathbf{F} \cdot \mathbf{I} \cdot \mathbf{F}^T + \frac{\partial w}{\partial I_2} \left(I_1 \mathbf{F} \cdot \mathbf{I} \cdot \mathbf{F}^T - \underbrace{\mathbf{F} \cdot \mathbf{C}}_{\mathbf{F}^T \cdot \mathbf{F}} \cdot \mathbf{F}^T \right) + \frac{\partial w}{\partial I_3} I_3 \mathbf{F} \cdot \underbrace{\mathbf{C}^{-1}}_{\mathbf{F}^{-1} \cdot \mathbf{F}^{-T}} \cdot \mathbf{F}^T \right] \\ \Leftrightarrow \boldsymbol{\sigma} &= 2J^{-1} \left[\frac{\partial w}{\partial I_1} \mathbf{B} + \frac{\partial w}{\partial I_2} (I_1 \mathbf{B} - \mathbf{B}^2) + \frac{\partial w}{\partial I_3} I_3 \mathbf{I} \right]. \quad \text{eq. 2-90} \end{aligned}$$

If a homogeneous deformation is considered that is characterized by triaxial tension in an orthonormal coordinate system, the tensile directions are the principal axes of the deformation and the left CAUCHY strain tensor is given by

$$\mathbf{B} = \sum_{i=1}^3 \lambda_i^2 \mathbf{n}_i \otimes \mathbf{n}_i, \quad \text{eq. 2-91}$$

where λ_i are the principal stretches and \mathbf{n}_i are the principal stretch directions with respect to the current configuration. Inserting eq. 2-91 into eq. 2-90, the nonzero components of the CAUCHY stress tensor are obtained, which are given here in index notation without summation over i :

$$\sigma_{ii} = 2J^{-1} \left[\frac{\partial w}{\partial I_1} \lambda_i^2 + \frac{\partial w}{\partial I_2} \lambda_i^2 (I_1 - \lambda_i^2) + \frac{\partial w}{\partial I_3} I_3 \right], \quad i = 1, 2, 3. \quad \text{eq. 2-92}$$

The shear-free deformation corresponds to a shear-free stress state, i.e. the stress components σ_{ii} are the principal stresses σ_i : For an isotropic material the deformation tensor and the corresponding stress tensor have the same eigenvectors.

2.3.4.2 Transverse isotropy

A transversally isotropic material is characterized by a single preferred direction, which is represented by a direction vector $\mathbf{a}_0 \in \mathbf{R}^3$ in the reference configuration \mathcal{B}_r . Additionally, the strain energy potential w must be unchanged by any rotation about \mathbf{a}_0 and by the reversal of the orientation of \mathbf{a}_0 :

$$w(\mathbf{F}) = w(\mathbf{F} \cdot \mathbf{Q}) \quad \text{eq. 2-93}$$

for all orthogonal \mathbf{Q} with $\mathbf{Q} \cdot \mathbf{a}_0 = \pm \mathbf{a}_0$.

More conveniently, a transversally isotropic strain energy potential w may be formulated as an isotropic function of the right CAUCHY strain tensor and the *structure tensor* that is formed by the dyadic product $\mathbf{a}_0 \otimes \mathbf{a}_0 = a_{0i} a_{0j} \mathbf{e}_i \otimes \mathbf{e}_j$, $i, j = 1, 2, 3$. Regarding relation eq. 2-84, consider the mapping of \mathbf{a}'_0 in \mathcal{B}'_r onto the corresponding direction vector \mathbf{a}_0 in \mathcal{B}_r :

$$\mathbf{a}_0 = \mathbf{Q} \cdot \mathbf{a}'_0 \Leftrightarrow \mathbf{a}'_0 = \mathbf{Q}^T \cdot \mathbf{a}_0. \quad \text{eq. 2-94}$$

Having in mind that the transpose of a vector is identical with the original vector, it can be seen that the structure tensor transforms between two different reference configurations in the same way like \mathbf{C} :

$$\begin{aligned} w(\mathbf{C}', \mathbf{a}'_0 \otimes \mathbf{a}'_0) &= w\left(\mathbf{Q}^T \cdot \mathbf{C} \cdot \mathbf{Q}, (\mathbf{Q}^T \cdot \mathbf{a}_0) \otimes (\mathbf{Q}^T \cdot \mathbf{a}_0)\right) \\ &= w(\mathbf{Q}^T \cdot \mathbf{C} \cdot \mathbf{Q}, \mathbf{Q}^T \cdot \mathbf{a}_0 \otimes \mathbf{a}_0 \cdot \mathbf{Q}). \end{aligned} \quad \text{eq. 2-95}$$

Thus, the symmetry requirement for a transversely isotropic material may be formulated as follows:

$$w(\mathbf{C}, \mathbf{a}_0 \otimes \mathbf{a}_0) = w(\mathbf{Q}^T \cdot \mathbf{C} \cdot \mathbf{Q}, \mathbf{Q}^T \cdot \mathbf{a}_0 \otimes \mathbf{a}_0 \cdot \mathbf{Q}) \quad \text{eq. 2-96}$$

for all proper orthogonal \mathbf{Q} . This requirement is fulfilled automatically if the strain energy potential of an unconstrained hyperelastic material is given as a function of the three principal invariants of \mathbf{C} and two additional invariants (often called “pseudo-invariants”) that depend on the structure tensor $\mathbf{a}_0 \otimes \mathbf{a}_0$ in addition to \mathbf{C} :

$$w = w(I_1, I_2, I_3, I_4, I_5), \quad \text{eq. 2-97}$$

where

$$I_4 = \mathbf{C} : \mathbf{a}_0 \otimes \mathbf{a}_0 = \mathbf{a}_0 \cdot \mathbf{C} \cdot \mathbf{a}_0 \quad \text{and} \quad \text{eq. 2-98}$$

$$I_5 = \mathbf{C}^2 : \mathbf{a}_0 \otimes \mathbf{a}_0 = \mathbf{a}_0 \cdot \mathbf{C}^2 \cdot \mathbf{a}_0. \quad \text{eq. 2-99}$$

The derivatives of I_4 and I_5 with respect to \mathbf{C} are given by

$$\frac{\partial I_4}{\partial \mathbf{C}} = \mathbf{a}_0 \otimes \mathbf{a}_0 \quad \text{and} \quad \text{eq. 2-100}$$

$$\frac{\partial I_5}{\partial \mathbf{C}} = \mathbf{a}_0 \otimes \mathbf{a}_0 \cdot \mathbf{C} + \mathbf{C} \cdot \mathbf{a}_0 \otimes \mathbf{a}_0. \quad \text{eq. 2-101}$$

The derivation of eq. 2-100 and eq. 2-101 is shown in detail in appendix A. The CAUCHY stress tensor for an arbitrary homogeneous deformation, is given by

$$\begin{aligned} \boldsymbol{\sigma} &= 2J^{-1} \mathbf{F} \cdot \left[\frac{\partial w}{\partial I_1} \mathbf{I} + \frac{\partial w}{\partial I_2} (I_1 \mathbf{I} - \mathbf{C}) + \frac{\partial w}{\partial I_3} I_3 \mathbf{C}^{-1} + \frac{\partial w}{\partial I_4} \mathbf{a}_0 \mathbf{a}_0 \right. \\ &\quad \left. + \frac{\partial w}{\partial I_5} (\mathbf{a}_0 \otimes \mathbf{a}_0 \cdot \mathbf{C} + \mathbf{C} \cdot \mathbf{a}_0 \otimes \mathbf{a}_0) \right] \cdot \mathbf{F}^T \\ \Leftrightarrow \boldsymbol{\sigma} &= 2J^{-1} \left[\frac{\partial w}{\partial I_1} \mathbf{B} + \frac{\partial w}{\partial I_2} (I_1 \mathbf{B} - \mathbf{B}^2) + \frac{\partial w}{\partial I_3} I_3 \mathbf{I} + \frac{\partial w}{\partial I_4} \mathbf{F} \cdot \mathbf{a}_0 \otimes \mathbf{a}_0 \cdot \mathbf{F}^T \right. \\ &\quad \left. + \frac{\partial w}{\partial I_5} \left(\mathbf{F} \cdot \mathbf{a}_0 \otimes \mathbf{a}_0 \cdot \underbrace{\mathbf{C}}_{\mathbf{F}^T \cdot \mathbf{F}} \cdot \mathbf{F}^T + \mathbf{F} \cdot \underbrace{\mathbf{C}}_{\mathbf{F}^T \cdot \mathbf{F}} \cdot \mathbf{a}_0 \otimes \mathbf{a}_0 \cdot \mathbf{F}^T \right) \right] \end{aligned}$$

$$\Leftrightarrow \boldsymbol{\sigma} = 2J^{-1} \left[\frac{\partial w}{\partial I_1} \mathbf{B} + \frac{\partial w}{\partial I_2} (I_1 \mathbf{B} - \mathbf{B}^2) + \frac{\partial w}{\partial I_3} I_3 \mathbf{I} + \frac{\partial w}{\partial I_4} \mathbf{a} \otimes \mathbf{a} + \frac{\partial w}{\partial I_5} (\mathbf{a} \otimes \mathbf{a} \cdot \mathbf{B} + \mathbf{B} \cdot \mathbf{a} \otimes \mathbf{a}) \right], \quad \text{eq. 2-102}$$

where $\mathbf{a} \otimes \mathbf{a}$ is the structure tensor in the current configuration. Considering again a shear-free triaxial deformation along the principal axes of \mathbf{C} and \mathbf{B} according to eq. 2-91 the following nonzero components of $\boldsymbol{\sigma}$ are obtained:

$$\begin{aligned} \sigma_{11} &= 2J^{-1} \left[\frac{\partial w}{\partial I_1} \lambda_1^2 + \frac{\partial w}{\partial I_2} \lambda_1^2 (I_1 - \lambda_1^2) + \frac{\partial w}{\partial I_3} I_3 + \left(\frac{\partial w}{\partial I_4} + 2 \frac{\partial w}{\partial I_5} \lambda_1^2 \right) a_1 a_1 \right], \\ \sigma_{22} &= 2J^{-1} \left[\frac{\partial w}{\partial I_1} \lambda_2^2 + \frac{\partial w}{\partial I_2} \lambda_2^2 (I_1 - \lambda_2^2) + \frac{\partial w}{\partial I_3} I_3 + \left(\frac{\partial w}{\partial I_4} + 2 \frac{\partial w}{\partial I_5} \lambda_2^2 \right) a_2 a_2 \right], \\ \sigma_{33} &= 2J^{-1} \left[\frac{\partial w}{\partial I_1} \lambda_3^2 + \frac{\partial w}{\partial I_2} \lambda_3^2 (I_1 - \lambda_3^2) + \frac{\partial w}{\partial I_3} I_3 + \left(\frac{\partial w}{\partial I_4} + 2 \frac{\partial w}{\partial I_5} \lambda_3^2 \right) a_3 a_3 \right], \\ \sigma_{12} = \sigma_{21} &= 2J^{-1} \left(\frac{\partial w}{\partial I_4} + \frac{\partial w}{\partial I_5} (\lambda_1^2 + \lambda_2^2) \right) a_1 a_2, \\ \sigma_{13} = \sigma_{31} &= 2J^{-1} \left(\frac{\partial w}{\partial I_4} + \frac{\partial w}{\partial I_5} (\lambda_1^2 + \lambda_3^2) \right) a_1 a_3, \\ \sigma_{23} = \sigma_{32} &= 2J^{-1} \left(\frac{\partial w}{\partial I_4} + \frac{\partial w}{\partial I_5} (\lambda_2^2 + \lambda_3^2) \right) a_2 a_3. \end{aligned} \quad \text{eq. 2-103}$$

Note that despite the shear-free deformation, the shear stresses do not vanish necessarily. Therefore, $\sigma_{11}, \sigma_{22}, \sigma_{33}$ are not principal stresses in general, but only in the special case that $a_i a_j = 0$ for $i \neq j$, i.e. only if the preferred direction \mathbf{a}_0 of the material in the reference configuration is identical with one of the principal axes of the deformation state. In this case, only one of the three components of \mathbf{a}_0 : a_{01}, a_{02} , or a_{03} – and correspondingly of \mathbf{a} – is nonzero, and therefore only the square of this nonzero component that does correspond to one of the normal stress components, necessarily, will not vanish.

2.3.4.3 Materials with two preferred directions, orthotropy

Because of its particular importance for modeling the elastic constitutive behavior of the aortic wall, the case of two preferred directions $\mathbf{a}_{0\alpha}$ and $\mathbf{a}_{0\beta}$ in the reference configuration is considered, finally. $\mathbf{a}_{0\alpha}$ and $\mathbf{a}_{0\beta}$ determine a plane that is chosen as the 1-2 plane with respect to an orthonormal basis $\mathbf{e}_1, \mathbf{e}_2, \mathbf{e}_3$:

$$\mathbf{a}_{0\alpha} = \sin \vartheta_\alpha \mathbf{e}_1 + \cos \vartheta_\alpha \mathbf{e}_2 \quad \text{eq. 2-104}$$

$$\mathbf{a}_{0\beta} = \sin \vartheta_\beta \mathbf{e}_1 - \cos \vartheta_\beta \mathbf{e}_2 \quad \text{eq. 2-105}$$

Initially, it is neither required that \mathbf{a}_{01} and \mathbf{a}_{02} are orthogonal with respect to each other, nor that they are symmetric with respect to the 1- and 2-axes [Figure 2-3].

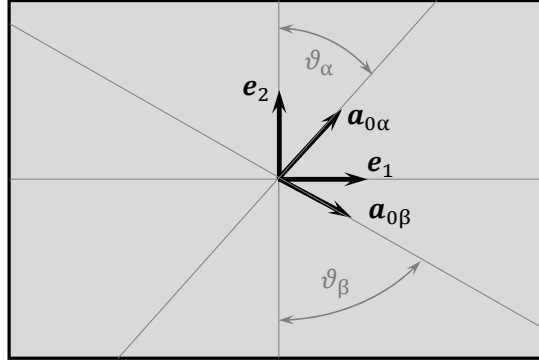


Figure 2-3 View of a material volume with two preferred directions $\mathbf{a}_{0\alpha}$ and $\mathbf{a}_{0\beta}$ in the $\mathbf{e}_1, \mathbf{e}_2$ -plane of an orthonormal coordinate system.

Each preferred direction is modelled by two (pseudo-) invariants according to eq. 2-98 and eq. 2-99:

$$I_{4\alpha} = \mathbf{C} : \mathbf{a}_{0\alpha} \otimes \mathbf{a}_{0\alpha} = \mathbf{a}_{0\alpha} \cdot \mathbf{C} \cdot \mathbf{a}_{0\alpha}, \quad I_{5\alpha} = \mathbf{C}^2 : \mathbf{a}_{0\alpha} \otimes \mathbf{a}_{0\alpha} = \mathbf{a}_{0\alpha} \cdot \mathbf{C}^2 \cdot \mathbf{a}_{0\alpha}, \quad \text{eq. 2-106}$$

$$I_{4\beta} = \mathbf{C} : \mathbf{a}_{0\beta} \otimes \mathbf{a}_{0\beta} = \mathbf{a}_{0\beta} \cdot \mathbf{C} \cdot \mathbf{a}_{0\beta}, \quad I_{5\beta} = \mathbf{C}^2 : \mathbf{a}_{0\beta} \otimes \mathbf{a}_{0\beta} = \mathbf{a}_{0\beta} \cdot \mathbf{C}^2 \cdot \mathbf{a}_{0\beta}. \quad \text{eq. 2-107}$$

In addition to this, another invariant, $I_{\alpha\beta}$, is introduced for the coupling of the two fiber directions. In literature $I_{\alpha\beta}$ is often referred to as eighth invariant I_8 :

$$I_{\alpha\beta} = \mathbf{C} : \mathbf{a}_{0\alpha} \otimes \mathbf{a}_{0\beta} = \mathbf{a}_{0\alpha} \cdot \mathbf{C} \cdot \mathbf{a}_{0\beta}. \quad \text{eq. 2-108}$$

The derivation of $I_{\alpha\beta}$ with respect to \mathbf{C} is given in detail in Appendix A. and reads as

$$\frac{\partial I_{\alpha\beta}}{\partial \mathbf{C}} = \frac{1}{2} (\mathbf{a}_{0\alpha} \otimes \mathbf{a}_{0\beta} + \mathbf{a}_{0\beta} \otimes \mathbf{a}_{0\alpha}). \quad \text{eq. 2-109}$$

For an arbitrary homogenous three-dimensional deformation, the CAUCHY stress tensor of an unconstrained material has the form:

$$\begin{aligned}
\boldsymbol{\sigma} = 2J^{-1}\mathbf{F} \cdot & \left[\frac{\partial w}{\partial I_1} \mathbf{I} + \frac{\partial w}{\partial I_2} (I_1 \mathbf{I} - \mathbf{C}) + \frac{\partial w}{\partial I_3} I_3 \mathbf{C}^{-1} \right. \\
& + \frac{\partial w}{\partial I_{4\alpha}} \mathbf{a}_{0\alpha} \otimes \mathbf{a}_{0\alpha} + \frac{\partial w}{\partial I_{5\alpha}} (\mathbf{a}_{0\alpha} \otimes \mathbf{a}_{0\alpha} \cdot \mathbf{C} + \mathbf{C} \cdot \mathbf{a}_{0\alpha} \otimes \mathbf{a}_{0\alpha}) \\
& + \frac{\partial w}{\partial I_{4\beta}} \mathbf{a}_{0\beta} \otimes \mathbf{a}_{0\beta} + \frac{\partial w}{\partial I_{5\beta}} (\mathbf{a}_{0\beta} \otimes \mathbf{a}_{0\beta} \cdot \mathbf{C} + \mathbf{C} \cdot \mathbf{a}_{0\beta} \otimes \mathbf{a}_{0\beta}) \\
& \left. + \frac{1}{2} \frac{\partial w}{\partial I_{\alpha\beta}} (\mathbf{a}_{0\alpha} \otimes \mathbf{a}_{0\beta} + \mathbf{a}_{0\beta} \otimes \mathbf{a}_{0\alpha}) \right] \cdot \mathbf{F}^T
\end{aligned} \tag{eq. 2-110}$$

$$\begin{aligned}
\Leftrightarrow \boldsymbol{\sigma} = 2J^{-1} & \left[\frac{\partial w}{\partial I_1} \mathbf{B} + \frac{\partial w}{\partial I_2} (I_1 \mathbf{B} - \mathbf{B}^2) + \frac{\partial w}{\partial I_3} I_3 \mathbf{I} \right. \\
& + \frac{\partial w}{\partial I_{4\alpha}} \mathbf{a}_\alpha \otimes \mathbf{a}_\alpha + \frac{\partial w}{\partial I_{5\alpha}} (\mathbf{a}_\alpha \otimes \mathbf{a}_\alpha \cdot \mathbf{B} + \mathbf{B} \cdot \mathbf{a}_\alpha \otimes \mathbf{a}_\alpha) \\
& + \frac{\partial w}{\partial I_{4\beta}} \mathbf{a}_\beta \otimes \mathbf{a}_\beta + \frac{\partial w}{\partial I_{5\beta}} (\mathbf{a}_\beta \otimes \mathbf{a}_\beta \cdot \mathbf{B} + \mathbf{B} \cdot \mathbf{a}_\beta \otimes \mathbf{a}_\beta) \\
& \left. + \frac{1}{2} \frac{\partial w}{\partial I_{\alpha\beta}} (\mathbf{a}_\alpha \otimes \mathbf{a}_\beta + \mathbf{a}_\beta \otimes \mathbf{a}_\alpha) \right]
\end{aligned} \tag{eq. 2-111}$$

The deformed preferred directions \mathbf{a}_α and \mathbf{a}_β are obtained as [cf. eq. 2-8] transformation of a line element]:

$$\mathbf{a}_i = \mathbf{F} \cdot \mathbf{a}_{0i}, i = \alpha, \beta. \tag{eq. 2-112}$$

For the shear-free triaxial deformation according to eq. 2-91, the deformation gradient is $\mathbf{F} = \text{diag}[\lambda_1, \lambda_2, \lambda_3]$ and thus

$$\mathbf{a}_\alpha = \lambda_1 \sin \vartheta_\alpha \mathbf{e}_1 + \lambda_2 \cos \vartheta_\alpha \mathbf{e}_2 \tag{eq. 2-113}$$

$$\mathbf{a}_\beta = \lambda_1 \sin \vartheta_\beta \mathbf{e}_1 - \lambda_2 \cos \vartheta_\beta \mathbf{e}_2. \tag{eq. 2-114}$$

Consider the three structure tensors for this case ($i, j = 1, 2, 3$):

$$\mathbf{a}_\alpha \otimes \mathbf{a}_\alpha = \begin{pmatrix} \lambda_1^2 \sin^2 \vartheta_\alpha & \lambda_1 \sin \vartheta_\alpha \lambda_2 \cos \vartheta_\alpha & 0 \\ \lambda_1 \sin \vartheta_\alpha \lambda_2 \cos \vartheta_\alpha & \lambda_2^2 \cos^2 \vartheta_\alpha & 0 \\ 0 & 0 & 0 \end{pmatrix} \langle \mathbf{e}_i \otimes \mathbf{e}_j \rangle \tag{eq. 2-115}$$

$$\mathbf{a}_\beta \otimes \mathbf{a}_\beta = \begin{pmatrix} \lambda_1^2 \sin^2 \vartheta_\beta & -\lambda_1 \sin \vartheta_\beta \lambda_2 \cos \vartheta_\beta & 0 \\ -\lambda_1 \sin \vartheta_\beta \lambda_2 \cos \vartheta_\beta & \lambda_2^2 \cos^2 \vartheta_\beta & 0 \\ 0 & 0 & 0 \end{pmatrix} \langle \mathbf{e}_i \otimes \mathbf{e}_j \rangle, \tag{eq. 2-116}$$

$$\mathbf{a}_\alpha \otimes \mathbf{a}_\beta = \begin{pmatrix} \lambda_1^2 \sin \vartheta_\alpha \sin \vartheta_\beta & -\lambda_1 \sin \vartheta_\alpha \lambda_2 \cos \vartheta_\beta & 0 \\ \lambda_2 \cos \vartheta_\alpha \lambda_1 \sin \vartheta_\beta & -\lambda_2^2 \cos \vartheta_\alpha \cos \vartheta_\beta & 0 \\ 0 & 0 & 0 \end{pmatrix} \langle \mathbf{e}_i \otimes \mathbf{e}_j \rangle. \quad \text{eq. 2-117}$$

Note that $\mathbf{a}_\alpha \otimes \mathbf{a}_\alpha$ and $\mathbf{a}_\beta \otimes \mathbf{a}_\beta$ are symmetric second order tensors whereas $\mathbf{a}_\alpha \otimes \mathbf{a}_\beta$ is an antimetric tensor. Moreover,

$$\mathbf{a}_\beta \otimes \mathbf{a}_\alpha = (\mathbf{a}_\alpha \otimes \mathbf{a}_\beta)^\top. \quad \text{eq. 2-118}$$

For the shear-free triaxial deformation according to eq. 2-91, the following nonzero components of the CAUCHY stress tensor are obtained:

$$\begin{aligned} \sigma_{11} = 2J^{-1} & \left[\frac{\partial w}{\partial I_1} \lambda_1^2 + \frac{\partial w}{\partial I_2} \lambda_1^2 (I_1 - \lambda_1^2) + \frac{\partial w}{\partial I_3} I_3 + \left(\frac{\partial w}{\partial I_{4\alpha}} + 2 \frac{\partial w}{\partial I_{5\alpha}} \lambda_1^2 \right) \lambda_1^2 \sin^2 \vartheta_\alpha \right. \\ & \left. + \left(\frac{\partial w}{\partial I_{4\beta}} + 2 \frac{\partial w}{\partial I_{5\beta}} \lambda_1^2 \right) \lambda_1^2 \sin^2 \vartheta_\beta + \frac{\partial w}{\partial I_{\alpha\beta}} \lambda_1^2 \sin \vartheta_\alpha \sin \vartheta_\beta \right], \end{aligned} \quad \text{eq. 2-119}$$

$$\begin{aligned} \sigma_{22} = 2J^{-1} & \left[\frac{\partial w}{\partial I_1} \lambda_2^2 + \frac{\partial w}{\partial I_2} \lambda_2^2 (I_1 - \lambda_2^2) + \frac{\partial w}{\partial I_3} I_3 + \left(\frac{\partial w}{\partial I_{4\alpha}} + 2 \frac{\partial w}{\partial I_{5\alpha}} \lambda_2^2 \right) \lambda_2^2 \cos^2 \vartheta_\alpha \right. \\ & \left. + \left(\frac{\partial w}{\partial I_{4\beta}} + 2 \frac{\partial w}{\partial I_{5\beta}} \lambda_2^2 \right) \lambda_2^2 \cos^2 \vartheta_\beta - \frac{\partial w}{\partial I_{\alpha\beta}} \lambda_2^2 \cos \vartheta_\alpha \cos \vartheta_\beta \right], \end{aligned} \quad \text{eq. 2-120}$$

$$\sigma_{33} = 2J^{-1} \left[\frac{\partial w}{\partial I_1} \lambda_3^2 + \frac{\partial w}{\partial I_2} \lambda_3^2 (I_1 - \lambda_3^2) + \frac{\partial w}{\partial I_3} I_3 \right], \quad \text{eq. 2-121}$$

and finally the in-plane shear component:

$$\begin{aligned} \sigma_{12} = \sigma_{21} = 2J^{-1} & \left[\left(\frac{\partial w}{\partial I_{4\alpha}} + \frac{\partial w}{\partial I_{5\alpha}} (\lambda_1^2 + \lambda_2^2) \right) \lambda_1 \sin \vartheta_\alpha \lambda_2 \cos \vartheta_\alpha \right. \\ & - \left(\frac{\partial w}{\partial I_{4\beta}} + \frac{\partial w}{\partial I_{5\beta}} (\lambda_1^2 + \lambda_2^2) \right) \lambda_1 \sin \vartheta_\beta \lambda_2 \cos \vartheta_\beta \\ & \left. - \frac{1}{2} \frac{\partial w}{\partial I_{\alpha\beta}} (\lambda_1 \sin \vartheta_\alpha \lambda_2 \cos \vartheta_\beta - \lambda_2 \cos \vartheta_\alpha \lambda_1 \sin \vartheta_\beta) \right]. \end{aligned} \quad \text{eq. 2-122}$$

Note that for an anisotropic material with two preferred directions, the shear stress does not vanish in general in response to a shear-free deformation, i.e. *the deformation and the stress tensor do not have the same eigenvectors* or principal directions. In turn, a loading of such a material by principal stresses, only, would in general result in a deformation state that includes shear. Equation eq. 2-122 shows that σ_{12} will only vanish, if $|\vartheta_\alpha| = |\vartheta_\beta|$ [cf. Figure 2-3] and if

$$\frac{\partial w}{\partial I_{4\alpha}} = \frac{\partial w}{\partial I_{4\beta}} \quad \text{and} \quad \frac{\partial w}{\partial I_{5\alpha}} = \frac{\partial w}{\partial I_{5\beta}}. \quad \text{eq. 2-123}$$

Remind that each partial derivative of w with respect to one of the invariants of \mathbf{C} can be regarded as an independent constitutive equation that contributes to the constitutive behavior of the material. Thus eq. 2-123 means: in addition to the “geometrical” symmetry of the two preferred directions with respect to the principal directions of the deformation tensor, both preferred directions have to possess the identical mechanical properties. In this case σ_{11} , σ_{22} and σ_{33} are the principal stresses and $\boldsymbol{\sigma}$ and \mathbf{B} have the identical principal directions. Moreover, the material with two preferred directions would be fully symmetric with respect to the 1-3 plane and the 3-2 plane. Since both preferred directions are situated in the 1-2 plane, the “isotropic” direction normal to the 1-2 plane, \mathbf{e}_3 , can be regarded as third preferred direction and the behavior of the material is also symmetric with regard to the 1-2 plane. Therefore, such a material can be regarded as *locally orthotropic*.

The continuum mechanical framework presented in this chapter will be relevant for the interpretation of the in vivo measurements of deformation and strain of the abdominal aortic wall that are presented in chapters 5 and 6 of this thesis: despite supposed biaxial tensile loading in longitudinal and circumferential direction as a result of transmural pressure and constant axial pretension force [cf. chapters 1.2 and 1.5] cyclic twist and in-plane shear were observed. Moreover, starting from this framework, the feasibility of constitutive parameter identification of an orthotropic strain energy function based on available in vivo data (cf. chapter 3) will be considered on a theoretical basis [see chapter 7.3].

3 A method for non-invasive full field strain measurement

3.1 Ultrasound measurement of aortic wall deformation

Ultrasound imaging is based on the propagation of mechanical pressure waves in a fluid or solid medium. The acoustical properties of a medium are characterized by its acoustic *impedance* Z that relates the local pressure disturbance p to the particle velocity v in the medium:

$$Z = \frac{p}{v}. \quad \text{eq. 3-1}$$

The acoustic impedance depends on the physical properties of the medium:

$$Z = \rho c, \quad \text{eq. 3-2}$$

where ρ is the density and c is the speed of sound in the respective medium. In solid media, the speed of sound depends on the elastic properties. E.g. the propagation velocity of transversal waves in a linear-elastic solid is given by

$$c_{solid,transversal} = \sqrt{\frac{E}{2\rho(1+\nu)}} = \sqrt{\frac{G}{\rho}}, \quad \text{eq. 3-3}$$

where E is the elastic modulus, ν is the POISSON's ratio and G is the shear modulus. Ultrasound waves are in part reflected and in part transmitted at boundaries between media with different acoustic impedances if the dimension of the interface exceeds the wavelength λ by a few times. If, in contrast, the dimension of a structure is much smaller than the wavelength of the ultrasound signal, the signal will be dispersed in all directions. This effect is observed in soft tissues due to their hierarchical microstructural composition [cf. e.g. chapters 1.3.2 and 1.3.3].

Due to the partial reflection at each interface, the scattering at microstructural components and the dissipative particle interactions, ultrasonic waves are attenuated when propagating through a medium, which sets a limit to their penetration depth. The shorter the wavelength of the ultrasound signal and the higher its frequency

$$f = c/\lambda \quad \text{eq. 3-4}$$

is, the more the signal is attenuated by scattering and the smaller its penetration depth will be. Therefore, diagnostic ultrasound measurements of structures such as the abdominal aorta that are located deeply in the human body have to balance the contradictory requirements of high resolution and great penetration depth: higher frequency and smaller wave length improve spatial resolution, but reduce the penetration depth at the same time. In diagnostic ultrasound, frequencies in the range between 1 MHz and 20 MHz are used corresponding to wave lengths between 1.6 mm and 0.08 mm.

In the ‘reflection mode’ that is mostly used in medical ultrasound imaging, the measurements of the temporal delay (‘time of flight’, *ToF*) between the emission of a wave package that was generated by piezoelectric elements, i.e. the transducer, and the registration of the reflected signal by the same elements provides the possibility to measure the distance *d* between the transducer and the site of reflection:

$$d = \frac{ToF \cdot c}{2}, \quad \text{eq. 3-5}$$

which is the basis of medical ultrasound imaging of internal structures of the body since different tissue types exhibit different acoustic properties.

The representation of the amplitude of the returning reflected wave package over time is called A-mode ultrasound. The representation of the amplitude as intensity on a gray scale against time is called B-mode. Both allow the measurement of a distance between two points in propagation direction of the ultrasound signal, e.g. the measurement of the diameter of a blood vessel. Note that this is a two-point measurement and that the 3D configuration of a blood vessel can be described only for a chosen site of measurement along the arterial tree [cf. Figure 1-6] and assuming a cylindrical shape. M-mode images are temporally subsequent B-mode images along the same propagation path plotted against time. The result is a two-dimensional image where the vertical axis is the propagation time of the signal corresponding to the distance between transducer and site of reflection according to eq. 3-5, whereas the second axis corresponds to the acquisition time of subsequent B-mode images. M-mode images allow the measurement of aortic diameter change during a cardiac cycle and, consequently, the computation of circumferential strain with regard to a chosen deformed reference configuration. 2D- or 3D-images are obtained by rotating (‘phased array’) and/or displacing (‘linear array’) a group of piezoelectric actuators/sensors and combining the B-mode images for each angle or position. 2D greyscale ultrasound typically has frame rates between 60 and 80 frames/s, which allows to capture the dynamics of the cyclic

deformation of the heart or of blood vessels for usual heart rates at rest between 60 and 80 beats per minute. 3D ultrasound provides volumetric images with frame rates ≤ 25 frames/s and it depends on the used device whether the cyclic deformation can be measured with sufficient accuracy.

In addition to M-mode imaging, the Doppler effect and speckle tracking are used to measure tissue motion and deformation [cf. Teixeira et al. 2015]. To correctly compute the velocity of a tissue volume using a Doppler-based method, however, the angle between the propagation direction of the ultrasound wave and the direction of the tissue velocity vector has to be known in advance. Doppler-based motion measurements are direction dependent.

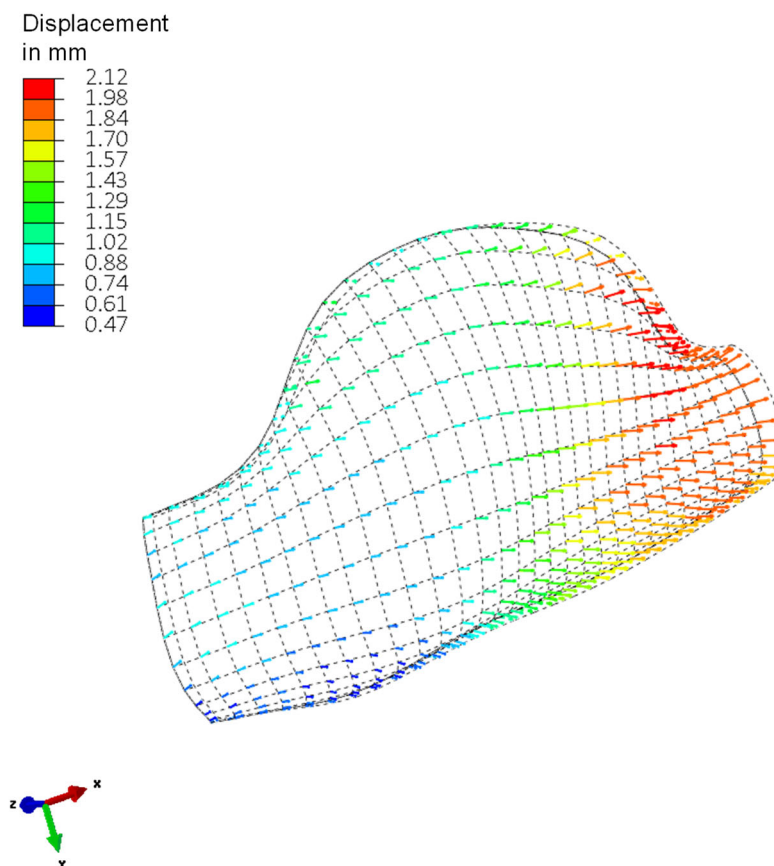


Figure 3-1 Displacement field of material points on the wall of a human AAA as measured by real-time 3D echocardiography combined with speckle tracking (4D ultrasound) [Image reprinted from Wittek et al. 2019 with permission].

In contrast, ultrasound speckle tracking imaging provides a direction independent method for 2D- or 3D-deformation measurement. Ultrasound speckle tracking imaging uses the fact that ultrasonic waves traveling through soft tissue are reflected and scattered by microstructural elements of the tissue. Because of the unique inhomogeneous and locally varying composition of biological soft tissues, reflected and scattered waves that – depending on the tissue region – interfere destructively or constructively generate speckle patterns that are uniquely related to different regions of soft tissue and remain

stable for finite translational as well as rotational deformation observed in the human body [Meunier 1998]. Thus, the motion of these tissue regions can be traced over the cardiac cycle by cross-correlation on radio frequency data [Chen et al. 2005]. This imaging technique does not only allow for the measurement of the global change of shape of the imaged structure but for the local allocation of specific tissue regions or material points. Compared to 3D speckle tracking, 2D speckle tracking is more widely-spread because of its higher frame rate and lower complexity of data acquisition and post-processing. It tracks the motion of tissue particles, i.e. the trajectories of material points [cf. chapter 2.1], within the 2D image plane. Doing so, 2D-speckle tracking ultrasound provides a LAGRANGIAN reference frame within the 2D image plane, only. Out of plane motion of the imaged structure – such as long axis contraction of the left ventricle [cf. chapter 1.3] when a transversal cross section of the heart is imaged – cannot be captured and may result in image decorrelation and measurement of artificial deformation [Chen et al. 2005]. Only real-time 3D ultrasound combined with speckle tracking, which is referred to as 4D ultrasound in this work, provides a LAGRANGIAN reference frame for 3D deformation measurements and is direction independent.

The conditions for imaging the blood filled lumen of blood vessels are quite good: the differences in the speed of sound and the density of abdominal soft tissues ($c_{soft\ tissue} = 1540\text{ m/s}$, $\rho_{soft\ tissue} \approx 1000\text{ kg/m}^3$) and of blood, ($c_{blood} = 1580 \dots 1600\text{ m/s}$, $\rho_{blood} \approx 1060\text{ kg/m}^3$) at the body temperature of 37°C [Goss et al. 1980] result in acoustic impedances of $Z_{blood} = 1.67 \dots 1.70 \times 10^6\text{ kg/(m}^2\text{s)}$ and $Z_{soft\ tissue} = 1.54 \times 10^6\text{ kg/(m}^2\text{s)}$, meaning a difference of 9 to 10%. In addition to this, blood has a low echogenicity (no reflectors or scatterers) and will appear as black in ultrasound images [Nichols et al. 2011]. Thus the interface between the vessel wall and the lumen can be detected very well in all variants of ultrasound imaging. In contrast, the aortic or arterial wall and the surrounding connective tissue have almost identical acoustic properties and the ‘border’ between both is more a continuous transition than a clear interface. This transition can be identified only in blood vessels, which are located very close to the surface of the body such as the common carotid artery. Because of the low penetration depth that is required, very high imaging frequencies can be used that allow to detect small scale structural changes of tissue composition. As a consequence, the wall thickness of blood vessels which are located deep inside the body such as the abdominal aorta, cannot be measured by ultrasound.

Originally, ultrasound speckle tracking imaging was developed to study the cyclic motion of the left and right ventricle of the heart [see e.g. Kapetanakis et al. 2005; Teixeira et al. 2015]. The application of 2D speckle tracking ultrasound has been expanded to assess vascular wall mechanics since Oishi et al. [2008] performed the first clinical study measuring human cyclic wall deformation by this method. In contrast, the application of 4D ultrasound was first established within the interdisciplinary project, part of which this thesis is [Karatolios et al. 2013; Teixeira et al. 2015; Derwich et al. 2017]. The term 4D ultrasound is used in this work for temporally resolved 3D ultrasound combined with speckle track-

ing, a measurement method that results in spatial trajectories or LAGRANGIAN motion functions of material points [cf. chapter 2.1] over the cardiac cycle. Often, this imaging technique is referred to as 3D speckle tracking echocardiography (3D-STE) in literature. This terminology is not used in this thesis because it implies the imaging of the heart, not the aorta. In contrast to 4D ultrasound or 3D-STE, 3D ultrasound is used in this thesis to refer to temporally resolved three-dimensional ultrasound without speckle tracking. This technique provides the shape of the imaged object, only, but not the unique allocation of the positions of material points and, consequently, not the local deformation of aortic wall surface segments.

This chapter is organized as follows: First, clinical acquisition of in vivo 4D ultrasound data of aortic walls is described [section 3.2]. Two variants of post-processing of the speckle tracking data are presented: one using the standard version of the proprietary Toshiba speckle tracking software (Advanced Cardiac Package (ACP), Toshiba Medical Systems, Otawara, Japan) [section 3.2.2.1] and one using a customized data interface of the ACP that provided highly resolved full-field displacement data of material points on the aortic wall [section 3.3.1 and 3.3.2]. This customized interface was designed in cooperation with and provided by Toshiba Medical Systems for the work conducted within this thesis. In sections 3.3.3 and 3.3.4 two different metrics of aortic wall deformation data are described that were developed and implemented within this thesis based on the newly available highly resolved full-field data. In chapters 3.4 and 3.5 first applications of the newly developed highly resolved full-field displacement measurements to in vivo data of volunteers and patients are reported and analyzed: Chapter 3.4 examines the effect of the increased spatial resolution of strain measurement – or reduction of the size of wall surface areas for which independent in-plane strain values can be determined - on the size of the measured maximum local strains and on the heterogeneity of the measured strain distributions. Chapter 3.5 gives an overview of the average size of three-dimensional displacements of material points that were observed in three patient groups that were characteristically different with respect to age and cardiovascular health. This study provides an estimate size of the primary measure of time-resolved 3D ultrasound combined with speckle tracking that is to be expected in clinical studies. This is an important information for the evaluation of the results of the validation of the customized 4D ultrasound full-field measurement of aortic wall motion that was performed within this thesis and that is presented in chapter 4.

3.2 Clinical data acquisition and post-processing

3.2.1 4D ultrasound examination and blood pressure measurement

Clinical data evaluated and analyzed in this thesis were acquired at the University Heart Center of the Philipps University Marburg and the Department of Vascular and Endovascular Surgery of the Goethe University Hospital Frankfurt (Main). Data acquisition and further scientific use of the anonymized data were approved by the local ethics committees. All volunteers and patients were examined after giving informed consent. All measurements were acquired with patients in supine position after 5 minutes rest. Minimum (diastolic) and maximum (systolic) blood pressure that occur throughout the cardiac cycle were measured at the brachial artery by sphygmomanometry. Volunteers and patients were asked to hold their breath during the ultrasound measurements. 4D ultrasound data were acquired by use of a commercial real-time 3D-echocardiography system (Artida[®], Toshiba Medical Systems, Otawara, Japan) that was equipped with a 3D transthoracic probe (Toshiba, PST-25SX, 1-4 MHz phased array matrix transducer). Figure 3-2 exemplarily shows five cross sectional views of the volumetric data set of a healthy infrarenal aorta.

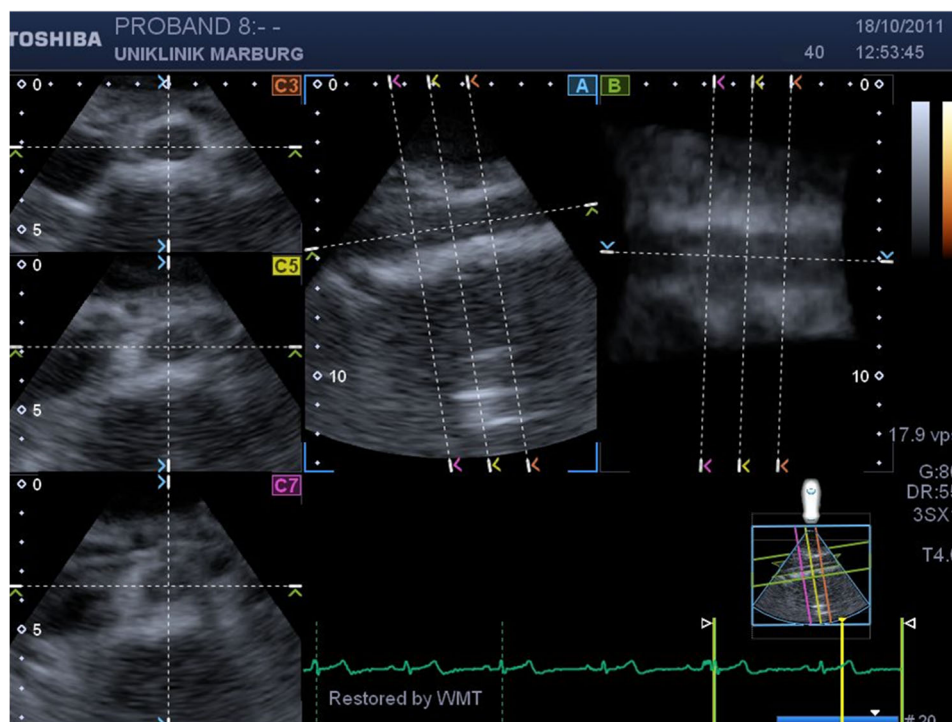


Figure 3-2 Representative example of a five-plane view of 3D volume ultrasound data. Plane A: longitudinal cross-sectional view. Plane B: a second longitudinal cross-sectional view orthogonal to plane A. Planes C3, C5 and C7: three short axis or transversal cross-sectional views of the volumetric image data. [Image reprinted from: Karatolios, Wittek et al. 2013 with permission from Elsevier]

In vivo measurements had a temporal resolution between 12.8 and 31.5 frames per second (fps), resulting in the identical number of volumetric images per cardiac cycle if a heart rate of about 60 beats per minute (bpm) is assumed [cf. Table 3-1]. This temporal resolution is sufficient to resolve the periodic deformation of the aortic wall with negligible error. This is illustrated by Figure 3-3 which exemplarily shows the cyclic length and diameter change of a healthy infrarenal aorta [see chapter 3.3.3.1 for detailed description of how diameter and segment length were computed from ultrasound data]. By comparison of the diameter curve with the typical curve of aortic pressure that is given in Figure 1-3, it can be seen that diameter follows pressure. No “singularities” in the pressure curve are to be expected. This is in line with the state of research [cf. chapter 1.5]. Only the incisura that indicates the closure of the aortic valve is lost. This disturbance in the pressure signal, however, is not relevant for the peak-to-peak amplitude of cyclic deformation of the aortic wall.

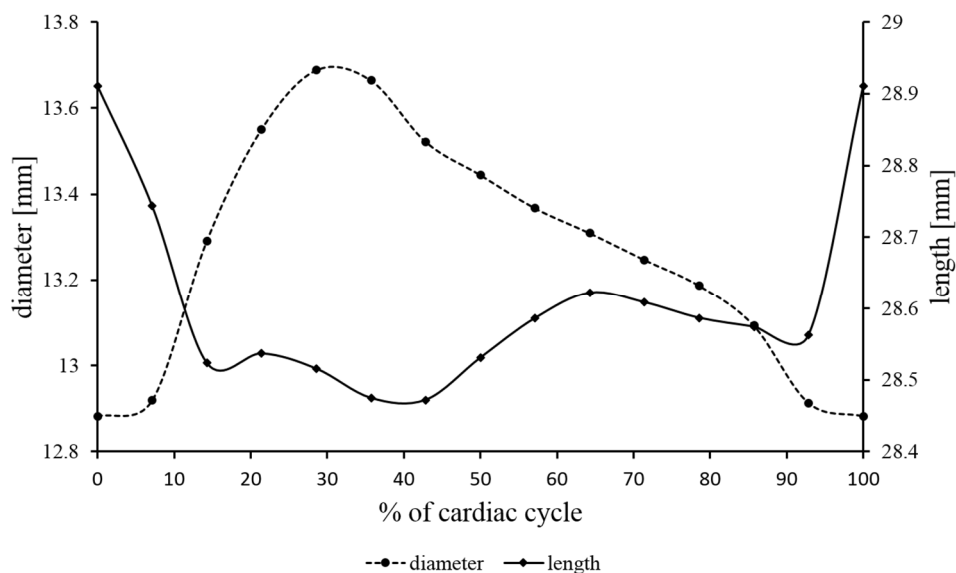


Figure 3-3 Cyclic length and diameter change of an abdominal aortic segment. Minimum length and diameter are observed at 43% and 0% of the cardiac cycle, respectively. [Image reprinted from Wittek et al. 2016b with permission from Springer Nature]

For the conversion of the measured time of flight of the ultrasound signal into distances between imaged anatomical structures [cf. eq. 3-5], the device assumes a constant speed of sound of 1540 m/s , which holds well for soft tissues in the human abdomen [Goss et al. 1980]. This results in a wave length $\lambda = 0.39 \text{ mm}$ of the ultrasound signal at a frequency $f = 4 \text{ MHz}$, which was used for all measurements. The voxel size of the volumetric grey scale representation of the ultrasound measurement between 0.28 and 0.59 mm was in the order of magnitude of the wave length of the signal.

Full volume data sets of $90^\circ \times 90^\circ$ resulted from 6 sub-volumes of $90^\circ \times 15^\circ$ that were imaged in subsequent cardiac cycles. The measurement was triggered by ECG with end-diastole as starting point (reference) of each cycle. End-diastole is defined as the point of time within the cardiac cycle when the relaxation and expansion of the left ventricle of the heart (LV) reaches its maximum, just before the

ejection of blood volume into the arterial system starts due to LV contraction. End-diastole coincides with minimum blood pressure in the arterial system. Maximum (systolic) blood pressure within the cardiac cycle is reached at the end of the contraction phase of the LV [cf. chapter 1.3].

3.2.2 Clinical post-processing: wall motion tracking

Clinical post-processing of the 4D ultrasound data was performed by K. Karatolios, MD, at the University Heart Center of the Philipps University Marburg, by W. Derwich, MD, at the Department of Vascular and Endovascular Surgery of the Goethe University Hospital Frankfurt and by the author himself using the proprietary speckle tracking algorithm provided by the Toshiba Advanced Cardiac Package (ACP, Toshiba Medical Systems, Otawara, Japan). The data sets were rotated to give two longitudinal and three transversal cross-sections of the volumetric data of the imaged aortic segment as shown in Figure 3-2 and Figure 3-4 a. The tissue close to the luminal border of the aortic wall as region of interest (ROI) for speckle tracking was masked manually in the two longitudinal cross sections [Figure 3-4 a].

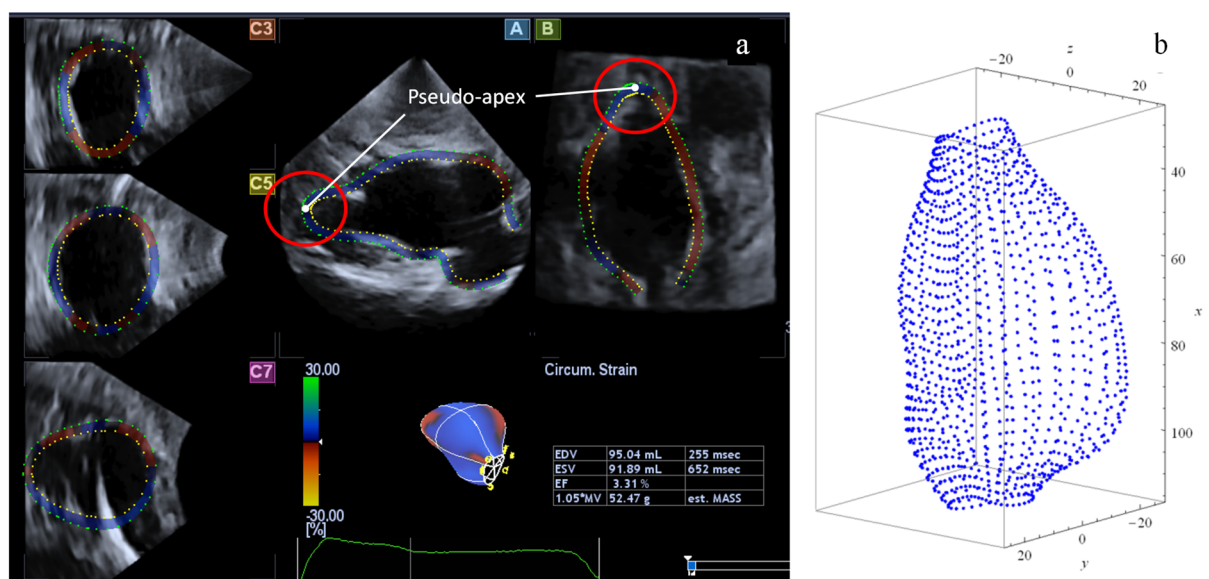


Figure 3-4 a) Five plane view of an AAA with a maximum diameter of 43.9 mm. The length of the imaged segment is about 80 mm. Segmentation of the wall area as region of interest for the wall motion tracking was performed manually in the A and B planes. Cross-sectional views C3, C5 and C6 show the automatic completion of the segmentation. A and B show the artificial pseudo-apex that is produced by the proprietary software's template that was designed for segmentation of the left ventricle of the heart. b) Field of 1188 discrete material points describing the diastolic configuration of the AAA wall as obtained by use of the Toshiba Advanced Cardiac Package. The artificial pseudo-apex was already removed from these data. [Image reprinted from Wittek et al. 2018 with permission from John Wiley and Sons]

The difference in acoustical impedance between blood and arterial wall as well as the low echogenicity of blood [cf. chapter 3.1] allow for a clear detection of the luminal side of the vessel wall, whereas the abluminal side of the wall cannot be detected clearly. Therefore, all measurements of wall motion were performed on the luminal side of the wall. Based on this information, the ACP completed

the three-dimensional ROI automatically. The accuracy of this automatic completion was then controlled by the observer, on the two longitudinal and three transversal cross sections of the volumetric data set, which can be shifted along the sample length. If necessary, the reconstructed 3D ROI was adjusted manually. This control was performed by the clinician who had acquired the data set and, for a second time, by the author of this thesis, who has developed, implemented and performed further post-processing of the 4D ultrasound data sets [cf. chapter 3.3].

The speckle tracking algorithm provided by the ACP divided the defined ROI into cubic template volumes of approximately $10 \times 10 \times 10 \text{ mm}^3$ for the purpose of pattern recognition in subsequent time steps. Motion estimation points were centered in these template volumes [Seo et al. 2009; Seo et al. 2011]. Since the ACP was designed for imaging the left ventricle of the heart [c.f. chapter 1.2, Figure 1-2], its segmentation template required an apical closure of the ROI at one end in any case. Thus, during the post-processing of each data set, an artificial “pseudo apex” was created, which did not correspond to any real structure [Figure 3-4 a] and therefore was removed in further post-processing steps [cf. 3.3.1].

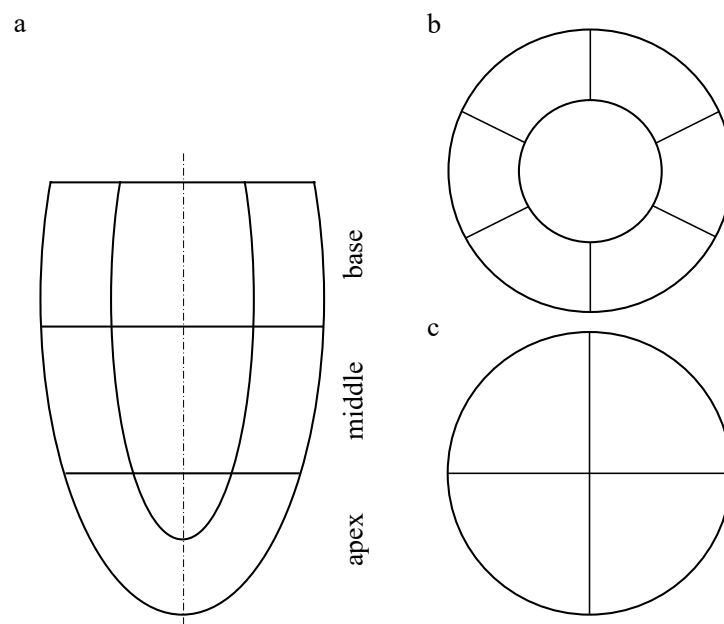


Figure 3-5 Subdivision of the masked region of interest for the speckle tracking algorithm according to the standard post-processing by the Toshiba Advanced Cardiac Package: a) The longitudinal cut shows 3 segments in longitudinal direction: base-, mid- and apical segment. b) The transversal cross-section of the base- and mid-segment illustrates its subdivision into 6 circumferential segments, each. c) The cross-sectional view of the (pseudo-) apex show its subdivision into 4 circumferential segments.

3.2.2.1 Standard post-processing

In-plane strain components (longitudinal, circumferential and shear) and radial strain were provided by the standard version of the ACP for 16 subsegments of the masked region of interest as shown in Figure 3-5: Longitudinally, the ROI was subdivided into three sections, base, middle and apex. Base and middle

section were divided into 6 circumferential subsegments, each, and the (pseudo-) apex into 4 circumferential subsegments. Because the apex was an artefact when the device was used for imaging blood vessels, only the strain components computed for the 12 segments of the base- and middle section could be used for analysis of aortic wall motion. The ACP standard post-processing provided separate strain values for each of these segments. This spatial resolution of strain imaging corresponds to the usual post-processing of 2D speckle tracking ultrasound where circular cross sections of the aortic or the LV wall are subdivided into six circumferential segments, for which circumferential and radial strain values and out-of-plane shear can be computed.

3.3 Deformation metrics based on customized 4D ultrasound wall motion data

3.3.1 Customized data interface

In addition to the described standard post-processing provided by the Toshiba ACP, a customized data interface was designed within this thesis in cooperation with Toshiba Medical Systems Europe. It allowed for the export of highly resolved wall deformation data compared to the 16 segments (including pseudo-apex) for which strain values were provided by the standard post-processing: 3D position vector fields of 1296 measuring points on the inner border of the masked ROI could be exported for each temporal frame throughout an entire cardiac cycle as ASCII file. These data allowed the computation of the complete in-plane strain tensor for wall surface areas with sizes about 2 mm^2 in non-aneurysmal aortae, compared to surface areas of between 90 mm^2 and 170 mm^2 when the standard post-processing was applied [see chapter 3.4 for a detailed comparison of the results obtained standard and customized post-processing]. The measuring points were organized into subsets along the longitudinal axis of the imaged wall segment that were called “heights”. Each height contained 36 measuring points that were distributed evenly over the circumference of the wall. These circumferential positions within the heights were called “degrees”, even though the average distance between two neighboring degrees was 10° . “Degree” and “height” are the technical terms by which longitudinal and circumferential position of a material point is referred to within the ACP and within the files exported using the customized interface. Therefore, these terms are used throughout this thesis.

The exported data included artificial “measurements” from the pseudo-apical region as well. The pseudo-apical closure was removed during post-processing of wall motion data using an in-house finite element (FE) preprocessor that was developed within this thesis [cf. chapter 3.3.4]. The apex-free end-

diastolic reference configuration of the aortic wall segment was visualized using WOLFRAM Mathematica 9 (or a later release of the software) [cf. chapter 3.3.4] and the author controlled by visual comparison with the five plane view of the volumetric ultrasound data [cf. Figure 3-4 a] whether the segmented and reconstructed configuration was free of artefacts. Remaining artefact-free fields of between $17 \times 36 = 612$ and $33 \times 36 = 1188$ motion estimation points for each temporal frame throughout the cardiac cycle were processed further. The positions of the identical measuring points in subsequent temporal frames describe the trajectory of a material point on the aortic wall throughout the cardiac cycle.

3.3.2 Motion function

The exported measuring points can be understood as current position vectors $\mathbf{x} \in \mathbf{R}^3$ of discrete finite tissue volumes, i.e. *discrete* material points X in the aortic wall plane in a continuum mechanical sense. Material points and corresponding position vectors describing different configurations are given with indices in order to emphasize that the obtained field functions are of a discrete, not properly continuous character:

$$\mathbf{x}_{i,j,k} = \mathbf{x}(X_{i,j}, t_k), \quad \text{eq. 3-6}$$

where

- $i = 1, \dots, n, n \leq 36$ refers to the “height” or position along the longitudinal axis of the aortic segment,
- $j = 1, \dots, 36$ refers to the “degree” or circumferential position as identified in the ASCII file that was exported from the Toshiba ACP and
- $t_k, k = 0, \dots, m$ marks the k^{th} temporal frame throughout the cardiac cycle for which wall motion data were obtained.

In each temporal frame, the position vector field $\mathbf{x}_{i,j,k}$ determined the current 3D configuration $\mathcal{B}_k = \mathcal{B}_t(t_k)$ of the imaged aortic wall segment [Figure 3-6]. The ECG-triggered measurement by the Toshiba Artida provided the end-diastolic configuration [cf. 3.2.1] as deformed reference configuration \mathcal{B}_r that coincided with minimum aortic blood pressure [cf. chapter 1.3], i.e. the minimum cyclic load acting on the wall that could be observed non-invasively in vivo. It was defined by the position vector field $\mathbf{X}_{i,j} = \mathbf{X}_{i,j}(X, t_r)$. In contrast, the position vector field $\mathbf{X}_0(X)$ that defined the *natural*, load- and stress-free configuration \mathcal{B}_0 [cf. chapter 2.1] of the aortic wall could not be observed in vivo and was unknown.

According to eq. 2-7, the displacement vector field $\mathbf{u}_{i,j,k}$ [Figure 3-1] that maps the chosen reference configuration \mathcal{B}_r onto any observed current configuration \mathcal{B}_k was obtained as

$$\mathbf{u}_{i,j,k} = \mathbf{x}_{i,j,k} - \mathbf{X}_{i,j}. \quad \text{eq. 3-7}$$

Using this displacement field, the discrete cyclic motion function $\chi: \mathcal{B}_r \rightarrow \mathcal{B}_k, k = 0, \dots, m$ of the aortic wall is given by

$$\mathbf{x}_{i,j,k} = \chi(\mathbf{X}_{i,j}, t_k) = \mathbf{X}_{i,j} + \mathbf{u}_{i,j,k}. \quad \text{eq. 3-8}$$

3.3.3 Quantification of the size and global deformation of aortic wall segments

In this section, deformation metrics are described that approximate the “global” deformation of whole imaged aortic wall segments based on the assumptions that these segments a) have a cylindrical shape and b) deform homogeneously. In a comparative clinical study of the wall motion of the proximal ascending aorta and the infrarenal abdominal aorta [cf. chapter 5], these metrics were used to analyze the cyclic 3D deformation of non-aneurysmal, young and healthy human aortae in vivo. The imaged segments exhibited diameters between 14 mm and 28 mm [cf. Table 5-2] and lengths between 20 mm and 40 mm [cf. Table 5-1]. The described deformation metrics were computed by use of in-house software that was designed and coded by the author in Visual Basic for Applications in Excel (Microsoft Corp., Redmond, WA, USA).

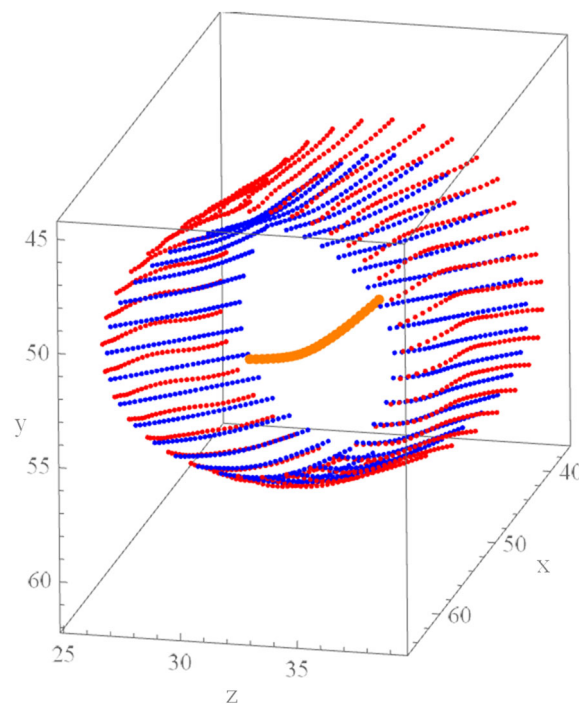


Figure 3-6 Visualization of primary data underlying global deformation analysis: Fields of position vectors of discrete material points describing two current configurations of an abdominal aortic wall segment of a 25 y.o. male volunteer as viewed from its caudal to its cranial end. In orange the lumen centerline is shown that was determined from the configuration that is shown in blue. [Image reprinted from Wittek, Karatolios et al. 2016b with permission from Springer Nature]

3.3.3.1 Lumen centerline, length, radius of curvature, diameter and volume

Current lumen midpoints along the aortic segment were calculated for each temporal frame as the centroids of the warped circumferential lines of each height [Figure 3-6] according to

$$\mathbf{c}_{i,k} = \frac{\sum_{j=1}^{36} \frac{\mathbf{x}_{i,j+1,k} + \mathbf{x}_{i,j,k}}{2} \cdot \|\mathbf{x}_{i,j+1,k} - \mathbf{x}_{i,j,k}\|}{\sum_{j=1}^{36} \|\mathbf{x}_{i,j+1,k} - \mathbf{x}_{i,j,k}\|}, \quad \text{eq. 3-9}$$

where $\mathbf{x}_{i,j,k}$ is the current position of the j^{th} discrete material point within the i^{th} “height” or subset, $i = 1, \dots, n$, at the k^{th} temporal frame along the length of the imaged segment; for $j = 36$: $\mathbf{x}_{i,j+1} = \mathbf{x}_{i,1}$,

and $\|\bullet\|$ is the norm of a vector.

These midpoints defined a curved centerline. The length of the aortic segment was obtained as the sum of the spatial distances between neighboring lumen midpoints. An averaged or global *radius of curvature* of the aortic segment was determined as the radius of the circle that was defined by the two end points and the mid-point of the curved centerline in the reference configuration \mathcal{B}_r . The centroid \mathbf{c}_g of the lumen centerline was obtained as

$$\mathbf{c}_g = \frac{\sum_{i=1}^{n-1} \frac{\mathbf{c}_{i+1,k} + \mathbf{c}_{i,k}}{2} \cdot \|\mathbf{c}_{i+1,k} - \mathbf{c}_{i,k}\|}{\sum_{i=1}^{n-1} \|\mathbf{c}_{i+1,k} - \mathbf{c}_{i,k}\|}. \quad \text{eq. 3-10}$$

The current global *diameter* was determined for each time step k as follows: A straight centerline was defined by the lumen midpoints of the two end cross-sections. Local radii $r_{i,j,k}$ were determined as minimum distance between each material point $\mathbf{x}_{i,j,k}$ on the aortic wall and the centerline. The average radius r_k of the aortic segment at each imaged time step throughout the cardiac cycle was calculated as mean of these local radii. Eventually the average or global diameter was obtained.

The current *volume* $V_k = V(t_k)$ was obtained from average radius and length as

$$V_k = \pi \times r_k^2 \times l_k. \quad \text{eq. 3-11}$$

Rotation $\vartheta_k = \vartheta(t_k)$ was defined as the angle between the radial line connecting the lumen mid-point of the cross-section to a specific material point on the wall at different time points throughout the cardiac cycle [Sengupta et al. 2008]. Without any limitation to the generality, the possible range of ϑ_k can be restricted to values between $-\pi/2 < \vartheta_k < \pi/2$, since rotations even close to $\pm \pi/2$ are not physiological. In accordance with the right-hand rule and the definitions that are usually applied to the left ventricle of the heart, positive values mean counter clockwise rotation and negative values mean

clockwise rotation as seen in direction of blood flow, i.e. from a position that is proximal to the heart in distal direction. The average global rotation of an aortic segment was obtained as mean of the rotation values that were calculated for all single discrete material points. The peak-to-peak rotation amplitude, describing the maximum range of rotational motion of an aortic segment throughout the cardiac cycle, was defined as the difference of maximum (counter clockwise) and minimum (clockwise) rotation.

3.3.3.2 Axial displacement and velocity

An overall axial unit vector \mathbf{a}_{seg} of an aortic segment was defined in direction of the straight line between the luminal midpoints of the two end cross sections of the segment. The *displacement* of a material point $X_{i,k}$ in direction of \mathbf{a}_{seg} was obtained as $\mathbf{u}_{i,j,k,axial} = \mathbf{u}_{i,j,k} \cdot \mathbf{a}_{seg}$. *Velocity* in direction of \mathbf{a}_{seg} was determined from displacement data by means of numerical differentiation with respect to time:

$$\dot{\mathbf{u}}_{i,j,k} = \frac{\mathbf{u}_{i,j,k+1} - \mathbf{u}_{i,j,k}}{\Delta t}. \quad \text{eq. 3-12}$$

Displacement and velocity along the aortic tree towards the heart were signed positively.

3.3.3.3 Longitudinal and circumferential strain, relative volume change and twist

Longitudinal strain $\varepsilon_{l,k}$, *circumferential strain* $\varepsilon_{c,k}$ and the *relative volume change* VC_k were defined as:

$$\varepsilon_{l,k} = \frac{l_k - l_{min}}{l_{min}}, \quad \text{eq. 3-13}$$

$$\varepsilon_{c,k} = \frac{d_k - d_{min}}{d_{min}}, \quad \text{eq. 3-14}$$

$$VC_k = \frac{V_k - V_{min}}{V_{min}}, \quad \text{eq. 3-15}$$

where l_{min} , d_{min} and V_{min} are minimum length, diameter and volume that were observed during the cardiac cycle, respectively. l_k , d_k and V_k indicate the corresponding values measured at the k^{th} temporal frame. The *cyclic strain* was defined as the peak-to-peak strain amplitudes $\Delta\varepsilon_l$, $\Delta\varepsilon_c$ and ΔVC . It was obtained for l_k , d_k and V_k assuming maximum cyclic values. VC is a biaxial measure combining longitudinal and circumferential deformation.

As already stated above, the end-diastolic initial frame of the ECG-triggered 4D ultrasound image acquisition [cf. Figure 3-3] coincides with minimum blood pressure that occurs at end-diastole of the

cardiac cycle [cf. chapter 1.3]. The minimum blood pressure is related to the minimum diameter of an aortic segment, whereas maximum diameter is related to maximum or systolic blood pressure. Consequently, the end-diastolic configuration is the reference for the computation of cyclic circumferential strain according eq. 3-14. Note that, in contrast, minimum or maximum values of length and volume were not necessarily observed at the same time steps [cf. Figure 3-3]. I.e. the measures for cyclic strain according to eq. 3-13, eq. 3-14 and eq. 3-15 do not describe the deformation of the aortic segment with regard to a common reference configuration. End-diastole serves as reference configuration for the description of cyclic circumferential deformation, only. Different configurations may serve as reference for the description of cyclic longitudinal and volumetric deformation. Therefore, eq. 3-13 and eq. 3-15 imply a change of reference configuration [cf. chapter 2, eq. 2-18 to eq. 2-19] with respect to the end-diastolic reference configuration provided by the ECG-triggered image acquisition.

The *twist* of an aortic segment was calculated as:

$$\gamma_k = \frac{\vartheta_{distal,k} - \vartheta_{prox,k}}{l_{ed}}, \quad \text{eq. 3-16}$$

where $\vartheta_{distal,k}$ is the rotation of the cross-section distal to the LV along the aortic tree, $\vartheta_{prox,k}$ is the rotation of the proximal cross-section and l_{ed} is the end-diastolic length of the aortic segment, which was chosen as reference for this purpose. Twist peak-to-peak amplitude Γ was obtained from the difference of maximum (counter clockwise, cct) and minimum (clockwise, ct) twist that were observed and is given as absolute value: $\Gamma = \|\gamma_{max} - \gamma_{min}\|$.

In addition to the peak-to-peak amplitudes of cyclic deformation, *systolic-diastolic* longitudinal and volumetric deformation was defined relating the systolic-diastolic length change $l_{sys} - l_{dia}$ and volume change $V_{sys} - V_{dia}$ to the diastolic length l_{dia} and volume V_{dia} :

$$\varepsilon_{l_{sys-dia}} = \frac{l_{sys} - l_{dia}}{l_{dia}}, \quad \text{eq. 3-17}$$

$$VC_{sys-dia} = \frac{V_{sys} - V_{dia}}{V_{dia}}. \quad \text{eq. 3-18}$$

Systolic-diastolic twist was defined as $\Gamma_{sys-dia} = \|\Gamma_{sys} - \Gamma_{dia}\|$. Diastole and systole were identified as the time steps where minimum and maximum diameters were observed, respectively, and diastolic and systolic segment length, volume and twist were obtained from the corresponding time steps.

All imaged geometries of the arterial segments represent – compared to a load free geometry of an excised aortic segment – deformed configurations under physiological loading. Therefore, neither the cyclic peak-to-peak amplitudes, nor the systolic-diastolic deformation measures describe the “true” strains with regard to a natural, stress- and deformation-free configuration \mathcal{B}_0 of the aorta.

3.3.3.4 Phase shift of longitudinal and circumferential strain

The time points $t_{l,max}$ and $t_{d,max}$ where maximum longitudinal and circumferential strain occurred, respectively, were identified. The *phase shift* of the maxima of longitudinal and circumferential strain was defined as

$$\varphi_{max} = \frac{t_{l,max} - t_{d,max}}{t_{cc}}, \quad \text{eq. 3-19}$$

where t_{cc} is the total time of one cardiac cycle.

3.3.3.5 Conclusion

In this section 3.3.3, a method for the quantification of the global multiaxial deformation of non-aneurysmal aortic segments based on full-field displacement measurements by 4D ultrasound was presented. The high temporal resolution of the displacement data available via the customized data interface was used to assess the full extent of multiaxial cyclic wall motion with regard to different reference configurations for different in-plane deformation components. Moreover, the fact that 4D ultrasound allows the LAGRANGIAN description of the motion $\chi(X, t)$ [cf. section 2.1 and eq. 3-8] of a field of discrete material points X was used: It was ensured that the measurements at different time points of the cardiac cycle, which served as basis for the quantification of the deformation, were taken at the same site of the observed object. An imaging method that provides an EULERIAN reference frame, by which measurements at the identical site within the field of view of the measurement device are obtained at different time points, might result in chimerical deformations if the observed object performs (large) rigid body motions within the field of view. In contrast, the spatial resolution of the discrete motion function $\chi(X, t)$ was not fully exploited, but metrics for the global, homogeneous deformation of aortic segments were presented.

3.3.4 Highly resolved fields of local in-plane strains

Additionally, a method for the highly spatially resolved full-field imaging of aortic wall motion was developed within this thesis: 4D ultrasound data were used to generate a finite element model of the imaged aortic or aneurysmal segment and to determine all in-plane components of the BIOT's strain tensor [cf. chapter 2.1, eq. 2-23] for aortic wall segments with sizes ranging from $\leq 2 \text{ mm}^2$ to $\geq 20 \text{ mm}^2$. The steps of the finite element preprocessing – reconstruction and discretization of the reference configuration, computation of the displacement boundary conditions, definition of local coordinate systems and input-file generation – were performed using an in-house software that was written

in Microsoft Visual Basic for Applications in Excel (Microsoft Corp., Redmond, WA, USA). The commercial FE solver Abaqus® 6.12 (Dassault Systems, Paris, France) was used for solving the direct boundary value problem.

3.3.4.1 Discretization of irregular aortic and aneurysmal wall geometries

Careful masking of the aortic wall with the Toshiba ACP [cf. chapter 3.2.2 and Figure 3-4] resulted in regular patterns of the exported discrete material points that allowed an automated FE meshing of the chosen reference configuration \mathcal{B}_r [Figure 3-7]. The discretization of the end-diastolic reference configuration was performed as suggested by Kroon and Holzapfel 2008 and Kroon 2010 based on virtual data: each position vector $\mathbf{X}_{i,j}$ [cf. section 3.3.1] was preserved as node of a 4-node structural element $e_{i,j}$, $i = 1, \dots, n - 1$, $j = 1, \dots, 36$ in the model. The quality of the mesh was checked using the standard settings of the commercial finite element preprocessor Altair Hypermesh and, if necessary, masking of the wall segment was repeated.

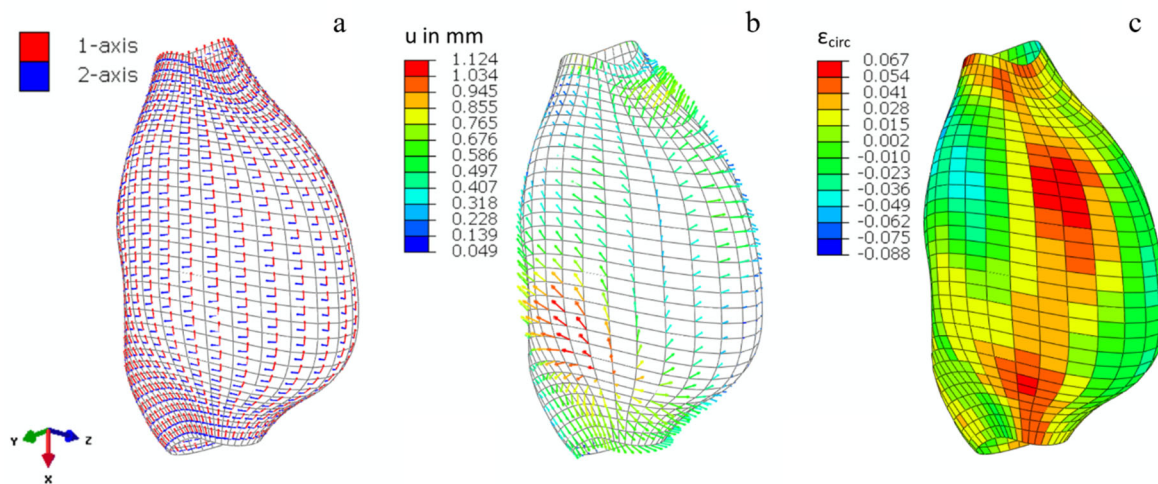


Figure 3-7 Post-processing and strain computation based on the exported 4D ultrasound wall motion data: a) discretized end-diastolic configuration with local axial (1-axis) and circumferential (2-axis) directions. The discrete material points [cf. Figure 3-4 b] are preserved as nodes of the mesh. b) Systolic displacement field. c) Distribution of local circumferential strains. [Image reprinted from Wittek et al. 2018 with permission from John Wiley and Sons]

3.3.4.2 Definition of local CARTESIAN coordinate systems

In order to obtain physiological meaningful in-plane strain components describing the longitudinal or axial and circumferential deformation of the vessel, local orthonormal basis systems were defined on the end-diastolic reference configuration for each material point that is represented as node in the FE model and each vessel wall region that is represented as element [Figure 3-7 a]: A preliminary overall axial vector \mathbf{a}_{seg} was defined by the straight line between the luminal midpoints of two cross sections of the aortic or aneurysmal segment [cf. section 3.3.3.1]. Depending on the shape and complexity of the

imaged geometry, either one “global” axial vector was defined for the complete imaged aortic section, or several axial vectors were defined for different sections along the length of the vessel which resulted in a curved, segmentally linear centerline. The minimum size of an axial section for which separate axial vectors were defined was determined by the distance between two neighboring subsets of discrete material points in longitudinal direction (“heights”). Using the position vectors of the neighboring material points, the preliminary unit vectors $\hat{\mathbf{e}}_1, \hat{\mathbf{e}}_2$ in approximate axial and circumferential direction were constructed that were tangential to the 3D surface in the respective material point. Then, a preliminary local “radial” vector was obtained as $\hat{\mathbf{e}}_3 = \mathbf{a}_{seg} \times \hat{\mathbf{e}}_2$. The local axial unit vector was obtained by projection of $\hat{\mathbf{e}}_1$ onto the plane that is defined by \mathbf{a}_{seg} and $\hat{\mathbf{e}}_3$

$$\mathbf{e}_1 = \frac{1}{N} [(\hat{\mathbf{e}}_1 \cdot \mathbf{a}_{seg})\mathbf{a}_{seg} + (\hat{\mathbf{e}}_1 \cdot \hat{\mathbf{e}}_3)\hat{\mathbf{e}}_3], \quad \text{eq. 3-20}$$

where $N = \|(\hat{\mathbf{e}}_1 \cdot \mathbf{a}_{seg})\mathbf{a}_{seg} + (\hat{\mathbf{e}}_1 \cdot \hat{\mathbf{e}}_3)\hat{\mathbf{e}}_3\|$.

The final local radial unit vector \mathbf{e}_3 was obtained from the cross product of the local axial unit vector \mathbf{e}_1 (global axial direction and tangential to the surface) and the preliminary vector $\hat{\mathbf{e}}_2$ that is tangential to the surface and not parallel to \mathbf{e}_1 : $\mathbf{e}_3 = \mathbf{e}_1 \times \hat{\mathbf{e}}_2$. Finally, the local orthonormal basis system was completed by the circumferential unit vector $\mathbf{e}_2 = \mathbf{e}_3 \times \mathbf{e}_1$. The appropriateness of the local axial and circumferential directions was checked visually by the author and, if necessary, adjustment was possible by defining an additional rotation of the local coordinate systems about the local radial direction. In large-displacement analyses, the local element coordinate systems rotate with the average rigid body motion of the material point, whereas the local nodal coordinate systems are a set of fixed Cartesian axes [Abaqus 6.12 2012c, 2012a].

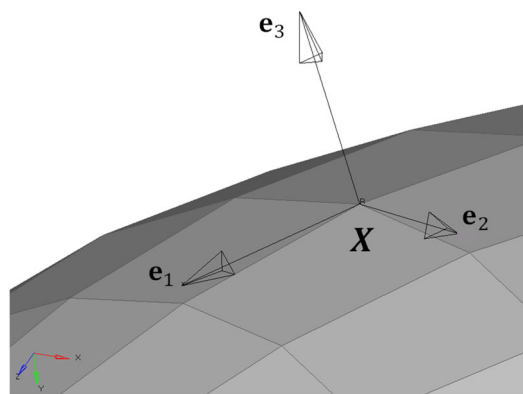


Figure 3-8 Local coordinate system defined in material point \mathbf{X} . \mathbf{e}_1 – longitudinal axis of the vessel, \mathbf{e}_2 – circumferential or tangential axis, \mathbf{e}_3 – radial axis. [Image reprinted from Wittek et al. 2017a with permission from SPIE]

3.3.4.3 Computation of BIOT's in-plane strain fields with regard to a chosen deformed reference configuration

In order to implement the discrete motion function given in eq. 3-8 that was obtained from 4D ultrasound measurements in a finite element model using Abaqus 6.12, the displacements $\mathbf{u}_{i,j,k}$ were applied as boundary conditions (BCs) to each node $\mathbf{x}_{i,j,r}$ of the FE model in the chosen reference configuration. The in-plane components of the BIOT's strain tensor $\boldsymbol{\varepsilon}$ with regard to the defined local coordinate systems were obtained for each element by numerical differentiation. Since every degree of freedom is constrained in the model, the resulting local strain values are independent of the ascribed material properties. For this study, a hyperelastic NEO-HOOKEAN material with $C_{10} = 0.01$ MPa was used [Abaqus 6.12 2012a]. In Abaqus/Standard first order finite-strain membrane elements of type M3D4R with reduced integration and hourglass control were used. [Abaqus 6.12 2012b].

Note: In-plane strain components ε_{kl} , $k, l = 1, 2$, with regard to a deformed reference configuration are obtained by this method, only, no "true" strains with regard to a load-free and undeformed configuration that cannot be accessed in vivo .

In addition to the components of the BIOT's strain tensor, the Area Change Ratio (ACR) or area strain, i.e. the ratio of the current area and the reference area of an element or surface section $e_{i,j}$, was introduced as comprehensive measure of the biaxial in plane deformation:

$$\begin{aligned} ACR_{i,j,k} &= ACR(e_{i,j}, t_k) = \frac{\Delta A(e_{i,j}, t_k)}{A_0(e_{i,j}, t_r)} \\ &= \lambda_1(e_{i,j}, t_k) \cdot \lambda_2(e_{i,j}, t_k) - 1 \\ &= (\varepsilon_1(e_{i,j}, t_k) + 1) \cdot (\varepsilon_2(e_{i,j}, t_k) + 1) - 1 \end{aligned} \quad \text{eq. 3-21}$$

where

$$\Delta A(e_{i,j}) = A(e_{i,j}, t_k) - A_0(e_{i,j}, t_r),$$

$i = 1, \dots, n - 1$ refers to the "height" or position along the longitudinal axis of the aortic segment ($n \leq 36$),

$j = 1, \dots, 36$ refers to the "degree" or circumferential position as identified in the ASCII file that was exported from the Toshiba ACP,

$t_k, k = 0, \dots, m$ marks the k^{th} temporal frame throughout the cardiac cycle for which wall motion data were obtained,

$A(e_{i,j}, t_k)$ is the current area of element or surface section $e_{i,j}$,

$A_0(e_{i,j}, t_r)$ is the reference area of element or surface section $e_{i,j}$,

$\lambda_1(e_{i,j}, t_k), \lambda_2(e_{i,j}, t_k)$ are the principal stretches of element $e_{i,j}$ in (longitudinal) 1 and (circumferential) 2 direction at t_k and

$\varepsilon_1(e_{i,j}, t_k), \varepsilon_2(e_{i,j}, t_k)$ are the principal BIOT's strains of element $e_{i,j}$ in (longitudinal) 1 and (circumferential) 2 direction at t_k , as computed by Abaqus 6.12 regarding rotational transformation of principal directions for finite deformation.

In order to quantify the full range of cyclic deformation, the time steps that showed the minimum and maximum mean strain with regard to the end-diastolic reference configuration throughout the cardiac cycle were identified *for each strain component, separately*. Then peak-to-peak strain amplitudes were calculated as difference between the local strain values of the configuration with maximum mean strain and those of the configuration with minimum mean strain:

$$\Delta\varepsilon_{l,i,j} = \varepsilon_{max(l),i,j} - \varepsilon_{min(l),i,j}, \quad \text{eq. 3-22}$$

where

i, j give the "height" and "degree" of the element $e_{i,j}$,
 l denotes the strain component: 1 – longitudinal, 2 – circumferential and 12 – in-plane shear,
 $max(l)$ and $min(l)$ indicate the time steps within the cardiac cycle at which maximum and minimum mean values of strain component l were observed.

These peak-to-peak strain amplitudes are referred to as cyclic strains in this work.

Note: Minimum and maximum mean values of the different strain components do not necessarily occur at the same time point within the cardiac cycle. Thus, the cyclic strains quantify the full range of deformation throughout the cardiac cycle for each strain component. However, the computation of cyclic strain according to eq. 3-22 separately for each component of the in-plane strain tensor, may imply the choice of a different reference configuration for each strain component [cf. section 3.3.3.3].

3.4 Effects of increased spatial resolution on in vivo strain measurement

The objective of the clinical study presented in this section [Karatolios, Wittek et al. 2013] was to investigate whether the method for imaging and calculation of highly resolved local wall strains that was described in sections 3.3.1, 3.3.2 and 3.3.4 of this chapter provides any additional benefit compared to the "standard post-processing" provided by the Toshiba ACP [cf. section 3.2.2.13.2.2.1] and to other 3D imaging methods that provide global changes of aortic shape and therefore allow the determination of homogeneous deformation metrics, only. For this purpose, cyclic circumferential peak-to-peak strain

amplitude was determined in three different ways. All three approaches were based on the identical 4D ultrasound data. Thus, all three approaches shared the identical frame rate and used the end-diastolic configuration of the imaged aortic segment as reference for the computation of strain. But the three methods differed in the spatial resolution or the size of aortic wall surface segments for which separate strain values were computed.

3.4.1 Study collective and in vivo data acquisition

The study was approved by the local Ethics Committee of the University of Marburg. Six adults without cardiovascular risk factors (e.g. no history of smoking, diabetes, hypertension and obesity) and without evidence of aortic disease were examined at the Clinics for Cardiac and Thoracic Vascular Surgery of the University Hospital Marburg after giving informed consent. Clinical variables including age, gender, body weight and blood pressure were obtained from each volunteer and patient [Table 3-1]. From each healthy subject and patient 4D ultrasound data of the epigastric or upper (proximal to the truncus coeliacus) segment of the abdominal aorta were recorded according to chapter 3.2.1.

Table 3-1 Clinical characteristics of study population [Reprinted from Karatolios, Wittek et al. 2013 with permission from Elsevier]

Patient ID	Age in years	Sex	BMI in kg/m ²	Heart rate in bpm	Systolic BP in mmHg	Diastolic BP in mmHg
V1	19	male	22	67	110	75
V2	20	male	26	60	120	70
V3	22	male	24	68	130	80
V4	44	male	26	71	120	80
V5	24	male	24	53	125	70
V6	49	male	25	49	130	75
Mean ± sd	29.7 ± 13.2		24.5 ± 1.5	61.3 ± 8.9	122.5 ± 7.6	75 ± 4.5

3.4.2 Computation of circumferential in-plane wall strain with different spatial resolutions

Firstly, assuming a perfectly cylindrical shape of the aorta, the average circumferential strain of complete imaged wall segments with lengths between 20 mm and 40 mm was calculated as the ratio of

systolic diameter change $\Delta d = d_{max} - d_{min}$ and minimum (end diastolic) reference diameter. This value is referred to as “*diameter ratio*” in this section:

$$diameter\ ratio = \frac{d_{max} - d_{min}}{d_{min}}. \quad \text{eq. 3-23}$$

This method corresponds to clinical practice where diameter, diameter change and circumferential strain are determined mostly by means of two-point measurements performed on just one cross section of the wall along the aortic tree. The results are then taken as representative for aortic segments with a length of several cm. Imaging data of single aortic cross sections can be obtained by standard 2D ultrasound data with appropriate temporal resolution [cf. chapter 3.1].

Secondly, the standard post-processing of the Toshiba ACP, as implemented in the UltraExtend workstation (Toshiba Medical Systems Corporation, Otawara, Japan) by default, was used to compute systolic circumferential strain [cf. section 3.2.2.1]: The tracked segment of the aorta was divided into sixteen 3D subsegments (including the pseudo-apex) automatically and wall strains were calculated for these. For strain analysis, the 12 base and middle segments could be used. The 4 segments of the "pseudo-apex" had to be excluded.

Thirdly, highly resolved strain fields were computed according to the customized post-processing described in chapter 3.3.4.

3.4.3 Dependency of the strain values and distributions on the spatial resolution

The diameter ratio provides one average strain value for each data set, only. In contrast, distributions of local strain values with different spatial resolution are obtained by standard and customized post-processing. The mean, the local peak value, the coefficient of variation and the ratio of the local peak value and the standard deviation of the obtained distributions of local strain values were determined for each data set (“wall motion indices”). The coefficient of variation of the distribution of local wall strains is referred to as *heterogeneity index*, the ratio of local peak value and standard deviation is called *local strain ratio* [cf. chapter 6.3].

Statistics was performed using WOLFRAM Mathematica 10.3 (Wolfram Research, Champaign, IL, USA). In order to compare the distributions of wall motion indices that were obtained for each data set, data were tested for normality first using the function ‘DistributionFitTest’. If both of two samples that were to be compared by means of a hypothesis test were distributed normally, values were given as mean \pm sd and a Student t test for matched pairs (t) was performed. Else, values were given as median [Q₁, Q₃], where Q₁ and Q₃ are the 1st and 3rd quartile, respectively and a Mann-Whitney U test (U) was performed. If more than two samples were compared, the Bonferroni-Correction for multiple testing was observed.

Table 3-2 Dimensions of imaged aortic wall segments and resolution of US-imaging and wall motion tracking data. [Reprinted after Karatolios, Wittek et al. 2013 with permission from Elsevier]

Patient ID	Length in mm	Minimum diameter in mm	Maximum diameter in mm	Voxel size in mm/voxel	Frame rate in Hz	Wall section area in mm ²	
						standard	customized
V1	36.1	14.9	18.0	0.59	15.9	141.2	2.0
V2	40.0	15.0	17.9	0.59	12.8	158.0	2.1
V3	33.9	15.6	17.2	0.59	13.5	139.4	2.1
V4	33.0	16.9	19.0	0.59	14.1	145.2	2.1
V5	22.6	14.7	15.8	0.35	17.9	87.0	1.2
V6	33.3	19.0	20.7	0.39	14.5	165.3	2.4
Mean ± sd	33.2 ± 5.8	16.0 ± 1.7	18.1 ± 1.7	0.52 ± 0.11	14,8 ± 1.9	139.4 ± 27.6	2.0 ± 0.4

3.4.4 Results

Table 3-2 gives the dimensions of all imaged aortic segments and the average end diastolic wall section area sizes obtained by standard and customized post-processing. The diameter ratio was determined for six healthy aortic segments with a length of 33.2 ± 5.8 mm and a minimum (diastolic) diameter of 16.0 ± 1.7 mm corresponding to a mean surface area of about 1700 mm². Using the standard post-processing, the imaged abdominal aortic wall segments were divided into 12 sections with a size of 139.4 ± 26.7 mm², for which separate strain values were computed. The customized post-processing procedure allowed the calculation of strains for 864 sections with an average size of 2.0 ± 0.4 mm² in the same aortic segments.

Table 3-3 gives a comparison of the results of the applied three different methods to compute the systolic circumferential strain of the abdominal aortae of 6 volunteers without cardiovascular risk factors. Mean values obtained for each single data set by standard and customized post-processing were in good agreement with the diameter ratio $\Delta d/d_0$. Observing the Bonferroni correction for multiple testing ($p > 0.0167$), no statistically significant differences were observed in the spatially averaged or global deformation of the wall segments as estimated by the diameter ratio and the means (Mean) of standard and customized circumferential strain distributions.

In contrast, the statistical indices characterizing the heterogeneity of local strain obtained by standard and by customized post-processing were significantly different. Local peak values (Peak, $p \leq 0.01$), the heterogeneity index (HI, $p \leq 0.01$) and the local strain ratio (LSR, $p \leq 0.05$) derived from standard post-processing were significantly lower compared to the corresponding values determined based on the customized post-processing procedure for the computation of highly resolved strain fields.

Table 3-3 Comparison of 3 different methods to compute the systolic distributions of circumferential strain and derived wall motion type indices of the abdominal aortae of 6 volunteers without cardiovascular risk factors. In the case of the local peak strain (Peak), the heterogeneity index (HI), as well as the local strain ratio (LSR), the differences between the results obtained by customized and by standard postprocessing are highly significant for $p \leq 0.01$. [Reprinted after Karatolios, Wittek et al. 2013 with permission from Elsevier]

Patient ID	$\Delta d/d_0$	Circumferential strain in %									
		Standard postprocessing					Customized postprocessing				
		Mean	Peak	HI	LSR	Mean	Peak	HI	LSR		
V1	20.8	19.2	33.5	0.41	1.75	23.7	57.3	0.44	1.75		
V2	19.3	17.8	26.8	0.25	1.51	18.2	39.5	0.43	1.51		
V3	10.3	11.0	18.8	0.35	1.71	10.2	25.3	0.51	1.71		
V4	12.4	12.4	16.3	0.19	1.31	12.5	28.0	0.32	1.31		
V5	7.5	6.7	10.5	0.25	1.57	6.7	23.9	0.52	1.57		
V6	9.0	9.3	13.9	0.31	1.49	8.0	19.1	0.50	1.49		
Mean \pm SD	13.2 ± 5.6	12.7 ± 4.9	20.0 ± 8.6	0.29 ± 0.08	1.56 ± 0.16	13.2 ± 6.5	32.2 ± 14.1	0.45 ± 0.08	1.56 ± 0.16		
Test / p							$t, p \leq 0.01$	$t, p \leq 0.01$		$t, p \leq 0.05$	

3.4.5 Discussion

In this section, three methods to determine and characterize cyclic circumferential strain of an abdominal aortic segment based on 4D ultrasound data were applied exemplarily to six young and healthy volunteers. The main difference between the three methods, the diameter ratio, standard and customized post-processing, was the size of the aortic wall segments, for which circumferential strain was computed, separately. The increased spatial resolution of the customized post-processing resulted in the detection of significantly higher local peak strains and, eventually, in a more appropriate mapping and quantification of heterogeneous strain distributions. This capability to detect locally confined peak strains and heterogeneous strain distributions, has the potential to gain clinical and diagnostic relevance in the monitoring of aortic aneurysms [cf. chapter 6].

Heterogeneous distributions of cyclic circumferential strain were observed in all aortic segments by both methods that allowed for the determination of local strain values, the standard and the customized post-processing. This finding is not trivial in aortae of young and healthy subjects. Mechanical homeostasis, i.e. the existence and uniform distribution of a physiologically optimal stress and strain state in blood vessel walls, which is maintained by active growth and remodeling of the wall in healthy arteries, is a widely accepted axiom in physiology and medicine [Kassab 2006; Cyron and Humphrey 2017]. A too narrow and literal understanding of mechanical homeostasis which might suppose completely homogeneous stress and strain distributions would contradict the current findings.

Moreover, often the human aorta is modelled mechanically as a hollow cylinder loaded with pulse pressure as suggested by using the Law of LAPLACE for calculating aortic wall stress [Kassab 2006; Pape et al. 2018; Astrand et al. 2011, 2011; Caro 2012]. This approach results in one strain value for an aortic segment, which represents a totally homogenous strain distribution in the aortic wall. However, justified this approach may be for many purposes, the findings of this study draw the attention to the limits of such an approach when applied to a biological structure with irregular geometry, varying wall thickness and elastic properties.

3.5 Characteristic size of aortic wall motion in vivo

The motion function $\mathbf{x}_{i,j,k} = \mathbf{X}_{i,j} + \mathbf{u}_{i,j,k}$ [cf. eq. 3-8 and eq. 3-6 for the explanation of the indices] of discrete material points is the primary measure obtained from the highly resolved, customized 4D ultrasound measurements. In order to quantify the relevant range of magnitude of the displacements $\mathbf{u}_{i,j,k}$, the in vivo 3D displacements of the infrarenal aortic segments of three characteristically different groups of volunteers and patients were evaluated.

Table 3-4 Patient data are given as median $[Q_1, Q_3]$, where Q_1 and Q_3 are the first and third quartile, respectively. Pulse pressure was obtained as difference of the maximum and minimum blood pressure observed throughout the cardiac cycle. For the groups of volunteers < 60 y. of age and > 60 y. of age the average diameter along the length of the imaged aortic segment is given, whereas for the group of AAA patients, the maximum diameter is given as measured clinically. [Reprinted from Wittek et al. 2017a with permission from SPIE]

	< 60 y.o.	> 60 y.o.	AAA
n	20	20	20
Age in y.	27.6 [26.7, 29.6]	71.0 [64.5, 74.0]	70.5 [64.5, 74.0]
Pulse pressure in mmHg	47.5 [40.0, 60.0]	60.0 [50.0, 70.0]	50.0 [50.0, 67.5]
Diameter in mm	14.1 [13.3, 15.5]	17.4 [13.9, 19.4]	44.0 [39.7, 51.5]

3.5.1 Study group

Data of 60 male patients and volunteers presented at the Clinics for Vascular and Endovascular Surgery of the University Hospital Frankfurt am Main were evaluated for this study. The study was approved by the local ethics committee. Patient data were divided into three groups: “young” patients < 60 y.o. without known cardiovascular risk factors ($n = 20$), “elderly” patients > 60 y.o. suffering from various cardiovascular diseases (in particular, arteriosclerosis) but without AAA ($n = 20$) and AAA patients > 60 y.o. ($n = 20$). An abdominal aorta was defined as aneurysmal when its maximum diameter exceeded 3.0 cm. Maximum diameter of the imaged AAAs as determined by clinical measurement was 49.0 ± 10.3 mm (mean \pm sd).

3.5.2 Data acquisition and customized post-processing

Data acquisition was carried out according to the protocol described in section 3.2.1. Temporal resolution of ultrasound imaging was median $[Q_1, Q_3] = 21.61 \text{ s}^{-1} [20.09 \text{ s}^{-1}, 32.21 \text{ s}^{-1}]$ in the young group, $20.09 \text{ s}^{-1} [20.09 \text{ s}^{-1}, 23.59 \text{ s}^{-1}]$ in the elderly group and $23.56 \text{ s}^{-1} [22.55 \text{ s}^{-1}, 25.49 \text{ s}^{-1}]$ in the AAA group. Length of the imaged aortic and aneurysmal segments was 26.4 mm [25.4 mm, 30.5 mm] in the young, 40.0 mm [32.7 mm, 44.8 mm] in the elderly and 69.7 mm [57.1 mm, 77.3 mm] in the AAA group. Patient data for the three groups are shown in Table 3-4. The elderly and the AAA groups were age matched. Pulse pressure as the dominant load leading to cyclic deformation of the aortic and aneurysmal wall was increased in the elderly and the AAA group compared to the young group. The difference reached statistical significance at the 5% level, though, only for the comparison of the young and the elderly group according to the Bonferroni correction for multiple testing ($p < 0.167$).

Customized post-processing of the 4D ultrasound data was performed according to sections 3.2.2 and 3.3.1 and the displacements of material points throughout the cardiac cycle were calculated using

eq. 3-7. Calculations were carried out with the in-house software for post-processing of the customized 4D ultrasound data that is described in section 3.3.3.

3.5.3 Wall displacement in young, elderly and AAA patients

The median value of cyclic 3D displacements was of a similar size in all three groups (young: median [1st quartile, 3rd quartile] = 0.89 mm [0.77 mm, 1.06 mm], elderly: 1.00 mm [0.56 mm, 1.36 mm], AAA: 0.98 mm [0.77 mm, 1.28 mm]). I.e. for the majority of patients and volunteers in all groups average displacements with a size of about 1 mm were observed in vivo. In particular, in 86% of the investigated AAA average displacements exceeding 0.7 mm were observed. In these data sets, only 15.5% [5.9%, 36,6%] of the material points showed displacements smaller than 0.7 mm and 2.9% [0.7%, 11.8%] of the material points showed displacements smaller than 0.5 mm. [Wittek et al. 2017b]

These findings are particularly noteworthy because several comparative studies performed by the author and collaborators showed for similar patient collectives that cyclic in-plane strain was significantly reduced from the young through the elderly to the AAA group [cf. Derwich et al. 2016; Wittek et al. 2017a; Wittek et al. 2018 and chapter 6 of this thesis]. The reduction of cyclic circumferential strain in the elderly and the aneurysmal patient groups indicated considerable stiffening of the wall tissue compared to younger subjects, which is in accordance with known degenerative changes of microstructure and elastic properties of the aortic wall due to ageing and AAA development [cf. chapter 1.7]. Almost constant 3D displacements of the aortic wall together with significantly reduced deformation or strain might indicate increased rigid body motion of the aortic wall in the elderly and the AAA group compared to the young. This hypothesis fits well with the known decrease of axial prestretch with age and AAA development [cf. chapter 1.6 and further literature cited there], but has to be proven in further research.

4 In vitro validation of full-field wall motion measurement

4.1 Introduction

4D ultrasound-based measurement and reconstruction of the 3D geometries of the heart and of large blood vessels has been validated previously *in vivo* and *in vitro* [Soliman et al. 2008; Seo et al. 2009; Park et al. 2011; Seo et al. 2011; Bihari et al. 2013; Alessandrini et al. 2016; Derwich et al. 2016]. However, none of these previous studies was transferable to the use of 4D ultrasound in this thesis in all relevant points: to the particular device [cf. 3.2.1], the high resolution of the full-field displacement data available via the customized data interface [cf. chapters 3.3.1 and 3.4], the global and local strain metrics that were computed based on this new type of *in vivo* full-field data [cf. chapters 3.3.3 and 3.3.4] and the application of 4D ultrasound to the aortic wall that was established within this thesis in cooperation with clinical partners: Originally, the used device was designed and validated for the assessment of left ventricular wall motion [Seo et al. 2009; Seo et al. 2011]. In the current project, it was used to measure the motion of the aortic wall, which is a far thinner structure undergoing smaller deformations, compared to the left ventricular wall. Thus, validation of 4D ultrasound measurement for this specific application seemed to be necessary.

Since 3D echocardiography combined with speckle tracking has been developed as an imaging method for clinically assessing left ventricular myocardium and function, several of the previous studies refer to deformation parameters of the myocardium that are indicative for left ventricular function [Soliman et al. 2008; Seo et al. 2009; Seo et al. 2011; Alessandrini et al. 2016]. Other studies have used other ultrasound devices, post-processing algorithms and routines than the ones that were applied within this thesis [Park et al. 2011; Kok et al. 2015]. Finally, an earlier validation study of the application of the Toshiba Artida and the Toshiba Advanced Cardiac Package to aneurysm-like structures, that was performed by one of the clinical cooperation partners involved in the project presented in this work, the Department of Vascular and Endovascular Surgery of the Goethe University Hospital [Bihari et al. 2013], did use silicone phantoms instead of aortic soft tissue and performed tests in distilled water at

room temperature. Both, specimen ($c_{silicone} \approx 1000 \text{ m/s}$) and medium, showed deviating speeds of sound compared to soft tissue ($c_{soft \text{ tissue}} \approx 1540 \text{ m/s}$) which might have impaired the results of the validation.

The objectives of the validation study that was performed in this thesis and is presented in this chapter were to quantify the *uncertainty* and the *reproducibility* of 4D ultrasound full-field displacement measurement of aortic wall tissue and derived strain fields (cf. Altman and Bland [1983] and Bland and Altman [1986] for methods and concepts of validation of measurement techniques). The validation addressed the measurement by use of the Toshiba Artida device itself, combined with post-processing with the customized ACP. Possible sources of uncertainty and impaired reproducibility of 4D ultrasound measurements were, firstly, inherent in its physical principle, e.g. the wavelength of the ultrasound wave might have restricted spatial resolution of the measurement. Secondly, the observer dependency of the ($c \approx 1483 \text{ m/s}$) measurement itself (hand-held probe) and of the semi-automatic segmentation of the vessel wall, which defined the initial geometrical shape and the region of interest for the speckle tracking algorithm, were possible sources of uncertainty. Finally, the parameters of the measurement such as the forming of the used wave packet, focusing and beamforming of the RF signal by control of the phased-array matrix probe and the post-processing of the RF data including the speckle tracking algorithm were proprietary technology and unknown to the author and the other collaborators of the project. It was the aim of the presented study to quantify the resulting mingled or lumped effect of different sources of uncertainty on the measurement. To identify and weight the influence of different sources of uncertainty was beyond the scope of this work. The uncertainty and reproducibility of a single 4D ultrasound measurement was to be quantified because measurements for diagnostic purposes are taken only once, in clinical practice.

Measurement uncertainty was assessed as *agreement* of the 4D ultrasound measurement with optical reference measurements. The reproducibility of the 4D ultrasound measurement was assessed in terms of its *test-retest reliability*, i.e. the degree of reproducibility of a measurement under identical circumstances (subject, device, observer) [Shrout and Fleiss 1979; Koo and Li 2016]. For this purpose, an Analysis of Variances of repeated ultrasound measurements under identical conditions was performed.

The current chapter is organized as follows: In section 4.2 the methods that were applied in the validation study are presented. Section 4.2.1 outlines the overall concept of the study. The experimental setup, the sample and the performed experiments are described in section 4.2.2. Section 4.2.3 is dedicated to the methods that were applied to assess the first objective of the validation study, i.e. the quantification of the agreement of 4D ultrasound and of optical measurements. Section 4.2.4 presents the approach for determining the test-retest-reliability of the 4D ultrasound deformation measurement, which was based on the evaluation of repeated measurements and post-processing. The results of the validation experiment are reported in section 4.3: Section 4.3.1 is dedicated to the agreement of ultrasound and optical measurements whereas section 4.3.2 addresses the reproducibility of the ultrasound

measurements. The chapter is concluded by the discussion of the validation results [section 4.4] and the limitations of the study [section 4.5].

4.2 Methods of the in vitro validation study

4.2.1 Design of the study

Using an existing custom built inflation-extension testing device [cf. 4.2.2.3], a tubular specimen of porcine aorta [cf. 4.2.2.1] was loaded physiologically by axial prestretch and cyclic pressure change that was applied with a frequency of 1 Hz [cf. chapters 1.2 and 1.5]. Eleven different combinations of axial prestretch, inner base pressure and cyclic pulse pressure were applied to the same specimen. From these eleven load cases, five were chosen for further evaluation that provided characteristically different deformed reference geometries (diameter, wall thickness) and cyclic deformation [Table 4-1].

Table 4-1 Parameters of the five different load cases that were applied to the porcine aortic specimen and characteristic values describing the deformed reference configuration and the cyclic deformation for each load case as obtained from optical reference measurements. ref. wt \equiv wall thickness in the deformed reference configuration, circ. \equiv circumferential.

	C01	C02	C04	C07	C08
Max./min. p in mmHg	113/26	105/83	128/45	101/94	158/68
Pulse pressure Δp in mmHg	87	22	83	7	90
Axial prestretch	1.31	1.31	1.42	1.61	1.61
Circ. prestretch	0.95	1.06	0.94	1.07	1.00
Deformed ref. wt in mm	1.6	1.4	1.4	1.3	1.2
Reference diameter in mm at p_{\min}	17.6	20.2	18.0	20.3	19.0
Cyclic diameter change in mm	3.60	0.87	3.23	0.23	2.82

For the purpose of quantifying the agreement of 4D ultrasound measurements with optical reference measurements, the resulting deformation was measured in parallel by 4D ultrasound and optically [Figure 4-1, cf. sections 4.2.2.5]. From optical data, one reference measurement was obtained for each load case as the mean of 3 subsequent load cycles. Post-processing of the optical data was fully automatized and performed only once for each load case [cf. 4.2.2.6]. In contrast, two successive 4D ultrasound measurements of each load case were taken. All 4D ultrasound measurements were taken by the same experienced observer. The ultrasound probe was not hand-held, but fixed by a custom-made mount, reducing the observer influence and standardizing the measurement procedure. Post-processing of each of the 10 4D ultrasound data sets was performed 10 times by one experienced observer, including the

observer dependent semi-automatic segmentation of the aortic wall as region of interest and the application of the proprietary speckle tracking algorithm. In total, 20 4D ultrasound evaluations were available for each load case. Results of repeated experiments were recorded, stored and analyzed in the sequence of their acquisition or generation. Each of the 100 4D ultrasound data sets was compared to the corresponding optical reference measurement. In contrast, for the purpose of quantifying the reproducibility of the 4D ultrasound measurement, an Analysis of Variances of the repeated ultrasound measurements and evaluations was performed [cf. section 4.2.4].

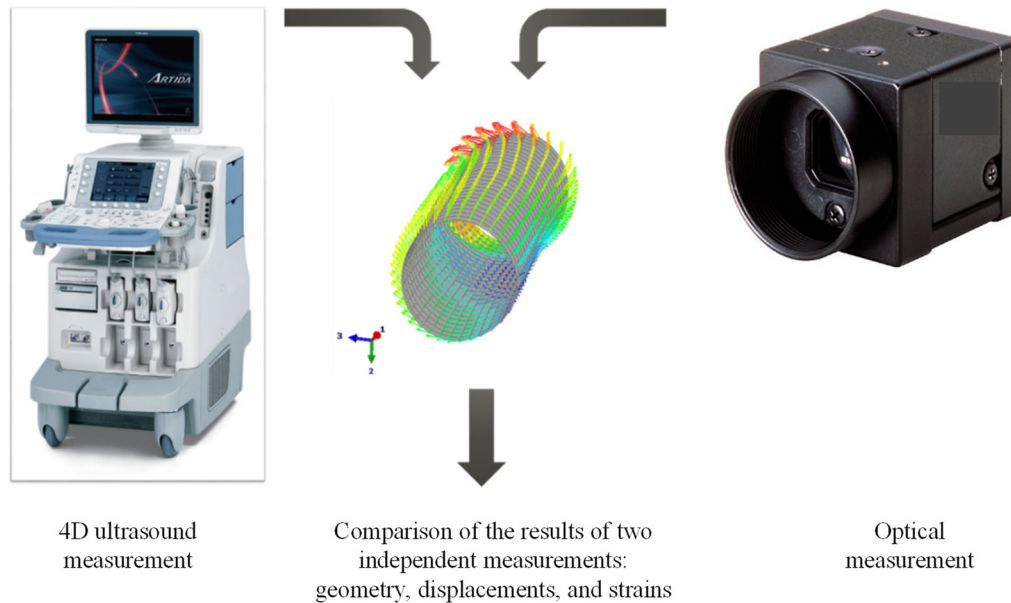


Figure 4-1 Illustration of the basic concept of the validation experiments performed to validate the measurement accuracy of 4D ultrasound full-field displacement measurement.

The post-processed 4D ultrasound data sets included the effects of all above-mentioned random sources of uncertainty. They did not include any fixed effects, such as the influence of different observers. All measurements and repeated post-processing were taken under identical circumstances.

The design of the validation study was developed by the author of this thesis in close cooperation with C. Blase (Cell and Vascular Mechanics Group, Department of Biology, Goethe University Frankfurt). The inflation-extension experiments with parallel 4D ultrasound and optical measurement [cf. chapter 4.2.2.5] were performed by C. Blase and W. Derwich (Department of Vascular and Endovascular Surgery, Goethe University Hospital Frankfurt). Post-processing of the optical data as described in section 4.2.2.6 of this chapter was performed by C. Blase. “Clinical” post-processing of the 4D ultrasound data including segmentation and speckle tracking using the customized version of the Toshiba ACP [cf. chapter 3.2] was done by the author.

4D ultrasound and optical measurements were not directly comparable: 4D ultrasound provided the fully three-dimensional motion function of discrete material points [eq. 3-6] on the inner or luminal surface of the wall as described in chapter 3. In contrast, optical measurements provided 2D diameter

measurements and 2D displacement fields from two mutually orthogonal views of the outer surface of the specimen. Moreover, ultrasound and optical data did neither share a common spatial, nor a common temporal reference system. Both data types did show diverging spatial and temporal resolution. The temporal synchronization and spatial registration of the ultrasound data and the optical data, which was a necessary precondition for the comparison of the measurement results from both sources, was developed and performed by the author of this thesis [cf. chapter 4.2.3.3 for synchronization and registration of diameter, diameter change and strain measurements and chapter 4.2.3.4 for synchronization and registration of full-field displacement measurements]. Finally, the statistical evaluation of the experimental results was conceived and performed by the author of this thesis.

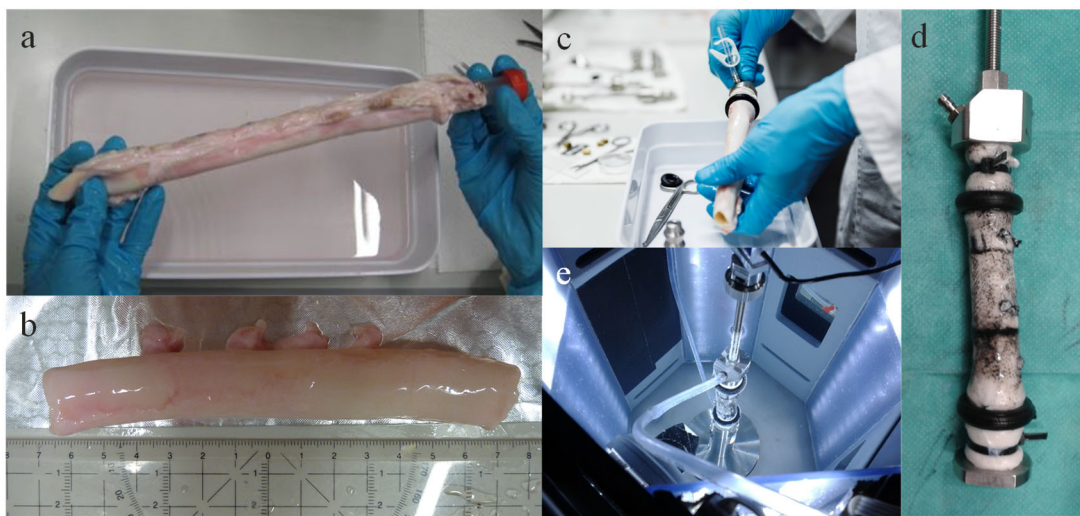


Figure 4-2 Preparation of the porcine aortic specimen. a) Abdominal aortic sample separated from attached tissue and side branches, b) shortened tubular segment that was chosen for the experiments with sealed ostia of removed side branches, c) fixation of the tubular specimen to custom mounts using custom made O-ring-like structures, d) mounted specimen with applied speckle pattern and marks for optical deformation measurement, e) view of the illuminated tank from top, in which a tubular specimen is mounted vertically. [Images: C. Blase, Cell and Vascular Mechanics Group, Goethe University Frankfurt]

4.2.2 Sample and experimental set up

4.2.2.1 Sample preparation

Thoracic aortas of young pigs (10 – 12 months) were obtained from a local slaughterhouse and stored in phosphate buffered saline (pH 7.2) with 10 % (v/v) dimethyl sulfoxide (DMSO) at -20°C . A straight tubular specimen of porcine aorta with dimensions of 15 mm x 130 mm (luminal diameter \times length in its load-free configuration) was carefully separated from attached tissue and side branches. The ostia of the side branches were sealed by careful sewing. The specimen was fixed to custom mounts using custom made O-ring-like structures. An irregular speckle pattern and additional marks were applied to

the surface of the specimen for the purpose of optical measurement of global axial deformation and the assessment of local deformation by means of digital image correlation (speckle tracking). [Figure 4-2]

4.2.2.2 Wall thickness measurement

After the experiments, ring-shaped cross sections were cut from both ends of the region of interest of the aortic specimen and were photographed [Figure 4-3]. Using ImageJ v. 1.48 [Schneider et al. 2012], the average load-free wall thickness of the specimen was determined to be $s_0 = 1.93$ mm.



Figure 4-3 Ring-shaped cross sections of the porcine aortic specimen for optical measurement of its load-free wall thickness. Handwritten notes give the sample number (“V15”) and identify the longitudinal position of the sample from which the two rings were cut (“unten”, “oben”). [Image: C. Blase, Cell and Vascular Mechanics Group, Goethe University Frankfurt.]

4.2.2.3 Experimental set up

A custom built inflation-extension set up that was previously available in the Cell and Vascular Mechanics Group (Goethe University Frankfurt/Main) was used to perform the experiments. A scheme of the experimental set up is given in Figure 4-4. The specimen was mounted in a cuboid water bath with heated saline (37°C, 0.9 % (w/v) NaCl) in order to provide acoustic properties of the medium close to the in vivo conditions, in particular, the sound velocity of 1540 m/s in human abdominal soft tissue [Goss et al. 1980]. Axial extension of the specimen could be adjusted by a manual linear guide, dynamic inflation was achieved by a pneumatic cylinder (CRDSNU, Festo, Esslingen, Germany), whose piston was driven by a linear motor (Electroforce LM1, Bose Corp., Framingham, MA, USA). The pressure difference between sample interior and water bath was measured by a differential pressure transducer. The axial force was measured by a force sensor. The deformation of the specimen was recorded by two 8-bit CMOS cameras (1.3 Megapixels, Ximea, Münster, Germany) with 8 mm focal length objectives (Tamron, Cologne, Germany), which provided two mutually orthogonal 2D views of the specimen. The

specimen was illuminated by eight LED strips fixed in the corners of the water bath to ensure uniform illumination of the specimen surface. The ultrasound transducer was directly coupled to the water bath through an opening in the side. Image and sensor data acquisition was controlled by custom LabVIEW programs (LabVIEW 2011, National Instruments, Austin, TX, USA) on a PC.

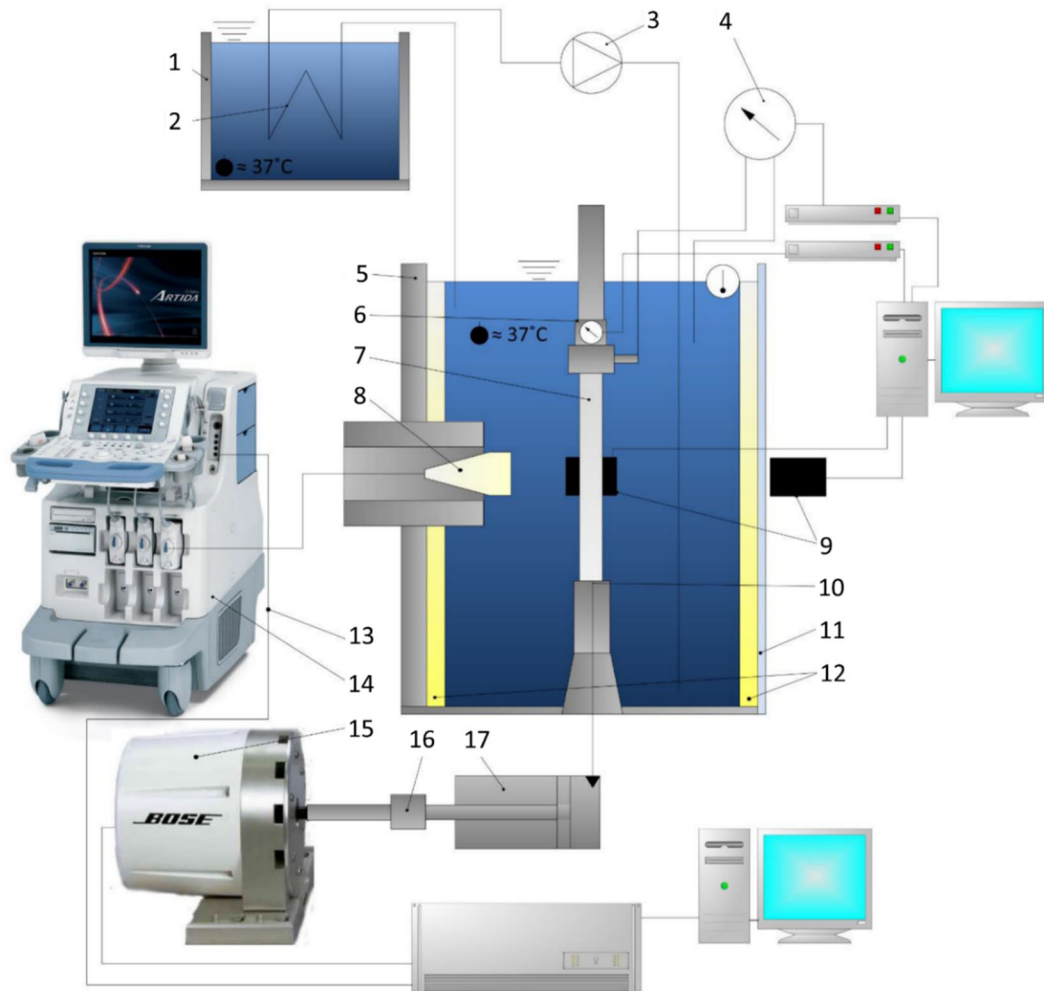


Figure 4-4 Inflation-extension testing device equipped with 4D ultrasound and optical measuring devices: 1) heated bath, 2) heat exchanger, 3) rotary pump, 4) differential pressure sensor, 5) tank (front), 6) axial force sensor, 7) sample (porcine aorta), 8) US probe fixed by custom made mount, 9) optical cameras, 10) pressuring tube, 11) tank, 12) illumination (LED), 13) trigger, 14) 4D ultrasound device, 15) linear motor, 16) coupling, 17) pressure cylinder. [Image: Bannenberg und Hegner 2014, Studienprojekt, Cell and Vascular Mechanics Group, Goethe University Frankfurt]

4.2.2.4 Load cases

In 5 experiments, constant axial prestretches of 1.31, 1.42 and 1.61 and pressure peak-to-peak amplitudes ranging from 7 mmHg to 90 mmHg were applied resulting in diameter changes from 0.19 mm to 3.66 mm [Table 4-1]. The loading of the specimen with cyclic pulse pressure at varying, but for each performed experiment constant, axial prestretch resulted in cyclic radial displacement. In contrast, cyclic length change could not be assessed using this experimental set up.

4.2.2.5 Simultaneous ultrasound and optical deformation measurement

The cyclic deformation of the specimen was measured in parallel by 4D ultrasound and optically. Figure 4-5 shows a scheme of the spatial arrangement of the 4D ultrasound probe and the two CMOS cameras in relation to the imaged aortic specimen together with the ultrasound probe coordinate system. The x -axis corresponded to the longitudinal direction of the specimen. The y -axis corresponded to the dominant propagation direction of the ultrasonic waves. Optically visible steel reference axes of coordinates [Figure 4-6 b] were used for the alignment of camera 2 in line with, and of camera 1 orthogonal to the y -axis of the ultrasound probe coordinate system [Figure 4-5]. Camera 2 gave a 2D view of the specimen as seen from positive y -direction, camera 1 was mounted orthogonal to camera 2 and to the propagation direction of the ultrasonic waves and gave a 2D view of the specimen as seen from positive z -direction of the transducer coordinate system. A reference for a common origin of the x -axis was defined by identifying the position of the tip of a plummet from ultrasound and optical measurements, which are shown in Figure 4-6 a and b, respectively. From ultrasound imaging data, the position of the tip was obtained as the mean of 10 evaluations of the data in order to minimize the random error of the measurement.

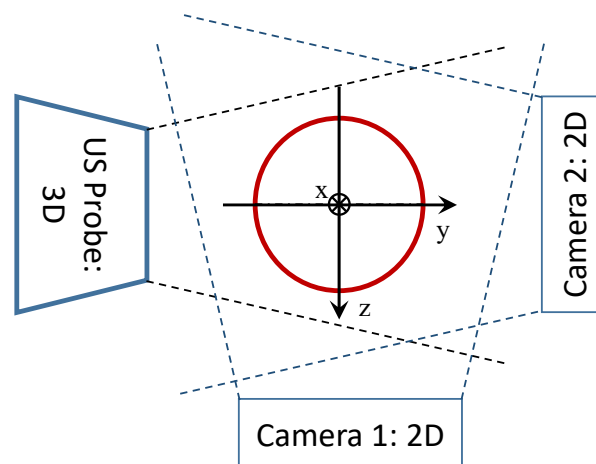


Figure 4-5 Set-up of ultrasound probe (“US probe”) and two CMOS cameras for simultaneous measurements. Camera 2 was positioned in line with and camera 1 was positioned orthogonal to the y -axis of the ultrasound probe coordinate system.

By 4D ultrasound, the three-dimensional position and deformation of the specimen's luminal surface was measured resulting in a discrete motion function of up to 1080 material points as described in detail in section 3.3. The lumen centerline of the specimen was calculated according to eq. 3-9. Characteristic dimensions of the aortic wall's deformed reference configurations as imaged by 4D ultrasound and 4D ultrasound imaging parameters are given in Table 4-2.

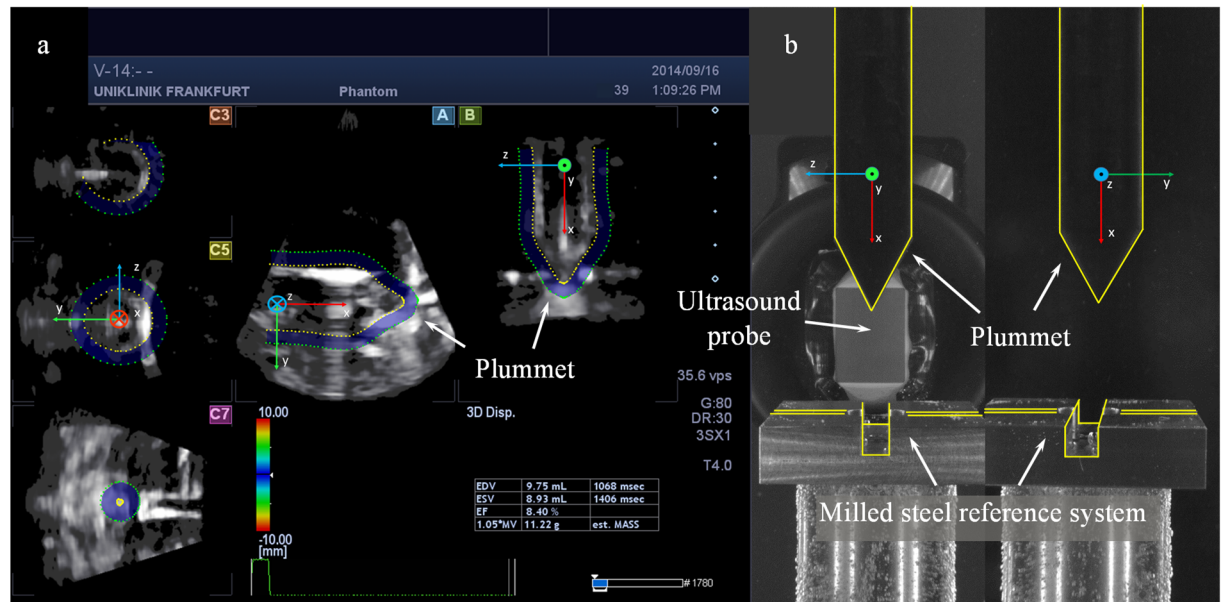


Figure 4-6 a) Ultrasound and b) optical reference measurements of a plummet as basis for transformation of both data types to a common coordinate origin in x-direction. The milled steel reference coordinate axes (b, bottom) were used for the alignment of the CMOS cameras with the ultrasound probe coordinate system [cf. Figure 4-5] Plummet and milled steel reference axes are highlighted in yellow for better recognizability.

Table 4-2 Characteristic dimensions of the aortic wall segments as imaged by 4D ultrasound and 4D ultrasound imaging parameters

	C01	C02	C04	C07	C08
Segment length in mm	31.4 ± 0.9	29.9 ± 0.5	36.2 ± 0.6	33.0 ± 0.4	36.3 ± 0.6
Luminal diameter in mm	14.3 ± 0.2	16.8 ± 0.2	15.2 ± 0.2	16.6 ± 0.3	16.3 ± 0.4
Frame rate in Hz	35.6	35.6	30.4	30.4	35.6
Spatial dist. of material points at deformed reference configuration in mm					
Axial direction	1.4 ± 0.04	1.3 ± 0.02	1.6 ± 0.02	1.4 ± 0.02	1.6 ± 0.03
Circ. direction	1.3 ± 0.02	1.5 ± 0.02	1.3 ± 0.02	1.5 ± 0.03	1.4 ± 0.04

Simultaneously, the deformation of the specimen's outer surface was measured optically by two 8-bit CMOS cameras with a resolution of 1280 x 1024 pixels corresponding to a pixel size on the specimen

surface of approx. 0.1 mm. Temporal resolution of optical measurements was about 25 images/s. Camera 1 and camera 2 captured the xy - and xz -components of the 3D displacement, respectively. This spatial arrangement allowed for the separate assessment and comparison of the accuracy of the 4D ultrasound measurement in propagation direction (y -axis) of the RF signal and orthogonal to the propagation direction (z -axis).

4.2.2.6 Post-processing of optical deformation data

Optical reference values were obtained for each experiment as the means of three subsequent measurements in order to minimize the measurement uncertainty.

Alignment and spatial calibration of the optical measurements was done separately for each camera by using a custom target. Linear functions for the pixel scale factor along the x -axis and the respective optical axis (z -axis, camera 1 and y -axis, camera 2) were established based on these data. Local reference diameter $d_{ref}^{opt}(x^{opt})$ and diameter change $\Delta d_{ref}^{opt}(x^{opt})$ of the specimen, spatially resolved along the x -axis of the optical coordinate system, were determined in the xy -plane applying an in-house threshold-based edge detection method [Figure 4-7].

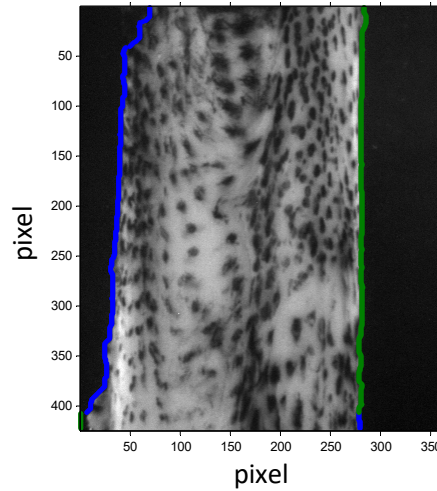


Figure 4-7 Determination of locally resolved diameter from optical image data by threshold-based edge detection.

Temporally resolved 2D displacement fields $u_y^{opt}(x_{ref}, y_{ref}, t_k)$ and $u_z^{opt}(x_{ref}, z_{ref}, t_k)$ in the xy - and the xz -plane, respectively, were determined using a digital image correlation (DIC) code proposed by Jones et al. [2014] [Figure 4-8]. Both, edge detection and DIC, were coded using MATLAB (The Mathworks, Inc., Natick, Massachusetts, USA). The subset region for the DIC was adjusted to different values, to check for bad or missing correlations for the displacement estimation. A subset size of 31 was chosen for all evaluations, since this gave robust results in all load cases while maintaining a high spatial

resolution. A threshold of the normalized 2D cross-correlation coefficient of 0.7 was used to exclude non correlating regions and avoid artificial displacement values.

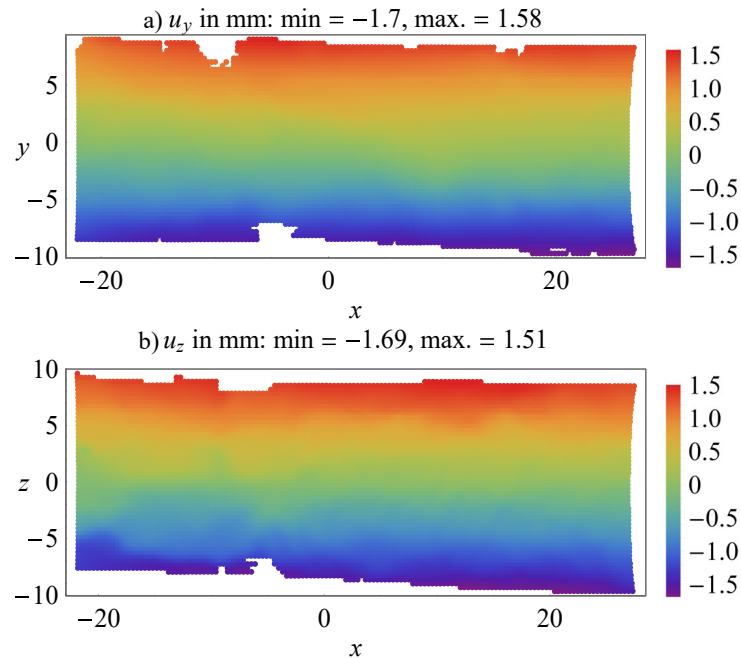


Figure 4-8 Exemplary displacement fields u_y^{opt} (a) and u_z^{opt} (b) as obtained from optical measurements using a DIC code that was coded in MATLAB.

Eventually, the 3D-centerline was constructed from the spatially resolved diameters in the xy - and xz -plane, respectively. For each x -position along the specimen, the y - and z -component of the center point was determined as the center of the diameter in the respective plane.

4.2.3 Quantification of the agreement of 4D ultrasound and optical measurements

4.2.3.1 The need for the registration of 4D ultrasound and optical data

Post-processing of optical measurements provided two types of data: 2D diameter as seen from camera 1 [cf. Figure 4-7] and 2D displacement fields as obtained from two mutually orthogonal views by camera 1 and 2 [cf. Figure 4-8]. Both types of data were obtained from optical measurements by means of different computational tools and resulted in different data formats. As a precondition for the comparison of ultrasound and optical measurements, comparable 2D data, i.e. diameter in one plane and two 2D displacement fields, had to be derived from the fully three-dimensional discrete motion function and registered on the different data sets obtained from optical measurements: ultrasound and optical data had to be synchronized and transformed to a common coordinate system, the field of view for which data

from both sources were available had to be identified, measurement points within the field of view with missing data from one source had to be identified and excluded from analysis and spatial and temporal resolution had to be adjusted. Because of the different data formats of optical reference data, this process was performed and, therefore, is described separately for diameter [section 4.2.3.3] and displacement field data [section 4.2.3.4]. Each step of this process implied editing of the data from both sources and care has been taken not to alter or manipulate the data in such a way that the agreement of the measured values appeared better than it actually was. All steps of the registration and comparison of 4D ultrasound and optical data were coded using WOLFRAM Mathematica 10 (Wolfram Research, Champaign, IL, USA).

4.2.3.2 Wall thickness correction of ultrasound data

In order to register the fully three-dimensional ultrasound data that were measured on the inner or luminal surface of the specimen on the two 2D sets of optical image data of the outer surface of the specimen, 4D ultrasound data were corrected for the deformed wall thickness, first. Using the incompressibility constraint [cf. chapter 1.5 for the incompressibility of aortic walls and chapter 2.3.2, eq. 2-65 for the incompressibility condition]:

$$J = \frac{V(t)}{V_0} = \det \mathbf{F} = \lambda_1(t) \cdot \lambda_2(t) \cdot \lambda_3(t) = 1, \quad \text{eq. 4-1}$$

where

- V_0 is the reference volume of the load-free and undeformed solid,
- $V(t)$ is the volume of the solid in any deformed current configuration at time point t
- J is the volume change and
- $\lambda_1(t), \lambda_2(t), \lambda_3(t)$ are the principal stretches in longitudinal, circumferential and radial direction, respectively,

the average deformed wall thickness s_r was computed for each of the five load cases (subjects) for the chosen deformed reference configuration, i.e. the minimum deformed diameter that was observed throughout cyclic loading:

$$s_r = \frac{1}{\lambda_{1,r} \cdot \lambda_{2,r}} \cdot s_0, \quad \text{eq. 4-2}$$

where $s_0 = 1.93$ mm is the average load-free wall thickness and $\lambda_{1,r}$ and $\lambda_{2,r}$ are the axial and circumferential prestretch, respectively. Prestretches and resulting deformed wall thickness are given for each load case in Table 4-1. Using the local nodal coordinate systems that were constructed for each data set by means of the in-house FEM preprocessor as described in section 3.3.4.2 [cf. Figure 3-8], the deformed

wall thickness was applied as radial offset to each material point $\mathbf{X}_{i,j}$ in the chosen reference configuration \mathcal{B}_r .

4.2.3.3 Registration and comparison of 4D ultrasound and optical measurements of diameter, diameter change and circumferential strain

Transformation to a common origin of the x-axis

Using the optical and 3D ultrasound reference measurements of the tip of a plummet [cf. Figure 4-6], a translational coordinate transformation was performed on optical diameter data and ultrasound data, so that data from both sources shared a common origin of the x -axis that corresponded to the longitudinal direction of the sample. After transformation of the x -coordinates onto a common origin, the common x -interval was determined for which optical and 4D ultrasound diameter data were available.

Since the axial length of the specimen was held constant throughout the load cycle in each of the performed experiments [cf. section 4.2.2] the identification of the common field of view in longitudinal (x -)direction could be performed prior to the synchronization of ultrasound and optical data.

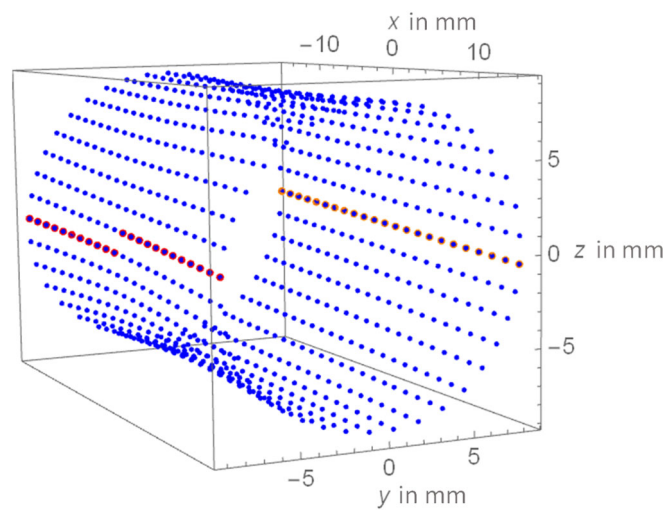


Figure 4-9 Identification of material points with minimum and maximum y -values from 4D ultrasound motion data.

Determination of diameter, diameter change and circumferential strain from 4D ultrasound motion data

In order to compare 4D ultrasound measurements to the available optical diameter measurements, diameter and its change in the xy -plane were extracted from the 4D ultrasound motion function $\mathbf{x}_{i,j,k}^{us} = \boldsymbol{\chi}^{us}(\mathbf{X}_{i,j}, t_k)$, where i refers to the “height” or axial position of the discrete material point \mathbf{x} , j refers to its “degree” or circumferential position and k refers to the temporal frame [cf. section 3.3.2,

eq. 3-6]. The $\mathbf{x}_{i,j,k}^{us}$ showing the minimum and maximum y -values, $\mathbf{x}_{i,\min(y_i),k}^{us}$ and $\mathbf{x}_{i,\max(y_i),k}^{us}$, respectively, were identified for each height i along the x -axis and for each temporal frame k throughout the measurement cycle [Figure 4-9]. For each frame k , 3rd order Hermite interpolation of minimum and maximum y -values along the x -axis was performed, separately, using the built-in WOLFRAM Mathematica function “Interpolation”. Interpolation functions $y_{min}(x)$ and $y_{max}(x)$ were evaluated for the x -positions of the lumen centerpoints $\mathbf{c}_{i,k}$ [cf. eq. 3-9] and the local diameter $d_{i,k}$ was obtained as the difference of the maximum and minimum y -values, related to $\mathbf{c}_{i,k}$:

$$d_{i,k}^{us} = d(\mathbf{c}_{i,k}^{us}) = y_{max}(\mathbf{x}(\mathbf{c}_{i,k}^{us})) - y_{min}(\mathbf{x}(\mathbf{c}_{i,k}^{us})). \quad \text{eq. 4-3}$$

Because diameter was obtained as the difference of the maximum and minimum y -values from image data, a deviation in the y_{min} - and y_{max} -positions which describe the contour, had no effect on the measurement result. Therefore a coordinate transformation to a common y -axis was not necessary.

Local diameter change $\Delta d_{i,k}^{us}$ was computed for each longitudinal position or “height” i with regard to the temporal frame r showing the minimum mean diameter $\bar{d}_r^{us} := \min\{\bar{d}_k^{us} | k = 1, \dots, m\}$, where $\bar{d}_k^{us} = \text{mean}\{d_{i,k}^{us} | i = 1, \dots, n\}$ as measured by ultrasound:

$$\Delta d_{i,k}^{us} = d_{i,k}^{us} - d_{i,r}^{us}, \quad \text{eq. 4-4}$$

Finally, local circumferential strain was obtained as

$$\varepsilon_{i,k}^{us} = \frac{\Delta d_{i,k}^{us}}{d_{i,r}^{us}}. \quad \text{eq. 4-5}$$

The configuration showing the minimum mean diameter was regarded as deformed reference configuration \mathbf{X}_r^{us} for all further evaluation of ultrasound data.

Adjustment of the spatial resolution of optical diameter data

Diameter values that were obtained from optical measurements showed a higher spatial resolution compared to ultrasound data. Ultrasound data sets were organized in 24 subsets or heights along the x -axis, typically, i.e. 24 local diameter values along the x -axis were obtained for each temporal frame. In contrast, about 350 local diameter values were obtained from optical data along the x -axis in the common field of view. In order to compare optical and ultrasound diameter measurements, the spatial resolution of optical data was reduced. The field of view was subdivided into i intervals along the x -axis corresponding to the lumen centerpoints \mathbf{c}_i of the ultrasound measurement [cf. section 3.3.3.1, eq. 3-9]:

$$x_i^{opt} = \begin{cases} \left[x(\mathbf{c}_i^{us}) - \frac{x(\mathbf{c}_{i+1}^{us}) - x(\mathbf{c}_i^{us})}{2}, x(\mathbf{c}_i^{us}) + \frac{x(\mathbf{c}_{i+1}^{us}) - x(\mathbf{c}_i^{us})}{2} \right], & i = 1 \\ \left[x(\mathbf{c}_i^{us}) - \frac{x(\mathbf{c}_i^{us}) - x(\mathbf{c}_{i-1}^{us})}{2}, x(\mathbf{c}_i^{us}) + \frac{x(\mathbf{c}_{i+1}^{us}) - x(\mathbf{c}_i^{us})}{2} \right], & 1 < i < n . \\ \left[x(\mathbf{c}_i^{us}) - \frac{x(\mathbf{c}_i^{us}) - x(\mathbf{c}_{i-1}^{us})}{2}, x(\mathbf{c}_i^{us}) + \frac{x(\mathbf{c}_i^{us}) - x(\mathbf{c}_{i-1}^{us})}{2} \right], & i = n \end{cases} \quad \text{eq. 4-6}$$

Since the sample dimension and ultrasound and optical fields of view were held constant in axial or x -direction throughout the load cycle, this division of the field of view along the x -axis was performed once, only, for the initial frame, and then applied to all other frames. The arithmetical mean of the optical local diameter values within each interval was determined and assigned to the x -position of the corresponding center point: $d_{i,k}^{opt}[x(\mathbf{c}_{i,k})]$. Local diameter change $\Delta d_{i,l}^{opt}$ was computed with regard to the temporal frame showing the minimum mean diameter $\bar{d}_r^{opt} := \min\{\bar{d}_l^{opt} | l = 1, \dots, o\}$, where o is the number of temporal frames of the optical measurement and $\bar{d}_l^{opt} = \text{mean}\{d_{i,k}^{opt} | i = 1, \dots, n\}$:

$$\Delta d_{i,l}^{opt} = d_{i,l}^{opt} - d_{i,r}^{opt} . \quad \text{eq. 4-7}$$

Finally, local circumferential strain was obtained as

$$\varepsilon_{i,l}^{opt} = \frac{\Delta d_{i,l}^{opt}}{d_{i,0}^{opt}} . \quad \text{eq. 4-8}$$

The configuration showing the minimum mean diameter was regarded as deformed reference configuration \mathbf{X}_r^{opt} for all further evaluation of optical data.

Note: For optical and ultrasound measurements, the respective minimum diameter values, \bar{d}_r^{opt} and \bar{d}_r^{us} , were chosen as reference to compute diameter change. These minimum values were not necessarily observed at the same time or frame within the loading cycle by ultrasound and optical measurement.

Temporal resolution and synchronization

Optical and ultrasound measurements did neither have a common temporal reference, nor the same frame rate. Therefore, 3rd order Hermite interpolation of the local optical diameter values over time was performed using default settings of the built-in WOLFRAM Mathematica function ‘Interpolation’. The resulting interpolation function was evaluated for the (normalized) time points t_k within the loading cycle for which ultrasound measurements were available. This resulted in vectors of local optical diameter measurement

$$d_i^{opt} = \{d_i^{opt}(t_1), d_i^{opt}(t_2), \dots, d_i^{opt}(t_m)\}, \quad i = 1, \dots, n \quad \text{eq. 4-9}$$

that corresponded to the ultrasound measurement with regard to the (x -) position along the longitudinal axis of the specimen (i^{th} “height”) and the time point k of evaluation.

Because of the missing common reference signal for ultrasound and optical measurements, both signals showed a varying mutual temporal delay and were synchronized for the purpose of comparison. In order to determine the temporal delay τ of the optical measurement with regard to the ultrasound data, the cross-correlation between the temporally resolved ultrasound and optical diameter change data was determined. Due to its particular importance for the evaluation of the maximum range of aortic deformation and elasticity in vivo, only the section of diameter change data throughout the load cycle were used as basis for the synchronization that showed increasing diameter. Starting with the minimum diameter and ending with the maximum diameter. First, the mean diameter change along the x -axis was calculated and frames with minimum (1) and maximum diameter change (q) were identified for both data types:

$$\overline{\Delta d}_k^{us} = \frac{1}{n} \cdot \sum_{i=1}^n \Delta d_{i,k}^{us}, \quad \text{eq. 4-10}$$

$$\overline{\Delta d}_k^{opt} = \frac{1}{n} \cdot \sum_{i=1}^n \Delta d_{i,k}^{opt}, \quad \text{eq. 4-11}$$

where

$i = 1, \dots, n, n \leq 36$ refers to the “height” or position along the longitudinal x -axis of the aortic segment and

$t_k, k = 0, \dots, m$ marks the k^{th} of in total m temporal frames throughout the load cycle.

The optical diameter change series was shifted cyclically using time increments of the size of one temporal frame of the ultrasound measurement:

$$\overline{\Delta d}_k^{opt} \rightarrow \overline{\Delta d}_o^{opt}, o = \begin{cases} k + \tau, & \text{if } k + \tau < m \\ k + \tau - m, & \text{else} \end{cases}, \tau = 0, \dots, m. \quad \text{eq. 4-12}$$

The non-parametric SPEARMAN’s Rank correlation coefficient $\rho(\overline{\Delta d}_k^{us}, \overline{\Delta d}_o^{opt})$ that is based on the evaluation of rank differences was calculated for the ultrasound diameter change time series, $\overline{\Delta d}_k^{us}, k = 0, \dots, q, (!)$ and each of the m cyclically shifted time series of optically measured diameter change. The maximum of the resulting correlation coefficients $\rho(\overline{\Delta d}_k^{us}, \overline{\Delta d}_o^{opt})$ was chosen and the temporal delay τ of the optical measurement with regard to the ultrasound measurement was determined. The local optical diameter, diameter change and strain data were shifted accordingly in order to obtain optimal synchronization between ultrasound and optical signals:

$$f_i^{opt}(t) \rightarrow \left\{ \begin{array}{l} f_i^{opt}(t + \tau), t + \tau < m \\ f_i^{opt}(t + \tau - m), t + \tau \geq m \end{array} \right\}, \quad \text{eq. 4-13}$$

where

- m is the number of frames recorded during one load cycle,
- i indicates the i^{th} subset along the height of the sample and, correspondingly, the x -position and
- f may denote local diameter, diameter change or circumferential strain.

Figure 4-10 exemplarily illustrates the synchronization of ultrasound and optical data.

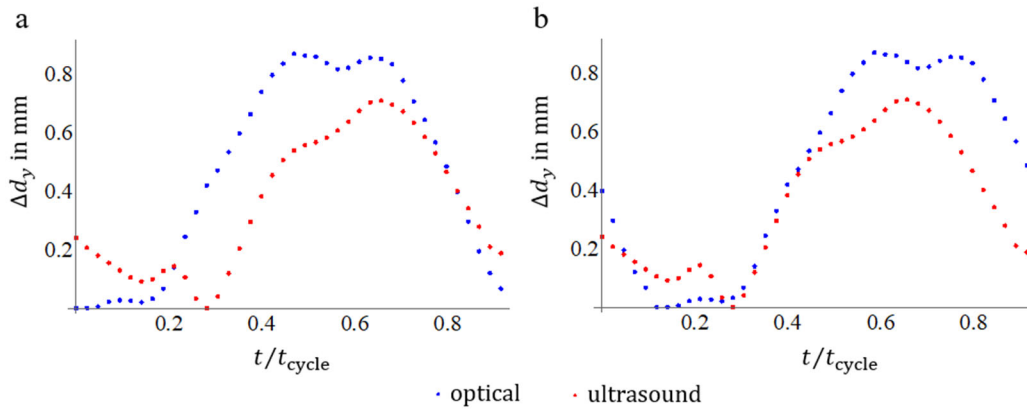


Figure 4-10 Optimal synchronization of ultrasound and optical time series: a) Original and b) cyclically shifted signals.

Approach to the comparison of ultrasound and optical diameter and strain measurements

After registration, ultrasound and optical diameter, diameter change and strain data of both sources were directly comparable with regard to the field of view, the coordinate system, spatial and temporal resolution and time sequence.

The deviation e (for “error”) of the ultrasound measurements from the corresponding optical measurements of the same subject or load case was evaluated for *local* values along the length of the specimen with regard to:

(i) diameter:
$$e_{i,k}^d = d_{i,k}^{US} - d_{i,k}^{opt}, \quad \text{eq. 4-14}$$

(ii) diameter change:
$$e_{i,k}^{\Delta d} = \Delta d_{i,k}^{US} - \Delta d_{i,k}^{opt} \text{ and} \quad \text{eq. 4-15}$$

(iii) circumferential strain:
$$e_{i,k}^\varepsilon = \varepsilon_{i,k}^{US} - \varepsilon_{i,k}^{opt} \quad \text{eq. 4-16}$$

and for “average” values, i.e. the arithmetical mean of the local values along the sample length with regard to

$$(i) \text{ diameter:} \quad e_{i,k}^{\bar{d}} = \bar{d}_{i,k}^{US} - \bar{d}_{i,k}^{opt}, \quad \text{eq. 4-17}$$

$$(ii) \text{ diameter change:} \quad e_{i,k}^{\Delta\bar{d}} = \Delta\bar{d}_{i,k}^{US} - \bar{d}_{i,k}^{opt} \text{ and} \quad \text{eq. 4-18}$$

$$(iii) \text{ circumferential strain:} \quad e_{i,k}^{\bar{\epsilon}} = \bar{\epsilon}_{i,k}^{US} - \bar{\epsilon}_{i,k}^{opt}. \quad \text{eq. 4-19}$$

All repeated measurements and evaluations of the ultrasound data were compared to the identical optical reference measurement, separately. Results of the comparison were given as median [IQR] where IQR is the interquartile range. For the agreement of local strain values, a Bland-Altman analysis was performed [Altman and Bland 1983; Bland and Altman 1986].

4.2.3.4 Registration and comparison of local displacement fields in the xy - and the xz -plane

4D ultrasound provided a temporally resolved full 3D motion function of discrete material points [cf. eq. 3-6]. In contrast, from optical image data two 2D functions of motion components in the xy - and the xz -plane were obtained:

$$\mathbf{x}_{xy,l,o}^{opt} = \mathbf{X}_{xy,l,1}^{opt} + \mathbf{u}_{y,l,o}^{opt}, \quad \text{eq. 4-20}$$

$$\mathbf{x}_{xz,m,o}^{opt} = \mathbf{X}_{xz,m,1}^{opt} + \mathbf{u}_{z,m,o}^{opt}, \quad \text{eq. 4-21}$$

where $\mathbf{X}_{xy,l,1}^{opt}$ and $\mathbf{X}_{xz,m,1}^{opt}$ are the initial configurations of the l^{th} material point in the xy - and of the m^{th} material point the xz -plane, respectively, as obtained from optical measurement and $\mathbf{u}_{y,l,o}^{opt}$ and $\mathbf{u}_{z,m,o}^{opt}$ are the displacements of the respective material points at frame $o = 1, \dots, q$. Both 2D data sets showed the same temporal and spatial resolution but did not share a common field of view and differed in the number (l, m) of motion estimation points. Motion estimation points in the xy - and the xz -plane could not be related with each other without assumptions on the cross-sectional shape of the specimen.

In addition, the 3D centerline of the aortic volume was available for each frame throughout the load cycle from ultrasound data. In contrast, the 3D centerline was available for the initial (reference) frame of the optical measurements, only.

Initially, optical and ultrasound displacement field data did neither share common temporal, nor spatial reference frame or resolution. Therefore, temporal resolution of the optical data had to be

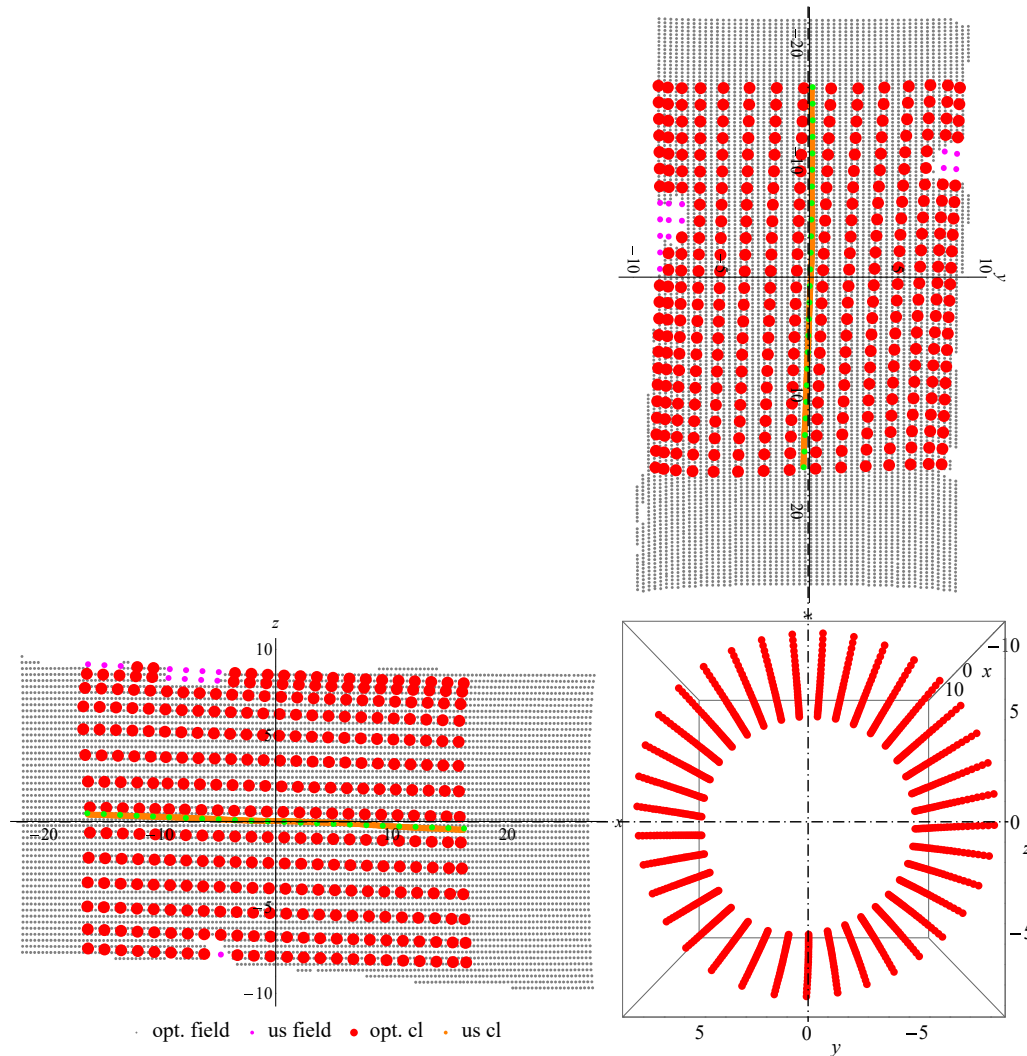


Figure 4-11 Exemplary illustration of the result of the registration of three-dimensional motion field data obtained by ultrasound on two-dimensional displacement field data in two planes as derived from optical image data. Red dots mark the 3D motion estimation points (discrete material points) as obtained from ultrasound measurements. Bottom right, the view in positive x - or longitudinal direction on the 3D ultrasound data describing a deformed configuration of the specimen is shown. Upper right, the 2D projection of the ultrasound motion estimation points visible by camera 1 on the optical field data in the xy -plane is shown. Bottom left the 2D projection of the ultrasound motion estimation points that are visible by camera two [cf. Figure 4-5] on the optical field data in the xz -plane is given. Ultrasound motion estimation points without corresponding optical data are highlighted in pink. The centerlines of the specimen as obtained from optical and from ultrasound measurements are shown as orange and green dots, respectively.

adjusted to the ultrasound frame rate and optical and ultrasound times series had to be synchronized and transformed to a common reference frame. Moreover, data from both sources had to be transformed to a common basis, 4D ultrasound motion functions of the optically visible material points of the specimen [cf. Figure 4-5] had to be identified and registered on the available 2D motion functions in the xy - and

the xz -planes that were available from optical measurements, Finally, spatial resolution of both data sources had to be adjusted. Figure 4-11 illustrates the registration task.

Transformation of the displacement field data to a common x -axis

As first step, optical and ultrasound displacement data were transformed to a common x -axis using the reference measurement of the tip of a plummet [cf. section 4.2.2.5, Figure 4-6 a, b] and the common x -interval, for which data from both sources were available, was identified.

Further steps of construction of and transformation to a common basis were carried out after temporal synchronization of the displacement time series and used the 3D-centerlines of the aortic lumen that were available from both data sources.

Temporal resolution and synchronization of optical displacement field data

Compared to optical diameter measurements, optical full-field data were derived independently and using a different method from the primary image data and showed a diverging temporal resolution and delay τ with regard to the ultrasound time series. Thus adjustment of the temporal resolution, determination of the temporal delay τ and synchronization with regard to the ultrasound measurement had to be performed separately for the optical displacement field data. The applied method followed the steps that are described in detail for the synchronization of the diameter time series in the previous section. The time series of the norm of the means of the absolute values of the (positive and negative) displacement components in y - and z -direction were determined for ultrasound and optical data in the common field of view:

$$u_{res,k} = \sqrt{(\text{mean}[|u_{y,i,k}|])^2 + (\text{mean}[|u_{z,j,k}|])^2}, \quad \text{eq. 4-22}$$

where $i = 1, \dots, n$ and $j = 1, \dots, m$ are the available measurements points for y - and z -displacement, respectively, and $k = 0, \dots, o$ indicates the temporal frame. These time series were used as benchmarks for temporal synchronisation. As a result, the initial frame of the unsynchronized optical data, for which the 3D centerline was available, was shifted to frame $1 + \tau$ of the common time reference.

Transformation of the displacement field data to a common y - and z -axis

The centroid \mathbf{c}_g of the lumen centerline [cf. 3.3.3, eq. 3-10] was used as origin of the common basis. It was estimated separately from 4D ultrasound and from optical data for frame $1 + \tau$: $\mathbf{c}_{g,1+\tau}^{us}$ and \mathbf{c}_g^{opt} , respectively.

The translational transformations

$$\hat{\mathbf{x}}_{i,j,k}^{us} = \mathbf{x}_{i,j,k}^{us} - \mathbf{c}_{g,1+\tau}^{us} \quad \text{eq. 4-23}$$

$$\hat{\mathbf{x}}_{xy,l,k}^{opt} = \mathbf{x}_{xy,l,k}^{opt} - \mathbf{c}_{g,xy}^{opt} \quad \text{eq. 4-24}$$

$$\hat{\mathbf{x}}_{xz,l,k}^{opt} = \mathbf{x}_{xz,l,k}^{opt} - \mathbf{c}_{g,xz}^{opt} \quad \text{eq. 4-25}$$

were applied to the 3D motion function obtained from 4D US and the xy - and xz -2D motion functions obtained from optical measurements, respectively.

In order to correct for possible angular deviation of the ultrasound and the optical x -axis, straight 2D centerlines in the xy - and the xz -plane were determined for optical and ultrasound data, each, by fitting linear models to the respective curved centerlines by linear regression using the WOLFRAM Mathematica function ‘LinearModelFit’: $y_c^{us}(x), y_c^{opt}(x), z_c^{us}(x), z_c^{opt}(x)$. The direction vectors of the centerlines in the xy - and xz -planes, $\mathbf{c}_{xy}^{us}, \mathbf{c}_{xy}^{opt}, \mathbf{c}_{xz}^{us}$ and \mathbf{c}_{xz}^{opt} , were obtained as: $\mathbf{c} = [1, f(1) - f(0)]$, where f is the respective linear fit of the centerline.

The deviation angles φ_{xy} and φ_{xz} between the optical and the ultrasound centerlines in the xy - and the xz -plane were determined as

$$\varphi_{xy} = \arccos\left(\frac{\mathbf{c}_{xy}^{opt} \cdot \mathbf{c}_{xy}^{us}}{|\mathbf{c}_{xy}^{opt}| \cdot |\mathbf{c}_{xy}^{us}|}\right), \quad \text{eq. 4-26}$$

$$\varphi_{xz} = \arccos\left(\frac{\mathbf{c}_{xz}^{opt} \cdot \mathbf{c}_{xz}^{us}}{|\mathbf{c}_{xz}^{opt}| \cdot |\mathbf{c}_{xz}^{us}|}\right). \quad \text{eq. 4-27}$$

Properly orthogonal rotation matrices \mathbf{Q}_z and \mathbf{Q}_y were constructed as

$$\mathbf{Q}_z = \begin{pmatrix} \cos(\varphi_{xy}) & -\sin(\varphi_{xy}) \\ \sin(\varphi_{xy}) & \cos(\varphi_{xy}) \end{pmatrix}, \quad \text{eq. 4-28}$$

$$\mathbf{Q}_y = \begin{pmatrix} \cos(\varphi_{xz}) & \sin(\varphi_{xz}) \\ -\sin(\varphi_{xz}) & \cos(\varphi_{xz}) \end{pmatrix}, \quad \text{eq. 4-29}$$

where \mathbf{Q}_z describes the rotation in the xy -plane about the z -axis and \mathbf{Q}_y describes the rotation in the xz -plane about the y -axis. Position vectors $\mathbf{x}_{xy,i,j,k}^{us}$ and $\mathbf{x}_{xz,l,m,k}^{us}$ of all current configurations that were observed throughout a measurement cycle were rotated about the z - and y -axis, respectively, to correct for angular deviation of the longitudinal or x -axis:

$$\hat{\mathbf{x}}_{xy,i,j,k}^{us} = \mathbf{Q}_z \cdot \mathbf{x}_{xy,i,j,k}^{us} \quad \text{eq. 4-30}$$

$$\hat{\mathbf{x}}_{xz,l,m,k}^{us} = \mathbf{Q}_y \cdot \mathbf{x}_{xz,l,m,k}^{us} \quad \text{eq. 4-31}$$

Derivation of 2D motion functions from 3D ultrasound data

The optically visible discrete material points in the xy - and the xz -plane were identified among all discrete material points $\mathbf{x}_{i,j,k}^{us}$ provided by the ultrasound measurement [Figure 4-12].

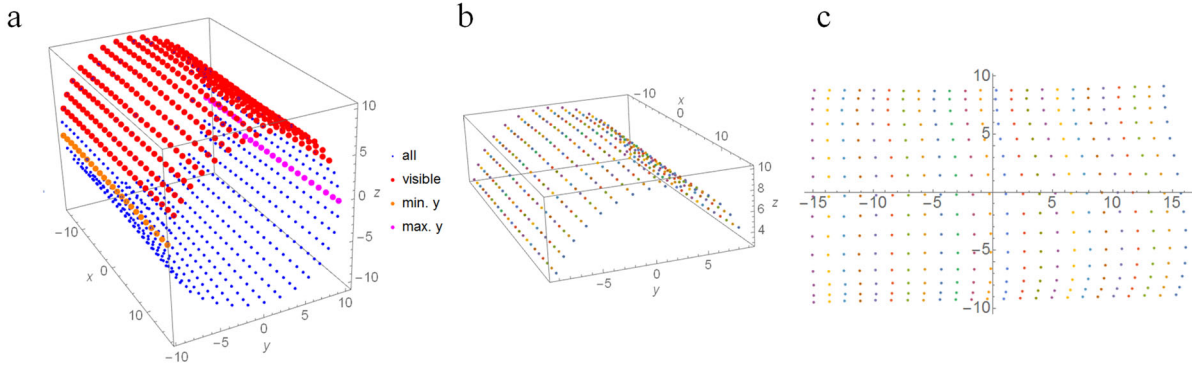


Figure 4-12 Derivation of the 2D reference configuration from 3D ultrasound data: a) Material points that are in the FOV of camera 1 [cf. Figure 4-6] are highlighted in red among all available 4D US material points, b) isolated and c) projected onto the xy -plane.

Two-dimensional motion functions for these optically visible material points in the xy - and the xz -plane were derived from the 3D motion function using the x - and y -components and the x - and z -components of the position vectors of the selected material points in their current configurations, respectively:

$$\hat{\mathbf{x}}_{xy,i,j,k}^{us} = \begin{pmatrix} \hat{x}_{i,j,k} \\ \hat{y}_{i,j,k} \end{pmatrix}, \quad \text{eq. 4-32}$$

$$\hat{\mathbf{x}}_{xz,l,m,k}^{us} = \begin{pmatrix} \hat{x}_{l,m,k} \\ \hat{z}_{l,m,k} \end{pmatrix}. \quad \text{eq. 4-33}$$

Transformation of 4D ultrasound and optical displacement field data to a common reference configuration

Displacement fields were computed from 4D ultrasound as well as from optical data with regard to the respective configuration showing the minimum mean resulting yz -displacement $\mathbf{u}_r = \min\{u_{res,k}, k = 1, \dots, m\}$ [cf. eq. 4-22].

For ultrasound data, 2D displacement fields were obtained as

$$\mathbf{u}_{y,i,j,k}^{us} = \hat{\mathbf{x}}_{xy,i,j,k}^{us} - \hat{\mathbf{X}}_{xy,i,j}^{us}, \quad \text{eq. 4-34}$$

$$\mathbf{u}_{z,l,m,k}^{us} = \hat{\mathbf{x}}_{xz,l,m,k}^{us} - \hat{\mathbf{X}}_{xz,l,m}^{us}, \quad \text{eq. 4-35}$$

where $\hat{\mathbf{X}}_{xy,i,j}^{us}$ and $\hat{\mathbf{X}}_{xz,l,m}^{us}$ are the chosen 2D reference configurations corresponding to the frame in which minimum resulting mean yz-displacement u_{res}^{us} was observed.

The reference configuration of optical displacement measurements was changed from the initial configuration $\mathbf{X}_{xy,p,1}^{opt}$, $\mathbf{X}_{xz,q,1}^{opt}$ to the configuration $\mathbf{X}_{xy,p,r}^{opt}$, $\mathbf{X}_{xz,q,r}^{opt}$ corresponding to the temporal frame for which the minimum mean resulting yz-displacement $u_r^{opt} = \min\{u_{res,k}^{opt}, k = 1, \dots, m\}$ was observed. p, q indicate the p^{th} and q^{th} optical measurement point in the xy - and the xz -plane, respectively. The new reference configurations in the respective planes were obtained as

$$\mathbf{X}_{xy,p,r}^{opt} = \mathbf{X}_{xy,p,1}^{opt} + \mathbf{u}_{xy,p,r}^{opt} \quad \text{and} \quad \mathbf{X}_{xz,q,r}^{opt} = \mathbf{X}_{xz,q,1}^{opt} + \mathbf{u}_{xz,q,r}^{opt}. \quad \text{eq. 4-36}$$

Displacements $\hat{\mathbf{u}}_{xy,i,k}^{opt}$, $\hat{\mathbf{u}}_{xz,i,k}^{opt}$ with regard to the changed reference configuration were then obtained as

$$\hat{\mathbf{u}}_{xy,i,k}^{opt} = \mathbf{x}_{xy,i,k}^{opt} - \mathbf{X}_{xy,i,r}^{opt} \quad \text{and} \quad \hat{\mathbf{u}}_{xz,i,k}^{opt} = \mathbf{x}_{xz,i,k}^{opt} - \mathbf{X}_{xz,i,r}^{opt}. \quad \text{eq. 4-37}$$

Adjustment of the spatial resolution of the optical displacement field data

Local optical displacement data showed a higher spatial resolution compared to ultrasound data [Figure 4-11]. Therefore, spatial resolution of optical data was reduced. For each visible 2D material point of the ultrasound measurement in the xy - and the xz -plane, $\hat{\mathbf{x}}_{xy,i,j,k}^{us}$ and $\hat{\mathbf{x}}_{xz,l,m,k}^{us}$, a neighbourhood was defined by the means of the half distances to its four neighboring material points accounting for the varying distances between two-dimensional material points that resulted from the projection of nearly equidistant material points on the surface of an almost cylindrical three-dimensional solid onto the xy - and the xz -planes [cf. Figure 4-12]. All optical measurement points in their (transformed) reference configuration $\mathbf{X}_{xy,p,r}^{opt}$, $\mathbf{X}_{xz,q,r}^{opt}$ that were situated within this neighborhood of the 4D US material points were identified. The arithmetical mean of their displacements was calculated for all temporal frames and assigned to the chosen reference configuration, $\hat{\mathbf{X}}_{xy,i,j}^{us}$ or $\hat{\mathbf{X}}_{xz,l,m}^{us}$, of the corresponding discrete material point that was obtained from 4D US measurements. Eventually, local optical and ultrasound 2D displacement fields in the xy -plane ($\mathbf{u}_{y,i,j,k}^{opt}$, $\mathbf{u}_{y,i,j,k}^{us}$) and the xz -plane ($\mathbf{u}_{z,l,m,k}^{opt}$, $\mathbf{u}_{z,l,m,k}^{us}$), where l, m indicate the position of the material point within the array of 4D ultrasound data and k indicates the temporal frame [cf. section 3.3.2], were obtained, that showed the same temporal and spatial resolution.

Approach to comparison of ultrasound and optical displacement field measurements

In contrast to the approach to the comparison of diameter, diameter change and circumferential strain, optical and ultrasound displacements were not compared for all frames, but only the displacement fields showing the maximum mean displacement were compared:

$$\mathbf{u}_{y,i,j,max}^{opt}, \quad \text{with} \quad \bar{\mathbf{u}}_{y,max}^{opt} = \max\{\bar{\mathbf{u}}_{y,k}^{opt}, k = 1, \dots, n\}, \quad \text{eq. 4-38}$$

$$\mathbf{u}_{z,i,j,max}^{opt}, \quad \text{with} \quad \bar{\mathbf{u}}_{z,max}^{opt} = \max\{\bar{\mathbf{u}}_{z,k}^{opt}, k = 1, \dots, n\}, \quad \text{eq. 4-39}$$

$$\mathbf{u}_{y,i,j,max}^{us}, \quad \text{with} \quad \bar{\mathbf{u}}_{y,max}^{us} = \max\{\bar{\mathbf{u}}_{y,k}^{us}, k = 1, \dots, n\}, \quad \text{eq. 4-40}$$

$$\mathbf{u}_{z,i,j,max}^{us}, \quad \text{with} \quad \bar{\mathbf{u}}_{z,max}^{us} = \max\{\bar{\mathbf{u}}_{z,k}^{us}, k = 1, \dots, n\}. \quad \text{eq. 4-41}$$

This was done because of the particular importance of the state of maximum deformation for the in vivo deformation estimation [see chapter 3.3.4.3, eq. 3-22], the in vivo determination of the local distensibility coefficient [cf. chapter 6.2, eq. 6-11] as well as for the approach to the inverse identification of the aortic wall's nonlinear and anisotropic constitutive behavior [cf. chapter 7].

4.2.4 Methods for the quantification of the test-retest reliability

Analysis of variance was performed for the maximum values of the

- (i) mean and local diameter,
- (ii) mean and local diameter change and
- (iii) mean and local circumferential strain,

that were obtained throughout the load cycle from 4D ultrasound measurement of the deformation of a porcine aortic specimen. A one-way random effects model [Altman and Bland 1983; Rencher and Schaalje 2008; Hartung et al. 2012; Li et al. 2015] was chosen for the analysis of variance of the results of repeated ultrasound measurement (2 times per load case) and post-processing (10 times per measurement) of the porcine aortic specimen's deformation under 5 different load cases [cf. section 4.2.1, Table 4-1]:

$$y_{ij} = \mu + S_j + e_{ij}, \quad \text{eq. 4-42}$$

where

- μ is the overall population mean,
- S_j is the deviation of the j^{th} subject, $j = 1, \dots, 5$, from the population mean and

e_{ij} is the random error in the measurement of the j^{th} subject in the i^{th} repetition of the test, $i = 1, \dots, 20$.

No fixed effect or systematic error was included in the model because the repeated ultrasound measurements and post-processing steps were carried out under identical conditions (operator, ultrasound device and settings, speckle tracking algorithm) and differences in the results were due to random sources, only. This assumption was verified by testing whether the succession of repeated experiments and post-processing showed any significant effects. The position of the median and the variance of the results of the 20 repeated evaluations of each of the 5 load cases were tested for dependency on the sequential position in the row of repetitions using the built-in WOLFRAM Mathematica 10 functions ‘LocationEquivalenceTest’ and ‘VarianceEquivalenceTest’, respectively.

Data were non-normally distributed. Therefore, non-parametric rank methods were used for the assessment of variances. The KRUSKAL-WALLIS test was used to test whether the distributions of the results from 20 repeated measurements and post-processing of the same load case were significantly different between 5 load cases, i.e. whether 4D ultrasound measurement was capable of significantly distinguishing the examined load cases. The KRUSKAL-WALLIS test was performed using the corresponding built-in WOLFRAM Mathematica 10 function.

In order to assess the test-retest reliability of a single measurement the intraclass correlation coefficient ICC(1,1) [Shrout and Fleiss 1979; Hartung et al. 2012; Li et al. 2015] was determined:

$$ICC(1,1) = \frac{\text{variation between subjects} - \text{variation within subjects}}{\text{variation between subjects} + (k - 1) \cdot \text{variation within subjects}}, \quad \text{eq. 4-43}$$

where $k = 20$ is the number of repeated tests. In literature [ibid.], the ICC is found as a measure for the reproducibility of normally distributed data, only. A closer look at the usual definition of the ICC reveals that this restriction results from the way of calculating the variations between and within subjects as the variance of normally distributed data. Since most of the data showed non-parametric distributions, variation between and within subjects was estimated in this work as follows using non-parametric rank methods:

$$\text{Variation between subjects} = \frac{k}{n - 1} \sum_{j=1}^n (\bar{r}_j - \bar{r}_{..})^2, \quad \text{eq. 4-44}$$

$$\text{Variation within subjects} = \frac{1}{n(k - 1)} \sum_{i=1}^k \sum_{j=01}^n (r_{ji} - \bar{r}_j)^2 \quad \text{eq. 4-45}$$

where

$\bar{r}_{..}$ is the mean of the ranks of all observations for all subjects,

- \bar{r}_j is the mean of the ranks of all observations for subject j and
 r_{ji} is the rank of the i^{th} observation for subject j .

Ranks were determined from all samples pooled. According to Koo and Li [2016], ICC values < 0.5 indicate poor reliability, values between 0.5 and 0.75 indicate moderate reliability, values between 0.75 and 0.9 are indicative of good reliability and values > 0.9 mean excellent reliability. The ICC was programmed using WOLFRAM Mathematica 10.

4.3 Results of the validation study

4.3.1 Agreement of 4D ultrasound and optical measurements

Table 4-3 gives an overview of the deviations of the 4D ultrasound measurements of average and local diameter, diameter change, circumferential strain in the xy -plane according to equations eq. 4-14 to eq. 4-19 and local displacements in y - and z -direction with the corresponding results of the optical reference measurement as obtained from the evaluation of all load cases pooled.

Table 4-3 Absolute deviations of the results of the 4D ultrasound measurements with respect to optical reference measurements. Results are given as median [IQR].

	Average	Local
Deviation of diameter in xy -plane and derived quantities		
Deviation of diameter in mm	-0.52 [0.79]	-0.55 [0.96]
Deviation of diameter change in mm	-0.01 [0.16]	0.00 [0.22]
Deviation of circumferential strain in %	-0.01 [0.98]	0.04 [1.21]
Deviation of displacements		
Deviation of u_y in xy -plane in mm		-0.04 [0.21]
Deviation of u_z in xz -plane in mm		0.01 [0.18]

Average and local diameter change, strain and local displacement measurement in y - and z -direction did not show any systematic error compared to optical reference measurements. In contrast to all other geometrical parameters that were assessed in this study, the measurements of the average and the local diameter values exhibited a systematic deviation: Compared to the optical reference measurement, ultrasound systematically underestimated the diameter of the specimen by more than 0.5 mm. Figure 4-13 illustrates the differences in the systematic and random error of the measurements of diameter and diameter change. Average and local diameter measurements showed the by far largest random errors of $IQR = 0.79$ mm and $IQR = 0.96$ mm, respectively, corresponding to the 95% confidence intervals

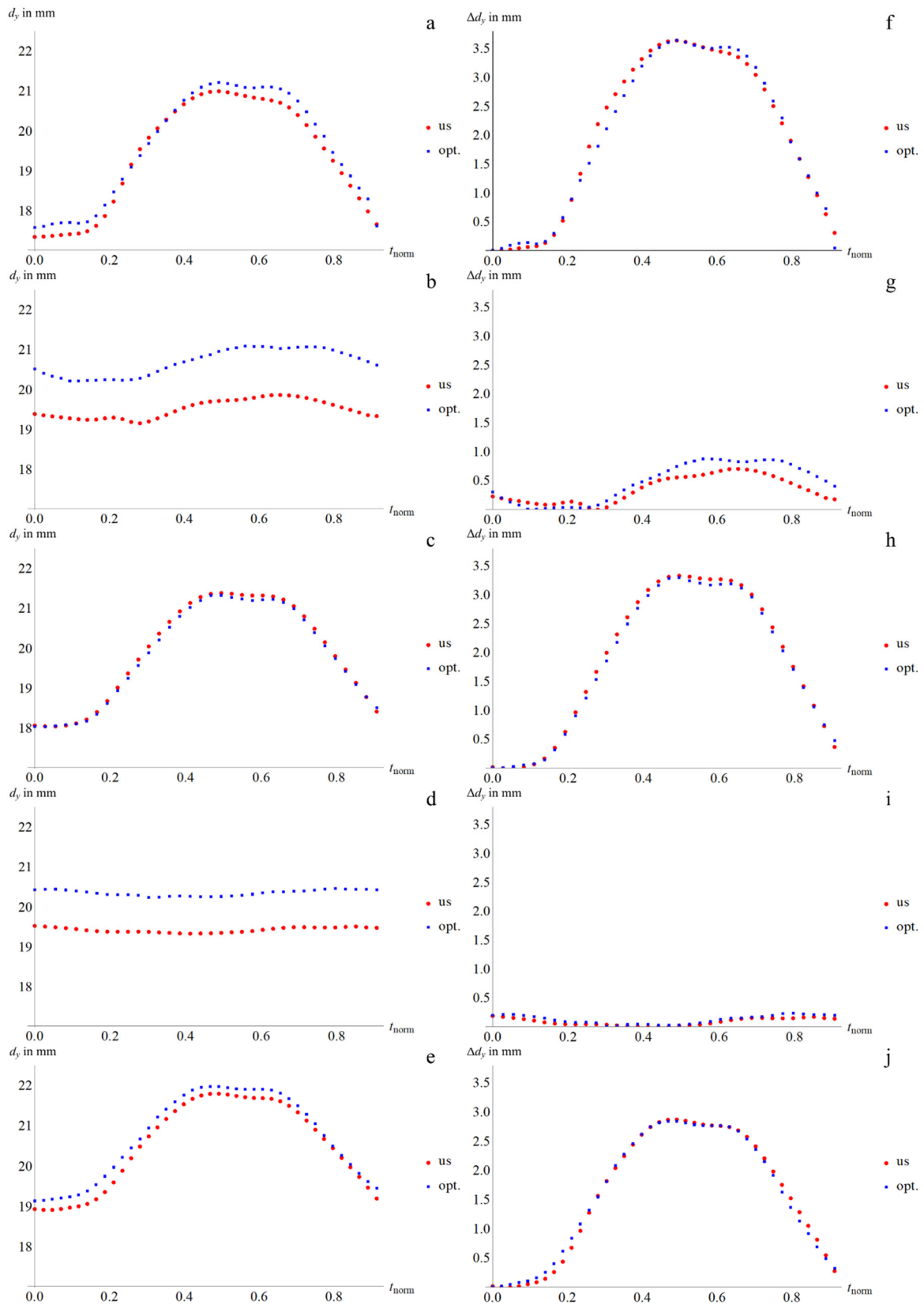


Figure 4-13 Spatially averaged diameter (left column: a, b, c, d, e) and diameter change (right column: f, g, h, i, j) over one load cycle that were observed for the five different load cases: C01 (a, f), C02 (b, g), C04 (c, h), C07 (d, i) and C08 (e, j). For each load case, the results of the optical reference measurement and the results of the 1st evaluation of the 1st ultrasound measurement, not the means of repeated measurements and evaluations, are shown, exemplarily.

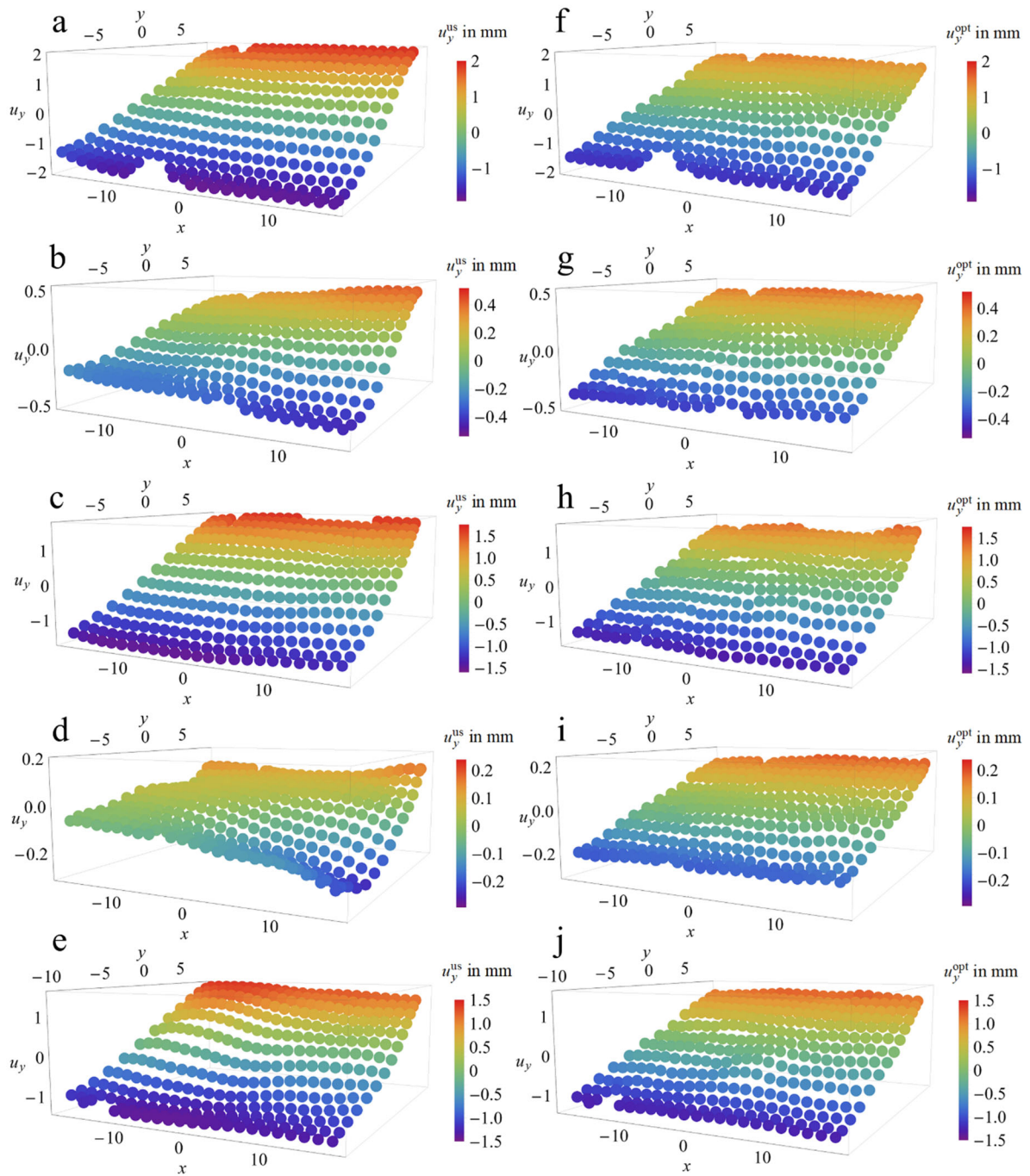


Figure 4-14 Illustrative comparison of the results of local displacement measurement in the xy -plane as obtained by 4D ultrasound (left column: a, b, c, d, e) and optically (right column: f, g, h, i). Exemplarily, the results of single ultrasound measurements and evaluations, not the means of repeated measurements and evaluations, are shown for the five load cases: C01 (a, f), C02 (b, g), C04 (c, h), C07 (d, i) and C08 (e, j). Therefore, this comparison illustrates the random error of a single measurement and evaluation, which is large compared to the negligible systematic error of repeated measurements and evaluations [cf. Table 4-3].

$[Q_{0.025}, Q_{0.975}] = [-1.58 \text{ mm}, 0.70 \text{ mm}]$ for average values and $[-1.78 \text{ mm}, 0.79 \text{ mm}]$ for local values. In contrast to this, a smaller random error of $\text{IQR} = 0.16 \text{ mm}$ or a 95% confidence interval of $[-0.32 \text{ mm}, 0.27 \text{ mm}]$ was found for average diameter change.

Compared to measures of average deformation along the length axis of the sample, local deformation measures exhibited slightly larger random error values, characterized by similar $\text{IQR} \approx 0.2 \text{ mm}$ and 95% confidence intervals of $[-0.41 \text{ mm}, 0.31 \text{ mm}]$ for diameter change in the xy -plane, $[-0.47 \text{ mm}, 0.49 \text{ mm}]$ for local displacements in the xy -plane and $[-0.32 \text{ mm}, 0.52 \text{ mm}]$ for local displacements in the xz -plane. Figure 4-14 gives a comparison of single 4D ultrasound full-field displacement measurements (not the mean of repeated measurements and evaluations) with the optical reference measurements for each of the five different load cases. Therefore, it illustrates the larger random error of a single 4D ultrasound measurement and evaluation, not the negligible systematic error of repeated measurements and evaluations. Though this is an exemplary representation of the validation results, only, it is worth noting that the displacement fields [see Figure 4-14 d, i] resulting from the load case with the smallest pulse pressure of 7 mmHg, only [cf. Table 4-1, C07], show the most considerable qualitative deviations.

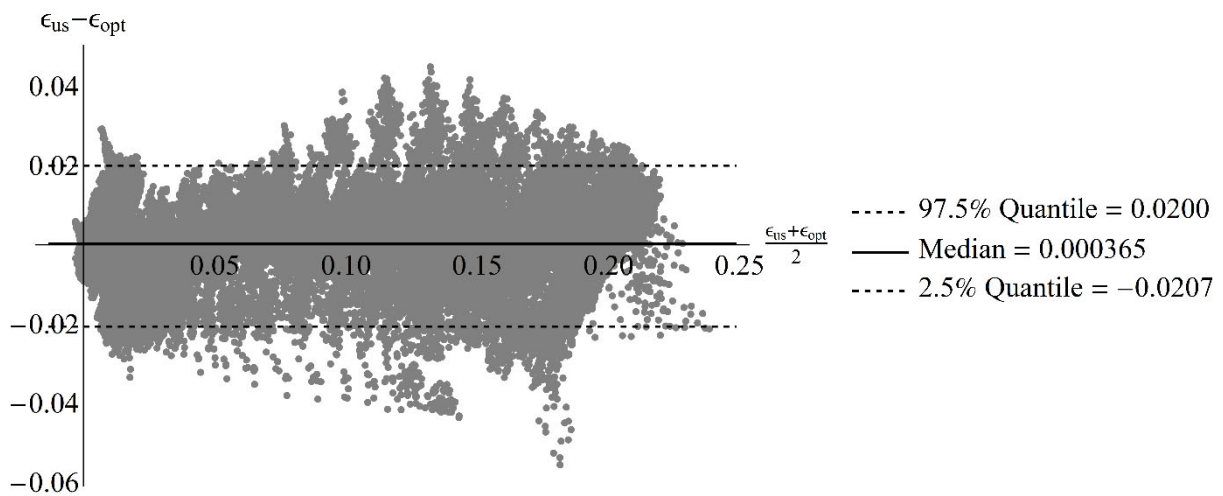


Figure 4-15 Bland-Altman plot showing the agreement of 4D ultrasound local strain measurements with optical reference measurements. The horizontal axis gives the mean and the vertical axis shows the deviation of 4D ultrasound and optical measurement. The horizontal solid and dashed lines mark the median and the borders of the 95% confidence interval of the distribution of local deviations, respectively. Dimensionless strain values are not given in %, here.

For circumferential strain, a random error of $\text{IQR} \approx 1\%$ was observed for spatially averaged and local values, the random error of local strain measurement ($\text{IQR} = 1.21\%$, $[Q_{0.025}, Q_{0.975}] = [-2.1\%, 2.0\%]$) being slightly larger than the random error of averaged strain ($\text{IQR} = 0.98\%$, $[Q_{0.025}, Q_{0.975}] = [-1.6\%, 1.6\%]$). The Bland-Altman plot of the agreement of local strain measurements by 4D ultrasound with the optical reference measurement is given in Figure 4-15. It shows that there is no clear dependency of the size and direction of the random error on the size

of measured strain. The absence of a relevant systematic error is shown in this diagram by the fact that the solid median line of the deviation distribution is almost identical with the zero line.

Table 4-4 Absolute error of averaged and local diameter, diameter change and circumferential strain for the five examined load cases.

	C01	C02	C04	C07	C08
Absolute error of average values for					
Diameter in mm	-0.31 [0.30]	-0.78 [0.35]	0.04 [0.50]	-1.17 [0.42]	-0.50 [0.71]
Diameter change in mm	-0.03 [0.12]	-0.13 [0.25]	0.04 [0.08]	0.13 [0.21]	0.00 [0.12]
Circumferential strain in %	-0.1 [0.8]	-0.6 [1.2]	0.2 [0.6]	0.7 [1.1]	0.1 [1.1]
Absolute error of local values for					
Diameter in mm	-0.28 [0.70]	-0.76 [0.57]	0.11[0.59]	-1.17 [0.57]	-0.44 [0.99]
Diameter change in mm	0.00 [0.21]	-0.13 [0.21]	0.04 [0.15]	0.10 [0.22]	0.00 [0.21]
Circumferential strain in %	0.1 [1.2]	-0.6 [1.0]	0.2 [0.9]	0.6 [1.1]	0.1 [1.4]

Table 4-4 reports the results for the agreement of ultrasound and optical diameter, diameter change and circumferential strain for each of the five load cases, separately. It is noteworthy that the two load cases with the smallest deformation (C02: $\Delta\bar{d} = 0.87$ mm, C07: $\Delta\bar{d} = 0.23$ mm, [cf. Table 4-1]) exhibited the largest absolute values of systematic deviation and values of absolute random error that were of the same size as the ones that were observed for load cases with larger deformations (C01: $\Delta\bar{d} = 3.60$ mm, C04: $\Delta\bar{d} = 3.23$ mm, C08: $\Delta\bar{d} = 2.82$ mm, [cf. Table 4-1]). This combination of large absolute error values and small deformation measures resulted in large relative systematic and random error values of up to 63.4% and 100%, respectively, for the small deformation load cases [Table 4-5]. In contrast, for large deformation load cases the observed sizes of systematic relative error of average and local diameter, diameter change and strain were between -3.8% and 0.2%, -0.9% and 1.3% and -0.4% and 1.1%, respectively. Corresponding values of random relative deviations were between 1.7% and 9.2%, the relative random error of local values being slightly larger than the relative random error of averaged values [Table 4-5].

Table 4-5 Relative error of averaged and local diameter, diameter change and circumferential strain for the five examined load cases.

	C01	C02	C04	C07	C08
Relative error of average values in % for					
Diameter	-1.7 [1.7]	-3.9 [1.7]	0.2 [2.8]	-5.7 [2.1]	-2.6 [3.8]
Diameter change	-0.9 [3.5]	-15.1 [28.6]	1.2 [2.5]	56.7 [93.2]	-0.03 [4.3]
Circumferential strain	-0.4 [4.0]	-14.3 [27.8]	0.9 [3.6]	63.4 [102.3]	0.8 [7.4]
Relative error of local values in % for					
Diameter	-1.6 [4.0]	-3.8 [2.8]	-0.6 [3.3]	-5.8 [2.8]	-2.3 [5.2]
Diameter change	-0.1 [5.9]	-15.1 [24.1]	1.3 [4.8]	43.1 [94.8]	0.0 [7.5]
Circumferential strain	0.4 [5.7]	-13.5 [23.4]	1.1 [4.9]	50.4 [103.8]	0.3 [9.2]

Table 4-6 Results of the repeated measurements and post-processing of five different load cases and the analysis of variances. H test refers to the KRUSKAL-WALLIS test.

	Diameter in mm		Diameter change in mm		Circumferential strain in %	
	average	local	average	local	average	local
C01	17.75 [0.22]	17.86 [0.22]	3.47 [0.27]	3.63 [0.10]	20.1 [1.7]	20.9 [0.9]
C02	17.44 [0.29]	17.56 [0.34]	0.68 [0.05]	0.75 [0.03]	3.4 [0.3]	3.8 [0.2]
C04	18.35 [0.30]	18.56 [0.50]	3.23 [0.13]	3.29 [0.03]	18.0 [1.2]	18.1 [0.7]
C07	16.84 [0.38]	17.05 [0.50]	0.42 [0.26]	0.50 [0.26]	2.2 [1.3]	2.6 [1.3]
C08	19.05 [0.57]	19.08 [0.76]	2.84 [0.10]	2.94 [0.09]	15.3 [1.0]	15.8 [1.2]
IQR	0.32	0.41	0.12	0.05	1.0	0.6
H test, <i>p</i>	< 0.001	< 0.001	< 0.001	< 0.001	< 0.001	< 0.001
ICC(1,1)	0.92	0.90	0.96	0.97	0.96	0.97

4.3.2 Reproducibility of 4D ultrasound measurements

4.3.2.1 Dependency on the sequence of performed test and evaluations

The successive order of the repeated measurement and evaluation ($k = 20$) of the examined load cases did not show any significant effect on the median (ANDERSON-DARLING K-Sample test, $p \geq 0.99$) or the variance (LEVENE test, $p \geq 0.98$) of the average and local results of diameter, diameter change and strain measurement. This result justified the assumption of a one-way random effects model for the analysis of variances and the choice of the ICC(1,1) for the rating of the repeatability [cf. 4.2.4].

4.3.2.2 Test-retest reliability and intraclass correlation coefficient

An overview of the results for repeated measurements and evaluations of the five different load cases [cf. 4.2.1] is given in Table 4-6. Repeated determination of average and local diameter showed a clearly larger IQR of 0.32 mm and 0.41 mm, respectively, compared to the variation of the repeated determination of average and local diameter change, which was characterized by an IQR of 0.12 mm and 0.05 mm, respectively. Figure 4-16 illustrates the differences in the repeatability of the measurement and evaluation of average diameter and diameter change, exemplarily. For repeated measurements of average and local strain, IQR values of 1.0% and of 0.6% were determined, respectively. These latter values are in the range of the random deviation of 4D ultrasound measurements from optical reference measurements [cf. Table 4-3]

The KRUSKAL-WALLIS test for non-parametric distributions proofed that the median values of the results of repeated tests were significantly different ($p < 0.001$) between the examined load cases for all deformation parameters. As well, for all examined deformation parameters ICC(1,1) values ≥ 0.90 were observed indicating excellent test-retest reliability of the 4D ultrasound displacement and strain measurement (including post-processing). The capacity of 4D ultrasound to characteristically distinguish the five load cases that were examined in this study is illustrated in Figure 4-17, Figure 4-18 and Figure 4-19 with regard to local diameter, diameter change and strain.

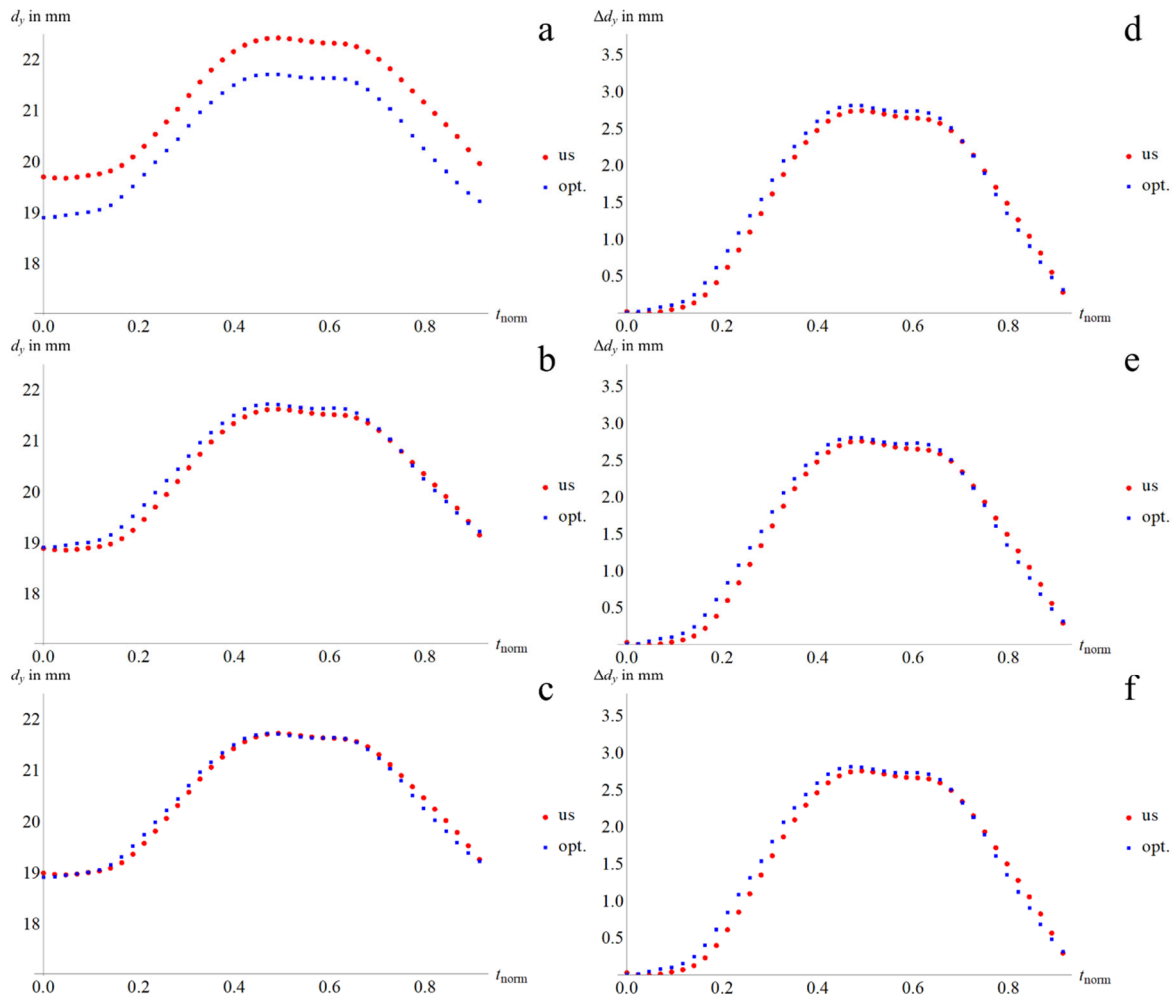


Figure 4-16 Exemplary illustration of the reproducibility of the measurement (including post-processing) of diameter and diameter change by 4D ultrasound. The left column (a, b, c) shows three repeated ultrasound measurements (red dots) of average diameter over time, each time compared to the identical optical reference measurement (blue dots) of the same experiment. The right column (d, e, f) shows three repeated ultrasound measurements (red dots) of average diameter change over time, each time compared to the identical optical reference measurement (blue dots) of the same experiment.

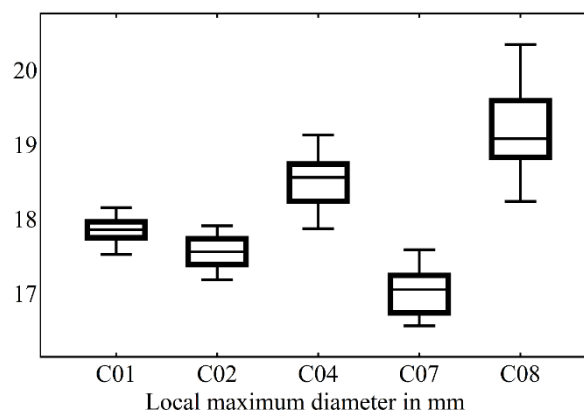


Figure 4-17 Results for the test-retest reliability of the measurement of the maximum value of local diameters along the sample that were observed throughout one load cycle. The distributions of 20 repeated evaluations of the 4D ultrasound measurement of five different loading conditions (C01, C02, C04, C07, C08, cf. Table 4-1) are compared. Boxes show the median and range of Q_1 to Q_3 , whiskers extend to minimum and maximum values, respectively (outliers are indicated by filled circles). KRUSKAL-WALLIS test $p < 0.001$, ICC(1,1) = 0.90.

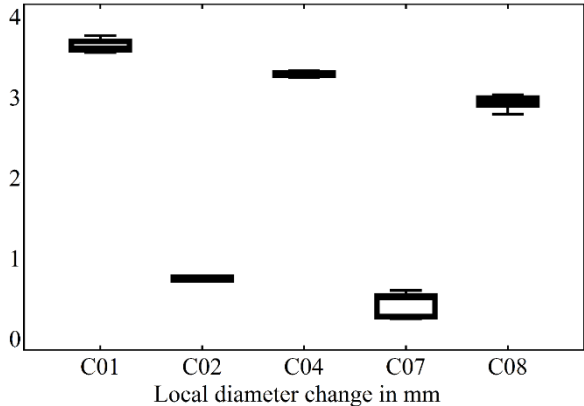


Figure 4-18 Results for the test-retest reliability of the measurement of the maximum value of local diameter change along the sample that was observed throughout one load cycle. The distributions of 20 repeated evaluations of the 4D ultrasound measurement of five different loading conditions (C01, C02, C04, C07, C08, cf. Table 4-1) are compared. Boxes show the median and range of Q_1 to Q_3 , whiskers extend to minimum and maximum values, respectively (outliers are indicated by filled circles). KRUSKAL-WALLIS test $p < 0.001$, ICC(1,1) = 0.97.

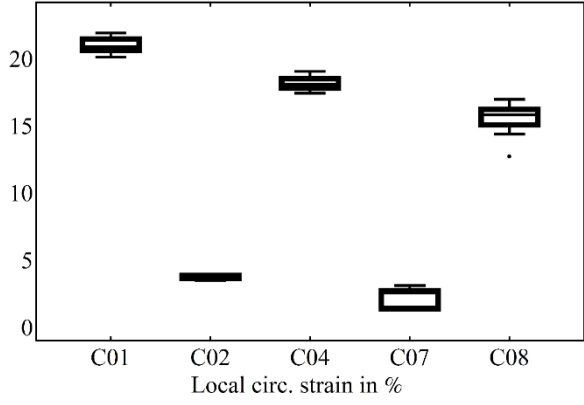


Figure 4-19 Results for the test-retest reliability of the measurement of the maximum value of local circumferential strain along the sample that was observed throughout one load cycle. The distributions of 20 repeated evaluations of the 4D ultrasound measurement of five different loading conditions (C01, C02, C04, C07, C08, cf. Table 4-1) are compared. Boxes show the median and range of Q_1 to Q_3 , whiskers extend to minimum and maximum values, respectively (outliers are indicated by filled circles). KRUSKAL-WALLIS test $p < 0.001$, ICC(1,1) = 0.97.

4.4 Discussion of the validation results

In this study the uncertainty and the test-retest reliability of 4D ultrasound were assessed. The uncertainty was determined by comparison to optical reference measurements, which, however, were subject to uncertainty themselves. The uncertainty of the optical measurements was mainly determined by the pixel size of 0.1 mm [cf. 4.2.2.5]. Their random error was minimized by determining the reference values as the means of three subsequent measurements. It is worth noting and an indication of the robustness of the results of this study that the agreement of 4D ultrasound measurements with optical measurements were of the same size for diameter change and local displacement (systematic error: median ≈ 0.0 mm, random error: IQR ≈ 0.2 mm): diameter change and local displacement were derived independently and based on different principles from primary optical image data.

In this study, for the measurement of the diameter, i.e. a relevant dimension of the specimen geometry, a systematic underestimation of about 0.5 mm to 0.6 mm and a 95% confidence interval of about 2.5 mm that characterized the random error were observed. In contrast, deformation measures such as diameter change, circumferential strain and displacement did not show any systematic error. Moreover, considerably smaller absolute random error was observed for these relative measurements of geometry change: 95% confidence intervals between 0.6 mm and 1.0 mm (corresponding to $1.96 \text{ sd} = \pm 0.3 \text{ mm} \dots \pm 0.5 \text{ mm}$ in case of normally distributed data) were determined for diameter change and displacement. A possible explanation for this difference in the accuracy of the measurement of geometrical dimensions and of deformation or displacement could be the fact that the geometry or shape of the measured structure was defined by manual segmentation of the wall in the A- and B-plane of the already post-processed and visualized data [cf. chapter 3.2], i.e. that shape measurement is strongly observer dependent. Manual segmentation was performed on a computer screen. DICOM image data on which the manual segmentation of the shape was performed typically exhibited a voxel size between 0.4 and 0.6 mm and were represented on the screen as images with a size of about $70 \times 70 \text{ mm}^2$, i.e. in a reduced scale. That means that a deviation of 0.5 mm to 1.0 mm from the true shape could not be controlled or avoided in the process of manual segmentation. In contrast, the measurement of deformation or displacement was performed automatically by the speckle tracking algorithm that was implemented in the Toshiba post-processing software (ACP). Starting from the manually segmented region, cubic template volumes of approximately $10 \times 10 \times 10 \text{ mm}^3$ were defined automatically by the software. Displacement of the center points of these template volumes in subsequent time steps was estimated by means of pattern recognition on the template volumes. Consequently, the uncertainty of the spatial location of these template volumes due to variation of manual segmentation and the observed systematic error of shape measurement were in the range of the voxel size of the DICOM data, i.e. $\approx 0.5 \dots 1.0$ mm. This means that the template volume with at size of 1000 mm^3 and the spatial pattern

which was the basis of motion estimation by the speckle tracking algorithm were substantially unchanged by and, consequently, estimated displacements were widely independent of variations due to the uncertainty of the manual segmentation, if segmentation was performed carefully. Another aspect worth recognizing in this context is, that speckle tracking using the ACP was not performed by digital image correlation on already post-processed DICOM data, but by means of cross-correlation on the original radio frequency data, which should contribute to a high accuracy and reliability of displacement measurements [Chen et al. 2005]. Still, because of the size of the measured structure, i.e. the specimen diameter of about 20 mm, which was comparable to the healthy human aorta, the systematic and random relative error of diameter measurement was small. Systematic relative error was between -5.8% and 0.2% and random relative error ranged from 1.7% to 5.2% [cf. Table 4-5].

It is noteworthy that the observed uncertainty of 4D ultrasound displacement measurement in y - and in z -direction were of the same size (systematic error: median ≈ 0.0 mm, random error: IQR ≈ 0.2 mm), because the accuracy of the 4D ultrasound measurement depended on completely different measurement principles in each direction: the y -direction corresponded to the propagation direction of the RF signal, i.e. the accuracy depended on the characteristics of this signal, wavelength and corresponding frequency, type of wave packet and beamforming. In contrast, the measurement accuracy in z -direction, i.e. orthogonal to the propagation direction, depended on the design and sequential control of the matrix array of the ultrasound probe. The fact, that equal systematic and relative uncertainty was observed in propagation direction and orthogonal to the propagation direction may allow the hypothesis that the uncertainty of highly resolved 4D ultrasound displacement measurements is direction independent. However, the uncertainty of displacement measurement in x -direction, which is orthogonal to the propagation direction as well, could not be assessed in this study.

The chosen load cases resulted in two distinct groups of experiments: three experiments (C01, C04, C08) showed diameter changes > 2 mm corresponding to displacements > 1 mm (“large deformations”), whereas the two other load cases (C02, C07) resulted in diameter changes < 1.0 mm corresponding to displacements < 0.5 mm (“small deformations”). Large deformation load cases showed negligible systematic error of diameter change and absolute random error values of IQR = 0.08...0.21 mm resulting in relative random error of IQR = 2.5...7.5%. In contrast, systematic deviation of diameter change measurement between -0.13 mm and +0.13 mm and larger absolute random error of IQR = 0.21...0.25 mm were observed for the small deformation load cases. These results indicate that the absolute error of the speckle tracking algorithm implemented in the ACP is independent of the size of the deformation or even requires a minimum deformation to work properly. In combination with the smaller size of the measured value, the larger absolute error values for the small deformation load cases resulted in large systematic relative errors between -15.1% and +56.7% and even larger relative random errors up to IQR = 94.8% [cf. Table 4-4 and Table 4-5].

In order to rate the implications of these results on the uncertainty of in vivo measurements, the results of the clinical study presented in chapter 3.5 should be considered. Surprisingly, 3D displacements of material points on aortic wall showed a size of ≈ 1 mm independent of age (< 60 y. o., > 60 y. o) and cardiovascular health state (healthy, atherosclerosis, AAA) and degree of arterial stiffening, which is known to be related to ageing [cf. chapter 1.7] and could be demonstrated in comparative clinical studies with similar patient groups [Derwich et al. 2016; Wittek et al. 2017a; Wittek et al. 2018; Disseldorp et al. 2019 and chapters 6 and 7]. That means, as to displacement, which is the primary measure of 4D ultrasound, almost all in vivo measurements belong to the large deformation group with negligible systematic error and small absolute and relative random error. If however strain as a derived deformation measure is observed, representative values are $< 5\%$ in case of aged atherosclerotic and AAA patients in vivo. In the current validation study, strain values of this size were observed in the small deformation cases, only [cf. Figure 4-19], and were accompanied by very large relative errors. However, in the current study, small strains necessarily were the result of small displacements, because the available experimental set up did not allow for any rigid body motion of the specimen. Moreover, displacements in the validation experiments always were displacements in radial direction. Therefore, the question remains unanswered how large are the systematic and random errors of measurements of small strains that result from large 3D displacements.

The assessment of the test-retest reliability of a single measurement showed that 4D ultrasound was able to reliably distinguish between the examined load cases and deformations, even in cases where the range of the imaged deformations was very similar. Nevertheless, the results of the current study indicate, how the error of displacement and strain measurement of a single aorta or patient, can be reduced significantly: The 95% confidence interval of repeated measurements resulted in non-negligible absolute and relative deviations from the reference measurements. These deviations were of approximately the same size for local and average values. This indicates that the random error of the distribution of repeated measurements represents the possible size of the systematic error of a single measurement. In contrast, the deviation of the median of repeated ultrasound measurements that represents the systematic error of the measurement method was of negligible size for all examined deformation metrics. Therefore, displacement and strain measurements of single aortic or aneurysmal wall that are intended for diagnostic use should be obtained as means of repeated examinations and evaluations of the same aortic segment.

The in vivo 4D ultrasound data that were collected and evaluated in the clinical studies presented in this work were obtained from single measurements and evaluations of individual aortic segments, only, not as means of repeated measurements and evaluations. However, in the studies presented in chapters 5 and 6 of this thesis, no single measurements of aortic walls were compared and tested for statistically significant differences, but only mean or median values of patient groups with sizes between 10 and 20 subjects. The results of the current validation study mean that the random error of a single measurement has no relevant effect on the mean or median of a distribution of between 10 and 20 measurements. In

chapter 7, single data sets were used as basis for the parameter identification of an anisotropic hyperelastic constitutive equation. There, the effect of the observed random – or, in a single measurement, possibly systematic – error on the results of the parameter identification was examined in a numerical verification experiment [cf. chapters 7.8 and 7.9].

4.4.1 Comparison of the validation results with literature values

3D and 4D ultrasound measurement of cardiovascular geometry and deformation has been validated previously in vivo and in vitro by comparison to measurements obtained by other imaging techniques. Park et al. [2011] have validated three-dimensional transthoracic ultrasound in an in vivo study by quantifying the agreement of measurements of the aortic-root geometry with cardiac multi-detector computed tomography (MDCT). I.e. the study aimed at the measurement of the geometrical dimensions of a structure. This approach is comparable to the measurement of the average reference diameter in the current study. Moreover, relevant dimensions of both examined structures, aortic root and porcine abdominal aorta, are of comparable size. For ultrasound data acquisition from the parasternal long-axis view, a Philips iE33 ultrasound device was used combined with a X3-1 matrix-array transducer. Post-processing was performed offline with the QLAB Advanced Ultrasound Quantification Software Release 8.1 (both, device and software, by Philips Medical Systems, Andover, MA, USA). In measurements of the end-diastolic volume in 12 patients (mean \pm sd = 14.1 \pm 5.7 mL) they found a mean difference between 3D ultrasound and MDCT of 0.5 mL or 3.5%, only, indicating small systematic deviation, which matches well with the relative error of average and local diameter measurement that was observed in the current study [cf. Table 4-5]. In contrast, the 95% confidence interval of the deviation of the 3D US measurement was 6.7 mL, which means a possible relative deviation of up to 50%. This by far exceeds the relative random error of diameter measurement (95% confidence interval \leq 14%) that was observed in the current study.

Soliman et al. [2008] have assessed the accuracy of the in vivo 4D ultrasound measurement of parameters that are characteristic for the function of the human LV by comparison to cardiac magnetic resonances tomography (MRI) measurements. The in vivo study included 17 patients (10 of them with impaired LV systolic function due to ischemia, i.e. with regionally reduced wall motion) and 7 healthy volunteers. Agreement of both imaging techniques was assessed by Bland-Altman analysis [Altman and Bland 1983; Bland and Altman 1986]. The 95% confidence interval of the relative deviation of 4D-US measurements was $-3.3 \pm 9.2\%$ for the end-diastolic LV volume, $-3.4 \pm 6.8\%$ for the end systolic LV volume and $0.2 \pm 6.2\%$ for the LV ejection fraction. These results are well in agreement with the observations of the current study. This applies in particular to the fact that geometrical dimensions (LV volume) were systematically underestimated and showed larger random error, whereas no systematic error and slightly smaller random error was observed for deformation measures (LV ejection fraction).

Using a MyLab 70 US system (Esaote, Maastricht, The Netherlands), Kok et al. [2015] have compared the results of CT based and 3D ultrasound based geometry registration of AAA in vivo and report similarity indices between 0.74 and 0.91 and Hausdorff distances (median [IQR]) ranging from 4.8 mm [3.1 mm] to 13.9 mm [9.9 mm]) in twelve patients. These metrics for the assessment of agreement are not comparable directly to the ones that were used in the current study.

Seo and coworkers [2009] have performed in vivo measurements of the LV of 10 ovine hearts. In addition to baseline measurements of the healthy LV, pharmacological stress tests were performed that affected LV function and deformation. Moreover, local ischemia and, consequently, local reduction of apical wall motion was induced by occluding the distal left anterior descending (LAD) coronary artery. Regionally varying longitudinal (LS), circumferential (CS) and radial strain (RS) were measured by 4D ultrasound speckle tracking using an Artida ultrasound system (Toshiba Medical Systems Co, Tochigi, Japan) and by sonomicrometry. In particular, areas with artificially reduced wall motion could be identified clearly. Both, 4D ultrasound speckle tracking and sonomicrometry-derived measurements of local LS, CS and RS in the apical region were reduced significantly as result of the occlusion of the LAD coronary artery. This gives evidence of the capability of 4D ultrasound speckle tracking to capture locally varying and heterogeneous strain distributions. Agreement between 4D ultrasound and sonomicrometry strain measurement was evaluated by Bland-Altman Plots comparing measurements under all conditions sampled. From these plots the following approximate means \pm 1.96 sd of the absolute deviation between both measurement types could be read off: LS: $1 \pm 11\%$, CS: $-3 \pm 13\%$, RS: $3 \pm 14\%$. Compared to the results of the current study (median [95% CI] = 0.0 % [-2.1%, 2.0%]), these by far larger systematic and random error values may be attributed to the measurement under in vivo conditions, which are less controlled compared to the in vitro experiments that were performed in the current study.

In 2013 our clinical cooperation partner, the Department of Vascular and Endovascular Surgery of the Goethe University Hospital has performed a first validation study of the deformation measurement of tubular structures using the Toshiba Artida 4D ultrasound system including speckle tracking by the ACP (Toshiba Medical Systems Co, Tochigi, Japan). Bihari et al. [2013] have measured the diameter and diameter change of silicon tubes under cyclic pressurization in vitro by laser micrometer and by 4D ultrasound. Diameter measurements were taken in propagation direction of the ultrasound signal [cf. Bihari et al. 2013, Figure 3]. In order to investigate the capability of 4D ultrasound speckle tracking to properly resolve local differences, diameter measurements were taken and compared at different positions along the longitudinal axis of an aneurysm shaped silicone phantom. Laser micrometer diameter values were obtained as the average of 4 pump cycles; each measurement was repeated five times. In contrast to the current study, Bihari and coworkers found systematic and random measurement deviations of similar size for diameter (mean \pm sd = 0.45 ± 0.33 mm) and diameter change (0.48 ± 0.34 mm). Larger deviations were observed for maximum cyclic pressure (0.55 ± 0.38 mm) in case of diameter measurements and in the middle section of the belly shaped aneurysm phantom (0.76 ± 0.2 mm) in case

of diameter change measurement, i.e. in the region where the phantom had its maximum diameter. In contrast to the current study, diameter was consistently overestimated by 4D ultrasound in all cases. In addition to diameter and its change, 3D displacement of a pattern of 2×4 points on the surface of the phantom wall was assessed by comparison to video photogrammetry. Measurement was repeated three times. Maximum differences between 4D ultrasound and video analysis were 0.24 mm, 0.54 mm and 0.76 mm in x -, y - and z -directions, respectively. I.e. in contrast to the current study, considerable differences between uncertainty in and orthogonal to the propagation direction y of the RF signal were observed. However, Bihari et al. [2013] did use silicone phantoms in a medium of distilled water at room temperature instead of aortic soft tissue in a physiological saline solution at 37°C . This might have impaired the measurement results because of the different speed of sound of phantom ($c_{\text{silicone}} \approx 1000 \text{ m/s}$) and medium ($c \approx 1483 \text{ m/s}$) compared to human abdominal soft tissue ($c_{\text{soft tissue}} \approx 1540 \text{ m/s}$) for which the 4D ultrasound system is optimized. Lower speed of sound in phantom and medium might have resulted in a larger time of flight of the RF signal, which, however, was converted into distance by the Toshiba software based on the assumption of $c_{\text{soft tissue}}$. This could explain why Bihari et al. [2013], in contrast to the current study, have observed an overestimation of the specimen diameter by 4D ultrasound measurement compared to laser micrometer measurement and why they found deviations of different sizes in and orthogonal to the propagation direction of the RF signal, since the deviation in the speed of sound affects measurement results in propagation direction in a different way than those in orthogonal direction.

In addition, some previous studies have assessed the reproducibility of 4D ultrasound measurements. Soliman et al. [2008] report values for the interobserver and the intraobserver variability of end-diastolic and end-systolic LV volume and of LV ejection fraction ranging from 5.1% to 7.6%. According to Bland and Altman [1986], inter- and intraobserver variability were computed as the absolute difference between 2 measurements divided by the average of the two measurements. These values can be understood as the percentage of the measurement results that can be explained by the uncertainty of repeated measurements. In contrast, the intraclass correlation coefficient that was applied in the current study can be understood as the proportion of the variability of the measurements that is explained by the variation between the examined subjects. Thus, inter- and intraobserver variability as used by Soliman et al. may roughly be related to the ICC as follows:

$$\text{intraobserver variability} \approx 1 - \text{ICC.} \quad \text{eq. 4-46}$$

Taken this, the results reported by Soliman et al. correspond to ICC values ranging from 0.949 to 0.924 which is in agreement with the results of the current study. However, Soliman et al. do neither report how many different observers performed which steps of data acquisition and post-processing, nor how often each observer performed these steps repeatedly in order to assess inter- and intraobserver variability

Seo et al. [2009] have quantified intra- and interobserver variability to be 8.9% and 9.8% for circumferential strain and 7.8% and 8.2% for longitudinal strain, respectively. Using eq. 4-46, these values correspond to ICC values of 0.911 and 0.902 for circumferential strain and to 0.922 and 0.918 for longitudinal strain.

In a recent study, our clinical cooperation partner, the Department of Vascular and Endovascular Surgery of the Goethe University Hospital, has investigated the reproducibility of average longitudinal and circumferential strain measurement using the methods that were developed in this thesis in an in vivo study including nine young and healthy and nine aged and atherosclerotic subjects [Derwich et al. 2016]. An intraclass correlation coefficient of 0.92 was determined for two observers with repeated examination (including all post-processing steps).

4.5 Limitations of the validation study

Limitations of this study are that no full 3D data were available as reference measurements and that the experimental set up did not allow for the assessment of measurement uncertainty in the x -direction that was orthogonal to the propagation direction of the RF signal and corresponded to the longitudinal direction of the examined specimen. Despite this, the experimental set up did allow the assessment of the measurement uncertainty in and orthogonal to the propagation direction (y - and z -direction, respectively). Comparably good results were obtained in both cases, indicating that the measurement uncertainty of 4D ultrasound is not direction dependent.

5 Comparative Analysis of ascending and abdominal aortic wall motion

5.1 Introduction

In the study underlying the present chapter [Wittek et al. 2016b], 4D ultrasound imaging was employed to quantify the 3D shape and cyclic deformation of the proximal ascending and the abdominal aorta in volunteers without known cardiovascular disease [Figure 5-1]. Previously, the cyclic deformation of aortic segments has been analyzed mainly in terms of diameter change and derived parameters, such as circumferential strain and relative change of the luminal cross-sectional area [cf. Martin et al. 2013 and citations therein]. Measuring the three-dimensional and dynamic cyclic deformation of the aorta in vivo is still a challenge.

Most available imaging techniques are either too slow to capture the dynamics of aortic wall motion (CT, MRI) or they do not provide 3D geometry data such as 1D and 2D ultrasound or cine phase contrast MRI or gated CT scans. It has been emphasized that any measurement of the cyclic deformation of the ascending aorta has to take into account its large rigid body motions [Morrison et al. 2009; Bell et al. 2014; Weber et al. 2014]: Imaging techniques like CT, MRI and 1D or 2D ultrasound usually provide measurements of e.g. aortic diameter with regard to an EULERIAN reference frame. The site of measurement is defined as a position (described by coordinates) in the field of view of the imaging device. In this case, different cross-sections along the aortic tree are measured at different time points of the cardiac cycle in case that the aortic segment moves cyclically in axial direction (“through plane motion”). Eventually, this might result in the measurement of chimerical deformations. This measurement error can be avoided by using a reference system that is attached to the measured object (LAGRANGIAN reference frame). Morrison et al. [2009], Weber et al. [2014] and Bell et al. [2014] have used anatomical landmarks such as aortic branches or the sinutubular junction [cf. Figure 5-1] to provide such a reference system and to assure that the measurements at different time points of the cardiac cycle are taken at the same site of the aorta.

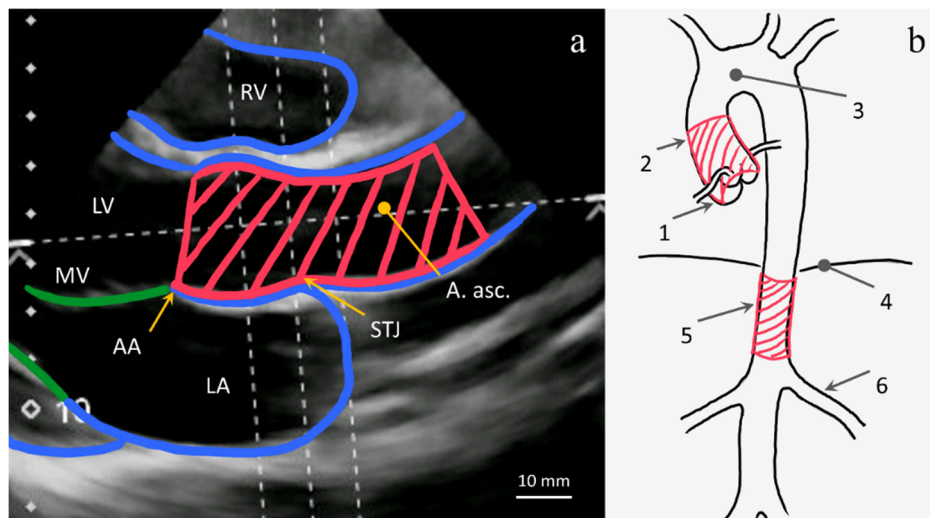


Figure 5-1 a) Imaged segment of the aortic root and proximal aorta of a 20 y.o. male volunteer in the long-axis-parasternal view. RV – right ventricle, LV – left ventricle, LA – left atrium, MV – mitral valve, AA – aortic annulus, STJ – sinotubular junction, A. asc. – proximal ascending aorta. The shown image represents a 2D cross-section of the volumetric image data. The analyzed segment of the proximal ascending aorta is highlighted in red. b) Schematic sketch of the aortic tree. Imaged segment of the proximal ascending aorta and the suprarenal abdominal aorta are highlighted in red. 1 – aortic annulus, 2 – ascending aorta, 3 – aortic arch, 4 – diaphragm, 5 – suprarenal abdominal aorta, 6 – renal arteries. [Image reprinted from Wittek et al. 2016b with permission from Springer Nature]

To the knowledge of the author, cyclic twisting deformation of the aorta has not been investigated previous to the underlying study and only few studies have addressed its cyclic longitudinal deformation. The aortic lumen can be easily distinguished from the surrounding tissue in images from various sources (MRI, CT, ultrasound) and therefore in most studies diameter and its pulsatile change has been measured. It is hard, however, to identify markers allowing for length and rotation measurements of a defined section of the aorta. Morrison et al. [2009] have used the ostia of aortic branches as markers for the determination of longitudinal strain of several segments of the aortic arch and the descending thoracic aorta. Bell et al. [2014] have used the aortic cusps and the brachiocephalic origin as anatomical markers for length measurements of the proximal aorta.

4D ultrasound is an imaging technique that has the potential to overcome these difficulties. As already explained in chapter 3.3, it provides highly resolved fields of trajectories of discrete material points of the arterial wall in a LAGRANGIAN reference frame and, thus, allows for the separation of the solid's deformation and its rigid body motion (translation and rotation). Length, diameter, volume and rotation, longitudinal and circumferential strain, relative volume change, twist and the phase shift between longitudinal and circumferential strain were determined for each aortic segment. In addition, the axial displacement and velocity of the proximal and distal end cross-section of imaged ascending aortic segments was calculated. The methods that were utilized for the determination of these kinematic parameters are described in detail in chapter 3.3.3. Ascending and abdominal aortic segments were compared with regard to these geometrical parameters. The findings obtained for these distinct aortic sites

were compared with respect to their physiological function, in particular, with regard to the mechanism of the proximal aorta's Windkessel function [cf. chapter 1.3].

Table 5-1 Patient data. Data were tested for normal distribution by means of the function 'DistributionFitTest' that is available in Wolfram Mathematica 9. Normal distribution was rejected for $p \leq 0.05$. If both of two samples that were to be compared by means of a hypothesis test were normally distributed, values were given as mean \pm sd and an unpaired 2-tailed t test (t test) was performed. Else, values were given as median $[Q_1, Q_3]$, where Q_1 and Q_3 are the 1st and 3rd quartile, respectively, and a Mann-Whitney U test (U test) was performed. [Reprinted after Wittek et al. 2016b with permission from Springer Nature]

	A. asc.	A. abd.	test	<i>p</i>
<i>n</i>	8	18		
Age in years	25.5 [20.0, 28.0]	25.5 [23.0, 29.0]	U test	0.66
Diastolic BP in mmHg	72.5 [70.0, 75.0]	75.0 [70.0, 80.0]	U test	0.53
Systolic BP in mmHg	115.0 [110.0, 120.0]	120.0 [110.0, 125.0]	U test	0.31
BMI in kg/m ²	23.5 \pm 1.9	23.3 \pm 2.4	t test	0.86
Sample length in mm	28.5 [23.5, 32.8]	26.2 [20.9, 37.9]	U test	0.68
Radius of curvature in mm	115.1 \pm 73.7	214.1 \pm 149.5	t test	0.09

5.2 Study collective and in vivo data acquisition

The study was approved by the local Ethics Committee of the University of Marburg. Eighteen young and healthy male adults were examined after giving informed consent. From each volunteer, 4D ultrasound data of the suprarenal abdominal aorta were acquired. The ascending aorta was imaged in all volunteers by transthoracic ultrasound. Due to the limited field of view in the long-axis parasternal view [cf. Figure 5-1 a], data sets could be acquired in eight volunteers, only. Clinical variables were obtained from each volunteer [Table 5-1]. Patient data were acquired and speckle tracking was performed offline as described in chapter 3.2. Voxel edge length of the image data ranged from 0.24 to 0.59 mm. Temporal resolution between 11 and 25 volumes/s resulted in 9 to 21 volumetric images of the aortic segments throughout the cardiac cycle [Table 5-2]. Ascending aortic segments ranging from the aortic annulus to the mid of the proximal aorta about 10 to 30 mm distal to the sinutubular junction [cf. Figure 5-1 a] were imaged from the long-axis-parasternal view. Segments of the suprarenal abdominal aorta were recorded by transabdominal ultrasound.

Table 5-2 4D ultrasound imaging parameters. Data were tested for normal distribution by means of the Wolfram Mathematica function ‘DistributionFitTest’. Normal distribution was rejected for $p \leq 0.05$. If both of two samples that were to be compared by means of a hypothesis test were normally distributed, values were given as mean \pm sd and an unpaired 2-tailed t test (t test) was performed. Else, values were given as median $[Q_1, Q_3]$, where Q_1 and Q_3 are the 1st and 3rd quartile, respectively, and a Mann-Whitney U test (U test) was performed. [Reprinted after Wittek et al. 2016b with permission from Springer Nature]

	A. asc.	A. abd.	test	p
Voxel size in mm/pix	0.59 [0.43, 0.59]	0.32 [0.28, 0.59]	U test	0.017
Frame rate in Hz	16.19 \pm 2.54	17.40 \pm 3.70	t test	0.411
Frames	13 [11, 14]	17 [14, 18]	U test	0.123

5.3 Statistics

Statistical analysis was performed by means of WOLFRAM Mathematica 9 (Wolfram Research, Champaign, IL, USA). Data were tested for normal distribution by means of the function ‘DistributionFitTest’. Normal distribution was rejected for $p \leq 0.05$. Since all geometrical parameters that were determined in this study were averaged values of the motion of a field of material points, values were given as mean \pm s.e.m. and, unless specified differently, an unpaired 2-tailed t test (t test) was performed if both of two samples that were to be compared by means of a hypothesis test were normally distributed. Else, values were given as median $[Q_1, Q_3]$, where Q_1 and Q_3 are the 1st and 3rd quartile, respectively, and a MANN-WHITNEY U test (U test) was performed. SPEARMAN’s rank correlation coefficient was used as nonparametric measure for the statistical dependency of two variables.

In order to adequately describe the complete range of cyclic deformation, longitudinal and circumferential strain, relative volume change and twist were determined for each data set according to chapter 3.3.3 and then mean or median values of these values are presented in the results section [Figure 5-3 to Figure 5-5, Figure 5-7, Figure 5-8]. When average time points of the occurrence of maximum values within the cardiac cycle are given in the text, the time point of occurrence was determined for each single data set and then mean \pm s.e.m. or the quartiles of the distribution of the different data sets was calculated. The values given in Figure 5-2 to Figure 5-5, Figure 5-7 and Figure 5-8 as well as mean \pm s.e.m. or median $[Q_1, Q_3]$ are the exact values, on which statistical hypothesis tests were based. In contrast, deformation curves over time that are shown in Figure 5-6, Figure 5-9 and Figure 5-10, were obtained by averaging deformation values that were measured in different volunteers *at the same point of time of the normalized cardiac cycle* with respect to the end-diastolic reference frame [cf. chapter

3.2.1]. Because the maximum deformation values occurred at slightly different stages of the cardiac cycle in different volunteers, these curves show lower maximum values than the exact values. As well, the time of the maximum/minimum values in these curves may defer from the exact value given in the text because of the different way of averaging. These figures are suited to illustrate some distinguishing features of ascending and abdominal aortic kinematics *qualitatively*, rather than giving the quantitatively exact values.

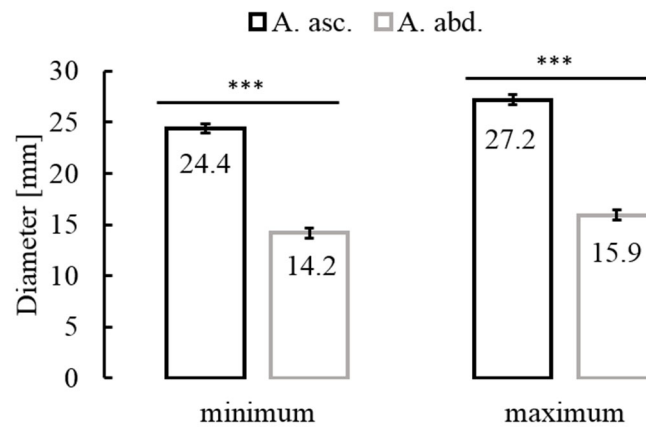


Figure 5-2 Minimum and maximum diameter of the ascending and abdominal aortic segments. *** means $p \leq 0.001$. [Reprinted from Wittek et al. 2016b with permission from Springer Nature]

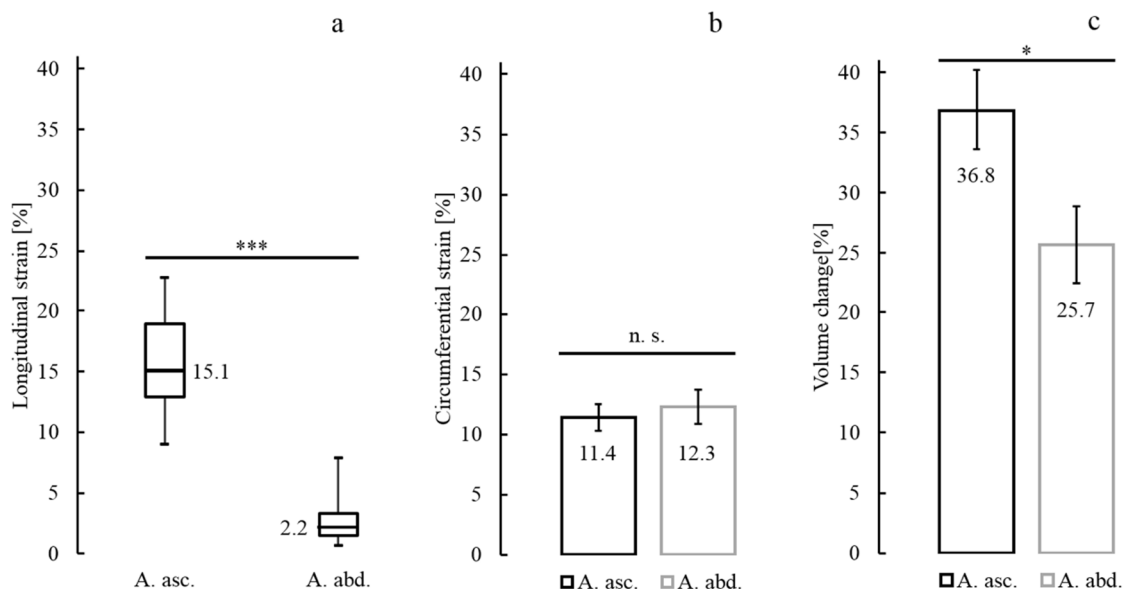


Figure 5-3 Cyclic longitudinal (a) and circumferential (b) strain and volume change (c) of the ascending and the abdominal aorta. *** means $p \leq 0.001$ and * means $p \leq 0.05$. [Reprinted from Wittek et al. 2016b with permission from Springer Nature]

5.4 Multiaxial deformation of the ascending and the abdominal aorta

Compared to the abdominal aortic segments, the systolic (maximum) and diastolic (minimum) diameters of the ascending aortic segments were on average 11.3 mm and 10.2 mm larger, respectively [Figure 5-2]. Ascending and abdominal aorta showed comparable cyclic circumferential strains. In contrast, the ascending aorta was subjected to significantly larger cyclic longitudinal strain and volume change than the abdominal aorta [Figure 5-3].

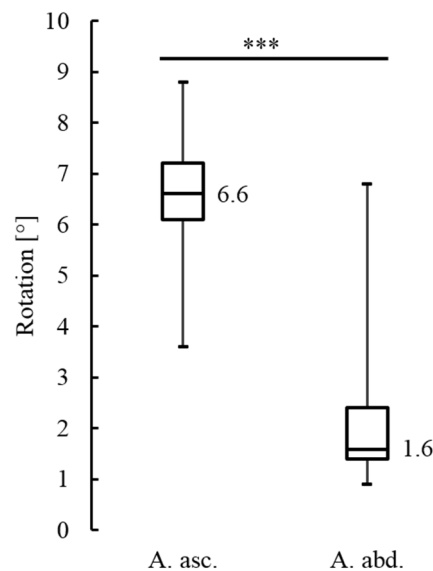


Figure 5-4 Absolute values of cyclic rotation amplitude of the ascending and the abdominal aorta. *** means $p \leq 0.001$. [Reprinted from Wittek et al. 2016b with permission from Springer Nature]

Moreover, significantly larger rotation [Figure 5-4] and twist amplitudes and counter clockwise twist were observed in the ascending aorta compared to the abdominal aorta, whereas no significant difference was found in clockwise twist [Figure 5-5]. The ascending aorta exhibited clockwise twist (ct) and counter clockwise twist (cct) of similar size during the cardiac cycle [Figure 5-5]. Maximum clockwise twist was observed in early systole at $22.1 \pm 9.0\%$ of the cardiac cycle, whereas maximum counter clockwise twist took place significantly later in end systole at $54.3 \pm 9.5\%$ of the cardiac cycle (paired t test, $p = 0.027$, illustrated qualitatively by Figure 5-6). In contrast, the examined abdominal aortae could be subdivided into two groups showing either almost only counter clockwise twist ($n = 12$, $cct = 0.99 \text{ }^\circ/\text{cm}$ [$0.59 \text{ }^\circ/\text{cm}$, $1.29 \text{ }^\circ/\text{cm}$] vs. $ct = 0.02 \text{ }^\circ/\text{cm}$ [$0.00 \text{ }^\circ/\text{cm}$, $0.20 \text{ }^\circ/\text{cm}$], WILCOXON Signed Rank test, $p = 0.005$) or clockwise twist ($n = 6$, $cct = 0.16 \pm 0.08 \text{ }^\circ/\text{cm}$, $ct = 2.03 \pm 0.73 \text{ }^\circ/\text{cm}$, paired t test, $p = 0.029$).

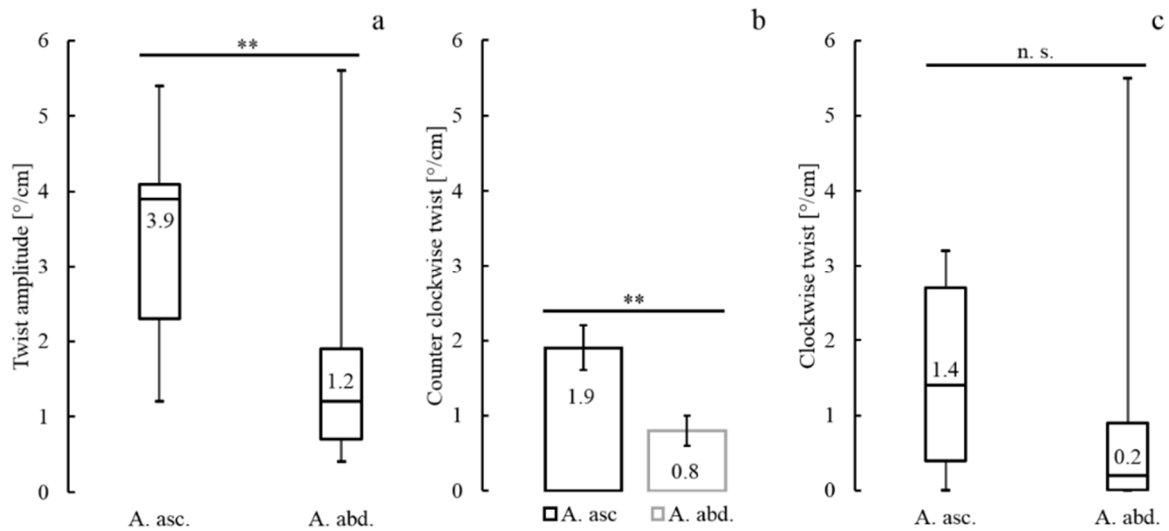


Figure 5-5 Absolute values of cyclic twist amplitude (a), counter clockwise (b) and clockwise twist (c) of the ascending and the abdominal aorta. ** means $p \leq 0.01$ and n.s. means $p > 0.05$. [Reprinted from Wittek et al. 2016b with permission from Springer Nature]

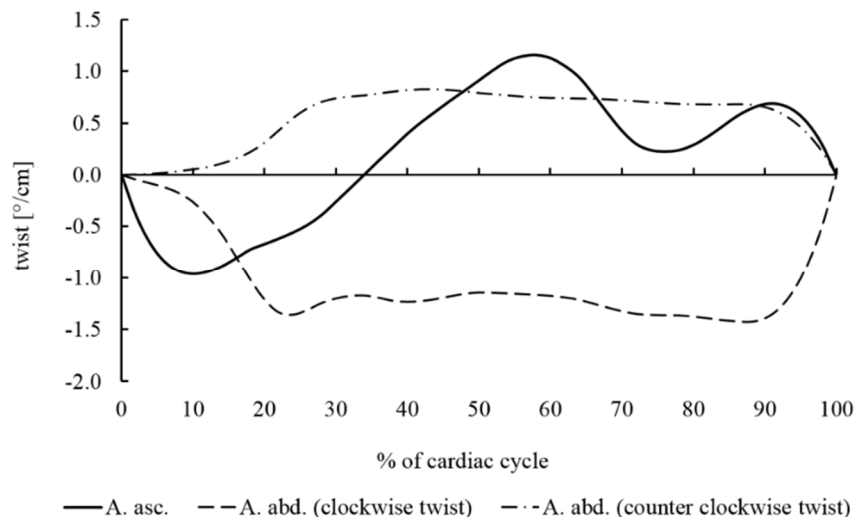


Figure 5-6 Mean curves of cyclic twist of the ascending aorta and two sub-groups of the examined abdominal aortae that show dominantly clockwise ($n = 6$) or counter clockwise ($n = 12$) twist. [Reprinted from Wittek et al. 2016b with permission from Springer Nature]

Compared to the cyclic deformation, systolic-diastolic [cf. chapter 3.3.2] longitudinal strain was significantly smaller in the ascending as well as the abdominal aorta [Figure 5-7 a, Figure 5-8 a]. In contrast, no significant difference was found in the cyclic and the systolic-diastolic volume change [Figure 5-7 b, Figure 5-8 b]. Cyclic twist amplitude was significantly larger than systolic-diastolic twist in the ascending as well as the abdominal aorta [Figure 5-7 c, Figure 5-8 c].

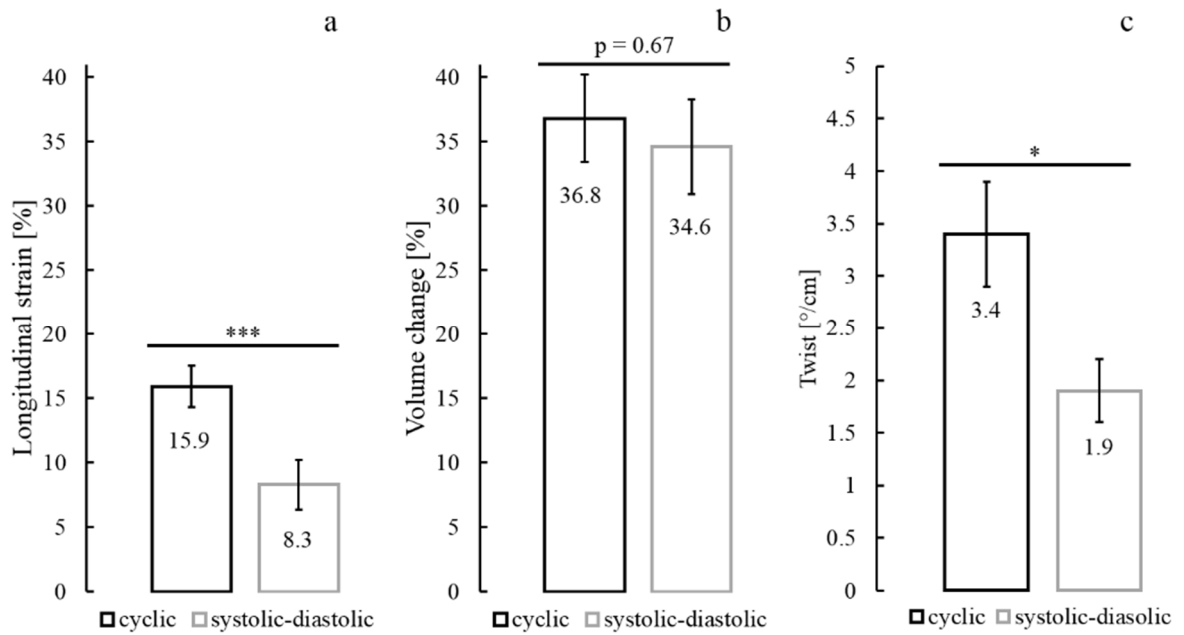


Figure 5-7 Cyclic and systolic-diastolic longitudinal (a), volumetric (b) and twist (c) deformation in the ascending aorta. * means $p \leq 0.05$, *** means $p \leq 0.001$. Paired t tests were performed. [Reprinted from Wittek et al. 2016b with permission from Springer Nature]

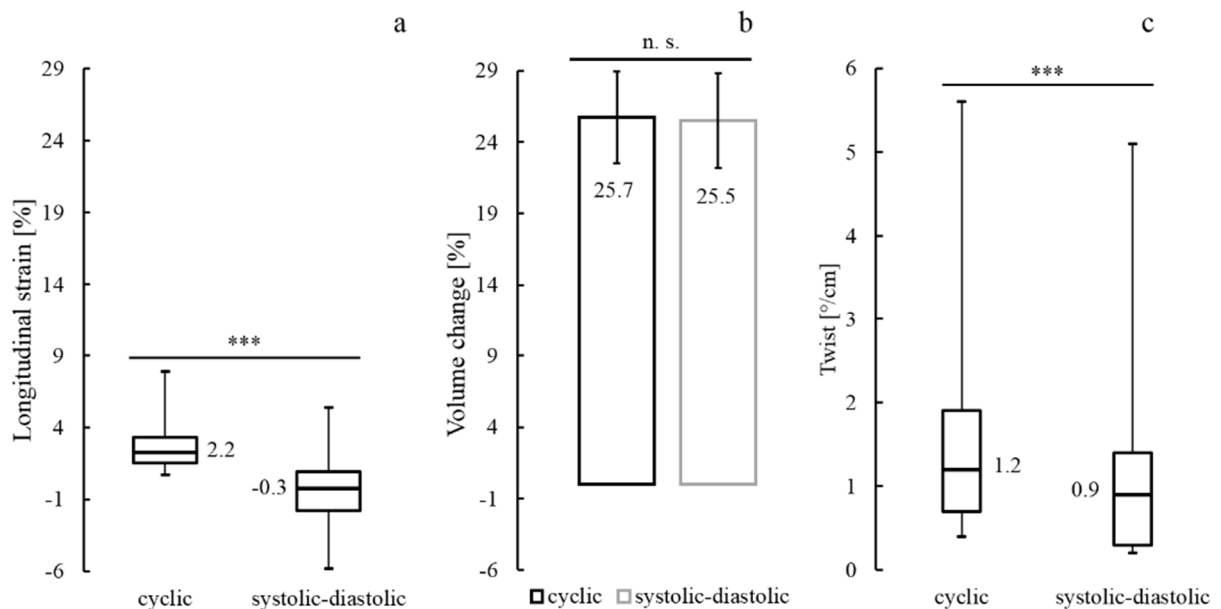


Figure 5-8 Cyclic and systolic-diastolic longitudinal (a), volumetric (b) and twist (c) deformation in the abdominal aorta. *** means $p \leq 0.001$. Paired t test was performed for volume change, WILCOXON signed rank test was applied to longitudinal strain and twist data. [Reprinted from Wittek et al. 2016b with permission from Springer Nature]

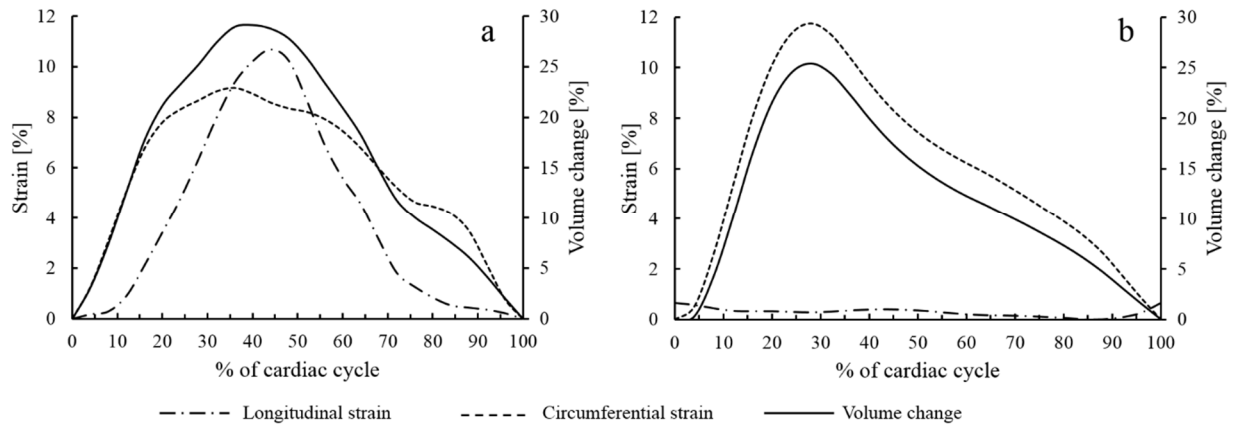


Figure 5-9 Mean curves of cyclic longitudinal and circumferential strain and of relative volume change in the ascending (a) and abdominal aorta (b). [Reprinted from Wittek et al. 2016b with permission from Springer Nature]

Cyclic changes of longitudinal and circumferential strains were not synchronous. Maximum longitudinal strain in the ascending aorta was reached $14.2 \pm 5.4\%$ of the cardiac cycle (paired t test, $p \leq 0.05$) after maximum circumferential strain, which is illustrated qualitatively by Figure 5-9 a. In contrast, in the abdominal aorta the mean phase shift of $-8.1 \pm 6.7\%$ between longitudinal and circumferential strain was not statistically significant (paired t-test, $p = 0.24$). Nonetheless, a marked phase shift could be found in all but two of the imaged abdominal aortae. This was evident when considering the absolute values of the phase shift in the abdominal aorta: $24.6 \pm 3.5\%$ (paired t-test, $p \leq 0.001$). However, twelve of the samples showed a negative phase shift ($-24.6 \pm 3.2\%$, peak longitudinal strain precedes peak circumferential strain), whereas six of the samples showed a positive phase shift ($24.8 \pm 8.1\%$). For illustration cf. Figure 3-3 and Figure 5-9 b. All six volunteers with predominant clockwise twist exhibit negative phase shift and, accordingly, all volunteers with positive phase shift exhibit counter clockwise twist (chi-square test for independence, $p \leq 0.05$).

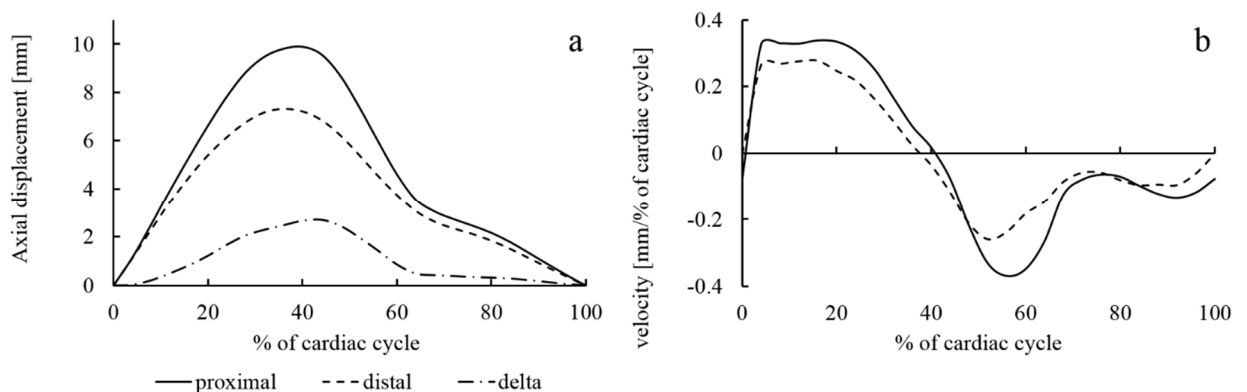


Figure 5-10 Mean axial displacements (a) and velocities (b) of the nodal points that define the end cross-sections of the imaged aortic segments. Proximal and distal end of the abdominal aorta were defined with respect to the distance from the heart. “delta” signifies the difference of proximal and distal displacement. Displacements along the aortic tree towards the heart are positively signed. [Reprinted from Wittek et al. 2016b with permission from Springer Nature]

The mean displacement and velocity along the vessel axis was determined for the proximal and distal end cross-sections of the imaged ascending aortic segments [cf. Figure 5-10 for qualitative illustration]. The distal cross-section was located 10 - 30 mm distally to the sinutubular junction. The proximal cross section was located close to the aortic annulus. The maximum displacement of the distal cross-section (7.8 ± 0.8 mm) was significantly smaller than the displacement of the proximal cross-section (10.3 ± 0.7 mm, paired t test, $p \leq 0.05$) as illustrated by Figure 5-10 a. During the first and second half of the cardiac cycle, greater velocity towards and away from the LV apex [cf. chapter , respectively, was observed at the aortic annulus, compared to mid-ascending aorta [Figure 5-10 b].

5.5 Relations between deformation patterns and physiological function

The cyclic three-dimensional deformation (longitudinal, circumferential, volumetric, rotation and twist) of eight proximal ascending and 18 suprarenal abdominal aortic segments was determined from 4D ultrasound imaging data that were acquired from young male volunteers without known cardiovascular disease and risk factors. Differences between the two segments of the aorta were found in the amplitude of length change, volume change, rotation and twist which were higher in the ascending aorta. The time course of the pulsatile deformation differed as well. Maximum length was reached approximately 15% (of the cardiac cycle) later than maximum diameter in the ascending aorta [cf. Figure 5-9 a]. The examined abdominal aortae did not show uniform behavior in this respect: in 12 cases, maximum longitudinal strain preceded maximum circumferential strain by about 25% of the cardiac cycle, in 6 cases maximum longitudinal strain was observed about 25% later in the cardiac cycle than maximum circumferential strain. Moreover, the ascending aorta exhibited alternating clockwise (in early diastole) and counter clockwise twist (in end-diastole) during the cardiac cycle, while the abdominal aorta was characterized by almost unidirectional, either clockwise ($n = 6$) or counter clockwise twist ($n = 12$) with respect to the end-diastolic reference frame. A statistical dependency between positive or negative phase shift (between circumferential and longitudinal strain) and predominantly counter clockwise or clockwise twist, respectively, was observed in the abdominal aorta.

Table 5-3 Comparison of diameter and circumferential strain values observed in this study with values reported in literature [Reprinted after Wittek et al. 2016b with permission from Springer Nature]

Reference	Imaging technique	n	age [y.]	Diameter [mm]				Circumferential strain [%]			
				diastolic		systolic		asc.		abd.	
This study	4D ultrasound	8	25.5 [24.5, 27.5]	24.4±0.4	14.2±0.5	27.2±0.5	15.9±0.5	11.4±1.1	12.3±1.4		
Astrand et al. (2011)	2D ultrasound	5	23...30		13.8±0.6		16.0±0.5		15.3±1.2		
Hickson et al. (2010)	Cine phase contrast MRI	28	20...29			28.5	16.0				
Martin et al. (2013)	Multi phase CT	15	30...49	29.9±2.8		32.5±2.5		9.2±3.0			
Morrison et al. (2009)	Cardiac gated CT	7						10.3±3.8	8.9±3.0*		

* Thoracic aorta close to the abdominal aorta

5.5.1 Comparison with literature

Systolic and diastolic diameters and the circumferential strains that were observed in this study using 4D ultrasound were in the range of the values that have been reported previously from measurements with other imaging techniques [Table 5-3]. Compared to the present study, Martin et al. [2013] reported larger diameters of the ascending aorta. This difference may be attributed mainly to the higher age of the study collective that was examined by Martin et al. [2013]. Several studies have reported an increase of the ascending aortic diameter with age [Morrison et al. 2009; Martin et al. 2013]. Hickson et al. [2010] have shown that this increase is strongest in the ascending aorta (0.96 mm per decade).

Morrison et al. [2009] and Martin et al. [2013] have observed smaller circumferential strains than the present study. This may be due to aortic stiffening associated with higher age of the patient groups examined in these studies [cf. chapter 1.7.1]. Both studies have reported the decrease of circumferential strain with age.

So far, there are very few works reporting *in vivo* data on cyclic longitudinal strains in humans. Morrison et al. [2009] have measured longitudinal strains of $2.0 \pm 0.5\%$ of the descending thoracic aorta in a collective of seven patients (31 to 51 yrs. old). This value is close to the cyclic strain that was observed in this study for the suprarenal abdominal aorta which is directly adjacent to the descending thoracic aorta downstream along the aortic tree [cf. Figure 1-6]. Longitudinal strain in the abdominal aorta is small, compared to circumferential strain. Bell et al. [2014] have investigated longitudinal strain of the proximal ascending aorta in a group of 375 patients (72 to 94 yrs. old). They observed a lengthening of the aortic root of 22% [17%, 32%] in men and of 21% [15%, 26%] in women. In the ascending aortic segment between the sinutubular junction and brachiocephalic origin they have measured 8.5% [6.9%, 10.3%] and 6.7% [5.1%, 8.2%] in men and women, respectively.

5.5.2 Physiological function of longitudinal strain in the ascending aorta

The observations of the current study regarding the abdominal aorta are in accordance with the widely accepted hypothesis that cyclic length change of arteries as response to cyclic pressure and diameter changes is minimized by axial prestrain of the vessel *in situ* [Schulze-Bauer et al. 2003; Schulze-Bauer and Holzapfel 2003; Horný et al. 2013]. Longitudinal prestrain of the abdominal aorta may reach values up to 40% in young human subjects and decreases with age. The limitation of cyclic length change by axial prestrain was understood as energetical optimization of the arterial function of carrying the pressure wave and blood flow wave [Schulze-Bauer et al. 2003], because – in most parts of the arterial tree – this function is not supported by axial length change of the vessel. Evidently, this hypothesis does not apply to the ascending aorta, where large cyclic amplitudes of axial strain are observed, which might coincide with reduced prestrain. This is suggested by findings by Han and Fung [1995], who have shown

in dogs and pigs that the degree of axial prestrain depends on the position in the aortic tree: in both species, axial strain of about 20% was observed in the ascending aorta, which then gradually increased along the aortic tree and reached about 60% in the infrarenal abdominal aorta.

Lengthening of the ascending aorta is driven by the cyclic motion of the aortic root - being located in the atrioventricular plane of the left ventricle (LV) - due to LV contraction [cf. chapter 1.3, Mercer 1969; Kozerke et al. 1999; Beller et al. 2004; Bell et al. 2014]. Following Maksuti et al. [2015] it was emphasized in chapter 1.2 that the main pumping mechanism of the heart is the cyclic long-axis motion of the atrioventricular plane, which causes reciprocal redistribution of blood volume between right and left atria and ventricles, respectively, while the total heart volume remains almost constant. One “energetically optimal” effect of this principle is that a portion of blood is transported from the atria to the ventricles without the need to accelerate its mass. Since the aortic annulus and aortic valve are located in the atrioventricular plane, too, a similar displacement pump mechanism might apply to the ejection of blood from the LV into the ascending aorta. The maximum displacement of the aortic annulus towards the LV apex of 10 mm [cf. Figure 5-10 a], that was observed in this study, combined with the systolic diameter of 27.2 mm [Figure 5-2] results in an increase of the volume of the ascending aorta by 5.8 ml. This additional aortic volume is “immersed” into the LV volume due to movement of the aortic root, so that a corresponding volume of blood is transported from the LV into the aorta without the need to accelerate its mass, which means less work for the LV during systole [cf. Maksuti et al. 2015]. In turn, the LV has to work against the elastic force of the stretched ascending aorta. This work is stored in the stretched aorta as potential energy [Bell et al. 2015]. When released during diastole, where longitudinal elastic recoil acts in direction of the vessel, it might help to accelerate the stored blood in systemic flow direction and contribute to the maintenance of flow during diastole more effectively than circumferential elastic recoil of the proximal aorta alone would do. Understood in this way, large cyclic longitudinal strain of the proximal aorta means an energetical optimization of the aortic function, as does the limitation of cyclic length change due to increased axial prestretch in the abdominal aorta.

The proximal aorta moves in direction of the LV apex in the first third of the cardiac cycle [cf. Figure 5-10 b], i.e. during the first part of the LV ejection phase. For this phase, blood flow velocities of about 150 cm/s are reported in literature [Nichols et al. 2011] that were measured by ultrasound Doppler, i.e. with reference to the unmoved ultrasound probe. In this study, an aortic wall velocity in the opposite direction was measured with a size of about 0.35 mm per % of cardiac cycle, i.e. 3.5 to 5.25 cm/s for a heart rate of 60 to 90 bpm. This means that the relative velocity between wall and blood and consequently wall shear stress might be slightly higher than estimated by US Doppler measurements. State of the art fluid-structure interaction models of the aortic root and the proximal aorta [Griffith 2012; Flamini et al. 2015] do not take into account longitudinal motion and strain of the aortic wall. Flamini et al. report maximum wall displacements (without specified direction) of 0.55 mm predicted by their model, only.

To the author's knowledge, the phase shift between maximum longitudinal and circumferential strain in the ascending aorta has not been described before. Circumferential strain is thought to closely follow the pressure course and maximum circumferential strain occurs at maximum pressure in the LV and the proximal aorta (mid-systole at one third of the cardiac cycle) [cf. chapter 1.3, Figure 1-3 and Figure 5-9]. Longitudinal strain is related to the contraction of the LV and maximum contraction of the LV, which is marked by minimum LV volume, is reached in end-systole/early diastole at about 50% of the cardiac cycle [cf. chapter 1.3 and e.g. Humphrey 2002]. Indeed, the maximum difference between the axial displacement of the aortic annulus and the mid-ascending aorta (longitudinal strain) was observed in the current study in end-systole/early diastole at $50.0 \pm 3.6\%$ of the cardiac cycle, i.e. at the same stage where maximum LV contraction is reported in literature. However, maximum displacement of the aortic annulus towards the LV apex was observed significantly earlier at $39.0 \pm 1.6\%$ of the cardiac cycle (paired t test, $p = 0.017$), almost simultaneously with maximum circumferential strain at $36.5 \pm 5.9\%$ (paired t test, $p = 0.71$) that might indicate maximum pressure. This means that maximum annulus displacement – as an indicator of maximum axial LV contraction – cannot explain the phase shift between longitudinal and circumferential strain. In the velocity diagram [Figure 5-10 b], the difference between maximum annulus displacement and maximum longitudinal strain is illustrated by the difference between the zero crossing of the annulus velocity and the crossing of the annulus and the distal velocity curves. The diagram qualitatively shows that – after maximum annulus displacement is reached, the motion of the aortic annulus, i.e. the part of the ascending aorta closest to the LV, away from the LV apex is slower than the motion of the distal cross-section in the same direction, resulting in still increasing longitudinal strain. It is known that the pressure gradient between LV and proximal aorta, which accelerates the blood in systemic flow direction at the beginning of the ejection phase, is reversed during end-systole/early diastole after the peak of LV pressure has been reached and when the myocardium starts to relax [cf. chapter 1.3 and e.g. Nichols et al. 2011]. This reversal of the pressure gradient first creates a force that closes the aortic valve [Bellhouse and Bellhouse 1968], acts on the atrioventricular plane and is oriented towards the LV apex, i.e. in opposite direction to the movement of the aortic annulus in this phase of the cardiac cycle. With the further decline of LV pressure after the closure of the aortic valve, the transvalvular pressure gradient increases until the opening of the mitral valve [Dagum et al. 1999] at about 50% of the cardiac cycle, i.e. until the time point when maximum longitudinal strain was observed in the current study. One might hypothesize that the transvalvular pressure gradient decelerates the motion of the atrioventricular plane away from the LV apex after maximum LV pressure was reached and thus accounts, at least in part, for the phase shift between longitudinal and circumferential strain.

The relative volume change VC is an illustrative parameter for the biaxial deformation of the aorta. Moreover, VC is the parameter that is physically relevant for the physiological Windkessel function of the ascending aorta, i.e. its ability to store a fraction of the volume of blood ejected by the left ventricle during systolic contraction, in order to preserve arterial blood pressure and to augment arterial blood

flow during diastole by elastic recoil of the aortic wall [Humphrey 2002; Beller et al. 2004; Nichols et al. 2011]. The phase shift of peak longitudinal and circumferential strain in the ascending aorta results in a “plateau” phase of the maximum VC of about 10% of the cardiac cycle, that cannot be observed in the curves of longitudinal and circumferential strain alone [Figure 5-9 a]. I.e. the storage of a maximum portion of blood volume in the ascending aorta is extended by this effect and its forwarding to the arterial system is delayed to a later phase of the pulse cycle, thus contributing to a more continuous blood flow throughout the cardiac cycle.

Because of the helical arrangement of the LV myofibers, axial contraction of the LV is coupled to opposite rotations of LV apex and base [cf. chapter 1.3 and e.g. Sengupta et al. 2008]. The LV base rotation might be the main reason of the average rotation amplitude of 6.6° that was observed in the current study in the proximal aorta [Figure 5-4]. In literature, LV base rotation with a comparable amplitude of about 6° to 7° was reported [Sengupta et al. 2008; Buckberg et al. 2015]. In many cases a counter clockwise rotation of the LV base was observed during early systole (isovolumetric contraction), which then is followed by a clockwise rotation during the ejection phase. This might explain the alternating clockwise (early systole) and counter clockwise twist (end systole) of the proximal aorta that was measured in the study reported in this thesis [Figure 5-5, Figure 5-6]. In contrast, no external rotational moment comparable to LV base rotation is known that acts on the abdominal aorta, in particular since any motion in the abdomen due to breathing was excluded during the ultrasound measurement [cf. chapter 3.2.1]. Accordingly, by far smaller rotational motion and twist were observed in the abdominal aorta. Moreover, predominantly unidirectional, either clockwise or counter clockwise twist was found. Twist increased with circumferential strain during the first half of systole and then remained at a more or less constant level almost until end diastole [Figure 5-6]. This twist under pressure change might result from asymmetry in the arrangement of the aortic wall’s preferred fiber directions with regard to physiological biaxial loading by blood pressure and axial prestress: in chapter 2.3.4.3 it was shown that the principal directions of the strain tensor and the stress tensor are not identical if the preferred fiber directions governing the anisotropic behavior are not symmetric with regard to the principal loading directions. I.e. though loading of a – open or closed ended – hollow cylinder by hydrostatic pressure and axial prestress will result in a shear-stress-free stress state, in-plane shear deformation may be observed.

Systolic-diastolic longitudinal strain and twist were found to be significantly smaller than the corresponding cyclic amplitudes in the ascending as well as in the abdominal aorta. Due to the phase shift between maximum longitudinal and circumferential strain, the true size of cyclic aortic deformation could only be recognized because a three-dimensional imaging technique with appropriate temporal resolution was applied. If measurements would have been performed at only two time points throughout the cardiac cycle, e.g. end-systole and end-diastole, significantly smaller systolic-diastolic longitudinal strain and twist would have been measured, only [Figure 5-7a, c; Fig. Figure 5-8a, c]. These findings motivated and justify the choice of different reference configurations for the description of cyclic longitudinal and circumferential strain and relative volume change [cf. chapter 3.3.3.3] and for the different

components of the in-plane strain tensor [cf. 3.3.4.3] in order to capture the full range of cyclic deformation.

5.5.3 Conclusions and limitations

Usually, the cyclic deformation of aortic segments is described by means of parameters that depend on the diameter change of the vessel alone, such as circumferential strain or the systolic-diastolic ratio of the cross-sectional area of the vessel lumen. The findings reported in this chapter show that this approach is well suited for the abdominal aorta where longitudinal strain and torsion were small and the cyclic deformation was almost uniaxial in circumferential direction. In contrast to this, the ascending aorta underwent a more complex multiaxial deformation with length and diameter changes of the same order of magnitude, a phase shift between both cyclic deformations and alternating twist during the cardiac cycle. These observations promote a deepened understanding of the proximal aorta's Windkessel function.

It is known, though not completely understood, that the mechanical environment of and load on endothelial cells and cells embedded in the aortic wall, plays a crucial role for its remodeling. In addition, such a complex cyclic deformation as was observed in the proximal aorta in the current study is known to be highly fatiguing to technical materials. This may account for increased degradation of non-living components of the aortic wall and thereby promote aortic stiffening with age as well as pathological processes such as dissection or aneurysm formation [cf. chapter 1.7 and Nichols et al. 2011].

The measurement of such a complex multiaxial deformation requires three-dimensional imaging using a LAGRANGIAN reference frame that is fixed to the imaged object. For the detection of the phase shift between longitudinal and circumferential strain, sufficient temporal resolution is required. Time resolved 3D ultrasound strain imaging provides these features and allows for better understanding of the physiology and pathophysiology of the cardiovascular system.

Using a transthoracic probe, only short segments of the proximal thoracic aorta were accessible by 4D ultrasound through the long-axis-parasternal view. In 10 patients, the image quality was not sufficient to perform 3D speckle tracking. Neither the aortic arch, nor the descending thoracic aorta could be imaged through the long-axis-parasternal view. These limitations could be overcome by using a 3D transesophageal probe, which was not available at the time when the measurements for this study were taken.

6 Locally varying elastic behavior of human aortae in vivo

6.1 In vivo measures of aortic elasticity in the physiological range

The elastic response of the aortic and of arterial walls to loading by pulse pressure has an important physiological function for maintaining and regulating circulation. Arterial stiffening has been identified as an independent risk factor and predictor of severe cardiovascular events and of diseases such as renal failure and dementia. [Cf. chapters 1.2, 1.6.1.]

The measurement of pulse wave velocity (PWV) is regarded as gold standard for clinical assessment of arterial elasticity or stiffness [van Bortel et al. 2012; Teixeira et al. 2015]. It is determined from measurements of the time delay between ventricular systole and the occurrence of peak pressure at defined sites of the arterial tree, e.g. the common carotid artery (Δt_c) and at the femoral artery (Δt_f) [cf. Figure 1-6]. Additionally, the distances between the left chamber of the heart and both sites of measurement along the arterial tree have to be known (s_c, s_f). Then, carotid-femoral pulse wave velocity is obtained as

$$PWV = \frac{\Delta t_f - \Delta t_c}{s_f - s_c}. \quad \text{eq. 6-1}$$

According to eq. 1-1, a ‘YOUNG’s modulus’ E can be determined from measured PWV . The determined modulus describes the functional elastic response of the whole aortic tree between its origin at the left ventricle, the common carotid artery and the femoral artery neglecting all differences between aortic segments. However, it is not a proper constitutive model describing the material properties of an isolated piece of tissue.

Other measures of the elastic behavior of the aortic and arterial wall relate the diastolic-systolic diameter change Δd or derived values to the pulse pressure Δp . Because of its high frame rate, ultrasound measurements are suitable to capture minimum and maximum cyclic diameter with negligible error. Common measures of arterial elasticity that can be determined based on ultrasound measurements are listed subsequently [cf. e.g. O'Rourke 1990; Fung 1997; O'Rourke et al. 2002; Nichols et al. 2011; Caro 2012; Teixeira et al. 2015].

$$\text{Compliance} = \frac{\Delta d}{\Delta p}. \quad \text{eq. 6-2}$$

Two variations of distensibility are commonly used: one is determined based on diameter change Δd and diastolic (i.e. minimum cyclic) diameter d_{dia} , the other based on the corresponding values of the cross-sectional area of aortic lumen (ΔA and A_{dia}), for which a circular shape is assumed, mostly:

$$\text{Distensibility (diameter)} = \frac{\Delta d}{d_{dia} \cdot \Delta p}, \quad \text{eq. 6-3}$$

$$\text{Distensibility (area)} = \frac{\Delta A}{A_{dia} \cdot \Delta p}, \quad \text{eq. 6-4}$$

$$\text{PEARSON'S elastic modulus} = \frac{\Delta p \cdot d_{dia}}{\Delta d}, \quad \text{eq. 6-5}$$

$$\text{YOUNG'S modulus} = \frac{\Delta p \cdot d_{dia}}{\Delta d \cdot h}, \quad \text{eq. 6-6}$$

where h is the wall thickness that can only be measured for superficial blood vessels. Finally, the

$$\text{Stiffness index } \beta_1 = \frac{\ln \frac{p_{sys}}{p_{dia}}}{\frac{\Delta d}{d_{dia}}}. \quad \text{eq. 6-7}$$

In contrast to PWV, these measures do not characterize the elastic response of the whole aortic tree, but describe the elastic behavior of a specific site along the aortic tree. I.e. the effects of the known changes of axial prestretch [Han and Fung 1995] and microstructural composition [Fung 1993] of the aortic wall in dependency of the distance from the heart on its cyclic elastic properties can be captured [Nichols et al. 2011]. However, none of these measures provides a characterization of the variation of the local elastic properties along the circumference of the vessel.

All these indices are not proper constitutive models of the aortic or arterial wall: Not the elastic properties of the isolated aortic wall tissue are identified, but the elastic response of the aortic wall

embedded in perivascular tissue and surrounded by various organs, which might contribute to the elastic response. Secondly, not the nonlinear and orthotropic constitutive behavior of the wall is modeled, but its circumferential secant modulus (or its inverse) in the physiological loading range. Despite these “deficiencies”, these indices allow for the identification the physiologically relevant elastic response of the aorta to the ejection of a blood volume and to the pressure wave travelling along the aortic tree. It is this elastic response that contributes to regulation and smoothing of pulse pressure and maintenance of continuous blood flow through the Windkessel effect [cf. chapter 1.3]. Compared to – from the continuum mechanical point of view – more ‘adequate’ constitutive equations, the most decisive advantage of the above-listed indices for aortic elasticity is the fact that they can be determined from non-invasive in vivo data, only, without the need for any assumption regarding the modeling of the circulation or the aortic wall [Teixeira et al. 2015].

Ribbers et al. [2007] first have applied 2D ultrasound with speckle tracking (2D-STE) for clinical measurement of aortic wall strain. Oishi et al. [2008] computed global circumferential strain as the mean of six segmental strain values in order to determine the stiffness index β_1 according to eq. 6-7. Since then, various groups have used 2D-STE in order to measure global and local circumferential strain of different segments along the aortic tree in different patient groups and were able to successfully identify correlations between aortic stiffness and various cardiovascular diseases [cf. Teixeira et al. 2015].

In abdominal aortic aneurysm (AAA) management ultrasound to date has two main clinical applications: Firstly, detection of the disease and rupture risk estimation by means of the two-point measurement of the maximum aortic diameter [cf. chapter 1.1]. Secondly, surveillance of the increase of diameter of small AAAs until the criterion for repair is reached [Iwakoshi et al. 2019]. In part, 3D ultrasound is used to reduce the uncertainty of maximum diameter measurement, the result of which depends on the angle between the imaging plane and the AAA centerline when 2D ultrasound is used. Ultrasound Doppler imaging can be used to detect blood flow between endografts, i.e. prostheses that should take the blood pressure instead of the diseased wall, and the wall. These so-called ‘endo-leaks’ are a common complication after endovascular repair of AAAs [cf. chapter 1.1].

Kok et al. [2015], Disseldorp et al. [2016b], Disseldorp et al. [2016a] and Disseldorp et al. [2019a] have reconstructed static configurations of the AAA wall from 3D ultrasound measurements and have used these in Finite Element wall stress analyses. Disseldorp et al. [2016a] and Disseldorp et al. [2019b] have used temporally resolved 3D ultrasound measurements of the AAA shape combined with pressure measurements in order to identify in vivo linear elastic moduli describing the homogeneous elastic behavior of the AAA wall.

The non-invasive in vivo method for full field measurement of the individual in-plane wall strains with high spatial and temporal resolution that was developed within this thesis (cf. chapter 3) allows for the investigation of the dynamic and locally varying pulsatile deformation of arterial walls. In this chapter, firstly, a new measure for the characterization of the individual aortic wall’s local elastic behavior in the physiological loading range is introduced (chapter 6.2): The highly resolved local deformation

measurements (cf. chapter 3.3.4) were normalized with regard to pulse pressure Δp to make sure that the observed differences between subjects are not only effects of varying loading by pulse pressure. Arterial deformation normalized by pulse pressure is known as distensibility coefficient [DC , cf. eq. 6-3]. As mentioned above, it is commonly regarded as linear approximation of the aortic wall's elastic behavior in the physiological loading regime and to be proportional to the inverse of the YOUNG's modulus. Despite its implicit dependency on geometrical information [see chapter 6.5 for detailed discussion of this aspect], it is a favorable *in vivo* measure for the aortic wall's elastic behavior because it is determined strictly non-invasively from dynamic *in vivo* imaging like ultrasound or magnetic resonance imaging and blood pressure measurement. No population-averaged assumptions have to be made concerning mechanically relevant information that cannot be measured *in vivo* like wall thickness, intra-abdominal pressure, or the impact of surrounding tissue and neighboring organs.

Aortic distensibility has been suggested as a predictor for aortic aneurysm rupture risk [Wilson et al. 2003; Hoegh and Lindholt 2009] and has been shown to correlate with an *in vitro* stretch based failure criterion in ascending thoracic aortic aneurysms [Trabelsi et al. 2017]. Based on highly resolved full field strain imaging, a novel definition of the local distensibility of a surface area of the aortic wall was developed in this thesis [Wittek et al. 2018] and is presented in this chapter.

Secondly, new biomarkers for pathophysiological changes of the aortic wall are presented in this chapter [cf. section 6.3] that can be derived from statistical analysis of the distributions of local wall strain [Karatolios, Wittek et al. 2013; Derwich et al. 2016; Wittek et al. 2017a; Wittek et al. 2018] and of local distensibility [Wittek et al. 2018]. These biomarkers aim at quantifying changes of the global and local stiffness and of the variability or heterogeneity of the wall's local elastic properties. It has been described in detail in chapter 1.7.2 that the development of an AAA is accompanied by degenerative changes in the microstructural composition of the wall and that these changes are closely related with, and eventually lead to mechanical failure of the wall under cyclic loading by pulse pressure. These degenerative processes are highly localized and result in local variations of wall thickness, elastic properties and wall strength [Thubrikar et al. 2001; Raghavan et al. 2006]. It is hypothesized in this thesis that "lumped" macroscopic effects of microstructural changes in the aortic and aneurysmal wall can be assessed and quantified by the suggested biomarkers and that these macroscopic effects are indicative for relevant pathophysiological changes in the wall. In order to evaluate the suitability of the developed methods to assess pathological changes of the individual aortic and aneurysmal wall, in a clinical study the proposed biomarkers were determined for and compared between groups of healthy subjects, AAA patients and age-matched patients without an AAA. The relation of the distensibility distribution indices (DDI) to parameters which are known (age) or supposed (maximum AAA diameter) to be related with (patho-) physiological changes of the aortic wall was evaluated within each group [cf. chapter 6.4].

6.2 The local distensibility coefficient

Approximating the artery as a thin walled cylinder, the distensibility coefficient according to eq. 6-4 commonly is formulated in terms of aortic diameter:

$$DC = \frac{\Delta A}{A_0 \Delta p} = \frac{d^2 - d_0^2}{d_0^2 \Delta p}, \quad \text{eq. 6-8}$$

where

- A_0, d_0 are the diastolic or minimum reference cross-sectional area and diameter of the arterial lumen, respectively,
- ΔA is the cyclic change of the cross-sectional area,
- d is the current luminal diameter and
- Δp is the pulse pressure.

Using the relation

$$\lambda_2 = \frac{d}{d_0} = \varepsilon_{22} + 1, \quad \text{eq. 6-9}$$

where λ_2 is the circumferential component of the left stretch tensor \mathbf{V} , the distensibility coefficient can be expressed in terms of the circumferential component ε_{22} of the BIOT's in-plane strain tensor [cf. chapter 2.1, eq. 2-23]:

$$DC = \frac{(\varepsilon_{22} + 1)^2 - 1}{\Delta p}. \quad \text{eq. 6-10}$$

This expression of the DC is bound to the underlying assumptions in the following points:

- (i) Thin walled structure: ε_{22} is assumed to be constant over the wall thickness.
- (ii) Geometrically regular cylindrical shape: If just one cross-sectional diameter and its change is assumed to perfectly describe the geometry of an aortic cross-section or axial section and its cyclic change, the same circumferential strain is obtained for each material point X on the aortic wall and:

$$\varepsilon_{22}(d, d_0) = \text{const.}$$

If, in contrast, circumferential strain is computed from the motion $\mathbf{x}_{i,j}$ of a field of discrete material points $X_{i,j}$, that was gathered by customized 4D ultrasound measurement [cf. section 3.3.2, eq. 3-6], a field of local strain values $\varepsilon_{22}(e_{i,j}, \Delta t) \neq \text{const.}$ is obtained that describe the local cyclic deformation

of aortic wall surface areas $e_{i,j}$ with sizes between 1 and 13 mm² (cf. chapter 3.3.4, Figure 3-7 c). Using these local strain values, we define a local distensibility coefficient

$$DC_l = DC(e_{i,j}) := \frac{(\varepsilon_{22}(e_{i,j}, \Delta t) + 1)^2 - 1}{\Delta p}. \quad \text{eq. 6-11}$$

This local distensibility coefficient is no longer bound to the assumption of a regular cylindrical shape of the vessel. In contrast, the geometrically irregular shape of the aortic and, in particular, the aneurysmal wall, is approximated by discretization into planar 1st order membrane elements $e_{i,j}$ and the exact cyclic strain and distensibility distributions are approximated by fields of segment wise constant local values. The assumption of a thin walled structure remains, since 4D ultrasound measurement currently does not allow to resolve radial differences of aortic wall motion. Therefore, the measured deformation of the wall was assumed to be constant over its thickness in the presented study.

It is noteworthy that the reasonable degree of discretization and the accuracy of the approximation was limited by the spatial resolution of the measured discrete motion function $\mathbf{x}_{i,j} = \chi(\mathbf{X}_{i,j}, t)$. The wall motion tracking algorithm generated a fixed number of discrete volumes in the ultrasound data to compute displacements (1296 discrete sub volumes). Depending on the size of the segmented structure, the distance between the center points of these sub volumes, i.e. the discrete material points, varied and accordingly the density (or “resolution”) at which displacement information was available. Since the discrete material points were the basis for the mesh generation, the resulting element size depended on the size of the overall structure: the elements were largest in the case of AAAs [cf. chapter 6.4.1, Table 6-2].

6.3 Indices for the characterization of the spatial distribution of the local elastic behavior

To characterize the spatial strain and distensibility distribution of the aortic or aneurysmal wall quantitatively, statistical parameters were calculated for each in-plane component of the BIOT’s strain tensor and for local distensibility [Karatolios, Wittek et al. 2013; Derwich et al. 2016; Wittek et al. 2017a; Wittek et al. 2018]:

- (i) Mean (“Mean”) and local maximum (“Peak”) strain/distensibility: The arithmetical mean and the local maximum of the strain/distensibility distribution.
- (ii) Local strain/distensibility ratio (“LSR”/“LDR”): The ratio of local maximum and mean strain/distensibility.

(iii) Heterogeneity index (“HI”) : The coefficient of variation, i.e. the ratio of the standard deviation and the mean of the strain/distensibility distribution.

Local strain/distensibility ratio and the heterogeneity index are similar measures that are indicative for the degree of local variation of the elastic behavior within the examined aortic segment. The two indices differ in the weighting of the influence of a single peak value on the characterization of the heterogeneity of the overall elastic properties.

6.4 Distributions of local elasticity in young, aged and aneurysmal aortic walls

6.4.1 Study group and data acquisition

For this study, 4D ultrasound and blood pressure data of 61 patients and volunteers presented at the Clinics for Vascular and Endovascular Surgery of the University Hospital Frankfurt am Main were evaluated. The study was approved by the local ethics committee. Patient data were divided into three groups: “young” volunteers < 40 y.o. without known cardiovascular risk factors ($n = 19$), “elderly” patients > 60 y.o. without AAA ($n = 20$) and AAA patients > 56 y.o. ($n = 22$). An abdominal aortic segment was defined as aneurysm when its maximum diameter exceeded 30 mm. Patient data are given in Table 6-1. In case of the young volunteers and the elderly patients, a mean diameter of the aortic segment was determined according to chapter 3.3.3. In case of aneurysms, the determination of an average diameter was not reasonable. Therefore, and because of its clinical relevance, the maximum local diameter that had been taken for diagnostic purposes based on 2D ultrasound imaging data, is given for the aneurysm group.

The elderly and the AAA groups were age matched. Elderly and AAA patients showed multimorbidity. Patients of both groups suffered from arterial hypertension (> 60 y.o.: $n = 14$, AAA: $n = 18$), hyperlipidemia (> 60 y.o.: $n = 9$, AAA: $n = 8$), peripheral occlusive disease (> 60 y.o.: $n = 9$, AAA: $n = 4$), stroke (> 60 y.o.: $n = 3$, AAA: $n = 2$) and coronary heart disease (> 60 y.o.: $n = 7$, AAA: $n = 8$). Prevalence of none of the aforementioned diseases was significantly different between both groups (Chi-square test for Independence, $p > 0.05$). All AAA except for two contained considerable intraluminal thrombus (ILT). In most cases, the complete wall was covered by ILT.

Table 6-1 Patient data are given as median [min., Q_1 , Q_3 , max.], where Q_1 and Q_3 are the first and third quartile, respectively. Mean of diastolic and systolic pressure is given. Pulse pressure was obtained as difference of the maximum and minimum blood pressure observed throughout the cardiac cycle. For the groups of volunteers < 40 y. of age and > 60 y. of age the average diameter along the length of the imaged aortic segment is given, whereas for the group of AAA patients, the maximum diameter is given as was measured clinically. [Reprinted from Wittek et al. 2018 with permission from John Wiley and Sons]

	< 40 y.o.	> 60 y.o.	AAA
<i>n</i>	19	20	22
Age in y.	27.4 [18.0, 26.6, 29.2, 37.7]	70.4 [60.8, 64.3, 74.0, 85.8]	71.4 [56.4, 64.8, 75.8, 82.6]
Mean pressure in mmHg	100 [83, 97, 100, 123]	105 [80, 100, 110, 125]	110 [80, 101, 130, 140]
Pulse pressure in mmHg	45 [40, 40, 60, 65]	60 [35, 52, 70, 90]	60 [30, 50, 70, 97]
Diameter in mm	13.5 [10.6, 12.5, 14.1, 18.6]	17.2 [13.9, 19.3]	49.2 [36.4, 43.7, 54.3, 69.5]

4D ultrasound examination of volunteers and patients and blood pressure measurement were carried out according to chapter 3.2.1. The length of the imaged aortic and aneurysmal segments and temporal resolution of ultrasound measurements are given in Table 6-2. Clinical post-processing of the data sets was done offline using the Toshiba Advanced Cardiac Package (ACP, Toshiba Medical Systems, Otawara, Japan) as described in detail in section 3.2.2. The discrete motion function [cf. chapter 3.3.2] of the aortic and aneurysmal wall was exported using the customized interface [cf. chapter 3.3.1] and highly resolved in-plane strain tensor fields were computed applying the methods described in chapter 3.3.4.

Table 6-2 4D ultrasound imaging parameters. [Reprinted from Wittek et al. 2018 with permission from John Wiley and Sons]

	< 40 y.o.	> 60 y.o.	AAA
Segment length in mm	26.2 [25.5, 30.4]	40.0 [32.8, 44.9]	65.5 [57.1, 73.3]
frame rate in Hz	23.1 [20.1, 32.2]	20.0 [20.0, 23.6]	24.1 [23.5, 31.5]
Av. element size in mm ²	1.4 [1.2, 1.6]	2.9 [1.8, 3.2]	9.5 [8.5, 13.2]

6.4.2 Statistics

Statistical analysis of group differences was performed with WOLFRAM Mathematica 10.3 (Wolfram Research, Champaign, IL, USA). All strain and distensibility distribution indices are continuous parameters. Using the function ‘LocationTest’, parameter sets of the different patient groups were tested for normality first. If both groups of parameters were normally distributed, an unpaired two-tailed t test (t) was performed. Else, a MANN-WHITNEY U test (U) was performed. Hypothesis tests on two data sets were performed with null hypothesis that the means or medians of the two data sets are equal. Since

three patient groups were compared, significance levels were determined observing the Bonferroni correction for multiple testing. Therefore, significance at the 0.05 and 0.01 levels corresponds to p -values smaller than 0.0167 and 0.0033, respectively. As not all parameters were distributed normally, parameter values are given as median $[Q_1, Q_3]$, where Q_1 and Q_3 are the first and third quartile, respectively. An observation x was considered to be an outlier of a distribution, if its distance from the interval $[Q_1, Q_3]$ was larger than $1.5 \times \text{IQR}$, where IQR is the interquartile range. For the determination of the dependency of the distensibility distribution indices on age and pulse pressure, a PEARSON correlation was applied if both groups were normally distributed, else a SPEARMAN's rank correlation coefficient (SPEARMAN's ρ) was used.

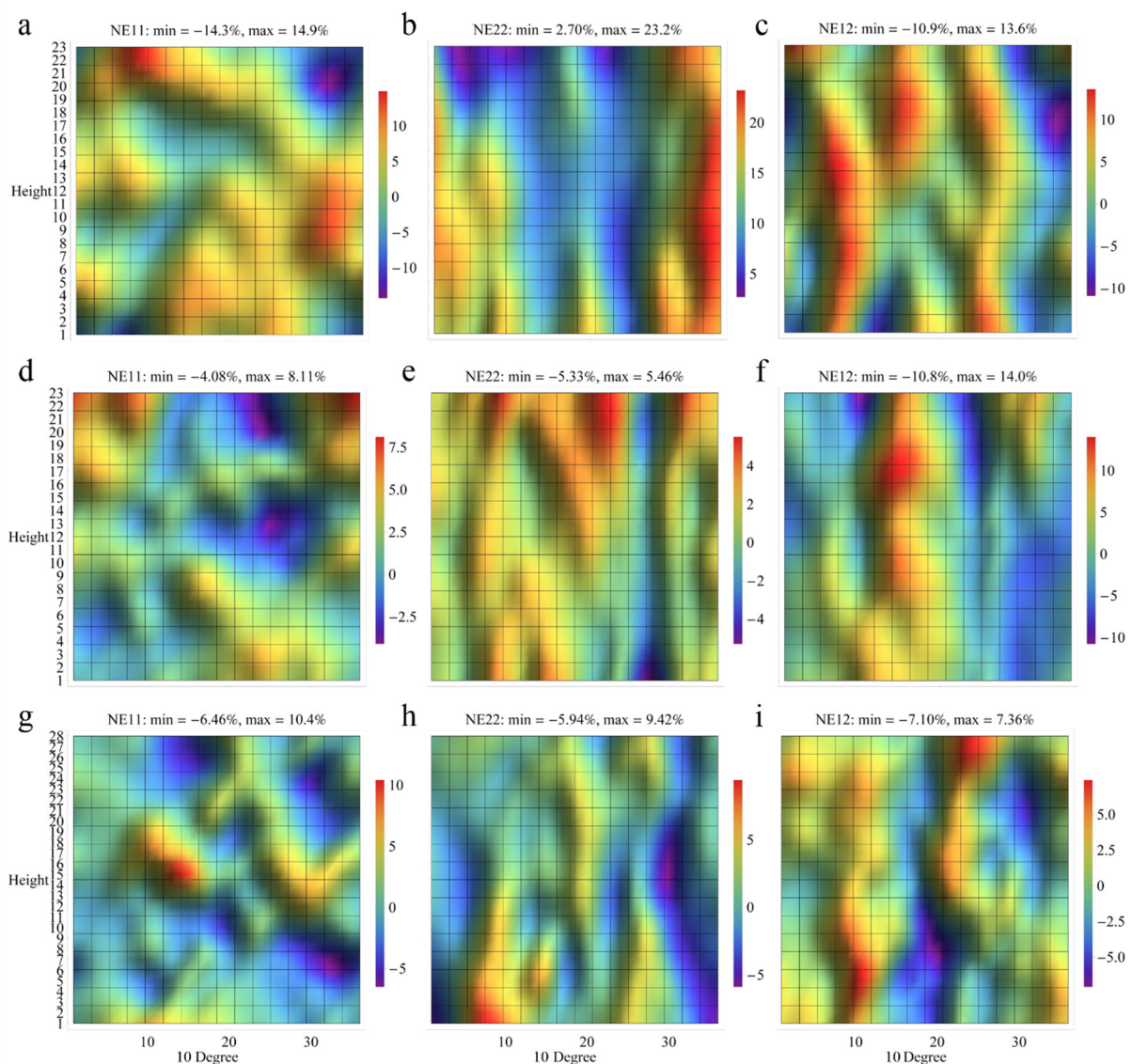


Figure 6-1 Strain amplitude maps of a young volunteer of 23 years (a, b, c), an elderly patient, 74 years of age (d, e, f) and a 74 y.o. AAA patient (g, h, i). NE11 means longitudinal strain, NE22 circumferential strain and NE12 in-plane shear. The horizontal axis (“10 Degree”) of the diagrams correspond to the circumference of the vessel and the vertical axis (“Height”) to the vessel’s longitudinal axis. A “Height” on average corresponds to a distance of 1.1 mm, 1.5 mm and 2.9 mm in the young volunteer, the elderly patient and the AAA patient, respectively. [Reprinted from Wittek et al. 2017a with permission from SPIE]

6.4.3 Comparison of strain distribution indices

Figure 6-1 exemplarily shows the fields of longitudinal, circumferential and in-plane shear peak-to-peak strain amplitudes that were obtained from single measurements of the aortic wall motion of a young volunteer of 23 years, an elderly patient, 74 years of age and a 74 y.o. AAA patient. For all included patients and volunteers, the strain distribution indices for all components of the in-plane strain tensor (longitudinal, circumferential, in-plane shear) and for area strain [cf. chapter 3.3.4, eq. 3-21] are given in Table 6-3, Table 6-4, Table 6-5 and Table 6-6.

Table 6-3 Mean strain in %. Results are given as median[Q_1 , Q_3], where Q_1 and Q_3 are the first and third quartile, respectively. t refers to an unpaired two-tailed t test, U indicates that a MANN-WHITNEY U test was performed. * and ** indicate that differences were significant at the 0.05 and 0.01 level, respectively, observing the Bonferroni correction for multiple testing.

	< 40 y.o.	> 60 y.o.	AAA	< 40 y.o. vs. > 60 y.o.	< 40 y.o. vs. AAA	> 60 y.o. vs. AAA
Longitudinal	1.5 [0.7, 2.1]	1.4 [1.0, 1.8]	0.7 [0.6, 1.1]	t, -	t, *	t, **
Circumferential	10.2 [6.5, 12.8]	1.9 [1.2, 2.7]	0.9 [0.5, 1.2]	t, **	U, **	U, **
In-plane shear	0.6 [0.4, 1.0]	0.7 [0.4, 1.1]	0.5 [0.4, 0.8]	U, -	U, -	t, -
Area	9.5 [6.5, 13.8]	2.5 [1.6, 3.2]	1.5 [1.0, 1.7]	t, **	U, **	U, *

6.4.3.1 Mean strains

A comparison of the mean strains that were observed in the three patient groups is given in Table 6-3. In the young group, mean aortic deformation was characterized by an almost uniaxial deformation state, mean circumferential strain (10.2%) being almost seven times larger than mean longitudinal strain (1.5%) and more than ten times larger than in-plane shear (0.6%). In contrast, in the elderly and the AAA group the in-plane strain state was characterized by mean longitudinal and circumferential strain of the same order of magnitude, circumferential strain being slightly larger and in-plane shear of approximately half the size of normal strain components. This levelling of in-plane strain components in the elderly and the AAA groups was due to significant reduction of mean circumferential strain to one fifth in the elderly (t test, $p < 0.0033$) and even to less than one tenth in the AAA group (Mann-Whitney U test, $p < 0.0033$), compared to the young group. In contrast, mean longitudinal strain was not significantly reduced in the elderly compared to the young group and in the AAA group a reduction to 50% was observed, only. Consequently, the differences in the multiaxial deformation metrics area strain was governed by the changes in circumferential strain.

In the young group, the local circumferential strain values showed a strong correlation with the local maximum principal in-plane strain values (Spearman's $\rho = 0.77$ [0.66, 0.85]) and local longitudinal strain correlated strongly with the local minimum principal in-plane strain (Spearman's

$\rho = 0.64$ [0.61, 0.70]. Neither the elderly, nor the AAA group exhibited this strong correlation between longitudinal/circumferential and in-plane principal strains [Figure 6-2].

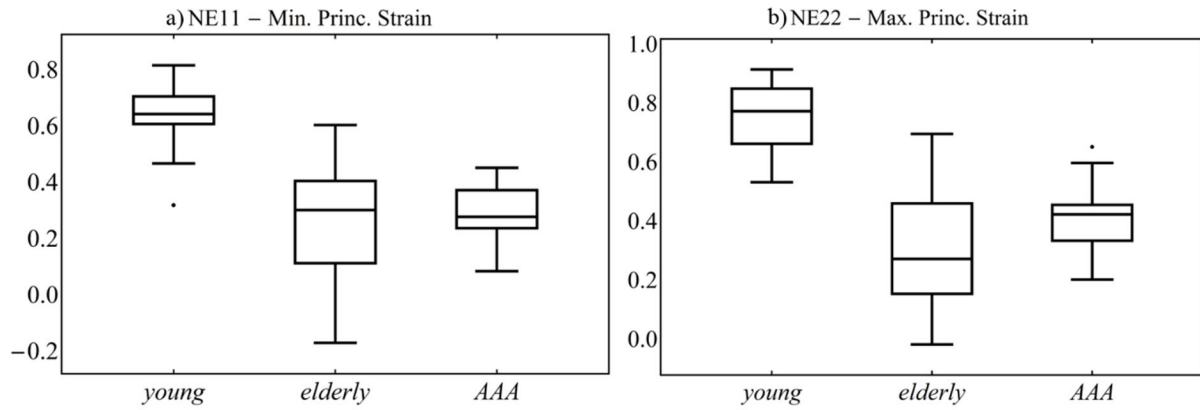


Figure 6-2 SPEARMAN'S ρ between longitudinal strain distributions and minimum in-plane principal strain distributions (a) and between circumferential strain distributions and maximum in-plane principal strain distribution (b) shown for the young (< 40 y.o.), the elderly (> 60 y.o.) and the AAA group.

Table 6-4 Local maximum strain in %. Results are given as median[Q_1 , Q_3], where Q_1 and Q_3 are the first and third quartile, respectively. t refers to an unpaired two-tailed t test (t), U indicates that a MANN-WHITHNEY U test was performed. * and ** indicate that differences are significant at the 0.05 and 0.01 level, respectively, observing the Bonferroni correction for multiple testing. 'o' indicates a tendency towards significance, i.e. $0.5 \geq p \geq 0.0167$.

	< 40 y.o.	> 60 y.o.	AAA	< 40 y.o. vs. > 60 y.o.	< 40 y.o. vs. AAA	> 60 y.o. vs. AAA
Longitudinal	10.9 [8.1, 13.8]	9.4 [7.7, 13.8]	5.6 [4.4, 9.9]	t, -	U, **	U, **
Circumferential	19.3 [15.8, 25.2]	9.9 [7.6, 11.7]	7.9 [6.2, 10.0]	t, **	U, **	U, -
In-plane shear	10.3 [6.6, 13.9]	10.6 [8.5, 13.1]	7.8 [5.7, 11.2]	t, -	t, -	t, o
Area	27.4 [22.0, 36.1]	14.4 [11.2, 18.0]	10.9 [8.6, 18.4]	t, **	U, **	U, -

6.4.3.2 Local maximum strain

The differences in local peak strains were less pronounced than the ones observed for mean strains [Table 6-4]. This applies to differences between strain components within each group as well as to differences between groups. In the young group, the largest local peak values were observed for circumferential strain, as well. But circumferential strain exceeded peak longitudinal strain or in-plane shear by factor two, only. The levelling of the size of in-plane strain components in the elderly and the AAA group as result of the significant reduction of circumferential strain was observed for local peak strain, too. However, none of the strain components, not even the multiaxial area strain, exhibited significant differences between all patient groups.

6.4.3.3 Local strain ratio

Table 6-5 shows the comparison of the local strain ratio between the three patient groups. A significant increase in circumferential local strain ratio was observed from the young (2.0 [1.8, 2.5]) through the elderly (4.3 [3.1, 6.1]) to the AAA group (6.8 [5.7, 14.5]). With regard to local longitudinal strain ratio and local in-plane shear ratio, no significant differences were found between patient groups. Area strain ratio showed a highly significant increase in the elderly and the AAA group, compared to the young group, but was not able to significantly differentiate between the elderly and the AAA group. In the young group, local strain ratio was smallest for circumferential strain, compared to longitudinal strain and in-plane shear. As already observed for mean and local maximum strain, the differences in the size of values obtained for the different in-plane strain components were levelled in the elderly and the AAA group. Local strain ratio assumed the by far largest values for in-plane shear in all groups.

Table 6-5 Local strain ratio. Results are given as median $[Q_1, Q_3]$, where Q_1 and Q_3 are the first and third quartile, respectively. t refers to an unpaired two-tailed t test (t), U indicates that a MANN-WHITHNEY U test was performed. * and ** indicate that differences are significant at the 0.05 and 0.01 level, respectively, observing the Bonferroni correction for multiple testing. 'o' indicates a tendency towards significance, i.e. $0.05 \geq p \geq 0.0167$.

	< 40 y.o.	> 60 y.o.	AAA	< 40 y.o. vs. > 60 y.o.	< 40 y.o. vs. AAA	> 60 y.o. vs. AAA
Longitudinal	7.0 [6.2, 9.2]	7.5 [5.5, 10.6]	7.33 [6.0, 11.7]	U, -	U, -	U, -
Circumferential	2.0 [1.9, 2.6]	5.17 [3.4, 6.8]	9.8 [5.9, 14.9]	U, **	t, **	U, **
In-plane shear	13.3 [8.2, 23.4]	15.6 [10.3, 19.6]	14.95 [11.8, 20.6]	t, -	t, -	t, -
Area	3.0 [2.5, 3.8]	5.1 [4.3, 8.7]	8.1 [5.9, 11.2]	U, **	t, **	U, -

6.4.3.4 Heterogeneity index

Qualitatively, the results obtained for the heterogeneity index show a similar picture as the local strain ratio [Table 6-6]: For the distributions of circumferential strains, highly significant differences at the 0.001 level were found between the young and the elderly and the young and the AAA groups and significant differences at the 0.05 level were observed between the elderly and the AAA group. Values of the circumferential heterogeneity index increased from the young through the elderly to the AAA group. In contrast, no significant differences in the heterogeneity of longitudinal strain and in-plane shear distributions were observed between different groups and the heterogeneity of area strain distributions characteristically separated the young group from both age matched patient groups but was not significantly different between the elderly and the AAA group. In the young and the elderly group, circumferential strain exhibited lower heterogeneity indices compared to longitudinal strain and in-plane

shear whereas the distribution of the longitudinal strain component was least heterogeneous in the AAA group. In all groups, the largest heterogeneity was observed for in-plane shear.

Table 6-6 Heterogeneity index. Results are given as median[Q_1, Q_3], where Q_1 and Q_3 are the first and third quartile, respectively. t refers to an unpaired two-tailed t test (t), U indicates that a MANN-WHITNEY U test was performed. * and ** indicate that differences are significant at the 0.05 and 0.01 level, respectively, observing the Bonferroni correction for multiple testing. 'o' indicates a tendency towards significance, i.e. $0.5 \geq p \geq 0.0167$.

	< 40 y.o.	> 60 y.o.	AAA	< 40 y.o. vs. > 60 y.o.	< 40 y.o. vs. AAA	> 60 y.o. vs. AAA
longitudinal	2.3 [1.2, 2.7]	2.1 [1.5, 3.1]	2.2 [1.5, 3.3]	U, -	U, -	t, -
circumferential	0.4 [0.3, 0.5]	1.6 [0.9, 2.1]	2.6 [1.5, 3.6]	U, **	U, **	t, *
in-plane shear	4.2 [2.9, 6.3]	5.3 [3.3, 6.5]	4.7 [3.3, 6.3]	U, -	U, -	t, -
area	0.6 [0.5, 0.9]	1.5 [1.2, 2.6]	2.0 [1.7, 3.2]	U, **	U, **	U, -

Significant and highly significant differences between all different patient groups were found for all circumferential strain distribution indices, except for the differences in local maximum strain between the elderly and the AAA group. Decreasing mean circumferential deformation and increasing heterogeneity of the spatial distribution of local circumferential deformations were observed from the young through the elderly to the AAA group. In contrast, only few indices that describe the spatial distribution of other in-plane strain components showed significant differences between groups and were not able to distinguish the wall motion of all groups.

6.4.4 Comparison of distensibility distribution indices between patient groups

The results for the comparison of the distensibility distribution indices between the three patient groups are shown in Figure 6-3. Mean distensibility was significantly different in all patient groups, with values decreasing from the young ($3.83 [2.83, 5.87] 10^{-3} \text{mmHg}^{-1}$) to the elderly ($0.67 [0.39, 0.87] 10^{-3} \text{mmHg}^{-1}$) and AAA group ($0.27 [0.20, 0.54] 10^{-3} \text{mmHg}^{-1}$). In contrast, significant differences in the maximum local distensibility values were observed between the young ($9.08 [7.79, 12.03] 10^{-3} \text{mmHg}^{-1}$) and both aged groups (elderly: $3.41 [2.29, 4.78] 10^{-3} \text{mmHg}^{-1}$, AAA: $2.59 [2.20, 3.68] 10^{-3} \text{mmHg}^{-1}$), only, but not between the elderly patients without AAA and the AAA group. It is of note that in one of the AAA patients the maximum local distensibility ($12.93 10^{-3} \text{mmHg}^{-1}$) was in the range of the fourth quartile of values observed in the young group [Figure 6-3 b]. Local distensibility ratio was significantly increasing from the young ($2.14 [1.99, 2.67]$) through the elderly ($5.27 [3.35, 6.86]$) to the AAA group ($9.83 [5.96, 14.80]$). The second index pro-

posed for the characterization of heterogeneous elastic behavior (heterogeneity index) showed a comparably significant increase from the young (0.42 [0.34, 0.48]) through the elderly (1.57 [0.92, 2.00]) to the AAA group (2.53 [1.53, 3.53]).

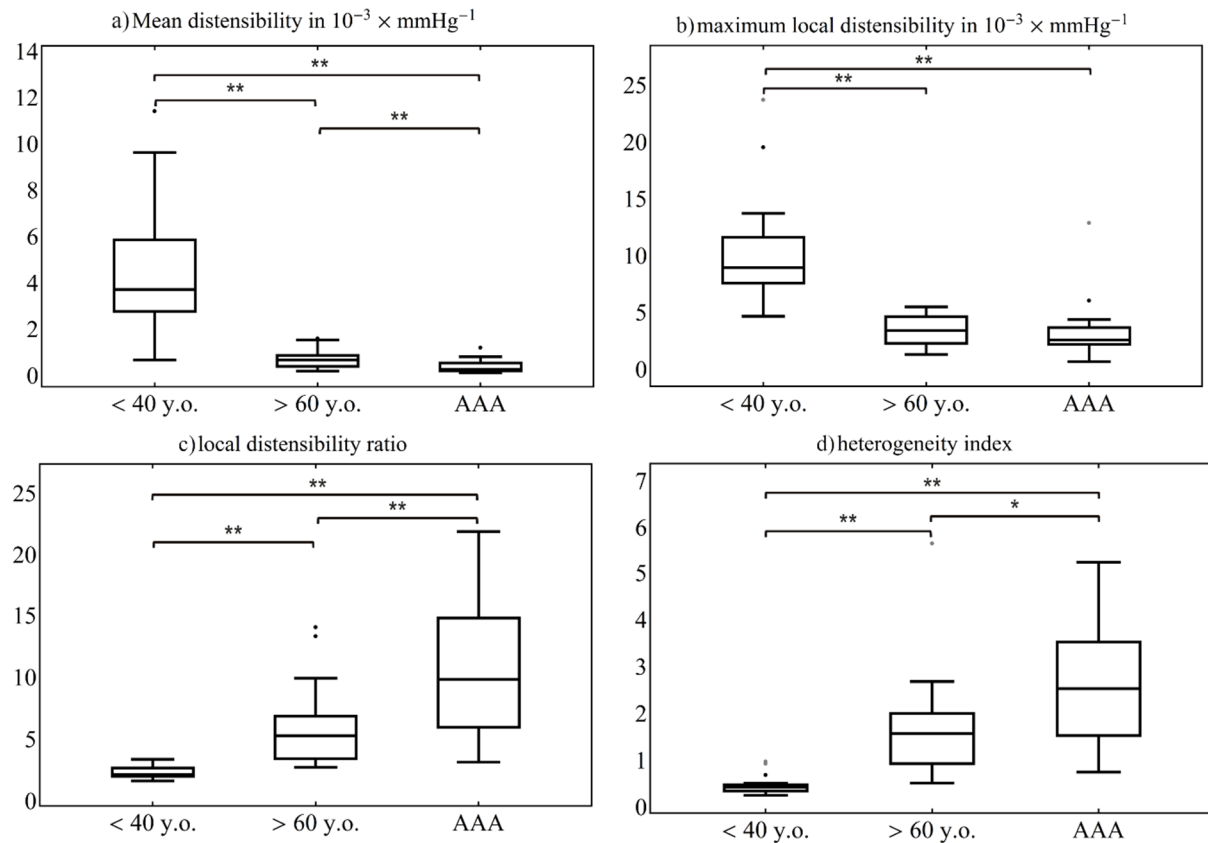


Figure 6-3 Comparison of local distensibility indices between groups. a) Mean of the local distensibility distribution, b) maximum of the distensibility distribution, c) ratio of maximum and mean distensibility, d) coefficient of variation of the distensibility distribution. Boxes show the median and range of Q_1 to Q_3 , whiskers extend to minimum and maximum values, respectively (outliers are indicated by filled circles). */** denote statistically significant differences (* $p < 0.0167$, ** $p < 0.0033$). [Reprinted from Wittek et al. 2018 with permission from John Wiley and Sons]

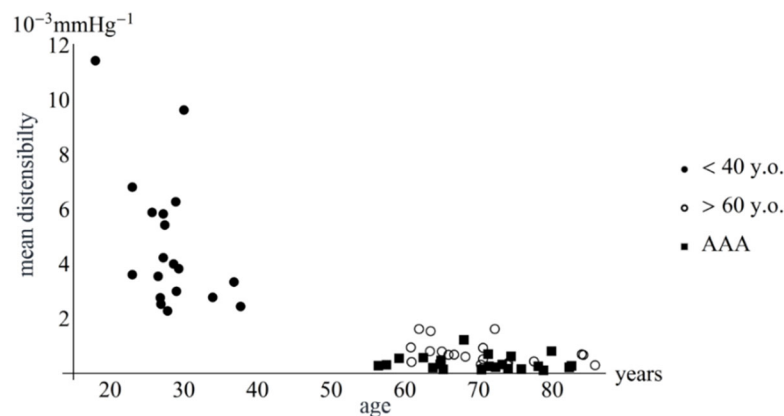


Figure 6-4: Mean distensibility vs. age for all volunteers and patients that were included in the study. [Reprinted from Wittek et al. 2018 with permission from John Wiley and Sons]

6.4.5 Correlation of distensibility distribution indices with age and diameter

The mean distensibility and the local distensibility ratio values of all volunteers and patients versus age are given in Figure 6-4 and Figure 6-5, respectively. Figure 6-4 suggests a non-linear relation between the mean distensibility and age. Figure 6-5 might suggest an almost linear increase of local distensibility ratio in the young and old group if three outliers were excluded from the latter, whereas the AAA group is distinctive in its wide dispersion. However, differences between subjects in different groups were not only due to age, but also due to pathology (cf. section 6.4.1). The data available for the non-aneurysmal patients was not sufficient to reliably fit a model for the age dependency of mean distensibility or local distensibility ratio.

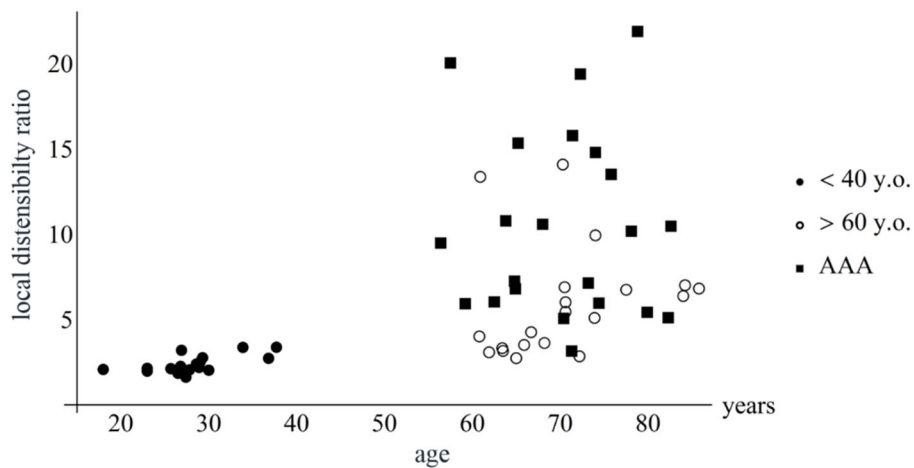


Figure 6-5: Local distensibility ratio vs. age for all volunteers and patients that were included in the study. [Reprinted from Wittek et al. 2018 with permission from John Wiley and Sons]

Within each group, the dependency of the distensibility indices on age and on the diameter was tested by correlation analysis, assuming a linear model. The results are given for age and diameter in Table 6-7 and Table 6-8, respectively. In the young group, mean distensibility showed a negative correlation with age, whereas local distensibility ratio increased significantly with age. In the elderly and AAA group, the dependency of mean distensibility on age was lost, while the correlation of local ratio and heterogeneity index with age was present in the elderly group as well, but not in the AAA group.

In the young group, the mean and maximum local distensibility showed a significant negative correlation with increasing average diameter, whereas both indices for the heterogeneity of the aortic wall's elastic behavior, local distensibility ratio and the heterogeneity index, showed highly significant positive correlations with the diameter. In contrast, in the elderly group and the AAA group, no statistically significant relation between distensibility distribution indices and diameter was observed at all [Table 6-8].

Table 6-7: Dependency of the distensibility distributions on age in the young, the elderly and the AAA group, respectively. -, * and ** indicate the absence of a statistically significant correlation, a statistically significant and a highly significant correlation, respectively. [Reprinted from Wittek et al. 2018 with permission from John Wiley and Sons]

	Test	Test statistic	p	
<hr/>				
< 40 y.o.				
Mean	Spearman Rank	-0.52	< 0.05	*
Maximum	Spearman Rank	-0.13	> 0.05	-
Local ratio	Spearman Rank	0.62	< 0.01	**
Heterogeneity	Spearman Rank	0.37	> 0.05	-
<hr/>				
> 60 y.o.				
Mean	Pearson	-0.38	> 0.05	-
Maximum	Pearson	-0.12	> 0.05	-
Local ratio	Spearman Rank	0.45	< 0.05	*
Heterogeneity	Spearman Rank	0.47	< 0.05	*
<hr/>				
AAA				
Mean	Spearman Rank	-0.21	> 0.05	-
Maximum	Spearman Rank	-0.16	> 0.05	-
Local ratio	Pearson	-0.01	> 0.05	-
Heterogeneity	Pearson	0.09	> 0.05	-
<hr/>				

Table 6-8: Dependency of the distensibility distributions on the diameter in the young, the elderly and the AAA group, respectively. In the young and the elderly group, the average vessel diameter was used. In contrast, in the AAA group the maximum diameter was used that was measured clinically. -, * and ** indicate the absence of a statistically significant correlation, a statistically significant and a highly significant correlation, respectively. [Reprinted from Wittek et al. 2018 with permission from John Wiley and Sons]

	Test	Test statistic	p	
<hr/>				
< 40 y.o.				
Mean	Spearman Rank	-0.68	< 0.01	**
Maximum	Spearman Rank	-0.54	< 0.05	*
Local ratio	Spearman Rank	0.65	< 0.01	**
Heterogeneity	Spearman Rank	0.64	< 0.01	**
<hr/>				
> 60 y.o.				
Mean	Pearson	-0.28	> 0.05	-
Maximum	Pearson	-0.10	> 0.05	-
Local ratio	Spearman Rank	0.29	> 0.05	-
Heterogeneity	Spearman Rank	0.28	> 0.05	-
<hr/>				
AAA				
Mean	Spearman Rank	-0.25	> 0.05	-
Maximum	Spearman Rank	-0.32	> 0.05	-
Local ratio	Pearson	0.15	> 0.05	-
Heterogeneity	Pearson	0.03	> 0.05	-
<hr/>				

6.4.6 Correlation of strain and distensibility distribution indices

All circumferential strain and corresponding distensibility distribution indices showed highly significant correlation within each group as well as in the total patient collective (SPEARMAN's rank correlation, $p < 0.01$). However, if the relative deviation of the actual mean and local maximum distensibility from the estimate of the linear regression model is considered [Figure 6-6], large deviations are not observed in the young group, but in aged patients and, in particular, in AAA patients. Eight patients were identified as outliers of the distribution of relative deviations from mean distensibility predictions. Two of

these were from the elderly group and six were AAA patients. Six outliers were observed in the distribution of deviations from estimated local maximum (peak) distensibility, among them two elderly and four AAA patients.

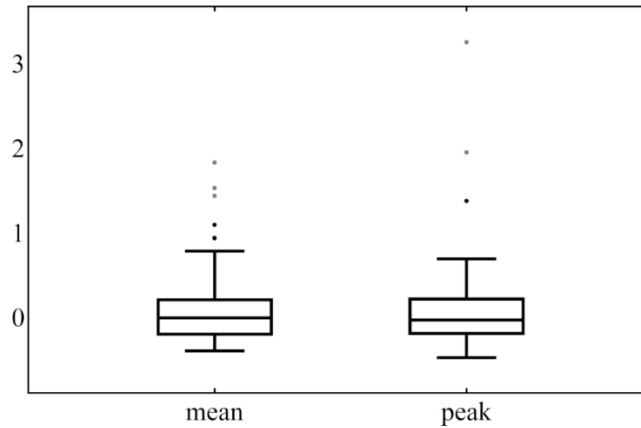


Figure 6-6 : Distribution of relative deviations of mean and peak distensibility from linear model predictions that are based on mean and peak circ. strain, respectively. Distributions are given for all volunteers and patients that were included in the study. Number of outliers shown seems to be lower than mentioned in the text because some values are so similar that they appear to be identical in the chart. [Reprinted from Wittek et al. 2018 with permission from John Wiley and Sons]

6.5 Discussion and limitations

In this chapter, a local formulation of the distensibility coefficient DC_l was introduced [eq. 6-11]. This new formulation of a local DC_l in combination with full field strain measurements by 4D ultrasound allows to estimate and analyze the individual, locally varying and heterogeneous cyclic elastic behavior of the geometrically irregular aortic and aneurysmal wall, strictly based on data that are available non-invasively in vivo and without the need for any modeling assumptions. In addition, the temporally and spatially resolved deformation of aortic segments and aneurysms was evaluated. In contrast to the analysis of strain distributions obtained by 4D ultrasound, as presented in chapter 6.4.3, the inclusion of information on the acting loads, to calculate the spatially resolved distensibility, allowed to rule out that observed differences might be caused by different pulse pressures, only. The comparison of the computed distensibility distributions to corresponding strain distributions showed that the correlation between distensibility and strain-based indices was highly significant, but large deviations between these indices were observed, in particular, in AAA patients [cf. 6.4.6, Figure 6-6].

Though all components of the in-plane strain tensor were available from 4D ultrasound imaging, only circumferential distensibility was calculated in this study, for two reasons: The analysis of the mean and local maximum values of all components of the BIOT's in-plane strain tensor showed that circumferential deformation governed abdominal aortic deformation, in particular, in the young group. This

effect was weakened in the elderly and the AAA group. Even more important was the finding that circumferential strain distribution indices provided the most powerful distinction between the three patient groups [Table 6-3, Table 6-4, Table 6-5 and Table 6-6].

The comparative study of young and two groups of age-matched elderly and diseased cardiovascular patients with and without aneurysms, that is presented here, proofed that the heterogeneous distributions of local distensibility can be used to classify the pathophysiological state of the aortic wall from non-invasive measurements. The rationale behind this approach are the known changes in microstructural composition of the aortic wall with age [cf. chapter 1.7.1] and with progression of AAA development [cf. chapter 1.7.2]: degradation of elastic components results in reduced distensibility of the wall [Nichols et al. 2011]. Though atherosclerotic plaque is not an effect of aging itself, it is ubiquitous in adults in western societies starting from early adulthood [Nichols et al. 2011] and will result in increasing heterogeneity of cyclic elastic behavior of the wall. As to the progression of AAA development, in particular, Lindeman et al. [2010] have investigated the reorganization of the collagen: Despite the fact that collagen concentration and cross-linking are even increased in AAA, collagen does not behave as a network any more. The tissue loses its ability to evenly distribute mechanical forces that are loaded on individual fibers resulting in local stress concentration and, potentially, overload. High variability in wall thickness was observed [Thubrikar et al. 2001; Raghavan et al. 2006]. Further factors that contribute to the local variability or heterogeneity of the AAA wall's elastic behavior are local vulnerabilities due to cystic degeneration of the media and calcifications at different length scales [Niestrawska et al. 2016; Niestrawska et al. 2019]. These changes at microscopic length scales are known to result in weakening of wall strength and increasing rupture risk but cannot be measured non-invasively in vivo. On the macroscopic level, they will result in a decrease of the mean distensibility and a local variation of wall distensibility, resulting in an increased heterogeneity of the distensibility field. We hypothesize that "lumped" macroscopic effects of microstructural changes in the aneurysmal wall can be assessed and quantified by the proposed distensibility distribution indices.

The mean of the distribution of local DC_l values as defined in eq. 6-11 corresponds to the common definition of arterial distensibility by relative change in cross-sectional area related to pulse pressure [see as well Oishi et al. 2008]. In the present study, mean distensibility was reduced with age and in AAA patients [Figure 6-3]. Age-related arterial stiffening has been reported in elastic arteries [O'Rourke 1990; O'Rourke 2007] and Nichols et al. [2011] emphasized that aging 'changes do not simply develop in the elderly but are progressive throughout life and are well developed by early adulthood'. This was confirmed in this study by the negative correlation of mean distensibility with age in the young group. According to Redheuil et al. [2010], the effect is decreasing with age, which was supported in the current study by the loss of correlation in the elderly group [Table 6-7]. The heterogeneity of the distensibility distribution increased with age and AAA development [Figure 6-3 c and d, Figure 6-5]. A positive correlation between the indices characterizing the heterogeneity of the elastic behavior (local ratio and heterogeneity index) and age was found in the young and elderly group but was not present in the AAA

group. These findings might suggest that the further reduction of mean distensibility and increase of local ratio and heterogeneity index from the age-matched elderly to the AAA group (Figure 6-3) was connected to the specific pathological changes of aneurysms.

Since the maximum diameter criterion is the current gold standard for clinical AAA rupture risk assessment [Debus et al. 2018; Wanhainen et al. 2019], the relation between the distensibility distribution indices and the aortic or aneurysmal diameter in each patient group was evaluated. Negative correlations of mean and local maximum distensibility and diameter in the young group between 20 and 40 years of age indicated aortic stiffening with increase of diameter. These findings are in accordance with Nichols et al. [2011] and citations therein, who state that ‘elastic arteries progressively stiffen as well as dilate’ with age. The observed highly significant positive correlation of the indices for heterogeneity of mechanical properties with increasing diameter in this group is in accordance with known adverse structural changes such as age-related arteriosclerosis and developing atherosclerosis, which is not age-related in itself but ubiquitous in adults in western societies [cf. chapter 1.7]. In contrast, no correlation between any of the distensibility distribution indices and diameter was observed in the elderly and, in particular noteworthy, in the AAA group. The author concludes, that the distensibility distribution indices provide independent *in vivo* information on the pathophysiological state of the AAA wall in addition to the maximum diameter criterion. The DDIs – and SDIs – are promising candidates as additional biomarkers for non-invasive *in vivo* evaluation of the mechanical state and stability of AAA walls. Niestrawska et al. [2019] suggested the use of the local strain ratio as presented in Wittek et al. [2018], one of the publications underlying this chapter, as *in vivo* equivalent of the ‘inflection point’ [cf. chapter 1.7.2] for the classification of AAAs according to the stage of disease progression.

This working hypothesis is encouraged by previous results of other groups that indicate that individual wall strain and distensibility might be the more powerful predictor of AAA rupture risk, not only compared to the diameter criterion, but also compared to peak wall stress that was proposed as biomechanical predictor for increased AAA rupture risk [Fillinger et al. 2002; Fillinger et al. 2003; Vorp 2007; Humphrey and Holzapfel 2012; Martufi and Christian Gasser 2013; Disseldorp et al. 2019b]: Wilson et al. [2003] showed that changes in distensibility are indicative for immediate rupture risk, Romo et al. [2014] have shown in *in vitro* experiments that local maximum strain (and distensibility) is an early and more reliable predictor of rupture compared to wall stress. In this context, locally confined areas of exceptionally large strain and distensibility in a stiffened AAA wall might indicate sites of the AAA wall that are prone to rupture. Duprey et al. [2016] have demonstrated that the physiological modulus, i.e. the inverse of the distensibility, correlates with an *in vitro* stretch based failure criterion in ascending thoracic aortic aneurysms.

Seen in the context of the aforementioned results by other groups, the results presented in this chapter indicate that the *in vivo* assessment and analysis of individual heterogeneous strain and distensibility distributions is a promising approach to better monitoring and understanding of structural changes in the AAA wall with the progression of the disease and, eventually, might contribute to better evaluation

of individual wall strength or rupture risk. In order to test this hypothesis, however, further studies are necessary. The relation between strain and distensibility distribution (indices) and the individual wall strength or rupture risk of an AAA has to be determined. This is a challenging task since no independent and reliable *in vivo* rupture risk or wall strength criterion is available for validation of a new one. Recently, Duprey et al. [2016] and, from the same group, Farzaneh et al. [2019] have proposed to determine individual strain- and stress-based rupture risk indices from mechanical failure tests on aortic aneurysm tissue samples that were excised intraoperatively. Combined with *in vivo* information on aneurysm geometry and blood pressure, these *in vitro* rupture risk indices can be used for validation of *in vivo* rupture risk predictors.

Between 20 and 37 deformed configurations of the aortic wall during one pulse cycle were obtained for each patient in this study. In contrast, only minimum and maximum blood pressure could be measured non-invasively *in vivo*. If the locally varying elastic behavior is to be assessed, two load cases were available, only, that were defined by pairs of minimum and maximum local deformation and homogeneous blood pressure, respectively. These data allowed for the determination of a linear model, only. In relevant literature, distensibility is widely accepted as linear approximation of the elastic behavior of arteries in the physiological range [e.g. Fung 1997; Nichols et al. 2011; Caro 2012]. However, the aortic and aneurysmal wall is an anisotropic and non-linear elastic composite [cf. chapter 1.5 and citations therein] consisting of three concentric layers with characteristically distinct constitutive behavior [cf. chapter 1.4.2, Holzapfel 2009; Weisbecker et al. 2012]. *In vivo*, it cannot be observed in a load-free configuration, but is exposed to cyclically varying blood pressure (that can be measured) and axial pre-stretch and -stress that cannot be measured. The load-free configuration of the excised aorta is not stress-free, its stress-free state consists of open-sector segments [cf. chapter 1.6 and citations therein] and it has been shown *in vitro* that the opening angle that is used to quantify the residual bending load varies between the distinct layers of the aortic wall [Holzapfel et al. 2007; Holzapfel 2009]. Layer-specific [Holzapfel 2009] and locally varying non-linear and anisotropic constitutive properties of the aortic wall [Lu and Zhao 2009; Zhao et al. 2009; Bersi et al. 2016] have been identified based on *in vitro* experiments on excised tissue samples. The author of this thesis has used heterogeneous strain fields obtained from 4D ultrasound imaging for *in vivo* parameterization of an adequate constitutive model [Gasser et al. 2006] based on the observation of two load cases, diastolic and systolic blood pressure, only [see chapter 7 and Wittek et al. 2013, Wittek et al. 2016a]. In turn, homogeneous material properties had to be assumed for the whole imaged structure. This assumption holds well for aortae of young volunteers. It is less appropriate for aged aortic walls and aneurysms, though it is still a state of the art assumption in AAA wall stress analyses [Farotto et al. 2018]. In this study, assessment of the local variation of elastic behavior and of the heterogeneity of its distribution was intended and therefore the approach was restricted to a linear model.

Evidently, an isotropic and linear model like the *DC* is not adequate for modeling the constitutive behaviour of a complex composite material. It is a linear approximation of the cyclic elastic behavior in

the physiological range, only. The physiological range itself depends on the individual loading conditions so that distensibility may change, even if the non-linear constitutive behavior remains the same: for a given material, an increase of mean and pulse pressure as observed in this study in both aged groups compared to the young group will result in an increased secant modulus of a stress-strain curve, the slope of which progressively increases with larger deformations [cf. Figure 1-10], i.e. in reduced distensibility in the loading range. It has been shown that larger axial prestretch increases circumferential distensibility of the aortic wall [Horný et al. 2014]. Axial prestretch of the human aorta is characteristically decreasing with age [Horný et al. 2012; Horný et al. 2013] so that the decrease of mean distensibility with age that was observed in this study [Figure 6-4] in accordance with e.g. Nichols et al. [2011], O'Rourke [1990], O'Rourke [2007] and O'Rourke and Hashimoto [2007] may not only result from a change in the constitutive behavior, but from the decrease in axial prestretch, too. Nevertheless, the cyclic elastic behavior in the physiological range proved to be a relevant and non-invasively detectable indicator for adverse systemic effects of changes in the aortic wall's constitutive behavior in various studies [O'Rourke et al. 2002; Todd J. Anderson 2006; O'Rourke and Hashimoto 2007; Gary F. Mitchell 2009; Mitchell et al. 2010].

In addition to this, the *DC* depends on geometrical parameters implicitly and, therefore, may not be regarded as a proper material parameter. For simplicity, this dependency is demonstrated here for uniaxial circumferential CAUCHY stress σ and BIOT's strain ε of a pressurized thin-walled cylinder: We assume the one-dimensional form of HOOKE's law as linear estimate of material properties:

$$\Delta\sigma = E\Delta\varepsilon, \quad \text{eq. 6-12}$$

where E is the YOUNG's modulus. The dependency of the cyclic CAUCHY stress on the pulse pressure is given by the law of LAPLACE (or YOUNG-LAPLACE equation)

$$\Delta\sigma = \Delta p \frac{r}{h}, \quad \text{eq. 6-13}$$

where p is the transmural pressure and r and h are the current radius and wall thickness, respectively. From eq. 6-12 and eq. 6-13

$$\Delta\varepsilon = \Delta p \frac{r}{Eh} \quad \text{eq. 6-14}$$

is obtained. Neglecting quadratic terms for $\Delta\varepsilon \ll 1$, eq. 6-10 simplifies to

$$DC \approx 2 \frac{\Delta\varepsilon}{\Delta p}. \quad \text{eq. 6-15}$$

With eq. 6-14, the following relation between the distensibility coefficient and the YOUNG's modulus is obtained:

$$DC = 2 \frac{r}{h} \cdot E^{-1}. \quad \text{eq. 6-16}$$

Equation eq. 6-16 shows that the DC does not only depend on the (linearized) material properties, but on a geometrical parameter, the radius-to-thickness ratio r/h . In contrast, the YOUNG's modulus $E = \Delta\sigma/\Delta\varepsilon$ is a "pure" elastic material parameter relating current stress to current strain. However, it cannot be determined from in vivo data, as long as the thickness h of the individual aortic wall cannot be measured non-invasively in vivo. For the time being, none of the available imaging techniques provides this information for a structure hidden so deep in the body as the human aorta with sufficient accuracy. Membrane stiffness $k = \Delta\tau/\Delta\varepsilon$, where $\Delta\tau = \Delta\sigma \cdot h = \Delta p \cdot r$ and thus $k = Eh$, could be considered as an alternative to the DC for thin-walled structures [e.g. Farzaneh et al. 2018; Disseldorp et al. 2019b]. The current radius (or for more complicated geometries the local principal radii) can be determined from various in vivo imaging data with sufficient accuracy. Nevertheless, like the DC , the membrane stiffness k still depends on an unknown geometrical parameter in the wall thickness h . Compared to the membrane stiffness that depends on h alone, the dependency of the DC on the ratio of radius and wall thickness, r/h , has the advantage that the geometrical dependency vanishes if the changes of r and h scale with the same factor. It was shown by Wolinsky and Glagov [1967a] that this is the case, approximately, for a wide range of adult mammalian species. Cyron and Humphrey [2017] have understood this as a mechanism serving to maintain an optimal homeostatic stress for which continuous remodeling of collagenous soft tissues reaches a mechanobiologically static state. Evidently, this assumption of a constant r/h -ratio will hold for healthy adults, only, not for AAAs where the remodeling of the aortic wall is impaired by pathology. Thubrikar et al. [2001], DiMartino et al. [2006], Raghavan et al. [2006], Raghavan et al. [2011] and Reeps et al. [2012] report values of (mean) diameter and wall thickness for a total of 201 unruptured and 17 ruptured AAAs. From these data the author computed $r/h = 17.1 \pm 5.2$ and $r/h = 12.6 \pm 3.4$ for unruptured and ruptured AAAs, respectively. In comparison to the value of 7.9 that was reported for the aged abdominal aorta by Learoyd and Taylor [1966], these values are considerably increased. It is particularly noteworthy that an increased r/h in AAAs will result in an *increase* of the DC [cf. eq. 6-16]. In contrast, in the results presented in this chapter the mean DC of the AAA group was *decreased* significantly compared to the non-aneurysmal aged group [Figure 6-3]. This shows that the implicit dependency of the DC on the geometrical parameter r/h does not dominate or eliminate the effects of pathologic changes that are to be assessed in this work. In contrast the deviation of the geometric parameter r/h might be understood as an indicator of pathological remodeling, which however according to Niestrawska et al. [2019] may result in stable or vulnerable remodeled AAA walls. Commonly, saccular AAA, that show a larger spread of local radii, are considered to be more prone to rupture than fusiform AAA [Pappu et al. 2008]. Raghavan et al. [2006] report minimum and maximum wall thicknesses of 0.23 mm and 4.26 mm in four AAAs with a median wall thickness of 1.48 mm and a median diameter of 60 mm, resulting in a median r/h of 20 and in radius to

thickness ratios of 130.4 for the minimum and 7.04 for the maximum wall thickness. For the site of minimum wall thickness, the factor r/h would result in a locally confined area of large distensibility in a generally stiff wall, which would be well captured by two of the proposed distensibility distribution indices, the local maximum distensibility and the local distensibility ratio. In this context, it is noteworthy that the lowest wall thickness was observed within a 1 cm radius of a rupture site.

Summing up, distensibility is not an “optimal” material parameter because of its dependency on a geometrical parameter. However, for the time being, it is not possible to determine the individual and geometry-independent material properties non-invasively in vivo without non-individual assumptions, because wall thickness cannot be measured. Therefore, and because of its relevance for understanding systemic cardiovascular effects, in the study that is presented here, the local formulation of the DC was considered as a reasonable in vivo approach to assess cyclic elasticity of the individual human aorta and its spatial heterogeneity. Because of the discussed deficiencies of the DC and DC_l as constitutive model, the author prefers to talk about the cyclic elastic behavior of the aortic and aneurysmal wall rather than its constitutive or material properties.

For the common calculation of distensibility from the diameter of the vessel, the assumption of a thin walled cylinder is made implicitly [cf. section 6.2]. We have already shown above that the introduced local formulation of the DC (eq. 6-11) is not restricted to cylindrical geometries. In contrast, the assumption of a thin wall is maintained in the current approach. Neither wall thickness, nor presence and local distribution of intra-luminal thrombus (ILT) [cf. chapter 1.7.2] could be determined reliably in each 4D ultrasound data set of an AAA that was included in this study. Strain variations in radial direction of the wall cannot be resolved by the measurement technique that is available, currently. The assumption of a thin walled structure is usually considered to be appropriate for the abdominal aorta (wall thickness to diameter ratio of 0.04 [Caro 2012]). In the case of AAA, the wall is thin compared to the diameter, too. However, the presence of ILT might add to the effective wall thickness. The role of ILT in the mechanics of AAA is under debate [Wilson et al. 2013]. Meyer et al. [2010] showed in a numerical study that the mechanical loading and resulting deformation of the AAA wall is scarcely influenced by the presence of ILT if it can be regarded as a porous solid and is not (completely) attached to the wall. Schurink et al. [2000] and Hinnen et al. [2005] have investigated the effect of ILT on conduction of blood pressure to the covered aneurysmal wall experimentally and found that mean and pulse pressure within the ILT and on the wall correlate well with luminal pressure and are only slightly reduced. This is consistent with the observation that a network of small channels (“canniculi”) is characteristic of ILT pseudo-tissue [Adolph et al. 1997; Wilson et al. 2013] so that it may be regarded as a porous solid. Swedenborg and Eriksson [2006] and Whittaker and Przyklenk [2009] report a liquid phase between ILT and aneurysm wall suggesting that thrombus may not be attached to the wall. Following the results of these studies that are reported by Wilson et al. [2013], the ILT is not part of the wall and the thin-wall assumption that was made in the study underlying this chapter holds. However, these properties may vary considerably in different ILT and cannot be determined non-invasively in vivo. Most

computational numerical analyses of AAA wall stresses that include ILT assume its perfect attachment to the wall (as reported in Wilson et al. 2013). In these cases, it is modelled to be able to bear tensile loads and reduces the load on the wall considerably [Metaxa et al. 2015]. If thrombus needs to be considered as a solid that is perfectly attached to the wall, distensibility of the wall itself would be underestimated by the approach that is presented here, where the possible stress shielding role of ILT was disregarded. Neither the assumption of constant strain and stress over wall thickness that is implied by the thin wall assumption, would hold, nor the assumption of homogeneous material properties in radial direction. Having in mind that the aortic wall is a three-layered composite, the latter assumption is a simplification even without considering ILT, though Niestrawska et al. [2016; 2019] have shown recently that this multi-layered structure is lost in most AAA.

7 Identification of the orthotropic and hyperelastic constitutive behavior of aortic walls in vivo

7.1 Introduction

In this chapter, an in vivo approach to the solution of two coupled inverse problems is described that has been developed in the course of this thesis: the in vivo identification of, firstly, the individual orthotropic and non-linear elastic constitutive behavior and, secondly, the load-free configuration of the human aortic or aneurysmal wall [Wittek et al. 2013; Wittek et al. 2016a; Wittek et al. 2019].

7.1.1 State of research

The inverse identification of the constitutive behavior of the human aortic and aneurysmal wall tends to be an ill-posed problem: on the one hand, a whole set of constitutive functions and parameters has to be identified [cf. chapter 2.3], on the other hand, the material response to only a few load cases can be observed non-invasively in vivo [cf. chapter 3.2.1]. Under such circumstances it may be difficult to either identify any solution or to identify a unique solution. It has been shown that the use of full-field measurements of heterogeneous displacement or strain fields is an appropriate means to improve the reliability of parameter identification based on a reduced number of observed load cases [Grediac et al. 2006; Pottier et al. 2011; Stéphane Roux and François Hild 2018]. The information on displacement or deformation at internal degrees of freedom in addition to the boundary conditions may compensate for the lack of knowledge of the constitutive behavior [Avril et al. 2008]. Kroon and Holzapfel [2008, 2009] and Kroon [2010] have published approaches to the inverse identification of the locally varying, heterogeneous, nonlinear elastic and anisotropic constitutive behavior of irregularly shaped membranes based on numerically generated heterogeneous full-field strain and on pressure data. Since the heterogeneity

of the deformation data was used to identify the local constitutive behavior, temporally resolved deformation and pressure data were necessary to assess the nonlinearity of the constitutive behavior. Kroon and Holzapfel have used a Finite Element Model Updating (FEMU) method. Based on information on the reference configuration and its loading, the deformed configuration was estimated using a numerical model that depended on the choice of constitutive parameters. Estimated and measured deformation were compared by means of an error function. In an iterative process, the constitutive parameters on which the finite element (FE) model depended were varied systematically, i.e. the FE model was ‘updated’ in every iteration and the error function was minimized with regard to the constitutive parameters. However, groundbreaking these works were, no experimental data were provided to which the method could be applied. Lu and Zhao [2009] and Zhao et al. [2009] from the same group first presented and experimentally validated an approach to in vitro identification of the locally varying isotropic, nonlinear elastic behavior of pressurized membranes that was based on time-resolved pressure and optical full-field deformation measurements. Since then several inverse approaches to the identification of the homogeneous or locally varying nonlinear and anisotropic constitutive behavior of arterial walls have been presented that are based on measurements of pressure and axial prestress and optical full-field measurements of displacement and strain in vitro [Avril et al. 2010; Badel et al. 2012; Pierron and Grédiac 2012; Genovese et al. 2013; Avril et al. 2015; Bersi et al. 2016; Stéphane Roux and François Hild 2018].

However, in an in vivo setting, it is still a challenge to gather sufficient experimental data. Many clinically available medical imaging techniques are either too slow (standard MRI) to capture the dynamics of the cyclic deformation of the human aorta and/or do not provide the complete irregular 3D configuration (2D ultrasound). Other clinically established imaging techniques are not suited for research because they are invasive (intravascular ultrasound) or not radiation-free (CT and, in particular, gated CT scans) and expose the patients and volunteers to risks that are ethically not acceptable. Moreover, in contrast to in vitro approaches, neither the load-free (natural) configuration of the aortic wall, nor all loading conditions corresponding to the imaged deformed configurations are known. Only minimum (diastolic) and maximum (systolic) blood pressure can be measured non-invasively in vivo without additional model assumptions. Therefore, several approaches to in vivo material identification have restricted themselves to linear elastic tangent moduli of the nonlinear elastic behavior in the physiological range. Such an approach was presented in the previous chapter 6, which however differed from previous ones in that it captured the locally varying response of the wall to physiological loading. Schulze-Bauer and Holzapfel [2003], Masson et al. [2008], Stålhand et al. [2004], Stålhand and Klarbring [2005], Stålhand [2009], Smoljkic et al. [2015] and Gade et al. [2019] have assumed the blood vessel as a thin-walled cylinder with closed ends in order to identify the non-linear and anisotropic elastic constitutive behavior of the arterial wall. The assumption of a cylindrical vessel geometry with closed ends allowed for the computation of axial and circumferential stress from blood pressure and diameter data using the well-known engineering formulas for wall stress in pipes [cf. the Young-Laplace equation eq. 6-13 for the ‘hoop’ stress]. Since only homogeneous stress and strain values were obtained

by this approach for each observed load case, temporally resolved diameter and pressure data throughout the cardiac cycle were necessary in order to identify the nonlinear elastic behavior of the wall. Temporally resolved pressure data cannot be measured non-invasively in vivo, but only estimated based on further assumptions for modeling the cardiovascular system. The main restriction of these approaches, however, is that the assumption of a perfect cylindrical shape of the vessel prevents their application to irregularly shaped aneurysms.

Using temporally resolved phase-contrast MR imaging Liu et al. [2012] have taken into account geometrically irregular configurations of human carotid arteries for the in vivo identification of the parameters of the isotropic nonlinear elastic MOONEY-RIVLIN model and of the load-free configuration of the arterial segment that cannot be imaged. They imaged several cross-sectional slices of the aortic wall with a temporal resolution of 30 frames per second and extracted the luminal (inner) and the outer contour of the wall from the 2D image data of each slice. In addition, diastolic and systolic blood pressure was measured. They applied a FEMU approach as well: The diastolic and systolic configurations of the arterial wall contours were estimated by means of an FE model that depended on assumed constitutive parameters. Measured and numerically estimated contours were compared and the deviation was minimized by means of systematically varying the constitutive parameters in an iterative process. Trabelsi et al. [2015] have suggested and successfully applied to in vivo data an approach that used the comparison of the measured and numerically estimated volume of geometrically irregular ascending aortic aneurysms to identify the parameters of an isotropic nonlinear constitutive model.

The works underlying this chapter [Wittek et al. 2013; Wittek et al. 2016a] were the first to present and verify an approach to the identification of the load-free configuration and the *anisotropic* nonlinear elastic constitutive behavior of irregularly shaped aortae and abdominal aneurysms that works based on clinically available in vivo data, which was proven by exemplary application to clinical data. The approach utilizes the non-invasive in vivo full-field displacement and strain measurement that is described in chapter 3: it provided the motion functions of discrete material points on the aortic wall [eq. 3-6.] as basis for continuum mechanical modeling. In addition, diastolic and systolic blood pressure measured at the brachial artery were available as in vivo information on the loading of the wall [cf. chapter 3.2.1]. I.e., despite 10 to 20 imaged current configurations of the aortic wall, for only two load cases information on the load acting on the structure and on its resulting locally varying and heterogeneous deformation was available as basis for the identification of the nonlinear elastic and anisotropic constitutive behavior. An iterative FEMU approach [cf. Avril et al. 2008] was chosen in order not to be restricted to vessel wall configurations that can be described analytically, e.g. cylindrical or spherical configurations, but to be able to capture real irregular configurations of aortae and aneurysms.

Since then, Liu et al. [2017, 2018, 2019c] have presented different approaches to the identification of the non-linear and anisotropic constitutive behavior of geometrically irregular aneurysms of the ascending aorta that are based on virtual, numerically generated full-field data, only, which might impair their claim to present approaches to in vivo constitutive parameter identification. One of their main

objectives was to significantly reduce computational cost of constitutive parameter identification compared to iterative FEMU approaches like the one that is presented in this thesis. In order to achieve this, they applied a multi-resolution direct search approach as well as a machine learning approach. Only recently, they have applied the proposed multi-resolution direct search approach to in vivo CT and blood pressure data of ascending thoracic aortic aneurysm patients [Liu et al. 2019b]. They compared the constitutive parameters that were identified based on in vivo data to those that were obtained from biaxial tensile test on excised tissue from the same patients in vitro. However, deviations between the constitutive parameters that were identified based on in vivo and on in vitro data were large.

7.1.2 Overview of the main steps of the inverse approach

To provide an overview of the FEMU approach that was developed within this thesis, the main steps of the method are briefly described here:

In vivo data acquisition: The discrete motion function [eq. 3-6] of an aortic wall segment was recorded by 4D ultrasound throughout the cardiac cycle and fields of heterogeneous in-plane BIOT's strains $\boldsymbol{\epsilon}^{US}$ with respect to the end-diastolic configuration were derived [cf. chapter 3.2 and 3.3 for the general approach and chapter 6.5 for the particular in vivo data that were used for this chapter]. In addition, diastolic and systolic blood pressure were measured.

Definition of a finite element model for the estimation of the deformation of the wall under physiological loading as a function of a chosen set of constitutive parameters: The diastolic configuration of the aortic segment was reconstructed from the positions of the material points in the end-diastolic state. A nonlinear anisotropic hyperelastic constitutive equation and a set of constitutive parameters were chosen for the characterization of the material [cf. chapter 7.4]. Physiological loading by transmural pressure and axial pretension force [cf. chapters 1.3 and 1.6] was applied and the diastolic and systolic in-plane strain distributions were computed [cf. chapter 7.6].

Identification of prestretches of the deformed reference configuration: Only deformed and prestressed configurations of the wall under physiological loading could be imaged in vivo. Therefore, an estimate of the load-free configuration was identified using an inverse optimal design approach. The solution of this inverse problem depended on the chosen constitutive parameters and had to be performed for each guess of constitutive parameters [cf. chapter 7.6.3]. Then, the direct boundary value problem was solved: the deformation of the estimated load-free configuration under physiological loading was computed in an FE analysis using the chosen constitutive behavior. As a result, an estimate of the prestretched and prestressed diastolic configuration was obtained.

Parameter identification: Because the arterial wall shows anisotropic behavior, constitutive parameter identification is a multiobjective optimization problem. The constitutive behavior was determined iteratively using a FEMU approach. In each iteration, the measured systolic in-plane strain distribution of the aortic wall with respect to the deformed diastolic reference configuration ($\boldsymbol{\epsilon}^{US}$) was checked with

the numerically estimated systolic in-plane strain distribution with respect to the deformed diastolic reference configuration ($\boldsymbol{\epsilon}^{model}$). The latter resulted from a FE analysis (FEA) of the aortic segment under physiological loads, i.e. transmural pressure and axial prestretch, and depended on a guess of the constitutive parameter set that was used in the analysis. The goodness of fit of the numerical model was quantified by means of an error function f_e that consisted of the weighted sums of squared residuals of the measured and the numerically estimated strain distributions. The construction of this error function reflected the multiobjectivity of the problem: f_e depended on the residuals of all in-plane strain components. A nonlinear optimization algorithm was used to vary the constitutive parameters and update the FE model systematically with new parameters in every iteration and to minimize the error function with regard to the unknown constitutive parameters. A mixed stochastic-deterministic approach was developed that includes a local search approach with multiple starting points for the deterministic algorithm.

Verification of the approach: The developed approach was verified by numerical experiments with regard to its ability to reproducibly identify a unique constitutive behavior of the aortic wall based on clinically available data, only [sections 7.8 and 7.9]. Firstly, it was tested whether the developed approach was capable to identify the numerical values of the parameters of the chosen constitutive model. Secondly, it was examined whether the stress-stretch curves along characteristic load-paths in the physiological domain could be determined, which represented the constitutive behavior independent of the choice of a specific constitutive model. Thirdly, it was checked in how far the developed approach was able to recover the load-free configuration of the wall segment sufficiently, that cannot be imaged in vivo. Finally, it was investigated how the measurement uncertainty that was determined in the validation of 4D ultrasound measurement [cf. chapter 4] affected the identification of the constitutive behavior.

Exemplary application to in vivo patient data sets: Eventually, the approach was applied to three in vivo 4D ultrasound data sets from male subjects of different age, health condition and showing varying peak-to-peak strain amplitudes in order to test the capability of the approach to identify age related and pathological changes of the elastic properties of the aortic wall: a 22 y.o. volunteer without known cardiovascular risk factors and diseases (HV), an 80 y.o. patient with peripheral arterial occlusive disease (PAOD) and a 58 y.o. patient with abdominal aortic aneurysm (AAA) [cf. sections 7.5.1, Table 7-2].

7.1.3 Organization of the chapter

The chapter is organized as follows: First, an overview of the assumptions that were made in this work for modeling the aortic wall in accordance with the state of research is given in section 7.2. Section 7.3 provides a theoretical basis for constitutive parameter identification of an orthotropic hyperelastic material based on the available in vivo data. In section 7.4, the constitutive equation is described that was chosen for modeling the orthotropic and nonlinear elastic behavior of aortic and aneurysmal walls. An overview of the in vivo full-field strain data and its acquisition is given in section 7.5. In section 7.6, the

computational FE model is explained in detail that estimates the cyclic strain field as function of a chosen set of constitutive parameters. The strategy of fitting the computational model optimally to the measured strain field data and, thus, identifying the individual constitutive parameters is developed in section 7.7. Section 7.8 provides information on the performed numerical verification experiments. In section 7.9, the results of the verification experiments are given. The results of the in vivo parameter identification are presented in chapter 7.10. The chapter concludes with a discussion of the developed methods and the obtained results [chapter 7.11] and final conclusions.

7.2 Assumptions for the patient-specific modeling

The deformation of the aortic wall and its passive elastic properties are described in this chapter based on the theory of finite non-linear elastic deformations [cf. chapter 2]. The approach of neglecting the viscoelastic properties of arterial walls is widely accepted since Fung et al. [1979] have introduced the concept of pseudoelasticity [cf. chapter 1.5], i.e. the approximation of the aortic wall's constitutive behavior in the reversible domain by time-independent hyperelastic models. Following Lawton [1954] and Carew et al. [1968], the aortic wall is modeled as an incompressible solid, which is a widely accepted state of the art assumption [cf. chapter 1.5 and e.g. Humphrey 2002; Nichols et al. 2011; Farotto et al. 2018], though this assumption has been questioned recently by Nolan and McGarry [2016].

In the current approach, the aortic wall is regarded as a single layered thin shell, often called the 'thin shell assumption', i.e. it is assumed to be a limp structure. Its in-plane loading and deformation are represented by the membrane stress and strain, which means that it is regarded to be constant across the thickness of the wall [cf. e.g. Kassab 2006, Fung 1993]. In in vitro studies, uniaxial or biaxial tensile tests can be performed separately for the three layers of the aortic wall, intima, media, adventitia [Holzapfel et al. 2007; Holzapfel 2008; Sommer et al. 2010; Weisbecker et al. 2012]. These data allow for layer-specific identification of the constitutive behavior. Moreover, the mean orientation of layer-specific fiber families and the dispersion of the fibers about these mean orientations can be measured from histological data [Holzapfel 2006] or Second Harmonic Imaging [Niestrawska et al. 2016; Niestrawska et al. 2019] in an in vitro setting. In this case, the measured mean orientations and dispersion can be understood as the preferred directions and the degree of anisotropy of the material, respectively. In the approach presented here however, 4D ultrasound imaging was used for acquiring in vivo measurements of locally resolved abdominal aortic wall motion of human subjects [cf. 3.2]. Given the available resolution, these in vivo measurements did neither provide image data on mean fiber orientation and dispersion of the fibers about this mean orientation, nor did they allow to differentiate between the motions of the three distinct layers of the aortic wall. Therefore, the aortic wall was modeled as a single layer with two preferred directions of anisotropy that are assumed to be symmetric to the local longitudinal and

circumferential in-plane axes and have the same mechanical properties [cf. Gasser et al. 2006]. In the presented approach, the preferred directions and the degree of anisotropy were identified in an inverse procedure together with the other parameters of the constitutive model [cf. 7.4] as suggested by Ogden [2009]. In *in vitro* experiments, Avril et al. [2010] and Marra et al. [2006] have successfully validated constitutive parameter identification using a one-layered aortic wall model. All approaches to *in vivo* identification of nonlinear elastic constitutive properties that were reported in section 7.1 have used one-layered wall models well. Consequently, in the current work, the preferred directions and the degree of anisotropy were treated as purely phenomenological parameters, which did not have a microstructural physical meaning. In accordance with most state of the art modeling approaches based on clinical data [cf. Farotto et al. 2018, Humphrey and Holzapfel 2012, Leemans et al. 2018], homogenous material properties were assumed for each imaged aortic segment, i.e. only one set of constitutive parameters was identified for each aortic segment.

The load-free configuration of the aortic segment was considered to be a stress-free natural configuration \mathcal{B}_0 . Residual internal stresses due to heterogeneity of the different layers of the wall that result in the opening angle of cut aortic rings [cf. chapter 1.6] were not taken into account. Recently, Maes et al. [2019] have presented and verified an approach to *in vitro* constitutive parameter identification of arterial tissue from planar biaxial tests that takes into account the residual stresses in the planar specimen due to the opening angle. The numerical verification experiment as well as the exemplary application of the approach to experimental data showed that taking into account the residual stresses or not, results in negligible deviations of the identified constitutive behavior.

As most other non-invasive imaging methods when applied to anatomical structures that are situated far from the surface of the body, 4D ultrasound imaging does not allow to measure the (varying) thickness of the aortic wall. Therefore, a constant wall thickness was assumed in the load-free configuration [cf. e.g. Joldes et al. 2018], resulting in varying wall thickness in deformed configurations due to heterogeneous in-plane deformation in combination with the incompressibility assumption [cf. chapter 1.5, chapter 2.3.2., eq. 2-65 and chapter 4.2.3.2, eq. 4-1]. Axial pretension force F_{red} and transmural pressure were considered as the dominant physiological loading of the aorta. This implies that the wall was regarded to be stress-free in radial direction in accordance with e.g. Joldes et al. [2015a], Joldes et al. [2017] and literature cited in Vorp [2007], Humphrey and Holzapfel [2012; Gasser] and Farotto et al. [2018]. The mechanical influence of wall shear stress due to blood flow was neglected since it is four to five orders of magnitude smaller than hydrostatic transmural pressure: Caro [2012] reports a shear stress of 0.53 Pa for the abdominal aorta, compared to 10.666 Pa of hydrostatic pressure on the wall that correspond to 80 mmHg and result in about seven times larger ‘hoop’ stress according to the law of Laplace for a vessel radius of 10 mm and a wall thickness of 1.5 mm. The axial pretension force F_{red} [cf. chapter 1.6] is assumed to be constant throughout the cardiac cycle in accordance with Schulze-Bauer and Holzapfel [2003], Smoljkic et al. [2015], Horny et al. [2013] and Weizsäcker et al. [1983].

In order to obtain transmural pressure from measured diastolic and systolic blood pressure values, intra-abdominal pressure was subtracted. In this way, the influence of perivascular tissue was considered in the current approach since the abdomen behaves like a hydraulic system [Keulenaer et al. 2009]. Moreover, for a set of dorsal nodes where the minimum measured radial displacement $\mathbf{u}_{dia-sys}^{US}$ was observed throughout the cardiac cycle all degrees of freedom (DOF) were fixed in the load-free and diastolic configurations and constrained by measured displacements $\mathbf{u}_{dia-sys}^{US}$ in the systolic configuration. Minimum cyclic displacement in the dorsal region was understood as indicating external support and restriction of wall motion through the spine. Preliminary results of Gallego et al. [2015] indicate that other influences of perivascular tissue are negligible. Petterson et al. [2019] emphasize the importance of regarding influence of perivascular tissue and spine support. Since wall thickness, reduced axial force and intra-abdominal pressure cannot be measured non-invasively in vivo, population-averaged data were used that are shown in Table 7-1.

Table 7-1: Non-individual modeling assumptions [Reprinted from Wittek et al. 2016a with permission from Elsevier]

Data set	Axial prestrain [%]	Constant wall thickness [mm]	Intra-abdominal pressure ^c [mmHg]
HV	31.0 ^a	1.5 ^b	7
PAOD	2.7 ^a	2.0 ^b	7
AAA	0.0 ^c	1.6 ^d	7

^a Calculated depending on the age of the patient according to Horny et al. [2011]

^b According to L. Horny, Faculty of Mechanical Engineering, Czech Technical University in Prague, personal communication, 13.04.2014

^c According to W. Derwich, Department of Vascular and Endovascular Surgery, University Hospital Frankfurt, personal communication

^d According to Gasser et al. [2010], Reeps et al. [2012] and Shum et al. [2010]

^e According to Keulenaer et al. [2009]

7.3 Theoretical basis for constitutive parameter identification in vivo

Holzapfel and Ogden [2009] and Ogden [2009] present a theoretical foundation of constitutive parameter identification of anisotropic materials based on planar biaxial in vitro tests. In this section, these considerations are adopted in order to theoretically investigate the feasibility of in vivo constitutive parameter identification based on 4D ultrasound measurements.

In eq. 2-111 the CAUCHY stress tensor for an orthotropic hyperelastic material with two preferred directions and without internal constraints is given. According to the previous section, it is assumed that arterial walls are incompressible and have two preferred directions in the wall plane that show identical material properties. Therefore,

$$\frac{\partial I_3}{\partial \mathbf{C}} = 0, \quad \text{eq. 7-1}$$

$$\frac{\partial w}{\partial I_{4\alpha}} = \frac{\partial w}{\partial I_{4\beta}} = \frac{\partial w}{\partial I_4} \quad \text{eq. 7-2}$$

and

$$\frac{\partial w}{\partial I_{5\alpha}} = \frac{\partial w}{\partial I_{5\beta}} = \frac{\partial w}{\partial I_5} \quad \text{eq. 7-3}$$

Thus the constitutive equation depends on the invariants I_1, I_2, I_4, I_5 and $I_{\alpha\beta}$ of the left CAUCHY-GREEN strain tensor \mathbf{B} , only. Consequently, the CAUCHY stress tensor for such a material reads as

$$\begin{aligned} \boldsymbol{\sigma} = & -p\mathbf{I} + 2 \frac{\partial w}{\partial I_1} \mathbf{B} + 2 \frac{\partial w}{\partial I_2} (I_1 \mathbf{B} - \mathbf{B}^2) + 2 \frac{\partial w}{\partial I_4} (\mathbf{a}_\alpha \otimes \mathbf{a}_\alpha + \mathbf{a}_\beta \otimes \mathbf{a}_\beta) \\ & + 2 \frac{\partial w}{\partial I_5} (\mathbf{a}_\alpha \otimes \mathbf{a}_\alpha \cdot \mathbf{B} + \mathbf{B} \cdot \mathbf{a}_\alpha \otimes \mathbf{a}_\alpha + \mathbf{a}_\beta \otimes \mathbf{a}_\beta \cdot \mathbf{B} + \mathbf{B} \cdot \mathbf{a}_\beta \otimes \mathbf{a}_\beta) \\ & + \frac{\partial w}{\partial I_{\alpha\beta}} (\mathbf{a}_\alpha \otimes \mathbf{a}_\beta + \mathbf{a}_\beta \otimes \mathbf{a}_\alpha). \end{aligned} \quad \text{eq. 7-4}$$

By means of 4D ultrasound, the deformation components in the wall (axial direction: 1; circumferential direction: 2) plane can be measured. Using the incompressibility condition [eq. 2-65], the radial deformation component (3-direction) can be expressed in terms of the in-plane components. Therefore, from 4D ultrasound measurements three-dimensional deformation of the aortic wall is obtained, neglecting shear in the 1-3 and the 2-3 planes. The deformation gradient and the left CAUCHY strain tensor assumes the following form:

$$\mathbf{F} = \begin{pmatrix} F_{11} & F_{12} & 0 \\ F_{21} & F_{22} & 0 \\ 0 & 0 & F_{33} \end{pmatrix} \langle \mathbf{e}_i \otimes \mathbf{e}_j \rangle, \quad \text{where } F_{33} = \frac{1}{F_{11}F_{22} - F_{12}F_{21}} \quad \text{eq. 7-5}$$

and

$$\mathbf{B} = \begin{pmatrix} B_{11} & B_{12} & 0 \\ B_{12} & B_{22} & 0 \\ 0 & 0 & B_{33} \end{pmatrix} \langle \mathbf{e}_i \otimes \mathbf{e}_j \rangle, \quad \text{where } B_{33} = \frac{1}{B_{11}B_{22} - B_{12}^2}. \quad \text{eq. 7-6}$$

The two preferred directions that are assumed to be symmetric with regard to the 1- and the 2-axis of a local coordinate system are described in the reference configuration by

$$\mathbf{a}_{0\alpha/\beta}(\varphi) = \sin\varphi\mathbf{e}_1 + /-\cos\varphi\mathbf{e}_2 . \quad \text{eq. 7-7}$$

Consequently, the deformed direction vectors $\mathbf{a}_{\alpha/\beta} = \mathbf{F} \cdot \mathbf{a}_{0\alpha/\beta}$ take the form

$$\mathbf{a}_{\alpha/\beta} = (F_{11}\sin\varphi + F_{12}\cos\varphi)\mathbf{e}_1 + /-(F_{21}\sin\varphi + F_{22}\cos\varphi)\cos\varphi\mathbf{e}_2 . \quad \text{eq. 7-8}$$

Consider the three structure tensors for this case:

$$\begin{aligned} \mathbf{a}_\alpha \otimes \mathbf{a}_\alpha &= (F_{11}\sin\varphi + F_{12}\cos\varphi)^2 \mathbf{e}_1 \otimes \mathbf{e}_1 + (F_{21}\sin\varphi + F_{22}\cos\varphi)^2 \mathbf{e}_2 \otimes \mathbf{e}_2 \\ &\quad + (F_{11}\sin\varphi + F_{12}\cos\varphi)(F_{21}\sin\varphi + F_{22}\cos\varphi)(\mathbf{e}_1 \otimes \mathbf{e}_2 + \mathbf{e}_2 \otimes \mathbf{e}_1) \end{aligned} \quad \text{eq. 7-9}$$

$$\begin{aligned} \mathbf{a}_\beta \otimes \mathbf{a}_\beta &= (F_{11}\sin\varphi + F_{12}\cos\varphi)^2 \mathbf{e}_1 \otimes \mathbf{e}_1 + (F_{21}\sin\varphi + F_{22}\cos\varphi)^2 \mathbf{e}_2 \otimes \mathbf{e}_2 \\ &\quad - (F_{11}\sin\varphi + F_{12}\cos\varphi)(F_{21}\sin\varphi + F_{22}\cos\varphi)(\mathbf{e}_1 \otimes \mathbf{e}_2 + \mathbf{e}_2 \otimes \mathbf{e}_1) \end{aligned} \quad \text{eq. 7-10}$$

$$\begin{aligned} \mathbf{a}_\alpha \otimes \mathbf{a}_\beta &= (F_{11}\sin\varphi + F_{12}\cos\varphi)^2 \mathbf{e}_1 \otimes \mathbf{e}_1 - (F_{21}\sin\varphi + F_{22}\cos\varphi)^2 \mathbf{e}_2 \otimes \mathbf{e}_2 \\ &\quad - (F_{11}\sin\varphi + F_{12}\cos\varphi)(F_{21}\sin\varphi + F_{22}\cos\varphi)(\mathbf{e}_1 \otimes \mathbf{e}_2 - \mathbf{e}_2 \otimes \mathbf{e}_1) \end{aligned} \quad \text{eq. 7-11}$$

and regard $\mathbf{a}_\beta \otimes \mathbf{a}_\alpha = (\mathbf{a}_\alpha \otimes \mathbf{a}_\beta)^T$ [eq. 2-118].

Specifying eq. 7-4 for \mathbf{F} , \mathbf{B} , $\mathbf{a}_\alpha \otimes \mathbf{a}_\alpha$, $\mathbf{a}_\beta \otimes \mathbf{a}_\beta$, $\mathbf{a}_\alpha \otimes \mathbf{a}_\beta$ and $\mathbf{a}_\beta \otimes \mathbf{a}_\alpha$ according to equations eq. 7-5 to eq. 7-11 provides the following components of the Cauchy stress tensor for this type of deformation:

$$\begin{aligned} \sigma_{11} &= -p + 2 \frac{\partial w}{\partial I_1} B_{11} + 2 \frac{\partial w}{\partial I_2} [I_1 B_{11} - (B_{11}^2 + B_{12}^2)] + 4 \frac{\partial w}{\partial I_4} (F_{11}\sin\varphi + F_{12}\cos\varphi)^2 \\ &\quad + 8 \frac{\partial w}{\partial I_5} (F_{11}\sin\varphi + F_{12}\cos\varphi)^2 B_{11} + 2 \frac{\partial w}{\partial I_{\alpha\beta}} (F_{11}\sin\varphi + F_{12}\cos\varphi)^2 , \end{aligned} \quad \text{eq. 7-12}$$

$$\begin{aligned} \sigma_{22} &= -p + 2 \frac{\partial w}{\partial I_1} B_{22} + 2 \frac{\partial w}{\partial I_2} [I_1 B_{22} - (B_{12}^2 + B_{22}^2)] + 4 \frac{\partial w}{\partial I_4} (F_{21}\sin\varphi + F_{22}\cos\varphi)^2 \\ &\quad + 8 \frac{\partial w}{\partial I_5} (F_{21}\sin\varphi + F_{22}\cos\varphi)^2 B_{22} - 2 \frac{\partial w}{\partial I_{\alpha\beta}} (F_{21}\sin\varphi + F_{22}\cos\varphi)^2 , \end{aligned} \quad \text{eq. 7-13}$$

$$\sigma_{33} = -p + \frac{\partial w}{\partial I_1} \frac{2}{B_{11}B_{22} - B_{12}^2} + \frac{\partial w}{\partial I_2} \frac{2(B_{11} + B_{22})}{B_{11}B_{22} - B_{12}^2} , \quad \text{eq. 7-14}$$

$$\begin{aligned} \sigma_{12} = \sigma_{21} = -p + 2 \frac{\partial w}{\partial I_1} B_{12} + 2 \frac{\partial w}{\partial I_2} [I_1 B_{12} - (B_{11} B_{12} + B_{12} B_{22})] \\ + 4 \frac{\partial w}{\partial I_5} B_{12} \{ (F_{11} \sin \varphi + F_{12} \cos \varphi)^2 + (F_{21} \sin \varphi + F_{22} \cos \varphi)^2 \} , \end{aligned} \quad \text{eq. 7-15}$$

$$\sigma_{13} = \sigma_{31} = \sigma_{32} = \sigma_{23} = 0 . \quad \text{eq. 7-16}$$

As already stated in chapter 7.2 it is assumed that

$$\sigma_{33} = 0 , \quad \text{eq. 7-17}$$

which is in accordance with the thin sheet assumption. From eq. 7-17 together with eq. 7-14, p can be determined:

$$p = \frac{\partial w}{\partial I_1} \frac{2}{B_{11} B_{22} - B_{12}^2} + \frac{\partial w}{\partial I_2} \frac{2(B_{11} + B_{22})}{B_{11} B_{22} - B_{12}^2} , \quad \text{eq. 7-18}$$

and the non-zero stress components take the form

$$\begin{aligned} \sigma_{11} = 2 \frac{\partial w}{\partial I_1} \left(B_{11} - \frac{1}{B_{11} B_{22} - B_{12}^2} \right) + 2 \frac{\partial w}{\partial I_2} \left[I_1 B_{11} - (B_{11}^2 + B_{12}^2) + \frac{(B_{11} + B_{22})}{B_{11} B_{22} - B_{12}^2} \right] \\ + 4 \frac{\partial w}{\partial I_4} (F_{11} \sin \varphi + F_{12} \cos \varphi)^2 + 8 \frac{\partial w}{\partial I_5} (F_{11} \sin \varphi + F_{12} \cos \varphi)^2 B_{11} \\ + 2 \frac{\partial w}{\partial I_{\alpha\beta}} (F_{11} \sin \varphi + F_{12} \cos \varphi)^2 , \end{aligned} \quad \text{eq. 7-19}$$

$$\begin{aligned} \sigma_{22} = 2 \frac{\partial w}{\partial I_1} \left(B_{22} - \frac{1}{B_{11} B_{22} - B_{12}^2} \right) + 2 \frac{\partial w}{\partial I_2} \left[I_1 B_{22} - (B_{12}^2 + B_{22}^2) + \frac{(B_{11} + B_{22})}{B_{11} B_{22} - B_{12}^2} \right] \\ + 4 \frac{\partial w}{\partial I_4} (F_{21} \sin \varphi + F_{22} \cos \varphi)^2 + 8 \frac{\partial w}{\partial I_5} (F_{21} \sin \varphi + F_{22} \cos \varphi)^2 B_{22} \\ - 2 \frac{\partial w}{\partial I_{\alpha\beta}} (F_{21} \sin \varphi + F_{22} \cos \varphi)^2 , \end{aligned} \quad \text{eq. 7-20}$$

$$\begin{aligned} \sigma_{12} = \sigma_{21} = 2 \frac{\partial w}{\partial I_1} \left(B_{12} - \frac{1}{B_{11} B_{22} - B_{12}^2} \right) \\ + 2 \frac{\partial w}{\partial I_2} \left[I_1 B_{12} - (B_{11} B_{12} + B_{12} B_{22}) + \frac{(B_{11} + B_{22})}{B_{11} B_{22} - B_{12}^2} \right] \\ + 4 \frac{\partial w}{\partial I_5} B_{12} \{ (F_{11} \sin \varphi + F_{12} \cos \varphi)^2 + (F_{21} \sin \varphi + F_{22} \cos \varphi)^2 \} . \end{aligned} \quad \text{eq. 7-21}$$

Here, the in-plane components of the CAUCHY stress tensor are given in general for an incompressible hyperelastic material with two preferred directions that are arranged symmetrically within the regarded plane and own the same mechanical properties. Note that eq. 7-19, eq. 7-20 and eq. 7-21 are two-dimensional specializations within a three-dimensional theoretical framework, i.e. their application is not restricted to purely two-dimensional problems. Three independent components of the stress tensor $(\sigma_{11}, \sigma_{22}, \sigma_{12})$ are related to three independent components of the strain tensor (B_{11}, B_{22}, B_{12}) . However, these equations involve five independent constitutive functions: $\partial w / \partial I_1$, $\partial w / \partial I_2$, $\partial w / \partial I_4$, $\partial w / \partial I_5$ and $\partial w / \partial I_{\alpha\beta}$. Thus, it is theoretically impossible to determine these five constitutive functions based on any experimental data that can be described by eq. 7-19, eq. 7-20 and eq. 7-21.

Therefore, Ogden [2009] proposes the use of reduced constitutive equations for the modeling of arterial walls that depend on two independent constitutive functions, $\partial w / \partial I_1$ and $\partial w / \partial I_4$, only. In this case, eq. 7-19, eq. 7-20 and eq. 7-21 simplify to

$$\sigma_{11} = 2 \frac{\partial w}{\partial I_1} \left(B_{11} - \frac{1}{B_{11}B_{22} - B_{12}^2} \right) + 4 \frac{\partial w}{\partial I_4} (F_{11} \sin \varphi + F_{12} \cos \varphi)^2, \quad \text{eq. 7-22}$$

$$\sigma_{22} = 2 \frac{\partial w}{\partial I_1} \left(B_{22} - \frac{1}{B_{11}B_{22} - B_{12}^2} \right) + 4 \frac{\partial w}{\partial I_4} (F_{21} \sin \varphi + F_{22} \cos \varphi)^2, \quad \text{eq. 7-23}$$

$$\sigma_{12} = \sigma_{21} = 2 \frac{\partial w}{\partial I_1} \left(B_{12} - \frac{1}{B_{11}B_{22} - B_{12}^2} \right). \quad \text{eq. 7-24}$$

The constitutive behavior of a such material can be determined from data corresponding to eq. 7-22 and eq. 7-23 alone, i.e. from biaxial test data, as well as biaxial test data combined with in-plane shear. Moreover, experimental data on in-plane stress and strain components are required in a range that is sufficient to reflect the non-linearity of the material.

As already explained in detail in chapter 3, 4D ultrasound provides the complete in-plane strain tensor at finite cyclic physiological deformations for wall surface areas with a size of about 10 mm² resulting in a discrete heterogeneous strain field. Figure 7-1 b-c shows the measured fields of longitudinal and circumferential wall strains that were used as basis of parameter identification in the current work: ranges $\geq 15\%$ of longitudinal and circumferential strain are covered in all cases. In contrast, information on the two independent variables that characterize physiological loading, transmural pressure and axial pretension force, was sparse: only two values of blood pressure could be measured non-invasively in vivo throughout the cardiac cycle, intra-luminal pressure was assumed to be constant and had to be estimated according to population averaged data. The resulting transmural pressure was assumed to act on the whole segment homogeneously. The axial pretension force F_{red} also was assumed to be constant throughout the cardiac cycle and had to be estimated based on literature data [cf. 7.2]. However, due to the information on the individual geometrically irregular configuration of the wall, this reduced

information on the loading of the wall translated into heterogeneous multiaxial in-plane stress fields that could be related to the measured strain fields. It was hypothesized that these data determine eq. 7-22, eq. 7-23 and eq. 7-24 in a sufficient range to identify unique estimates of the constitutive functions $\partial w/\partial I_1$ and $\partial w/\partial I_4$. This hypothesis was tested in the performed verification experiment [cf. section 7.8 and 7.9].

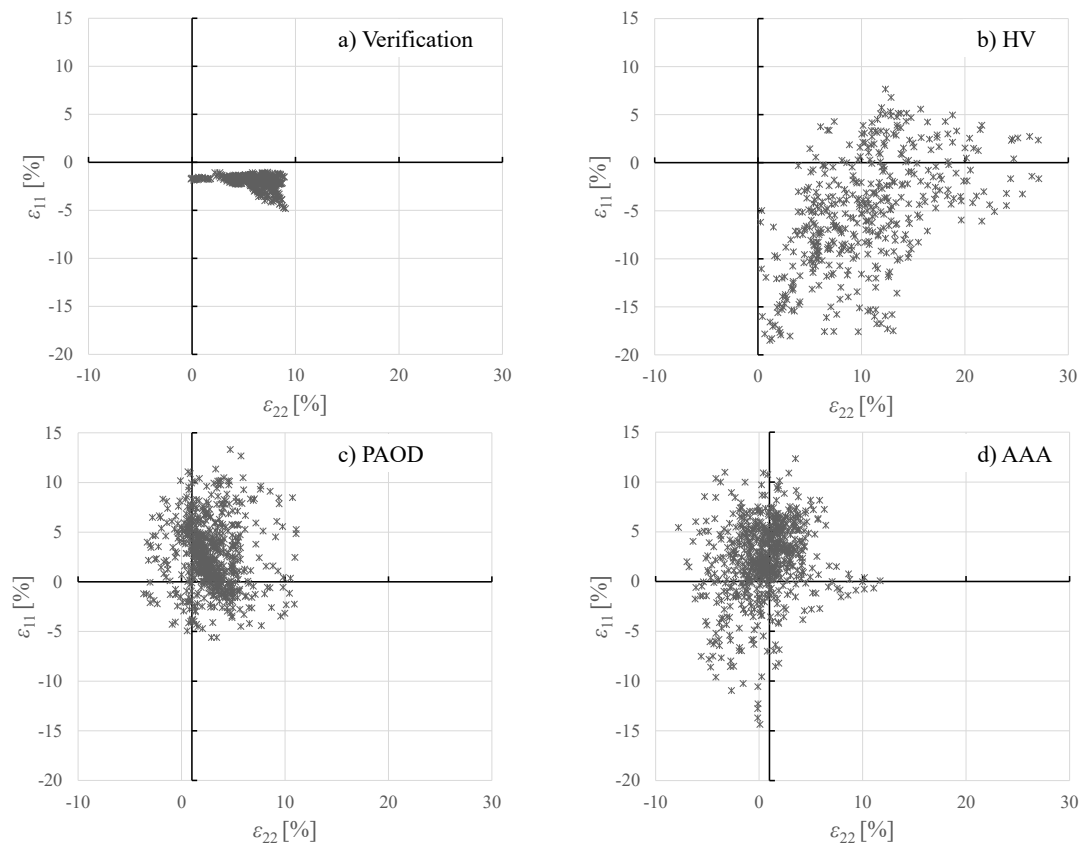


Figure 7-1: Fields of systolic strain states of aortic wall segments: a) numerically generated data by the master FE model of the verification experiment [cf. section 7.8], b) – d) in vivo data of the healthy volunteer, the PAOD patient and the AAA patient, respectively. Each point in the scatter plots describes the strain state of an aortic wall segment of 2 to 10 mm². The strain state is characterized by the combination of longitudinal (ϵ_{11}) and circumferential (ϵ_{22}) strain. Shear strain (ϵ_{12}) is not shown in this representation. [Reprinted from Wittek et al. 2016a with permission from Elsevier]

7.4 Constitutive equation

An invariant-based strain energy function proposed by Gasser et al. [2006] was chosen as constitutive equation describing the anisotropic hyperelastic behavior of the aortic wall. It is conform with eq. 7-22 to eq. 7-24. It is available as built-in feature of Abaqus® 6.12 and subsequent releases (Dassault Systems, Paris, France) and represented here without the distinction of a deviatoric and a volumetric term that is relevant for compressible materials only:

$$w(\mathbf{C}, \mathbf{a}_{0i} \otimes \mathbf{a}_{0i}) = \mu(I_1 - 3) + \frac{k_1}{2k_2} \sum_{i=\alpha}^{\beta} (e^{k_2(E_i)^2} - 1), i = \alpha, \beta \quad \text{eq. 7-25}$$

where

$$E_i = \kappa(I_1 - 3) + (1 - 3\kappa)(I_{4i} - 1) \quad \text{eq. 7-26}$$

I_1 is the first invariant of the right CAUCHY strain tensor \mathbf{C} . I_{4i} , $i = \alpha, \beta$ denotes a mixed tensor invariant of \mathbf{C} and the structural tensor $\mathbf{a}_{0i} \otimes \mathbf{a}_{0i}$ that governs the anisotropic response of the constitutive equation. $\mathbf{a}_{0\alpha}$ and $\mathbf{a}_{0\beta}$ are spatial vectors within the wall plane that denote the preferred directions of the material in the reference configuration. Their radial components are zero. They are assumed to be symmetric to the local in-plane orthonormal unity vectors \mathbf{e}_1 and \mathbf{e}_2 . Because of the symmetry, both direction vectors can be determined by the angle φ that is measured between $\mathbf{a}_{0\alpha}$ and the positive direction of the circumferential axis \mathbf{e}_2 : $\mathbf{a}_{0\alpha/\beta}(\varphi) = \sin\varphi\mathbf{e}_1 + /- \cos\varphi\mathbf{e}_2$. Moreover, it is assumed that both preferred directions own the same mechanical properties, which is ensured by the fact that the identical parameters – k_1 , k_2 and κ – are used in both terms that are related to the preferred directions. This renders the constitutive behavior locally orthotropic. Thus, eq. 7-25 is of the form described by equations eq. 7-22 to eq. 7-24 and can be determined from experimental in-plane stress and strain data covering a sufficient range.

The constitutive equation is composed of a tensor linear NEO-HOOKEAN part and an exponential FUNG-type part for each direction vector. The NEO-HOOKEAN part depends on I_1 alone and therefore is purely isotropic. The exponent [eq. 7-26] of the FUNG-type part again is split into an isotropic NEO-HOOKEAN part and anisotropic parts for each preferred direction that depend on the pseudo-invariants $I_{4\alpha}$ and $I_{4\beta}$. The influence of the tensor linear and the exponential parts on the strain energy is weighted by the relation between the parameter μ (tensor-linear part) and the parameters k_1 and k_2 (exponential parts). Within the exponent E_i [eq. 7-26], the isotropic and the anisotropic contribution are weighted by the parameter κ ($0 \leq \kappa \leq 1/3$), which therefore determines the degree of anisotropy of the constitutive behavior: it is strongly anisotropic for $\kappa = 0$, whereas it is purely isotropic for $\kappa = 1/3$. The non-

linear and anisotropic contribution of E_i to the mechanical response of the material is only accounted for at positive strains, which is enforced by the term $\langle E_i \rangle \stackrel{\text{def}}{=} 1/2 (|E_i| + E_i)$ that equals zero for $E_i < 0$, i.e. for compressive deformation states. In these cases, the material behaves like a NEO-HOOKEAN solid.

In addition to the above mentioned restriction for κ , restrictions of the parameter space of μ, k_1 and k_2 can be derived from the requirement of strict convexity of the strain energy function [cf. chapter 2.3.2]: $\mu > 0, k_1 > 0$ and $k_2 > 0$ [cf. Gasser et al. 2006]. Finally, the parameter space of the angle φ can be constrained between 0° and 90° due to the local orthotropy of the material [cf. chapter 2.3.4.3.]. μ and k_1 are stress-like parameters, k_2 and κ are dimensionless. For κ close to $1/3$ the structural tensor and therefore the parameter φ describing the preferred directions of the structural tensor has only little effect on the mechanical response of the material. In turn, φ is not determined sufficiently in inverse parameter identification. In this approach, the parameters that determine the preferred directions and the degree of anisotropy, φ and κ , respectively, were treated as purely phenomenological parameters, which do not have a microstructural physical meaning.

In order to compare the identified materials, stress-stretch curves for biaxial stretches were calculated: The CAUCHY stress tensor [cf. eq. 2-67] was specified for plane stress ($\sigma_{33} = 0$), homogenous deformation according to principal axes ($\mathbf{C} = \lambda_1^2 \mathbf{N}_1 \mathbf{N}_1 + \lambda_2^2 \mathbf{N}_2 \mathbf{N}_2 + \lambda_3^2 \mathbf{N}_3 \mathbf{N}_3$) and the incompressibility condition $J = 1 \Leftrightarrow \lambda_3 = 1/\lambda_1 \lambda_2$, where $J = \lambda_1 \lambda_2 \lambda_3$ is the volume change, and deformations where $E \geq 0$ and therefore $\langle E \rangle = E$:

$$\begin{aligned} \boldsymbol{\sigma} = & \left[2\mu \left(\lambda_1^2 - \frac{1}{\lambda_1^2 \lambda_2^2} \right) + 4k_1 E e^{k_2 E^2} \left((\kappa + [1 - 3\kappa] \sin^2 \varphi) \lambda_1^2 - \frac{\kappa}{\lambda_1^2 \lambda_2^2} \right) \right] \mathbf{n}_1 \mathbf{n}_1 \\ & + \left[2\mu \left(\lambda_2^2 - \frac{1}{\lambda_1^2 \lambda_2^2} \right) + 4k_1 E e^{k_2 E^2} \left((\kappa + [1 - 3\kappa] \cos^2 \varphi) \lambda_2^2 - \frac{\kappa}{\lambda_1^2 \lambda_2^2} \right) \right] \mathbf{n}_2 \mathbf{n}_2 \end{aligned} \quad \text{eq. 7-27}$$

where

$$E = \kappa(\lambda_1^2 + \lambda_2^2 + 1/\lambda_1^2 \lambda_2^2 - 3) + (1 - 3\kappa)(\lambda_1^2 \sin^2 \varphi + \lambda_2^2 \cos^2 \varphi - 1) . \quad \text{eq. 7-28}$$

7.5 Non-invasive in vivo data

In chapter 3, all field variables were given with indices in order to emphasize that *discrete* fields were obtained from 4D ultrasound measurements, only, not proper continuous fields. In the current chapter, however, this index notation for discrete fields is not used in order to avoid an excess of indices.

7.5.1 Patient data

Systolic and diastolic brachial blood pressure measurements and 4D-US volume data sets of three male volunteers of different age and health states were selected from previously acquired data in accordance with the approvals of the local Ethics Committees of the University Clinics Marburg, Germany and the Goethe University Hospital, Frankfurt am Main, Germany: one volunteer without cardiovascular risk factors (HV) and two patients with different vascular diseases, one peripheral aortic occlusive disease patient (PAOD) and a patient with a small, saccular abdominal aortic aneurysm without intraluminal thrombus (AAA) [Table 7-2]. In vivo data had been acquired according to chapter 3.2.1.

Voxel edge length of the image data was 0.59, 0.56 and 0.39 mm, temporal resolution was 13.5, 17.7 and 20.1 volumes/s resulting in 11, 17 and 19 imaged configurations of the aortic wall segments throughout the cardiac cycle for the HV, PAOD and AAA data, respectively.

Table 7-2: Patient data. [Reprinted from Wittek et al. 2016a with permission from Elsevier]

Data set	Age in y.	Sex	BMI in kg/m ²	Blood pressure in mmHg	Pathology	Length in mm	max./min. diameter in mm
HV	22	m	22.4	130/80	--	24.7	16.9/15.2
PAOD	80	m	28.4	135/80	arterial hypertension, PAOD	27.0	15.9/15.5
AAA	58	m	26.3	120/80	arterial hypertension, AAA ($d_{max}^*=32$ mm)	53.5	28.3/28.1

* In contrast to the maximum and minimum diameter (averaged along the length of the imaged segment) that were computed from the 4D ultrasound data, the local maximum diameter of the AAA is given here additionally as the clinically relevant measure.

7.5.2 Diastolic-systolic in-plane strain fields from 4D ultrasound measurements

Post-processing of the data sets was done offline as described in chapter 3.2.2. The motion function of discrete material points [eq. 3-6] was exported as ASCII file. The average diameter of the aortic segment was determined for each aortic segment and each time step throughout the cardiac cycle according to chapter 3.3.3. In case of the AAA the clinically measured maximum diameter was determined for the mid bulge region, additionally. The configurations showing the maximum and minimum (average) diameter [Table 7-2] were identified as systolic and diastolic configurations, respectively.

Based on the exported motion function of the aortic wall, FE preprocessing was performed according to chapter 3.3.3: The diastolic configuration \mathbf{X}_{dia} of each aortic segment was used as deformed reference configuration $\mathcal{B}_r = \mathcal{B}_{dia}$. The AAA wall configuration was reconstructed, discretized into 4-node structural elements and local nodal and element coordinate systems were defined in \mathcal{B}_{dia} according to chapter 3.3.3. The displacement vector field $\mathbf{u}_{dia-sys}$ was calculated as $\mathbf{u}_{dia-sys} = \mathbf{x}_{sys} - \mathbf{X}_{dia}$, where \mathbf{x}_{sys} and \mathbf{X}_{dia} are the measured position vectors of a material point X in its systolic and diastolic configuration, respectively. The discrete motion function $\chi: \mathcal{B}_{dia} \rightarrow \mathcal{B}_{sys}$:

$$\mathbf{x}_{sys} = \chi(\mathbf{X}_{dia}) = \mathbf{X}_{dia} + \mathbf{u}_{dia-sys} \quad \text{eq. 7-29}$$

that describes the deformation from the (measured) diastolic to the (measured) systolic configuration was implemented numerically by applying the displacement vectors $\mathbf{u}_{dia-sys}$ as boundary conditions (BCs) to each node of the FE model in its diastolic configuration. The systolic in-plane strain field $\boldsymbol{\epsilon}^{US}$ with respect to the diastolic configuration was computed using Abaqus 6.12. For this purpose, it was necessary to attribute a thickness and material properties to the shell elements of the numerical model: a constant thickness of 1 mm and a hyperelastic NEO-HOOKEAN material suited for finite deformation with $C_{10} = 0.01$ MPa were chosen [cf. chapter 3.3.3].

The heterogeneous strain distributions shown in Figure 7-1 b – d were obtained for the three subjects. Compared to the HV data set, the average systolic strains were much smaller in the two patient data sets (e.g. 10%, 2.6% and 0.5% circumferential strain for HV, PAOD and AAA, respectively; cf. Figure 7-12). However, the distribution of strain states in the patient data sets was quite heterogeneous, covering a range of 15% to 20% of longitudinal and circumferential strain.

Annotations:

- (i) The results of this analysis did not depend on modeling assumptions about elastic properties, wall thickness or residual loads, but on the imaged diastolic reference configuration \mathcal{B}_{dia} and the measured displacement field $\mathbf{u}_{dia-sys}$ alone, because every degree of freedom in the model was constrained [cf. chapter 3.3.3.3].

- (ii) For the current purpose, the last step of the post-processing procedure described in chapter 3.3.3.3 was omitted: The cyclic peak-to-peak amplitude was not determined for each component of the in-plane strain tensor, separately, but for all in-plane strain components the systolic strains with respect to the diastolic configuration were computed. This different approach was chosen here, because numerical estimation of the motion function $\chi^{model}: \mathcal{B}_r \rightarrow \mathcal{B}_t^{model}$ and of the corresponding in-plane strain distribution by a FE model [see section 7.6] was possible for those current configurations \mathcal{B}_t , only, for which non-invasively measured loads, i.e. blood pressure, were known.

7.6 Model-based estimation of systolic in-plane strains

7.6.1 Displacement and strain field as a function of the chosen constitutive model

In contrast to the computation of BIOT's in-plane strain fields as described in sections 3.3.3 and 7.5.2, where measured displacements $\mathbf{u}_{dia-sys}$ were used as boundary conditions, physiological loads were used as boundary conditions in this type of FEA: the measured individual diastolic and systolic blood pressure, the population averaged intra-abdominal pressure and population averaged, but personalized, axial prestrain [c.f. section 7.2, Table 7-1]. The diastolic-systolic motion function

$$\chi_{dia-sys}^{model}: \mathcal{B}_{dia} \rightarrow \mathcal{B}_{sys}^{model}, \quad \chi_{sys}^{model} = \mathbf{X}_{dia} + \mathbf{u}_{dia-sys}^{model} \quad \text{eq. 7-30}$$

and the corresponding in-plane BIOT's strains $\boldsymbol{\varepsilon}^{model}$ were estimated numerically by a direct nonlinear FEA. The obtained numerical estimate of the in-plane strain tensor field depended on the chosen constitutive model [cf. section 7.4] and the constitutive parameter vector that was attributed to the model:

$$\boldsymbol{\varepsilon}^{model} = \boldsymbol{\varepsilon}^{model}(\mu, k_1, k_2, \kappa, \varphi). \quad \text{eq. 7-31}$$

7.6.2 Reference configuration, FE discretization and boundary conditions

In this second type of FE models, only the position vectors \mathbf{X}_{dia} were used from the data provided by the 4D ultrasound measurement, but not the measured motion function $\chi(\mathbf{X})$. Based on these data, reconstruction and discretization of the diastolic configuration \mathcal{B}_{dia} and definition of local nodal and element coordinate systems was performed as described in sections 3.3.4.1 and 3.3.4.2. Simulia Abaqus[®] 6.12 was used as FE-solver and nonlinear, quasistatic Abaqus/Standard FE analyses were performed. In

contrast to the method described in section 3.3.4.3, first order finite-strain shell elements of type S4R with reduced integration and hourglass control were used. S4R shell elements account for the change of shell thickness in geometrically nonlinear analysis. Cross-sectional behavior was calculated by numerical integration through the shell thickness during analysis. Non-linear bending stiffness resulted from varying tensile stresses through shell thickness due to bending, only, and was small for the assumed thin shells. [Abaqus 6.12 2012a]

The discretization obtained by the described FE preprocessing based on 4D ultrasound data was determined by the spatial resolution of the measured discrete diastolic configuration B_{dia} , which provided a “native” mesh since the discrete material points \mathbf{X}_{dia} were used as nodes of first order shell elements. In order to determine the appropriate degree of mesh refinement, a convergence study was performed using 4D ultrasound data of a healthy aortic segment with only slightly irregular geometry and an AAA segment with strongly irregular geometry [cf. appendix B for detailed information]. The results showed that the “native” degree of discretization was appropriate for the non-aneurysmal aortae: only negligible differences in minimum and maximum values and spatial distribution of local stress and strain values were observed. In contrast, for the aneurysmal geometry convergence was achieved for a refinement of the “native” mesh by factor 4, i.e. one “native” element was split into 4 elements using Altair Hypermesh 12.0 (Altair Engineering GmbH, Böblingen, Germany). The material points obtained from 4D ultrasound were preserved in this mesh and a node set containing these material points was defined in the model.

A reduced axial force and hydrostatic pressure were applied as physiological BCs. The influence of surrounding tissue was taken into account by subtracting intra-abdominal pressure from the measured blood pressure values and applying the resulting transmural pressure as BC. External support of the aortic wall by the spine was considered in the model by fixing all degrees of freedom of some dorsal (i.e. located towards the back of the body, close to the spine) nodes in the diastolic configuration and applying the measured displacements $\mathbf{u}_{dia-sys}^{US}$ to these nodes as BCs when estimating the systolic strain distribution. These additional BCs were applied to those dorsal nodes where the minimum measured cyclic radial displacement was observed, which was understood as an indication of fixation of the wall to the spine.

7.6.3 In-plane strains as a function of the chosen constitutive behavior

For the computation of the in-plane strain fields depending on a chosen set of constitutive parameters, four direct boundary value problems and one inverse problem were solved using nonlinear finite element method (FEM):

7.6.3.1 Estimation of the reduced axial force F_{red}

Age-dependent axial prestrain was estimated according to Horny et al. [2011] and corresponding axial displacement was applied as BC to the free end of the diastolic configuration. The reduced axial force F_{red} [cf. chapter 1.6] was obtained in a direct FEA as resulting reaction force. F_{red} then was held constant during subsequent finite element analyses of the mechanical response of the aortic segments to physiological transmural pressure. Since the axial prestrain of the AAA was assumed to be zero [cf. Table 7-1], the step of determining the reduced axial force was omitted in this case.

7.6.3.2 Inverse identification of the load free configuration \mathcal{B}_0 of the aortic segment and of diastolic prestresses and prestretches

The FE mesh of the diastolic configuration \mathcal{B}_{dia} , that was generated from 4D ultrasound data as described above, is stress and strain free. However, it was reconstructed from image data of the aortic segment under diastolic physiological loading, i.e. axial pretension force F_{red} and diastolic transmural pressure. Applying these physiological loads as BCs to the FE model of the stress and strain free diastolic configuration would lead to artificial deformations and eventually to the identification of wrong constitutive parameters [Gee et al. 2010]. Several solutions to the inverse problem of determining physiological prestrains/-stretches and -stresses have been proposed in recent years [Lu et al. 2007b, 2007a; Rajagopal et al. 2007; Lu et al. 2008; Gee et al. 2009; Gee et al. 2010; Sellier 2011; Zhao et al. 2011; Riveros et al. 2013; Joldes et al. 2015b]. In the present study, the iterative optimal design algorithm proposed by Sellier [2011] was coded in WOLFRAM Mathematica 9 and used to solve this problem [Wittek et al. 2013]: in a first, step the load-free configuration \mathcal{B}_0 of the aortic segment that cannot be imaged in vivo was determined. I.e. the inverse motion function $\chi^{-1}: \mathcal{B}_{dia} \rightarrow \mathcal{B}_0$ was estimated. Here, a brief outline of the main steps of the used algorithm is given:

- (i) The imaged diastolic configuration \mathbf{X}_{dia} of the aortic segment was taken as an initial guess $\mathbf{X}_{0,1}$ of its load-free configuration \mathbf{X}_0 .
- (ii) Physiological BCs were applied to the guessed load-free configuration $\mathbf{X}_{0,j}$, where index j denotes the number of the iteration. The solution of this direct elastostatic problem by use of the FEM resulted in a guess of the diastolic displacement field $\mathbf{u}_{0-dia,j}$ and a diastolic current configuration $\mathbf{x}_{curr,j} = \mathbf{X}_{0,j} + \mathbf{u}_{0-dia,j}$.
- (iii) Case A: The HAUSDORFF distance exceeds the chosen convergence criterion δ , i.e. $\max\{|\mathbf{x}_{curr,j,i} - \mathbf{x}_{dia,i}|, i = 1, \dots, n\} > \delta$, where n is the number of nodes in the model, $\mathbf{x}_{curr,j,i}$ and $\mathbf{x}_{dia,i}$ are the position vectors of the i^{th} node of the estimated and the measured diastolic current configuration, respectively. An updated guess of the load-free configuration $\mathbf{X}_{0,j+1}$ was obtained by subtracting the difference vectors $\mathbf{x}_{curr,j} - \mathbf{x}_{dia}$ between the guessed and the measured diastolic

configuration from the position vectors that defined the preceding guess of the load free configuration $\mathbf{X}_{0,j}$: $\mathbf{X}_{0,j+1} = \mathbf{X}_{0,j} - (\mathbf{x}_{curr,j} - \mathbf{x}_{dia})$. The algorithm continues with the next iteration starting from (ii).

- (iv) Case B: $\max\{|\mathbf{x}_{curr,j,i} - \mathbf{x}_{dia,i}|, i = 1, \dots, n\} \leq \delta$. $\mathbf{X}_{0,j}$ was taken as the true load-free configuration \mathbf{X}_0 and step (ii) gave the diastolic distributions of prestrains/-stretches and prestresses.

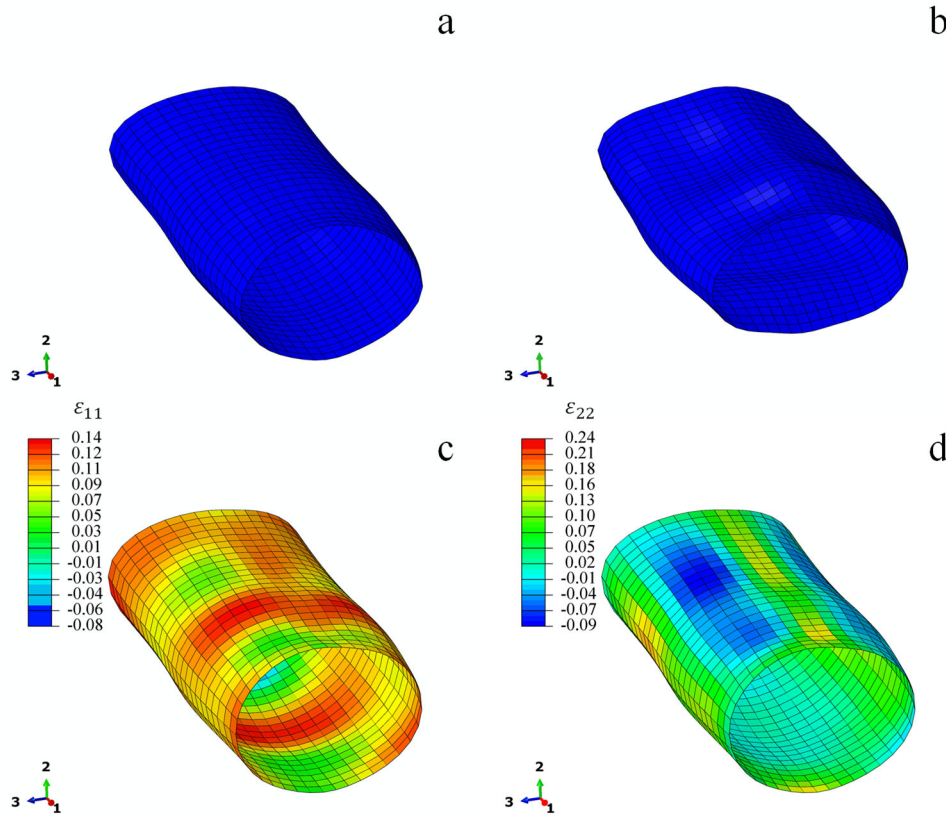


Figure 7-2 Steps of the prestressing procedure of an exemplary data set: a) discretized diastolic configuration without prestrains, b) load free configuration that was identified by inverse FE and the recovered diastolic configuration with c) axial (ϵ_{11}) and d) circumferential prestrains as obtained by direct FE. [Reprinted from Wittek et al. 2013 with permission from Elsevier]

In this study a local convergence criterion was chosen, permitting a Hausdorff distance, i.e. a maximum local deviation of $\delta \leq 0.01$ mm between imaged and prestrained diastolic configuration. The algorithm converged on average in about 40 iterations. Figure 7-2 shows the diastolic configuration of an exemplary data set without prestrains as reconstructed from 4D-US data (a), the calculated load-free (b) and the prestrained and prestressed diastolic configuration (circumferential (c) and longitudinal strain (d)). The solution of this inverse problem depended on the chosen constitutive parameter vector.

7.6.3.3 Systolic strain field with respect to the diastolic configuration

In a two-step direct FEA the reduced axial force F_{red} and diastolic and systolic transmural pressure were applied as BCs to the estimated load free geometry and the deformed diastolic and systolic configurations \mathbf{x}_{dia}^{model} and \mathbf{x}_{sys}^{model} were computed. The displacement vector field $\mathbf{u}_{dia-sys}^{model}$ which describes the motion from the diastolic to the systolic configuration was calculated as $\mathbf{u}_{dia-sys}^{model} = \mathbf{x}_{sys}^{model} - \mathbf{x}_{dia}^{model}$. Eventually, the systolic in-plane strains $\boldsymbol{\varepsilon}^{model}$ with respect to the diastolic configuration were computed: Only those diastolic-systolic displacement vectors $\mathbf{u}_{dia-sys}^{model}$ that were related to the discrete material points X as obtained from 4D ultrasound were applied as BC to the “native” stress and strain free mesh of the diastolic configuration that was used as well for strain computation from measured 4D ultrasound data. The thin shell assumption (uniform stress and strain across the thickness of the wall, cf. section 7.2) was accounted for by reading out membrane strains from the mid-layer of the shell elements, only. The numerically estimated systolic in-plane strains $\boldsymbol{\varepsilon}^{model}$ with respect to the diastolic configuration were directly comparable to the measured strain field $\boldsymbol{\varepsilon}^{US}$ [cf. 7.5.2]. In contrast to $\boldsymbol{\varepsilon}^{US}$, $\boldsymbol{\varepsilon}^{model}$ was a function of the chosen constitutive parameter vector $(\mu, k_1, k_2, \kappa, \varphi)$.

7.7 Constitutive parameter identification strategy

7.7.1 Finite Element Model Updating workflow

An iterative Finite Element Model Updating workflow was developed to identify the five parameters of the constitutive equation [eq. 7-25] characterizing the non-linear and locally orthotropic elastic properties of the imaged wall segments. An overview of the workflow is given in Figure 7-3. In each iteration, the systolic in-plane strain distribution $\boldsymbol{\varepsilon}^{US}$ with respect to the diastolic configuration \mathcal{B}_{dia} was compared to the numerically estimated in-plane systolic strain distribution $\boldsymbol{\varepsilon}^{model}$ with respect to the diastolic configuration \mathcal{B}_{dia} that depended on a guess of the constitutive parameter set. The deviation of $\boldsymbol{\varepsilon}^{model}(\mu, k_1, k_2, \kappa, \varphi)$ from $\boldsymbol{\varepsilon}^{US}$ was quantified by means of an error function f_{err} that was minimized during the iterative optimization process with respect to the unknown constitutive parameter vector $(\mu, k_1, k_2, \kappa, \varphi)$. The minimization of f_{err} with regard to the unknown constitutive parameters was a *nonlinear, multivariate and multi-objective optimization problem* [Ehrgott 2005; Kaliszewski et al. 2016]:

- (i) *nonlinear*: The chosen constitutive equation [eq. 7-25] and, therefore, the error function depends on the parameters k_2 , κ and φ nonlinearly. Moreover, the FEAs by which the strain distributions are calculated contain geometric nonlinearities due to large-displacement effects;
- (ii) *multivariate*: f_{err} is a function of the five constitutive parameters to be identified;

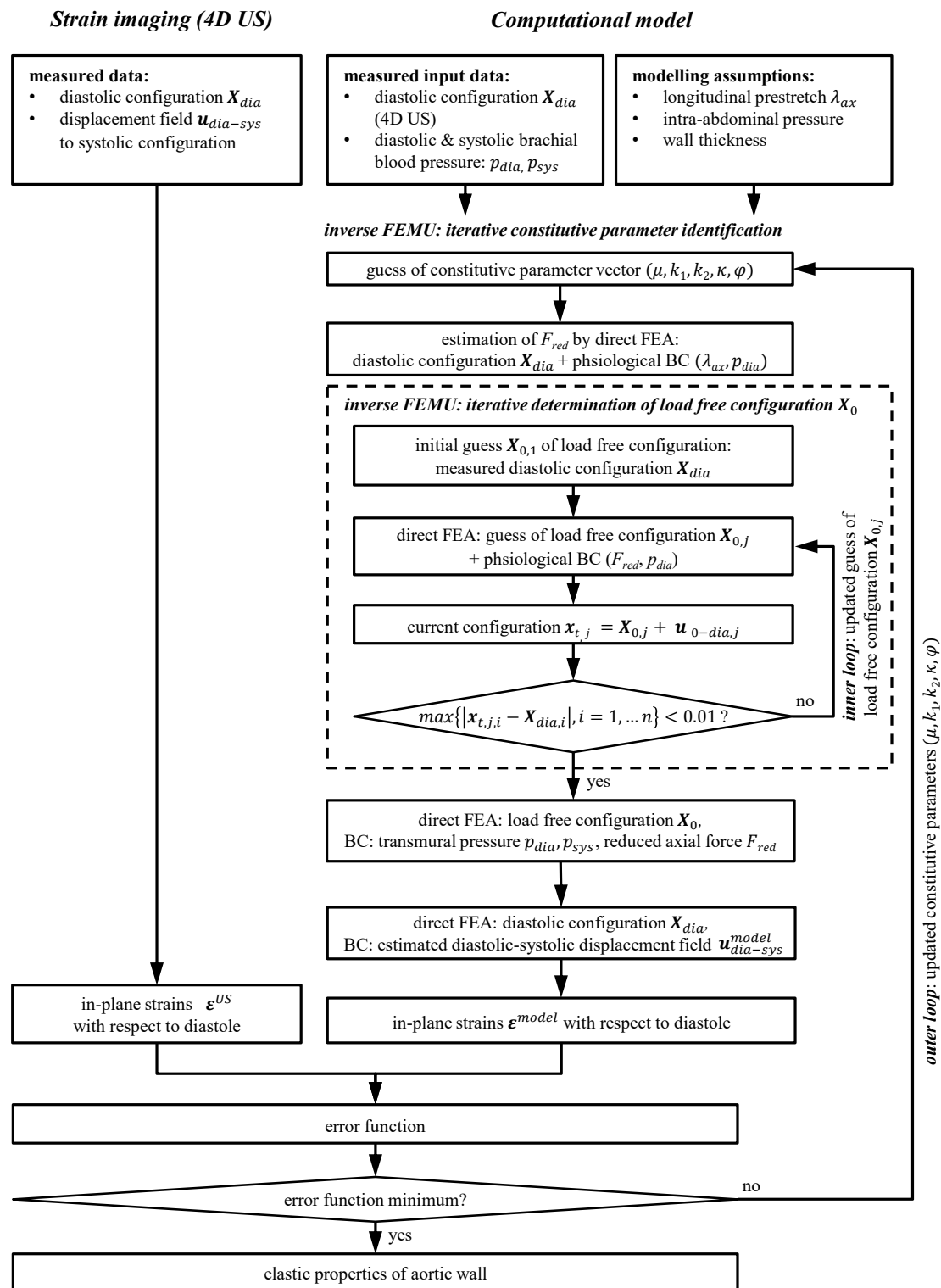


Figure 7-3 Flow chart of the Finite Element Model Updating method (FEMU). [Reprinted from Wittek et al. 2016a with permission from Elsevier]

(iii) *multiobjective*: Since aortic walls are anisotropic, the three independent in-plane components of the BIOT's strain tensor depend in different ways on the constitutive parameters, they are different objectives of the optimization process that have to be met by the same set of constitutive parameters.

Such problems usually exhibit a so-called ‘trade-off’ situation [Collette and Siarry 2004; Ehrgott 2005]: the minimization of the deviation of one estimated strain component from measured data goes along with increasing deviation of another component. This problem has to be reflected by the construction of the error function f_{err} .

7.7.2 Error function

In order to quantify the deviation of the computationally estimated strains $\boldsymbol{\varepsilon}^{model}$ from the measured distribution $\boldsymbol{\varepsilon}^{US}$, an error function f_{err} was defined that consisted of the squared residuals of measured and estimated in-plane strains. The following error function was used for the HV and the PAOD data:

$$f_{err} = \frac{1}{n} \sum_i \sum_{j=1}^n w_i (\varepsilon_{i,j}^{model}(\mu, k_1, k_2, \kappa, \varphi) - \varepsilon_{i,j}^{US})^2, \quad \text{eq. 7-32}$$

where i marks the in-plane components of the BIOT's strain tensor with regard to local element coordinates (11 - axial, 22 - circumferential, 12 - shear) and n is the number of tissue segments for which local strain values were measured [see section 7.5.2] and estimated by the FEA [see section 7.6]. The multi-objectivity of the problem is reflected by the fact that all in plane strain components contribute to the error function, separately. The influence of each strain component on f_{err} is weighed by factors w_i with

$$\sum_i w_i = 1. \quad \text{eq. 7-33}$$

Because of the trade-off between the different objectives of the optimization, the weighting factors w_i had to be chosen in such a way that the contributions of the three in-plane strain components to the error function were well balanced. In this study, $w_{11} = 2/5$, $w_{22} = 2/5$ and $w_{12} = 1/5$ were chosen for the axial, circumferential and in plane shear components of the HV and the PAOD data, respectively.

Since the use of this error function resulted in far too stiff elastic properties in the case of the AAA data, a different error function was used in this case:

$$f_{err}^{AAA} = \sum_{i=1}^2 w_i \cdot \text{median} \left\{ (\varepsilon_{i,l,j}^{model}(\mu, k_1, k_2, \kappa, \varphi) - \varepsilon_{i,l,j}^{US})^2, j \in \{1, \dots, n\} \right\} \quad \text{eq. 7-34}$$

where $w_1 = 1/5$ and $w_2 = 4/5$ were chosen for weighting the axial and circumferential strain, respectively. In-plane shear, that was small compared to the other in-plane strain components in all data sets [cf. Figure 7-12], was omitted in this case.

7.7.3 Optimization algorithm

Nonlinear, multivariate and multiobjective optimization problems usually exhibit several local optima. Deterministic gradient based or hill climbing algorithms alone are not suited for such problems since their results depend strongly on the initial guess of the parameters and they are likely to get stuck in a local optimum, missing the global minimum. To overcome these limitations, a combined stochastic/deterministic approach was developed in this work: First, a MONTE CARLO algorithm was used to determine 300 constitutive parameter vectors that were physically and numerically possible, i.e. for which the direct boundary value problems (deformation of the aortic segment under diastolic and systolic physiological loading) and the inverse problem of determining the load free geometry could be solved. The six constitutive parameter vectors with the minimum error function values were then used as start parameter sets for a deterministic non-linear NELDER-MEAD simplex algorithm (Nelder and Mead 1965). The NELDER-MEAD algorithm was run three times for each start parameter set. A stochastic element was introduced at this stage by randomizing the determination of the corners of the initial simplex. MONTE CARLO and NELDER-MEAD algorithms were programmed in house using WOLFRAM Mathematica 9 (Wolfram Research, Champaign, IL, USA) and were modified to regard the limits of the parameter space [cf. section 7.4]. The values of the error function being in the order of 10^{-3} , a maximum difference of the error values of 10^{-9} between the best and the worst corner of the simplex was chosen as convergence criterion of the NELDER-MEAD simplex algorithm, which converged on average in about 120 iterations.

Since the identification of the load-free configuration \mathbf{X}_0 and of the prestrains in the deformed reference configuration constituted the inner loop of the nested constitutive parameter identification procedure [f. Figure 7-3]: The solution of this inverse problem depended on the guess of the constitutive parameter vector and thus, it had to be solved in every iteration of the optimization procedure. Each iteration of the NELDER-MEAD simplex algorithm as well as the MONTE CARLO algorithm included about 20 to 40 iterations of the optimal design algorithm determining the load-free geometry. Thus, parameter optimization for each data set required between 49,200 and 98,400 iterations. Convergence of the whole FEMU method for one data set was achieved in a time period of about two weeks running two optimizations in parallel on a quad core CPU with 32 GByte of RAM. Time to convergence could be reduced to 1 - 2 days by simple parallelization of the processes. In principle, all 300 MONTE CARLO runs could be performed in parallel as well as the subsequent 18 runs of the NELDER-MEAD algorithm.

7.8 Numerical verification experiment

A numerical experiment was performed to verify the parameter estimation procedure: A reasonable but arbitrarily chosen parameter set (master material, see Table 7-3) was assigned to a likewise chosen geometry. This constituted the load-free reference configuration (master model). Using Simulia Abaqus® 6.12 the direct elastostatic problem was solved for two load steps:

- (i) 55 mmHg transmural pressure and a reduced axial force F_{red} inducing axial prestrain of $\varepsilon_{ax} = 12\%$ and
- (ii) 110 mmHg, F_{red} was held constant.

Resulting in-plane deformation fields were computed for these load steps [Figure 7-4]. Out of these assumed and numerically generated data, only those that were available by measurements in the in vivo situation were used as input data for constitutive parameter identification with the FEMU approach described in the previous section: transmural pressures of 55 and 110 mmHg, the diastolic configuration \mathbf{x}_{dia} that corresponded to load case (i) and the displacement field $\mathbf{u}_{dia-sys}$ that mapped this configuration onto the systolic configuration \mathbf{x}_{sys} that corresponded to load case (ii). These three vector fields describe the motion of the aortic wall with regard to the deformed reference configuration \mathbf{x}_{dia} , not with regard to the load-free geometry. The distribution of in-plane longitudinal and circumferential strains that corresponded to this motion is shown in Figure 7-1 a.

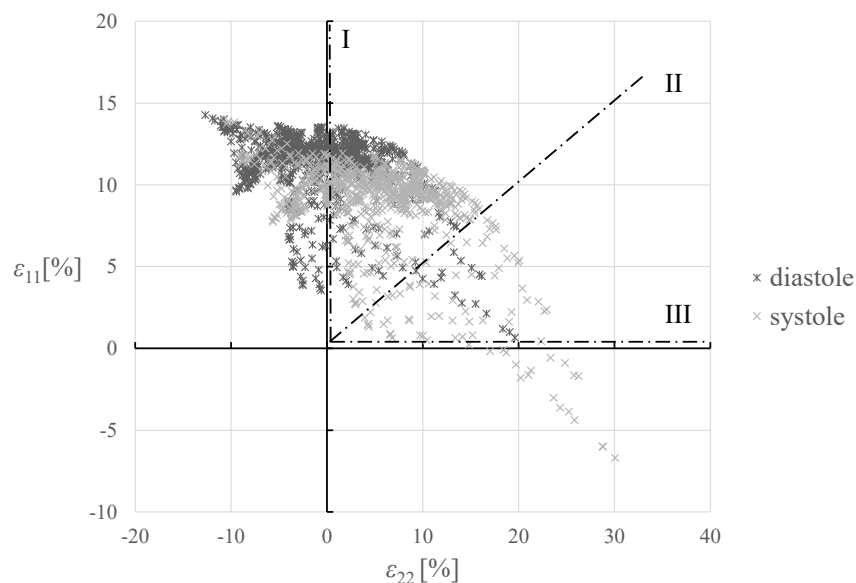


Figure 7-4: Numerically generated distribution of biaxial strain states with regard to the load free geometry. I – uniaxial longitudinal strain, II equi-biaxial strain, III uniaxial circumferential strain. [Reprinted from Wittek et al. 2016a with permission from Elsevier]

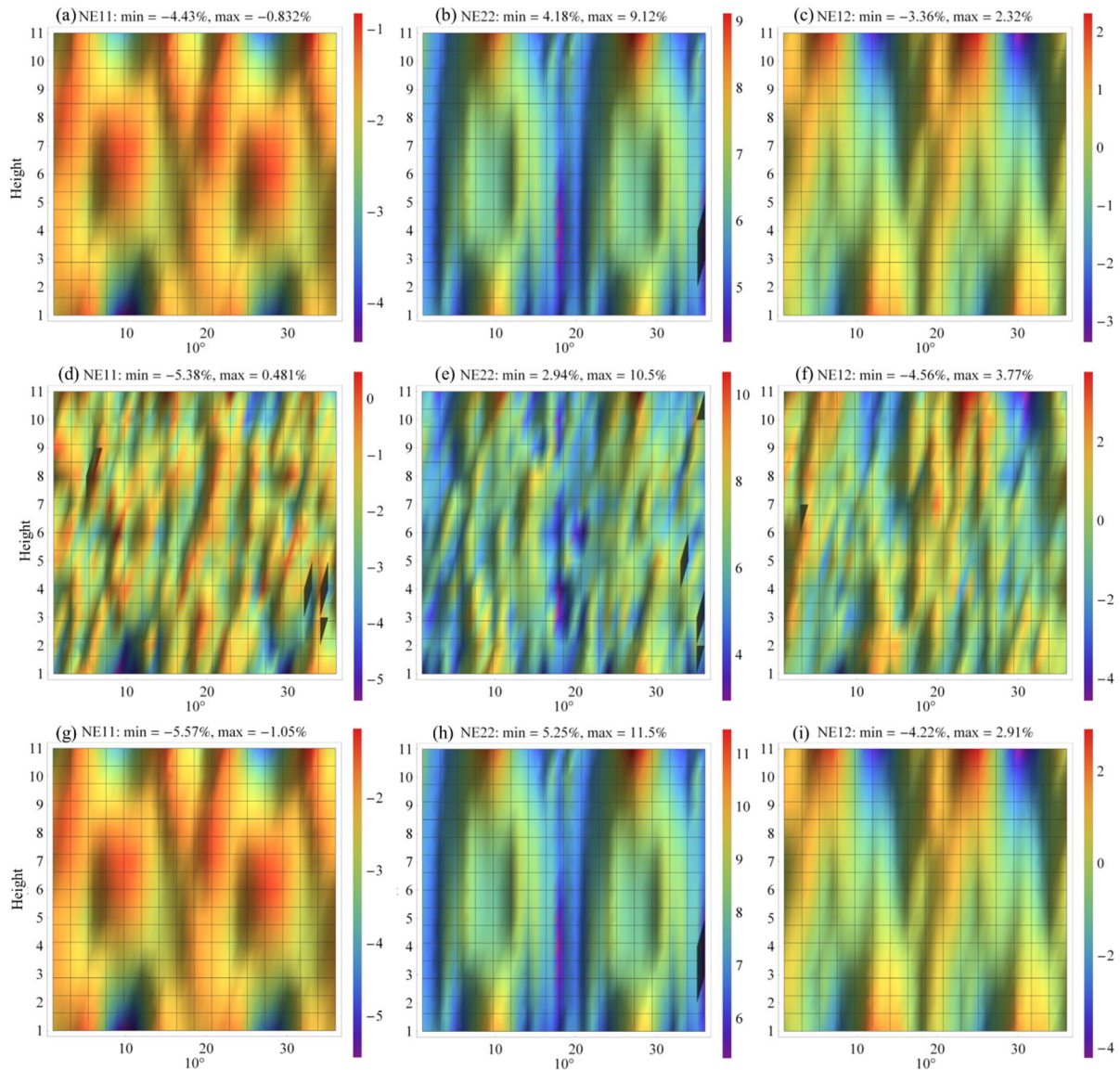


Figure 7-5 Numerically generated in-plane strain fields without superimposed error (a, b, c), with superimposed random error (d, e, f) and with superimposed systematic error (g, h, i). NE11, NE22 and NE12 indicate the longitudinal, circumferential and shear strain in the wall plane, respectively, according to the local coordinates systems that were defined using in-house software [cf. 3.3.4.2.]. ‘Height’ and ‘10°’ indicate the position of the tissue segment in longitudinal and circumferential direction of the imaged wall segment, respectively. 0° and 18° correspond to the anterior and posterior face of the vessel wall. Height 1 and 11 indicate the cranial and caudal endings of the imaged wall segment, respectively.

This numerical experiment was repeated for five times in order to assess the repeatability and uniqueness of the inverse constitutive parameter identification. In a second experiment, the numerically generated systolic strain field data were corrupted by a random error of $\pm 2.1\%$ that was identified as 95% confidence interval of local strain measurement by 4D ultrasound in the validation study that was performed within this thesis [cf. chapter 4.3.1, Fig. 4-15]. In a third numerical experiment, a systematic error was superimposed on the strain field data that were assumed to represent the basic truth: the corrupted data were obtained from the basic truth strain field by multiplication with a constant factor c . In this way a systematic error could be induced that was not constant in all elements but varied smoothly depending

on the spatial location. c was chosen so that the mean circumferential strain deviated from the true mean by +1.6%, which was the upper limit of the possible systematic error of circumferential strain in a single measurement [cf. chapter 4.3.1]:

$$\frac{1}{m} \sum_{i=1}^m c \cdot \varepsilon_{22,i} = \left(\frac{1}{m} \sum_{i=1}^m \varepsilon_{22,i} \right) + 0.016$$

$$\Leftrightarrow c \bar{\varepsilon}_{22} = \bar{\varepsilon}_{22} + 0.016$$

$$\Leftrightarrow c = 1 + \frac{0.016}{\bar{\varepsilon}_{22}}, \quad \text{eq. 7-35}$$

where m is the number of elements for which separate local strain values were available and $\bar{\varepsilon}_{22}$ is the arithmetical mean of local circumferential strain values. The same systematic error was applied to all in-plane strain components which describes a worst case scenario. Numerically generated in-plane strain fields with and without superimposed noise are shown in Figure 7-5.

In order to compare the resulting material properties to the known master material the axial and circumferential components of the CAUCHY stress tensor (σ_{11} and σ_{22} respectively, cf. eq. 7-27) were plotted for both parameter sets along three paths in the λ_1, λ_2 -plane: uniaxial longitudinal and circumferential stretch and equi-biaxial stretch. The coefficient of determination $R^2 = 1 - SS_{err}/SS_{tot}$ was calculated to judge the quality of fit of the stretch-stress curves of the identified material along each of the stretch paths to the respective curves of the given material. The *residual sum of squares* SS_{err} and the *total sum of squares* SS_{tot} were defined as follows:

$$SS_{err} = \sum_{i=1}^m (\sigma_{j,i}^{model} - \sigma_{j,i}^{master})^2 \quad \text{eq. 7-36}$$

$$SS_{tot} = \sum_{i=1}^m (\sigma_{j,i}^{master} - \bar{\sigma}_j^{master})^2 \quad \text{eq. 7-37}$$

where $j = 1, 2$ indicates the longitudinal and circumferential component of the CAUCHY stress tensor, respectively. $\sigma_{j,i}^{master}$ are the CAUCHY stress values calculated by use of the master parameter set for one of the stretch paths, m is the number of stress values calculated along each stretch path, $\bar{\sigma}_j^{master}$ is the mean of these stress values and $\sigma_{j,i}^{model}$ are the stress values calculated by use of the identified best fit parameter set for the same path.

As already stated above, the inverse identification of the motion function $\chi^{-1}: \mathcal{B}_{dia} \rightarrow \mathcal{B}_0$ [cf. 7.6.3] depended on the chosen constitutive parameter vector. The HAUSDORFF distance d_H was calculated for

each identified constitutive parameter set as a measure for the accuracy of the recovery of the load free master configuration \mathbf{X}_0 :

$$d_H = \max\{|\mathbf{X}_{0,i}^{model} - \mathbf{X}_{0,i}^{master}|, i = 1, \dots, n\}, \quad \text{eq. 7-38}$$

where n is the number of discrete material points describing the load free configuration.

Table 7-3 Comparison of the constitutive parameters of the master material and the parameter values that were identified by the FEMU approach based on numerically generated data. The last column gives the Hausdorff distance between the load free configuration that was recovered using the identified constitutive parameter set and the master configuration.

	μ_1 in MPa	k_1 in MPa	k_2	κ	φ in $^\circ$	Hausdorff distance in mm
Master	0.071	0.567	353.64	0.261	68.8	
<i>Estimates based on input data without noise</i>						
Parameter vector 1	0.072	0.593	331.92	0.260	68.5	0.02
Parameter vector 2	0.071	0.576	352.12	0.261	68.7	0.06
Parameter vector 3	0.074	0.500	353.00	0.260	68.3	0.08
Parameter vector 4	0.071	0.649	323.10	0.261	68.7	0.06
Parameter vector 5	0.073	0.482	367.10	0.262	68.8	0.10
Max. deviation in %	3.2	-15.0	-8.6	± 0.4	-0.5	
<i>Estimate based on data with superimposed error</i>						
Random Error	0.068	0.883	277.87	0.258	70.2	0.30
Deviation in %	-4.2	55.7	-21.4	-0.8	2.0	
Systematic Error	0.066	0.307	157.97	0.252	66.2	1.35
Deviation in %	-7.2	-45.9	-55.3	-3.4	-3.9	

7.9 Results of the verification experiment

A comparison of the constitutive parameters characterizing the master material and the five estimates that were identified based on strain field data without superimposed error is given in Table 7-3. Maximum deviations of parameter values between -15% and $+3.2\%$ were observed for the three parameters that govern the stiffness of the material, μ , k_1 and k_2 . In contrast, very small deviations $< 1\%$ were observed for κ and φ , the two parameters that characterize the degree and the preferred directions of the anisotropy.

Despite the observed deviation of the parameter values, the equi-biaxial longitudinal (index 1) and circumferential (index 2) CAUCHY stress-stretch curves of the five estimates are almost identical to the stress-stretch curves characterizing the master material, which is indicated by values of the non-linear coefficient of determination $R^2 \geq 0.978$ [Figure 7-6]. In all five cases, the load-free configuration was recovered with a Hausdorff distance ≤ 0.10 mm [Figure 7-7 a]. Figure 7-7 b shows the worst estimate of the load free configuration that was obtained in the numerical verification experiment.

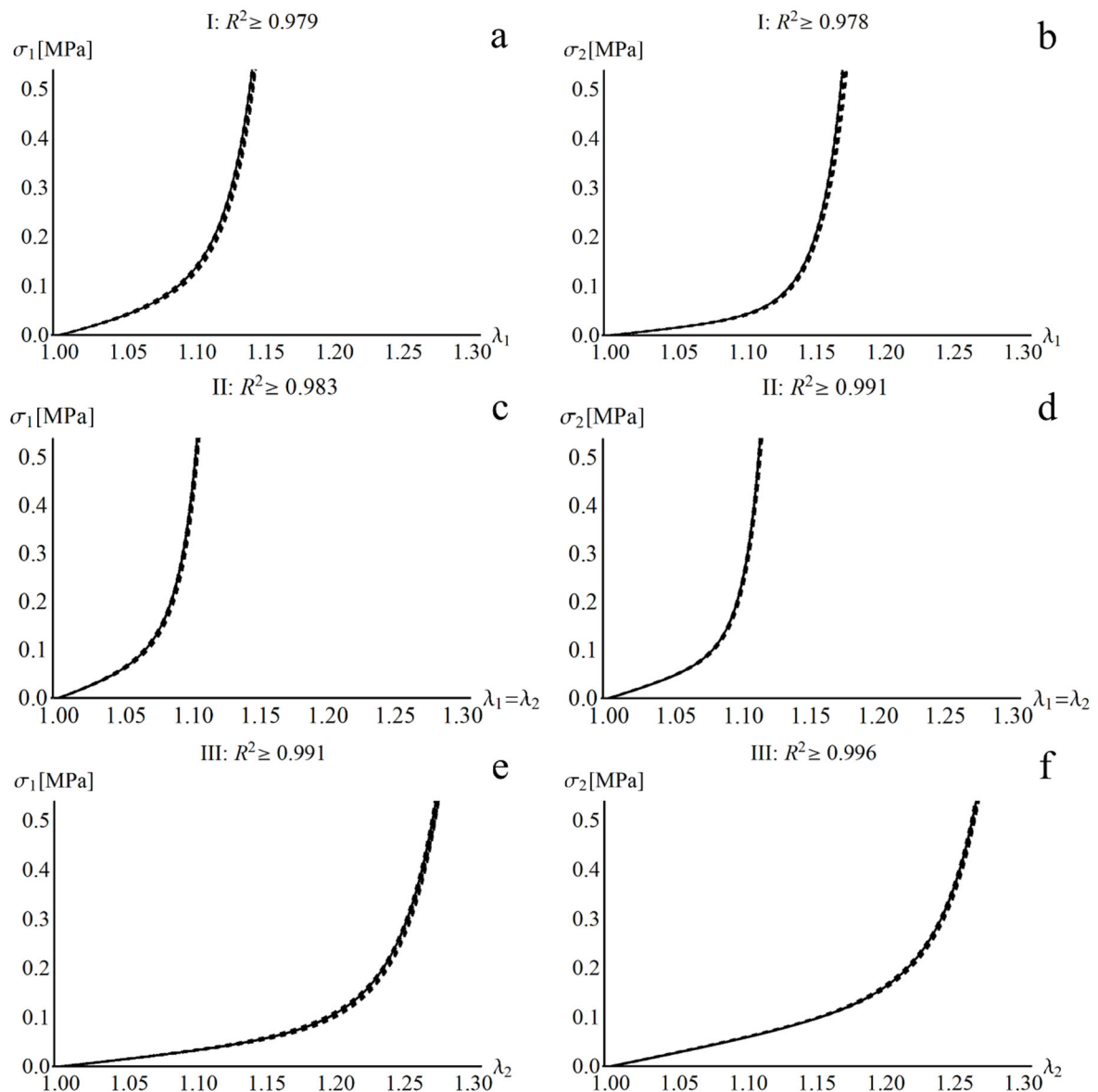


Figure 7-6: Comparison of the CAUCHY stress functions for the master parameter set (solid line) and the five estimates (dashed lines) of the constitutive parameter vector along the selected stretch paths I-III indicated in Figure 7-4. a and b: uniaxial longitudinal stretch (I), c and d: equi-biaxial stretch (II), e and f: uniaxial circumferential stretch (III). σ_1 and σ_2 are the principal in-plane CAUCHY stresses. The coefficient of correlation for the master stress-stretch curve and the worst estimate is given for each stretch path.

The quantitative distribution of in-plane strains of the numerical master model was matched almost exactly by the model using the inversely identified constitutive parameter vector 1 [Figure 7-12 a]. The

deviation of longitudinal strain and in-plane shear per element was 0.02% and the deviation of circumferential strain per element was 0.01% [Figure 7-13].

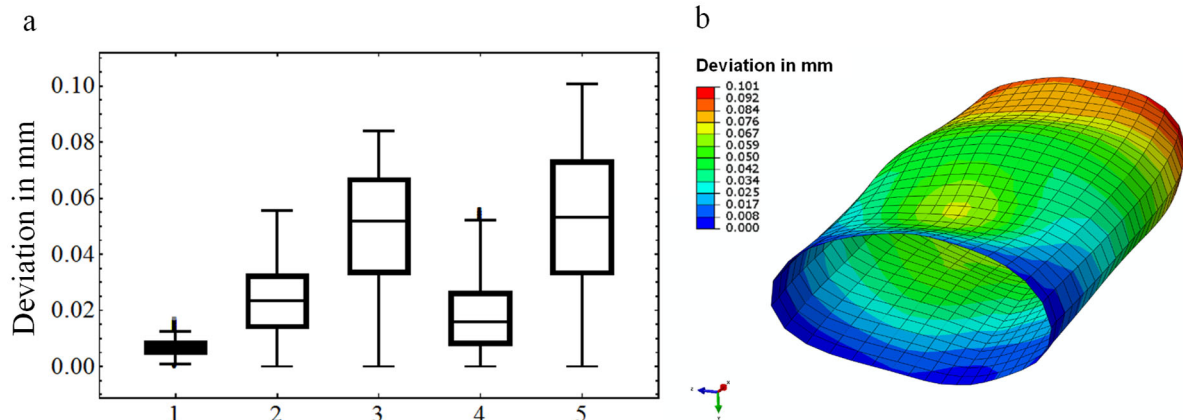


Figure 7-7 Deviation between the load-free configuration of the master model and the five configurations that were inversely identified based on strain distributions without superimposed error. a) Box-Whisker plots of the distributions of the nodal deviations of the five estimates from the initially given configuration. Upper and lower boundaries of the boxes indicate the 1st and 3rd quartile, respectively, the solid line at the center of the boxes indicates the median, upper and lower endings of the whiskers indicate the maximum and minimum values, respectively. Outliers are indicated by dots. The maximum value of each distribution marks the Hausdorff distance between given and estimated configuration. b) Nodal deviations of the worst estimate [cf. Table 7-3, parameter vector 5] plotted on the initially given configuration.

Based on strain-field data with superimposed random error [cf. section 7.8, Figure 7-5 d-f], the constitutive parameters $\mu = 0.068$ MPa, $k_1 = 0.883$ MPa, $k_2 = 277.87$, $\kappa = 0.258$ and $\varphi = 70.2^\circ$ were identified. This corresponds to deviations of -4.2% , 55.7% , -21.4% , -0.8% and 2.0% , respectively. Despite this considerably increased deviation, the longitudinal and circumferential stretch-CAUCHY stress curves of the identified material show coefficients of determination $R^2 > 0.9$ along all stretch paths [Figure 7-8, dashed lines]. This still indicates a good agreement with the master material. The load-free configuration was recovered with a median deviation of 0.18 mm per material point and a Hausdorff distance of 0.3 mm [Figure 7-9].

In contrast, the use of strain field data with superimposed systematic error according to eq. 7-35 resulted in a larger deviation of all constitutive parameters, but k_1 . Moreover, the parameters μ_1, k_1 and k_2 that govern the stiffness of the material, consistently showed smaller values compared to the master material. This indicates that the identified constitutive behavior is too distensible in all spatial directions. This is confirmed by the comparison of the stress-stretch plots that are given in Figure 7-8 (dashed-dotted lines). Also the accuracy of the identification of the load-free configuration decreased significantly: it was recovered with a median deviation of 0.81 mm and a Hausdorff distance of 1.5 mm, only.

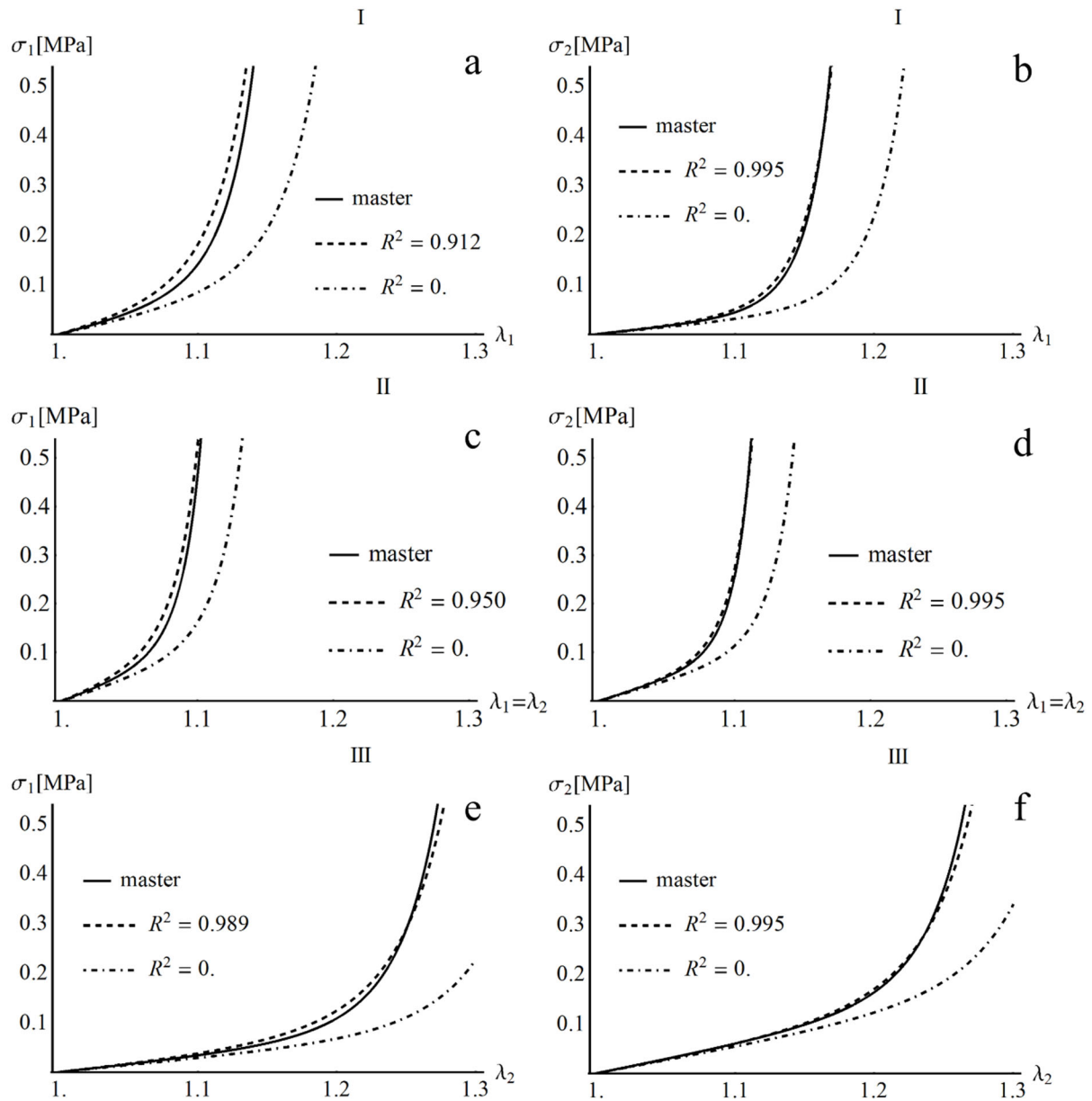


Figure 7-8 Comparison of the CAUCHY-stress response of the master material (solid line) and the materials that were identified using the inverse FEMU approach based on numerically generated data with overlaid random (dashed line) and systematic (dashed-dotted line) measurement error [cf. section 7.8]. σ_1 and σ_2 indicate the longitudinal and circumferential stresses, respectively, along the stretch paths I-III which are shown in Figure 7-4.

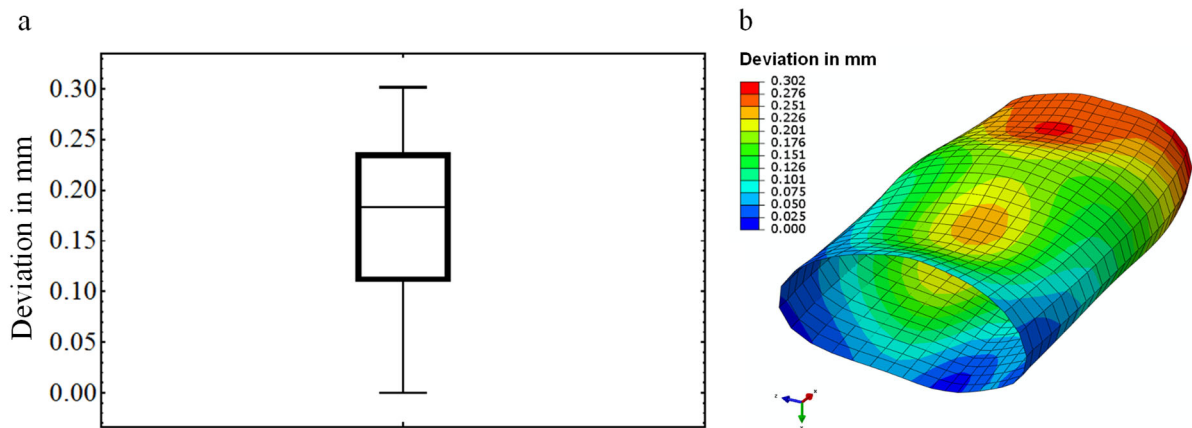


Figure 7-9 Deviation between given load free geometry that was used for numerical generation of deformation data in the verification experiment and the load free geometry that was inversely identified based on full-field strain data with overlaid random error. a) Nodal deviation plotted on the load-free configuration, b) Box-Whisker plots of the distribution of the nodal deviations between the estimated and the initially given load-free configuration. Upper and lower boundaries of the box indicate the 1st and 3rd quartile, respectively, the solid line at the center of the box indicates the median, upper and lower endings of the whiskers indicate the maximum and minimum values, respectively. The maximum value of the distribution marks the Hausdorff distance between given and estimated configuration.

7.10 Individual constitutive behavior identified based on in vivo data

7.10.1 Constitutive parameters and stress-stretch curves

The constitutive parameters of the three best fits obtained for each data set are given in Table 7-4. The corresponding plots of the longitudinal and circumferential CAUCHY stress curves along an equi-biaxial stretch path ($\lambda_1 = \lambda_2$) are shown in Figure 7-10. First, the material properties that were defined by the best fit parameters obtained for each data set are presented. Then, the best fit parameters were compared to other results of the optimization with a worse error function value.

The most distensible material properties were identified for the HV data set. Longitudinal and circumferential CAUCHY stress curves were characterized by an almost linear region with a small increase of stress up to $\lambda \approx 1.2$ corresponding to 20% of BIOT's strain, which then was followed by a transition to a steep exponential increase for larger stretches. $\kappa = 0.28$ indicates a moderate anisotropy of the aortic wall. The preferred directions governing the anisotropic behavior [cf. section 7.4] were oriented more towards the circumferential than the longitudinal direction of the vessel ($\varphi = 19.5^\circ$).

Table 7-4 Parameter values for the three best fits obtained for each data set. The last column gives the relative deviation of the error value with regard to the best fit obtained. [Reprinted from Wittek et al. 2016a with permission from Elsevier]

	μ in MPa	k_1 in MPa	k_2	κ	φ in $^\circ$	relative deviation of f_{err} in %
HV						
Best Fit	0.0782	0.00082	169.01	0.28	19.5	
2nd	0.0799	0.00209	189.973	0.30	8.1	0.83
3rd	0.0767	0.00681	131.784	0.29	18.6	0.93
PAOD						
Best Fit	0.1554	0.6093	874.89	0.002	85.6	
2 nd	0.1581	0.7678	719.65	0.0001	87.3	0.06
3 rd	0.1636	0.7555	745.13	0.001	88.8	0.15
AAA						
						relative deviation of f_{err}^{AAA} in%
Best Fit	0.2280	4.7362	1960.65	0.21	4.6	
2 nd	0.2214	3.9424	867.10	0.18	11.7	0.09
3 rd	0.2278	3.2544	335.20	0.20	8.0	0.98

For the aortic walls of the PAOD as well as the AAA patient, much stiffer elastic properties were identified, indicated by strongly increased values for the parameters μ , k_1 and k_2 [Table 7-4]. The stretch-stress curves [Figure 7-10] show that, in comparison to the HV material, the linear stress response in the small stretch region has vanished almost completely. Both materials show exponentially increasing stresses already for deformations smaller than $\lambda = 1.05$ ($\varepsilon = 5\%$).

The PAOD aortic wall exhibits a strongly anisotropic behavior. $\kappa = 0.002$ means that the influence of the direction vectors $\mathbf{a}_{0\alpha}$ and $\mathbf{a}_{0\beta}$ on the stress response of the material is weighted nearly with the factor $1 \equiv 100\%$ [cf. section 7.4]. $\varphi = 85.6^\circ$ means that both direction vectors are almost perfectly aligned with the longitudinal vessel axis and consequently with each other. This characterizes a transversely isotropic rather than an orthotropic behavior [cf. chapter 2.3.4 and e.g. Ogden 2009]. I.e. the much stiffer contribution of the exponential part of the constitutive equation [eq. 7-25] to the stress response, governed by $k_1 = 0.6093$ MPa and $k_2 = 874.89$, acts only in axial direction of the aorta, whereas the circumferential stress response depends more on the much more compliant ($\mu = 0.1554$ MPa) isotropic NEO-HOOKEAN term.

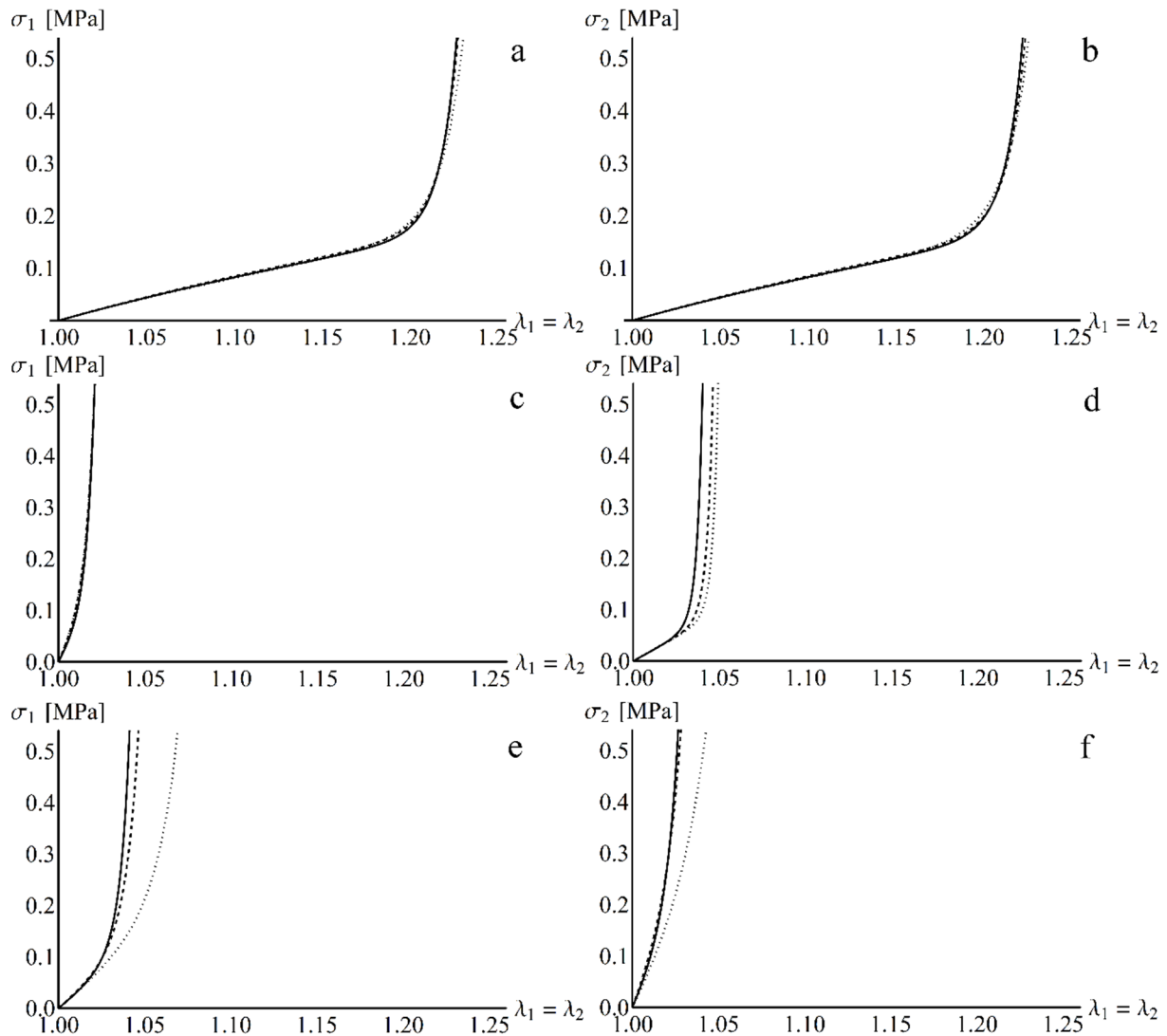


Figure 7-10 Equi-biaxial stretch plots of longitudinal and circumferential CAUCHY stresses for the three best constitutive parameter fits obtained for HV (a, b), PAOD (c, d) and AAA (e, f) data. Solid line – best fit, dashed line – 2nd best fit, dotted line – 3rd best fit. [Reprinted from Wittek et al. 2016a with permission from Elsevier]

The AAA exhibited a nearly transversely isotropic rather than an orthotropic behavior, too: in this case both direction vectors are almost aligned with the circumferential, not the longitudinal direction of the AAA ($\varphi = 4.6^\circ$). $\kappa = 0.21$ indicates moderately anisotropic elastic properties of the AAA, i.e. the isotropic part of the exponential FUNG-type term notably contributes to the stress-response of the wall as well [cf. section 7.4]. Consequently, the stiffness transverse to the preferred direction(s) does not only depend on the more distensible tensor linear NEO-HOOKEAN part and its parameter $\mu = 0.2280$ MPa, but also on the much stiffer exponential FUNG-type part and its stiffness determining parameters $k_1 = 4.7362$ MPa and $k_2 = 1960.65$.

In addition to the best fit constitutive parameters and equi-biaxial stretch-stress plots, the results for the fits with the 2nd and 3rd best values of the penalty functions are displayed in Table 7-4 and Figure 7-10. In case of the HV aortic segment, the three resulting Cauchy-stress curves are almost identical

[Figure 7-10 a, b] despite deviations in the numerical values of k_1 and k_2 which together govern the stiffness of the exponential contribution to the stress response of the material. Therefore, a decrease of the k_2 value can be compensated in part by increasing k_1 . In case of the PAOD patient, the stiffness of the circumferential stress response decreases slightly [Figure 7-10 d] with increasing error function values, whereas the AAA wall shows decreasing stiffness of both stress components along the equi-biaxial stretch path [Figure 7-10 e, f] with increasing f_{err}^{AAA} . Despite these deviations, the three different fits that were obtained for the same aortic wall identified consistent basal material characteristics in each case, such as overall stiffness, degree and preferred directions of anisotropy. This corresponds to the small relative deviations of the error values obtained for the three best fits. In particular, the values of the parameters μ and κ proved to be highly reproducible. In case of the angle φ that determines the preferred directions of the material, the reproducibility was highest for the PAOD patient. This constitutive behavior exhibits the strongest degree of anisotropy ($\kappa < 0.002$ for all three fits) and therefore the angle φ was determined best in the inverse identification procedure [cf. section 7.4].

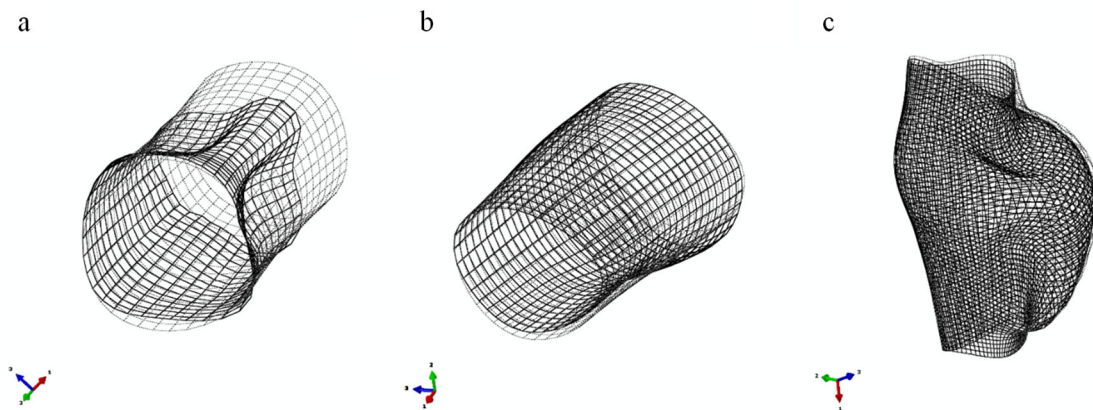


Figure 7-11 Estimated load free (solid black lines) and imaged diastolic configurations (light gray lines) of the HV (a), PAOD (b) and AAA (c) aortic wall samples. [Reprinted from Wittek et al. 2016a with permission from Elsevier]

7.10.2 Estimated load-free configurations and recovery of in vivo in-plane strain states

Figure 7-11 gives a comparison of the estimated load-free and the imaged diastolic configurations. It can clearly be seen that the differences between the estimated load-free and the measured diastolic configuration are largest in case of the most compliant HV aortic segment, for which the largest diastolic-systolic deformations were measured. In contrast, the estimated load-free configurations were much closer to the imaged diastolic configurations in case of the much stiffer PAOD and AAA segments.

Figure 7-12 b – d gives a comparison of the median and IQR of systolic in-plane strain distributions with respect to the diastolic configuration as measured by 4D ultrasound in vivo and estimated by FEA depending on the identified constitutive parameters. The median absolute deviation per element between

estimated and measured strains was between 1.3% and 3.8%. Figure 7-13 gives a detailed review of the deviation for all in-plane strain components and aortic segments.

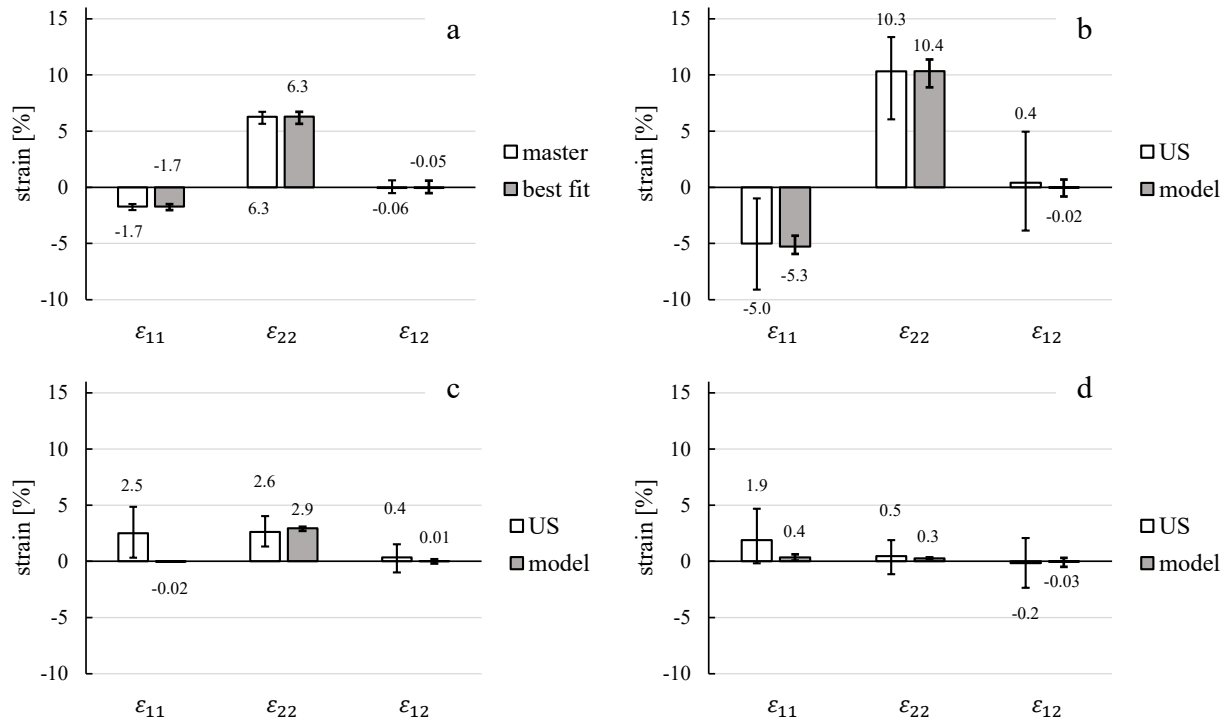


Figure 7-12: Comparison of given and estimated in-plane strain distributions (median [Q₁, Q₃]) of a) numerical verification experiment, b) HV, c) PAOD and d) AAA. ϵ_{11} – axial strain, ϵ_{22} – circumferential strain, ϵ_{12} – in-plane shear. [Reprinted from Wittek et al. 2016a with permission from Elsevier]

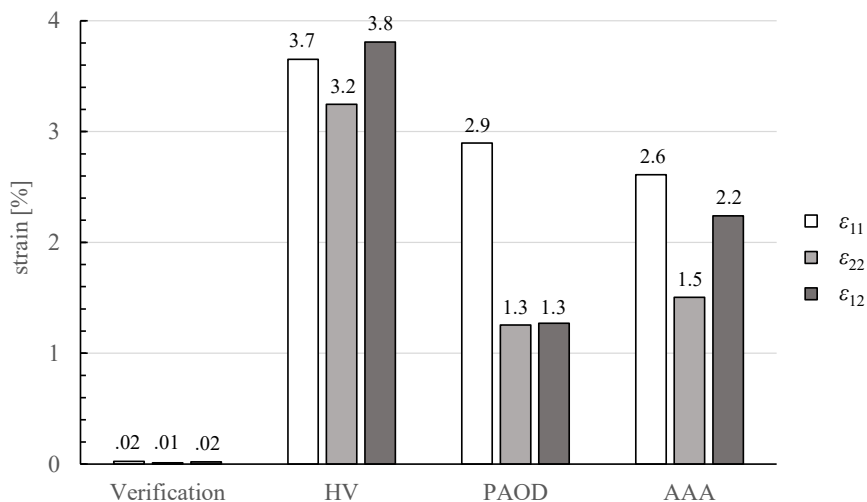


Figure 7-13: Median deviation of absolute values of in-plane strain components per element. [Reprinted from Wittek et al. 2016a with permission from Elsevier]

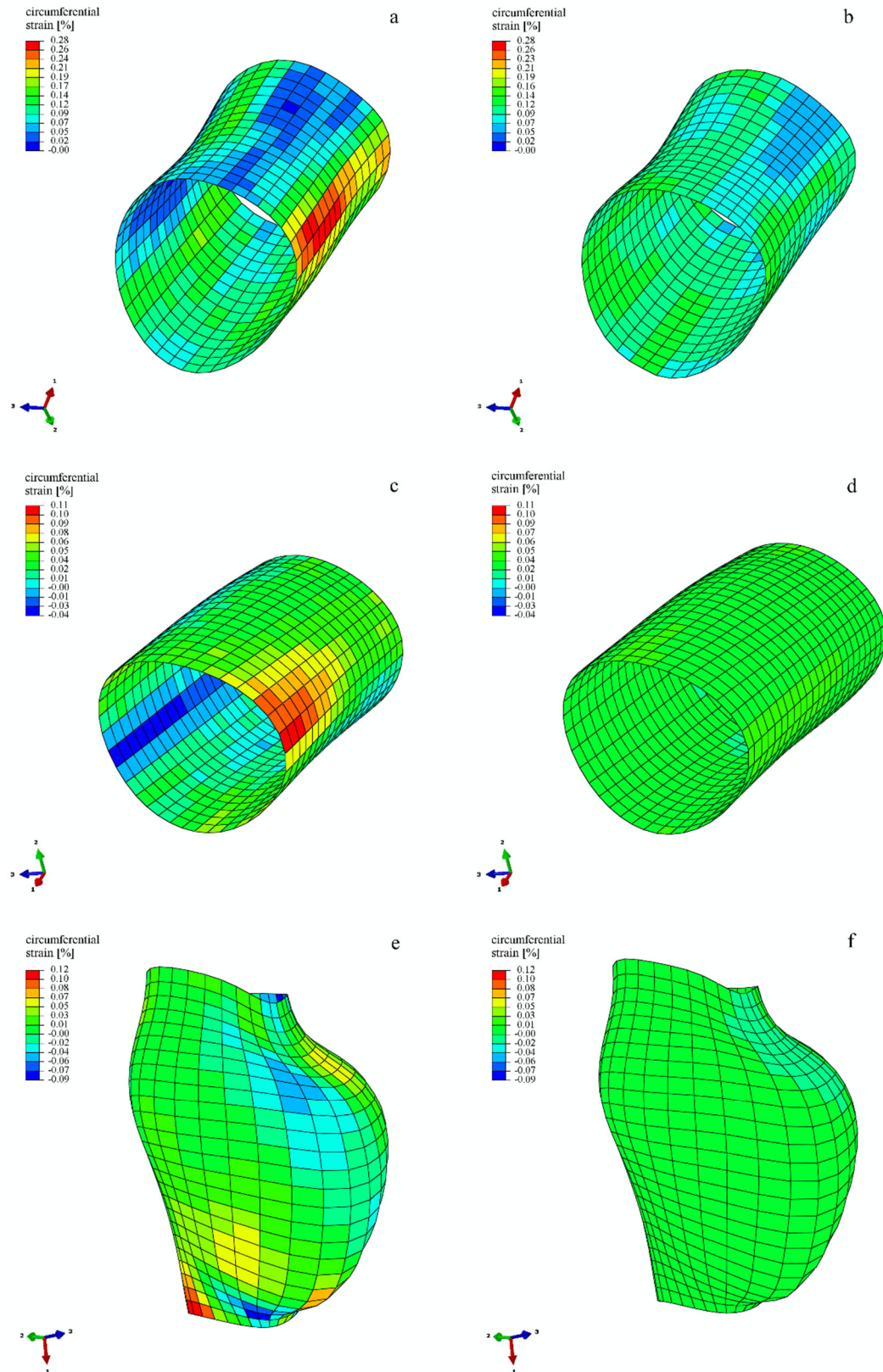


Figure 7-14: Comparison of the distributions of circumferential Biot's strains as measured by 4D ultrasound (a, c, e) and estimated by FEA depending on the identified constitutive parameters (b, d, f). a and b, c and d and e and f give results for data sets HV, PAOD and AAA, respectively. [Reprinted from Wittek et al. 2016a with permission from Elsevier]

The deviation between median values of estimated and measured circumferential strain and in-plane shear distributions was $\leq 0.43\%$ for all aortic segments. This applies as well for the median of the longitudinal strain distribution of the HV sample, where the measured strain distribution showed a negative median, i.e. a systolic shortening of the aortic segment compared to the diastolic configuration. In contrast, the deviation of the median longitudinal strain was much higher in the PAOD and the AAA segment (2.53% and 1.53%, respectively). In both cases, the measured strain distributions showed positive values, i.e. a systolic lengthening of the aortic segments.

In all samples and for all strain components, the IQR of the *estimated* strain distribution – indicated by the error bars in

Figure 7-12 – was much smaller than the one of the *measured* distribution. This indicates that the FE models, compared to the strain fields that were observed in vivo, predicted much more homogeneous strain states, which is illustrated in Figure 7-14. It shows the more pronounced minimum and maximum circumferential strains, steeper gradients and greater heterogeneity of the measured strain distributions.

This applies in particular to the distal neck region of the AAA Figure 7-14 e (bottom), where distinctive minimum and maximum strain regions were found in a relatively small area. Consequently, the median strain deviation per element of 1.5% that is given in Figure 7-13 is considerably higher than the deviation of the median value of the circumferential strain distribution [cf. Figure 7-12 d: 0.2%]. In case of the HV sample the deviation per element is 3.2 ... 3.8% for all in-plane strain components indicating that the weighting factors w_i of the error function were chosen adequately [c.f. section 7.7.2]. This applies as well to the AAA sample where the deviation per element ranges from 1.5% to 2.6%. In contrast, the estimated strain state of the PAOD sample showed a much greater deviation per element of the longitudinal strain (2.6%) compared to circumferential strain and in-plane shear (1.3%, each).

7.11 Discussion and conclusions

The presented FEMU approach for the inverse identification of the five parameters of a non-linear and anisotropic constitutive equation was verified in a numerical experiment and influences of random and systematic error in the measured strain data on the identification results were examined. Constitutive parameters of the infrarenal aortic walls of a healthy volunteer (HV), a patient suffering from peripheral arterial occlusive disease (PAOD) and of an abdominal aortic aneurysm (AAA) were identified based on non-invasive in vivo measurements of brachial diastolic and systolic blood pressure and of heterogeneous strain distributions of the aortic wall by 4D ultrasound. In addition to the numerical parameter values, the equi-biaxial CAUCHY stress-stretch curves were given as representation of the identified material properties that is independent of the chosen constitutive equation. The proposed method includes the determination of the unknown load-free geometry of the aortic segment as well as the prestretches

and -stresses in the imaged diastolic reference configuration. The systolic strain states with respect to the diastolic configuration that were estimated by the computational models depending on the identified constitutive parameters were compared to the strain states that were measured in vivo.

The approach to constitutive parameter identification that is presented in this chapter based on Wittek et al. [2016a] is an advanced version of the FEMU method that was previously developed within the work on this thesis and first published in Wittek et al. [2013]. Compared to this first approach, the advanced FEMU approach is characterized by two major changes:

- (i) The computational model was fitted to the measured systolic strains *with respect to the diastolic configuration*, not to systolic strains with respect to the – computationally estimated – load free configuration. In Wittek et al. [2013], the load free geometries and the diastolic strain distributions were identical for the ‘benchmark’ and the ‘estimation’ model. Both models differed in systolic strain increments compared to the diastolic strain distribution. These strain increments resulted from measured diastolic-systolic displacements $\mathbf{u}_{dia-sys}$ in the ‘benchmark’ model (independent of the assumed constitutive parameters) and from the deformation response of the finite element model to loading by systolic transmural pressure in the ‘estimation’ model. The latter depended on the assumed constitutive parameters. The diastolic strain distribution that depended on modeling assumptions was common to both models and may have had a tendency to dampen the differences of measured and estimated strain distributions.
- (ii) With a Hausdorff distance of $\delta \leq 0.01$ a more strict local convergence criterion was chosen for the identification of the load free configuration. In contrast, the sum of nodal deviations that was used in the 2013 approach is a global convergence criterion that allowed larger deviations at single nodes.
- (iii) The optimization algorithm was modified in order to avoid getting stuck in local minima of the error function:
 - a. Compared to Wittek et al. [2013], the number of valid constitutive parameter vectors obtained by the stochastic Monte Carlo algorithm was increased from 250 to 300.
 - b. The six best results of the Monte Carlo algorithm were used in the current approach as start parameter sets for the deterministic second part of the optimization procedure, not only the best fit.
 - c. An additional stochastic element has been introduced into the deterministic NELDER-MEAD algorithm:
- (iv) In order to identify five constitutive parameters, the Nelder-Mead algorithm needs six estimates of the parameter vector that constitute the vertices of the simplex. One of these vertices is constituted by the start parameter vector that was obtained from the Monte Carlo algorithm in the stochastic/deterministic approach used in this thesis. The other five vertices of the initial simplex have to be constructed. Like the start parameter vector, the choice of the initial simplex may determine the optimization result in nonlinear, multivariate and multiobjective optimization problems where the objective functions [cf. eq. 7-32 and eq. 7-34] may have several local minima. Usually, this construction of the vertices of the initial simplex from the start parameter vector is done in a deterministic way so that repeated runs of the Nelder-Mead simplex algorithm that use the identical start

- (v) parameter vector will always give the same results. In the approach that was developed in this thesis, this process of constructing the initial simplex from the start parameter vector was randomized and
- (vi) the Nelder-Mead algorithm was run thrice for each start parameter set so that repeated optimization runs starting from the identical estimate of the constitutive parameter vector, nonetheless used different start simplices, i.e. in different search areas for the optimum.

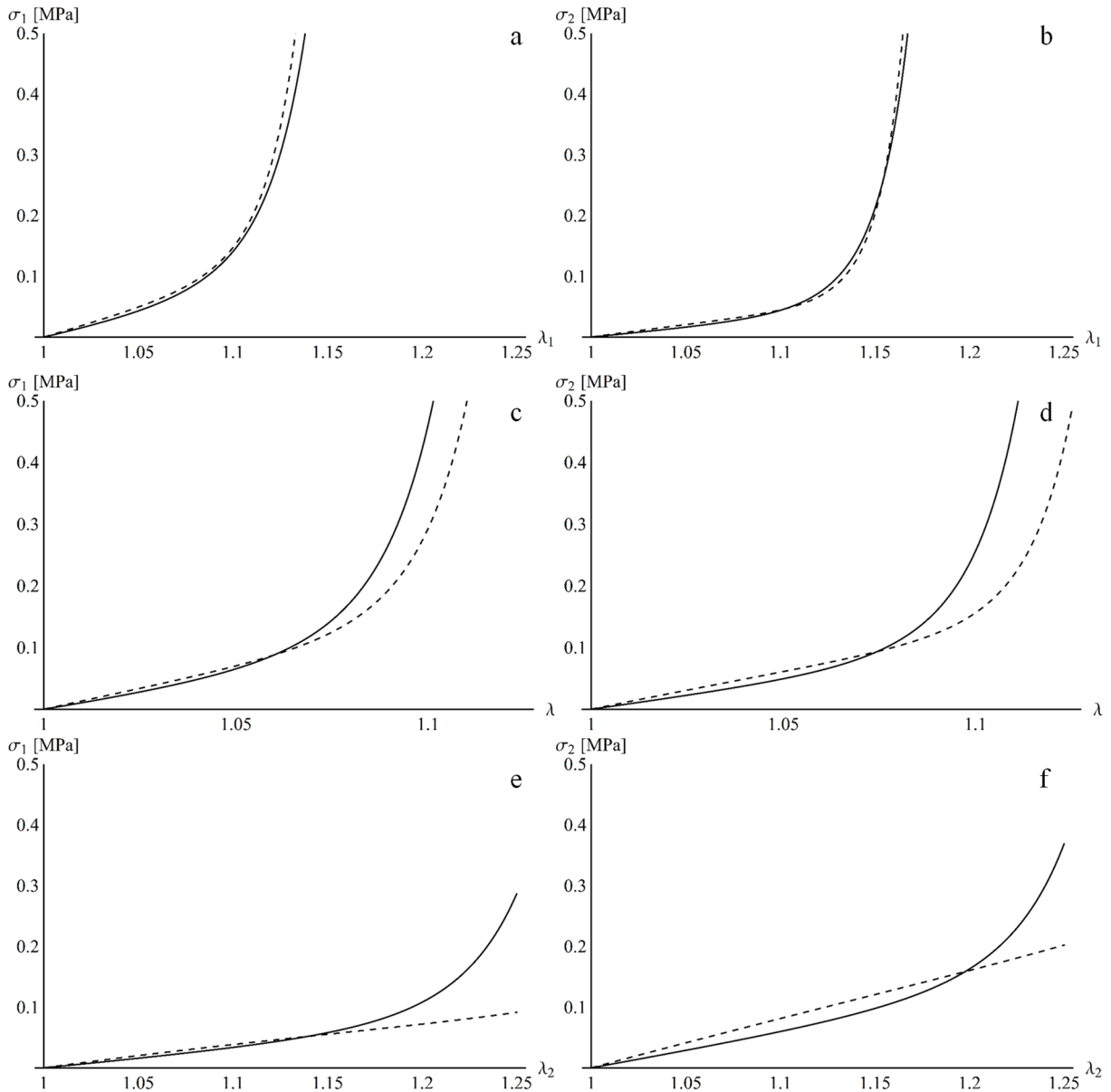


Figure 7-15 Results of the numerical verification experiment that was conducted in Wittek et al. [2013]. Solid lines represent the master material that was used for the numerical generation of data. Dashed lines show the material behavior that was identified using the 2013 inverse FEMU approach based on the numerically generated data [cf. section 7.8]. σ_1 and σ_2 indicate the longitudinal and circumferential stresses, respectively, along the stretch paths I (a, b), II (c, d) and III (e, f) which are shown in Figure 7-4. [Reprinted after Wittek et al. 2013 with permission from Elsevier]

These changes resulted in a substantial improvement of the results of the verification experiment without superimposed error [cf. section 7.9], for which the same numerically generated input data as in Wittek et al. [2013] have been used. The 2013 version of the FEMU approach was able to recover the systolic strain distribution and to identify a stress-stretch relation that coincided well with the master material along load paths I and II [cf. Figure 7-4 and Figure 7-15 a – d], i.e. in the range of multi-axial deformations that were well represented in the input deformation field. However, the deviation of the estimated material's stress response to the master material increased with the distance of the deformation state from this well represented range of input deformations. This means that the predictive value of the identified model for load cases other than the observed ones was very limited. The numerical values of the estimated constitutive parameters showed deviations up to 86% compared to the values of the master parameter vector. The results of the numerical verification experiment that was performed in Wittek et al. [2013] are given in Table 7-5.

Table 7-5 Constitutive parameter values that were identified in the verification experiment using the FEMU approach presented in Wittek et al. [2013]. [Reprinted after Wittek et al. 2013 with permission from Elsevier]

Data set	Parameters				
	μ in MPa	k_1 in MPa	k_2	κ	φ in $^\circ$
Master	0.071	0.567	353.64	0.261	68.8
Estimation	0.105	0.078	193.36	0.194	73.8
Rel. difference	47%	-86%	-45%	-26%	7%

In contrast, the enhanced method that is presented in detail in this thesis is able to identify the master parameter values with a maximum deviation of only 15% [cf. Table 7-3] resulting in identical constitutive behavior in a large range of finite deformations even for deformation states that are sparsely represented in the numerically generated input data (e.g. path III, uniaxial circumferential strain in Figure 7-4 and Figure 7-6). The recovery of the load free configuration was improved considerably as well, reducing the Hausdorff distance between identified and originally given configuration from 0.2 mm to 0.1 mm in the numerical verification experiment without superimposed error. Thus, the identified constitutive parameters can be used for simulations of load cases other than the experimentally observed ones.

The repeated identification of the constitutive behavior based on numerically generated strain data that were not corrupted by measurement uncertainty indicates that the solution of the inverse problem is unique with regard to the identified CAUCHY stress-stretch curves, i.e. the elastic behavior at finite deformations, and the load-free configuration. In contrast, the solution is non-unique with respect to the parameters of the chosen constitutive equation. This applies in particular to the parameters μ , k_1 and k_2 which jointly determine the nonlinear “stiffness” of the material so that changes in the value of one parameter can be compensated by adaption of the others, thus resulting in similar constitutive behavior in the physiological range of finite deformation [Wittek et al. 2013]. In contrast, unique parametrization

was observed in case of the parameters that determine the degree and preferred directions of the orthotropy, κ and φ .

These results confirm the feasibility of the proposed FEMU approach based on full-field deformation data to recover the parameters of a complex constitutive equation as well as the load-free geometry from just two observed deformation states (deformed geometries under diastolic and systolic hydrostatic pressure, but unknown load-free geometry). In case of homogeneous strain and stress states – as would result from a pressurized cylindrical tube with constant wall thickness and consisting of homogeneous material – this would result in a two-point strain-stress curve and allow for the determination of a linear elastic modulus, only. In contrast, the use of heterogeneous strain distributions allows for the inverse identification of a complex anisotropic and non-linear elastic constitutive behavior and of the irregular load-free geometry. The strain distributions calculated from the measured in vivo data were more heterogeneous than the numerically generated data used in the verification experiment and, thus, are likely to provide an even better basis for constitutive parameter identification [cf. Figure 7-1 a and b-d]. This applies to the two pathological data sets as well, even though the average strain amplitude is much smaller than in the HV data set. On the other hand, the use of simplifying modeling assumptions and incomplete knowledge of BCs can affect the reliability of in vivo constitutive parameter estimation [Reeps et al. 2010]: Values for wall thickness and longitudinal prestrain were assumed based on population averaged data that may deviate from individual values. The FE models contained homogenizing assumptions such as constant wall thickness and homogeneous material properties. The impact of these factors have to be the subject of further studies.

These results were confirmed by the parameter identification based on strain field data with superimposed random error in the scale of the measurement uncertainty of 4D ultrasound that was determined in the validation study [cf. chapter 4]: the deviation of the identified parameters μ_1 , k_1 and k_2 from the master parameters was considerably increased, whereas the agreement of the estimated values of κ and φ as well as the agreement of the CAUCHY stress-stretch curves were only slightly affected. This shows that the approach is robust with regard to random measurement uncertainty. In contrast, a deviation of the mean of the strain distribution by +1.6% marks a systematic overestimation of the cyclic deformation and results in the identification of a too distensible elastic behavior and large deviations of the recovered load free configuration. The systematic error in the numerically generated strain data [cf. section 7.8] was chosen in the size of the 95% confidence interval characterizing random error of the mean strain that was observed in the validation study [cf. chapter 4] in 20 repeated observations/evaluations of the same experiment. This means that a *single* observation/evaluation may show a systematic error of this size. Therefore, the identification of the constitutive behavior and the load free configuration based on a single in vivo measurement as presented in section 7.10, may result in considerable deviations of both and has exemplary character, only, in this study. In the validation study of 4D ultrasound measurement uncertainty and reliability, no systematic error of mean or local strain was observed in repeated measurements and evaluations. This result points the way to the improvement of the method in order to obtain

reliable individual results for a patient: future work has to address the computation of spatially resolved strain fields that represent the mean of repeated ultrasound measurements and evaluations as basis for reliable identification of individual constitutive parameters.

In the approach presented here, the estimated load-free configuration was assumed to be stress-free. Residual internal stresses due to heterogeneity of the different layers of the wall that result in the opening angle of cut aortic rings [Fung 1991] were not taken into account. In an in vitro study, Labrosse and coworkers [Labrosse et al. 2009] have observed that taking into account internal residual stresses or not did neither have an effect on the identified parameters of an anisotropic Fung-type constitutive model, nor on the simulated deformation of the aortic segment. Only the radial distribution of wall stresses was affected. A recent study by Maes et al. [2019] confirms these findings with respect to parameter identification. The effect of internal residual stresses appears to be negligible for the purpose of constitutive parameter identification. The hypothesis of uniform stress and strain across the wall thickness is associated with the thin shell assumption. It was implemented in the current approach by regarding the stress and strain state observed in the midlayer of the shell as representation of the in-plane wall stress throughout the thickness of the shell. Recently, Joldes et al. [2018] and Liu et al. [2019a] have proposed similar approaches to easily implement the uniform stress hypothesis in FE models of the aortic wall.

Exemplary application of the developed FEMU to 4D ultrasound data sets of three aortic wall segments from volunteers of different age and pathology resulted in the reproducible identification of three distinct and (patho-) physiologically reasonable constitutive behaviors [cf. chapter 1]. Based on the HV data set, the most compliant material was identified. This moderately anisotropic material was characterized by a slow, almost linear increase of stress for strains up to 20% that was followed by a transition to steep exponential increase for larger strains. The slow linear stress increase for small strains usually is attributed to the high content of elastin in young and healthy arteries, whereas the exponential stress gradient for higher strains indicates the increasing recruitment of embedded collagen fibers at the borders of the physiological deformation range [Wuyts et al. 1995; Marsh et al. 2004]. This linear and compliant region of the material has vanished almost completely in the constitutive behavior that was identified for the PAOD and the AAA data sets. In contrast, these materials were characterized by a steep exponential stress response to small deformations. These findings are consistent with the known degradation of the elastic components of aortic walls with age, which is enforced by pathologies such as atherosclerosis and aortic aneurysms, and the resulting high collagen content of the atherosclerotic and aneurysmal wall [Schlatmann and Becker 1977]. Accordingly, the AAA wall shows the stiffest behavior of the three aortic walls that were investigated in this study. The obtained equi-biaxial stress-stretch relations [Figure 7-10] are comparable to those presented in Gasser et al. [2012] that were obtained from biaxial tensile testing of aneurysm wall material harvested during open surgical repair. One of the distinctive structural changes that that were observed by Niestrawska et al. [2019] in AAAs compared to the healthy aortic wall, is the change of the wall's anisotropic behavior: Healthy aortic walls

showed orthotropic behavior, characterized by two symmetrically arranged mean collagen fiber directions with a mean angle $\varphi \approx 25^\circ$ to the circumferential axis [cf. chapter 1.4.3]. In contrast, a transversally isotropic material was found in stage 1- and stage 2-AAAs with a single preferred direction oriented in circumferential direction [cf. chapter 1.7]. The results of the in vivo parameter identification fit very well to these findings: an orthotropic material with two preferred directions and $\varphi \approx 20^\circ$ was identified for the HV, whereas for the AAA a transversally isotropic material was identified. Both preferred directions were almost perfectly aligned with the circumferential axis [cf. Table 7-4]. According to the findings by Niestrawska et al. [2019] this transversally isotropic behavior of stage 1 and stage 2 AAAs was not only distinctive with regard to healthy aortae, but also with regard to stage 3 AAAs that showed isotropic behavior. In addition to the significant changes in material symmetry, Niestrawska et al. [2019] identified a characteristic increase of the mechanical ‘stiffness’ parameters μ and k_1 with disease progression. A comparable increase was observed in the current study from the HV, through the PAOD to the AAA. Even though these promising agreements are based on exemplary evaluations of single data sets, only, they open up the prospect to use individual constitutive parameters that were identified in vivo as additional biomarkers for the evaluation of AAA disease progression.

The deviation between the median values of the estimated and measured circumferential strain and in-plane shear distributions was $< 0.43\%$. Larger deviations of 2.53% and 1.53% were observed only in the median longitudinal strains of the PAOD and the AAA FE model. The negative median longitudinal strain of the HV sample is matched very well by the FE model depending on the identified constitutive parameters (deviation of -0.2%). This behavior is consistent with the modeling assumptions: Inflation of a tube without closed ends that is loaded axially with a constant force F_{red} will lead to circumferential expansion and the material will respond with transverse contraction, i.e. negative longitudinal strain. In contrast, the PAOD and AAA measurements showed positive longitudinal strains, i.e. circumferential extension and axial lengthening at the same time. With the used BCs and hyperelastic constitutive equation [eq. 7-25], such a behavior cannot be modeled without additional time-dependent axial forces. In case of the PAOD patient aorta, no additional axial force results from increasing hydrostatic pressure. In consequence, the identified constitutive behavior limits the shortening of the sample to -0.02% by identifying a transversely isotropic material with a longitudinally oriented preferred direction that shows only minimum transverse contraction. In contrast, due to the strongly saccular geometry of the AAA [Figure 7-14 e, f], the systolic increase in hydrostatic pressure exerts an axial force component on the wall, as well. Here the circumferential orientation of the mean material direction that is associated with the stiffer exponential part of the constitutive equation renders the structure less stiff in longitudinal direction to allow for some systolic lengthening as response to the slight increase in the axial forces acting on the structure. The difference of systolic shortening and lengthening is not a characteristic difference between young/healthy and elderly/diseased aortae. In a cohort of 37 healthy volunteers, 14

aortae showed systolic lengthening and 23 systolic shortening. In 23 elderly subjects and 34 AAA patients, systolic lengthening was found in 10 and 15 subjects, respectively. The others exhibited systolic shortening.

The size of the deviation per element that ranges from 1.3% to 3.8% for all in-plane strain components seems to be acceptable, considering the uncertainties that affect a FE model that is based on in vivo data. For the most part, the observed deviation per element can be attributed to the fact that the FE models are not capable to recover the degree of heterogeneity of the measured strain distributions. This is most probably due to the homogenizing modeling assumptions such as constant wall thickness and homogeneous material parameters. Only the imaged irregular geometries introduce some degree of heterogeneity into the simulated strain distributions, which is amplified by the nonlinearity of the material. This approach holds very well for the HV data, but is less appropriate for the PAOD and the AAA data, where additional sources of heterogeneity such as local variations of wall thickness and elastic properties (calcifications, plaque, agglomerations of adipocytes) can be expected that are not included in the model at present. These, however, are common simplifications in state of the art FEA of thrombus free AAA [cf. the reviews by Humphrey and Holzapfel 2012; Avanzini et al. 2014; Martufi et al. 2014; Gasser 2016; Farotto et al. 2018 and original work e.g. by Joldes et al. 2015a; Kok et al. 2015; Gade et al. 2019].

Different approaches have been proposed to identify spatially varying material properties based on full-field data. Usually these approaches are applied to in vitro data [Zhao et al. 2009; Avril et al. 2010], where samples with constant known wall thickness are used or local wall thickness can be measured, or to numerically generated data [Kroon and Holzapfel 2009; Smoljkic et al. 2015; Liu et al. 2017; Liang et al. 2018], where all relevant parameters other than the constitutive behavior are known. In contrast, when applying an inverse approach to in vivo data, heterogeneous strain distributions that cannot be explained by irregular geometry may have two sources: variation of wall thickness or variation of constitutive behavior. To date, the data that are available in vivo do not allow to identify the source of heterogeneity. Thus, inverse identification of varying wall thickness and constitutive behavior on a data basis as was available in the present work is an ill-posed problem [Kabanikhin 2008] and the author considers it a reasonable decision to restrict the approach to the identification of an averaged constitutive behavior.

8 Summary and outlook

Using a modified 3D echocardiography device that was equipped with a speckle tracking algorithm, a method for the non-invasive full field displacement and strain measurement of aortic wall motion was developed and clinically established in cooperation with clinical partners. In an in vitro study, the measurement method was validated with respect to agreement with optical reference measurements and its reproducibility. The validation study showed that 95% confidence interval of the mean as well as the local strain values is about $\pm 2.1\%$ if these values are obtained from a single evaluation of a single measurement. In contrast, the measurement uncertainty is almost zero if mean and local strain values are determined as the arithmetical mean of repeated measurements and evaluations. 2.1% means a relative error of between 100% and 200% when the average size of the most relevant circumferential strain values in aged and AAA patients (1.9% and 0.9%, respectively; cf. Table 6-3) is considered. Thus, data sets of single patients are reliable only if they are determined as means of repeated measurements or evaluations. A clinical workflow for data acquisition and evaluation, which takes into account these results of the validation study, has to be established in future if diagnostic use is intended. In contrast, the results of the clinical studies that are presented in chapters 3, 5 and 6 are not compromised by the identified random error of a single measurement: group mean or median values were compared, only. Only in chapter 7 single data sets were used as basis for constitutive parameter identification. Therefore, the effect of the measurement uncertainty on the identified constitutive behavior was investigated.

The modified 4D ultrasound measurement made accessible in vivo information on the locally varying elastic deformation of human aortic and aneurysmal walls under cyclic loading by pulse pressure with high temporal and spatial resolution. Previous to this work, comparable full field data were available from optical laboratory measurements, i.e. from excised tissue samples, only.

Two methods for the in vivo identification of the individual elastic properties were developed that take into account the geometrically irregular configurations of real blood vessels and, therefore, are applicable to aortic aneurysms:

Firstly, a local distensibility coefficient was defined. Distensibility is a common simplifying, uniaxial (in circumferential direction) and linear approximation of the orthotropic and nonlinear elastic properties of aortic walls. However, it is determined based on in vivo data, only, without further modeling assumptions and captures the physiologically relevant elastic response of the aortic wall to cyclic loading by blood pressure. Given the fact that only two load cases – minimum and maximum blood pressure

– were available non-invasively in vivo, the restriction to a linear model allowed to access, for the first time, the locally varying elastic behavior of the wall and its heterogeneous distribution.

Secondly, based on these full field strain data, a method for the identification of the parameters of a constitutive equation that adequately models the orthotropic and nonlinear elastic properties of aortic walls was developed. This was possible because full field measurements of the heterogeneous strain distributions were available and the geometrically irregular configuration of the wall was taken into account: Depending on the local curvature of the wall, the loading by the identical blood pressure translates into a range of stress-strain relations that proved to be a sufficient basis for the reproducible identification of the orthotropic and nonlinear elastic constitutive behavior in a numerical verification experiment. Despite the newly available full field data, a series of non-individual modeling assumptions was necessary for this approach. Using the heterogeneity of the strain field for the identification of the nonlinear behavior, on the other hand necessitated the assumption of homogeneous material properties throughout the imaged aortic segment, which is a simplifying assumption if biological structures are considered.

The discussion of the limitations of both developed approaches to the identification of the individual elastic properties – uniaxial and linear, but locally varying distensibility and homogeneous orthotropic hyperelasticity – shows that biomechanical modeling and underlying assumptions are shaped strongly by available data. This applies in particular to work that is based on human in vivo data.

Both approaches were applied to exemplary patient data in clinical studies. The results demonstrated the potential use of the identified constitutive parameters as well as the statistical analysis of the obtained strain and distensibility distributions as additional biomarkers for aortic health and for disease progression of AAAs. The correlation of these new in vivo indices with AAA disease progression, wall strength or rupture risk is a promising hypothesis. However, this hypothesis has to be validated and tested in further clinical studies. This is a challenging task, because to date no independent and reliable in vivo or in vitro criterion for AAA disease progression and rupture risk is available against which the predictive value of the new biomarkers could be validated. In fact, the deficiencies of the established clinical criteria, maximum diameter and growth rate, gave rise to the research presented in this thesis.

9 References

- ABAQUS 6.12. 2012a. Abaqus Analysis User's Manual, Providence, RI, USA.
- ABAQUS 6.12. 2012b. Abaqus Theory Manual, Providence, RI, USA.
- ABAQUS 6.12. 2012c. Abaqus Theory Manual, Providence, RI, USA.
- ADOLPH, R., VORP, D.A., STEED, D.L., WEBSTER, M.W., KAMENEVA, M.V. AND WATKINS, S.C. 1997. Cellular content and permeability of intraluminal thrombus in abdominal aortic aneurysm. *J Vasc Surg* 25, 5, 916–926.
- ALBERTS, B., JOHNSON, A., LEWIS, J., RAFF, M., ROBERTS, K. AND WALTER, P. 2007. *Molecular biology of the cell*. Garland Science Taylor & Francis Group, New York, NY.
- ALESSANDRINI, M., HEYDE, B., QUEIROS, S., CYGAN, S., ZONTAK, M., SOMPHONE, O., BERNARD, O., CRAENE, M. de, O'DONNELL, M. AND D'HOOGHE, J. 2016. Detailed Evaluation of Five 3D Speckle Tracking Algorithms using Synthetic Echocardiographic Recordings. *IEEE TRANSACTIONS ON MEDICAL IMAGING*.
- ALTMAN, D.G. AND BLAND, J.M. 1983. Measurement in Medicine. The Analysis of Method Comparison Studies. *The Statistician* 32, 3, 307.
- ASTRAND, H., STALHAND, J., KARLSSON, J., KARLSSON, M., SONESSON, B. AND LANNE, T. 2011. In vivo estimation of the contribution of elastin and collagen to the mechanical properties in the human abdominal aorta: effect of age and sex. *J Appl Physiol (1985)* 110, 1, 176–187.
- AVANZINI, A., BATTINI, D., BAGOZZI, L. AND BISLERI, G. 2014. Biomechanical Evaluation of Ascending Aortic Aneurysms. *Biomed Res Int* 2014, 820385.
- AVOLIO, A.P., CHEN, S.G., WANG, R.P., ZHANG, C.L., LI, M.F. AND O'ROURKE, M.F. 1983. Effects of aging on changing arterial compliance and left ventricular load in a northern Chinese urban community. *Circulation* 68, 1, 50–58.
- AVRIL, S., BADEL, P. AND DUPREY, A. 2010. Anisotropic and hyperelastic identification of in vitro human arteries from full-field optical measurements. *J Biomech* 43, 15, 2978–2985.
- AVRIL, S., BERSI, M.R., BELLINI, C., GENOVESE, K. AND HUMPHREY, J.D. 2015. Regional identification of mechanical properties in arteries. *Computer Methods in Biomechanics and Biomedical Engineering*, 1–2.
- AVRIL, S., BONNET, M., BRETELLE, A.-S., GREDIAC, M., HILD, F., IENNY, P., LATOURTE, F., LEMOSSE, D., PAGANO, S., PAGNACCO, E. AND PIERRON, F. 2008. Overview of identification methods of mechanical parameters based on full-field measurements. *Exp Mech* 48, 4, 381–402.
- AZELOGLU, E.U., ALBRO, M.B., THIMMAPPA, V.A., ATESHIAN, G.A. AND COSTA, K.D. 2008. Heterogeneous transmural proteoglycan distribution provides a mechanism for regulating residual stresses in the aorta. *AJP: Heart and Circulatory Physiology* 294, 3, H1197-205.
- BADEL, P., AVRIL, S., LESSNER, S. AND SUTTON, M. 2012. Mechanical identification of layer-specific properties of mouse carotid arteries using 3D-DIC and a hyperelastic anisotropic constitutive model. *Comput Methods Biomech Biomed Eng (Computer methods in biomechanics and biomedical engineering)* 15, 1, 37–48.
- BARNETT, G.O., MALLOS, A.J. AND SHAPIRO, A. 1961. Relationship of aortic pressure and diameter in the dog. *Journal of applied physiology* 16, 545–548.

- BECQUEMIN, J.-P., PILLET, J.-C., LESCALIE, F., SAPOVAL, M., GOUEFFIC, Y., LERMUSIAUX, P., STEINMETZ, E. AND MARZELLE, J. 2011. A randomized controlled trial of endovascular aneurysm repair versus open surgery for abdominal aortic aneurysms in low- to moderate-risk patients. *J Vasc Surg* 53, 5, 1167-1173.e1.
- BELL, V., MITCHELL, W.A., SIGURETHSSON, S., WESTENBERG, JOS J M, GOTAL, J.D., TORJESEN, A.A., ASPELUND, T., LAUNER, L.J., ROOS, A. de, GUDNASON, V., HARRIS, T.B. AND MITCHELL, G.F. 2014. Longitudinal and circumferential strain of the proximal aorta. *J Am Heart Assoc* 3, 6, e001536.
- BELL, V., SIGURDSSON, S., WESTENBERG, JOS J M, GOTAL, J.D., TORJESEN, A.A., ASPELUND, T., LAUNER, L.J., HARRIS, T.B., GUDNASON, V., ROOS, A. de and MITCHELL, G.F. 2015. Relations between aortic stiffness and left ventricular structure and function in older participants in the age, gene/environment susceptibility-reykjavik study. *Circ Cardiovasc Imaging* 8, 4, e003039.
- BELLER, C.J., LABROSSE, M.R., THUBRIKAR, M.J. AND ROBICSEK, F. 2004. Role of aortic root motion in the pathogenesis of aortic dissection. *Circulation* 109, 6, 763–769.
- BELLHOUSE, B.J. AND BELLHOUSE, F.H. 1968. Mechanism of Closure of the Aortic Valve. *Nature* 217, 5123, 86–87.
- BERSI, M.R., BELLINI, C., DI ACHILLE, P., HUMPHREY, J.D., GENOVESE, K. AND AVRIL, S. 2016. Novel Methodology for Characterizing Regional Variations in the Material Properties of Murine Aortas. *J Biomech Eng* 138, 7.
- BIHARI, P., SHELKE, A., NWE, T.H., MULARCZYK, M., NELSON, K., SCHMANDRA, T., KNEZ, P. AND SCHMITZ-RIXEN, T. 2013. Strain Measurement of Abdominal Aortic Aneurysm with Real-time 3D-Ultrasound Speckle Tracking. *Eur J Vasc Endovasc Surg* 45, 4, 315–323.
- BLAND, J.M. AND ALTMAN, D.G. 1986. Statistical methods for assessing agreement between two methods of clinical measurement. *Lancet* 1, 8476, 307–310.
- BLANKENSTEIN, J.D. 2005. Dutch Randomized Endovascular Aneurysm Management (DREAM) trial group: two-year outcomes after conventional or endovascular repair of abdominal aortic aneurysms. *N Engl J Med* 352, 2398–2405.
- BOUTOUYRIE, P., TROPEANO, A.I., ASMAR, R., GAUTIER, I., BENETOS, A., LACOLLEY, P. AND LAURENT, S. 2002. Aortic stiffness is an independent predictor of primary coronary events in hypertensive patients: a longitudinal study. *Hypertension* 39, 1, 10–15.
- BUCKBERG, G.D., HOFFMAN, J.I.E., COGHLAN, H.C. AND NANDA, N.C. 2015. Ventricular structure-function relations in health and disease: Part I. The normal heart. *European journal of cardio-thoracic surgery: official journal of the European Association for Cardio-thoracic Surgery* 47, 4, 587–601.
- BUIJS, R.V.C., WILLEMS, T.P., TIO, R.A., BOERSMA, H.H., TIELLIU, I.F.J., SLART, R.H.J.A. AND ZEEBREGTS, C.J. 2013. Calcification as a Risk Factor for Rupture of Abdominal Aortic Aneurysm. *European Journal of Vascular and Endovascular Surgery* 46, 5, 542–548.
- BYROM, F.B. 1969. *The hypertensive vascular crisis. An experimental study.* Heinemann monograph. Heinemann Medical, London.
- BYROM, F.B. AND DODSON, L.F. 1948. The causation of acute arterial necrosis in hypertensive disease. *J. Pathol.* 60, 3, 357–368.
- CANHAM, P.B., FINLAY, H.M., DIXON, J.G., BOUGHNER, D.R. AND CHEN, A. 1989. Measurements from light and polarised light microscopy of human coronary arteries fixed at distending pressure. *Cardiovasc Res* 23, 11, 973–982.
- CARDAMONE, L., VALENTÍN, A., EBERTH, J.F. AND HUMPHREY, J.D. 2009. Origin of axial prestretch and residual stress in arteries. *Biomechanics and modeling in mechanobiology* 8, 6, 431–446.
- CAREW, T.E., VAISHNAV, R.N. AND PATEL, D.J. 1968. Compressibility of the Arterial Wall. *Circulation Research* 23, 1, 61–68.
- CARLSSON, M., CAIN, P., HOLMQVIST, C., STAHLBERG, F., LUNDBACK, S. AND ARHEDEN, H. 2004. Total heart volume variation throughout the cardiac cycle in humans. *American journal of physiology. Heart and circulatory physiology* 287, 1, H243–50.

- CARLSSON, M., UGANDER, M., MOSEN, H., BUHRE, T. AND ARHEDEN, H. 2007. Atrioventricular plane displacement is the major contributor to left ventricular pumping in healthy adults, athletes, and patients with dilated cardiomyopathy. *American journal of physiology. Heart and circulatory physiology* 292, 3, H1452-9.
- CARO, C.G. 2012. *The mechanics of the circulation*. Cambridge University Press, Cambridge, UK, New York.
- CHEN, X., XIE, H., ERKAMP, R., KIM, K., JIA, C., RUBIN, J.M. AND O'DONNELL, M. 2005. 3-D correlation-based speckle tracking. *Ultrason Imaging* 27, 1, 21–36.
- CHUONG, C.J. AND FUNG, Y.C. 1986. Residual Stress in Arteries. In *Frontiers in Biomechanics*, G. W. SCHMID-SCHÖNBEIN, S. L.-Y. WOO AND B. W. ZWEIFACH, Eds. Springer New York, New York, NY, 117–129.
- COHEN, J.R., MANDELL, C., CHANG, J.B. AND WISE, L. 1988. Elastin metabolism of the infrarenal aorta. *Journal of Vascular Surgery* 7, 2, 210–214.
- COLLETTE, Y. AND SIARRY, P. 2004. *Multiobjective optimization. Principles and case studies*. Decision engineering. Springer, Berlin.
- CRONENWETT, J.L., MURPHY, T.F., ZELENOCK, G.B., WHITEHOUSE, W.M., JR, LINDENAUER, S.M., GRAHAM, L.M., QUINT, L.E., SILVER, T.M. AND STANLEY, J.C. 1985. Actuarial analysis of variables associated with rupture of small abdominal aortic aneurysms. *Surgery* 98, 3, 472–483.
- CYRON, C.J. AND HUMPHREY, J.D. 2017. Growth and Remodeling of Load-Bearing Biological Soft Tissues. *Meccanica* 52, 3, 645–664.
- DAGUM, P., GREEN, G.R., NISTAL, F.J., DAUGHTERS, G.T., TIMEK, T.A., FOPPIANO, L.E., BOLGER, A.F., INGELS, N.B., JR AND MILLER, D.C. 1999. Deformational dynamics of the aortic root: modes and physiologic determinants. *Circulation* 100, 19 Suppl, II54-62.
- DARLING, R.C., MESSINA, C.R., BREWSTER, D.C. AND OTTINGER, L.W. 1977. Autopsy study of unoperated abdominal aortic aneurysms. The case for early resection. *Circulation* 56, 3 Suppl, II161-4.
- DEBUS, E.S. AND GROSS-FENGELS, W. 2012. *Operative und interventionelle Gefäßmedizin*. SpringerLink Bücher. Springer Berlin Heidelberg, Berlin, Heidelberg.
- DEBUS, E.S., HEIDEMANN, F., GROSS-FENGELS, W., MAHLMANN, A., MUHL, E., PFISTER, K., ROTH, S., STOSZCZYNSKI, C., WALTHER, A., WEISS, N., WILHELMI, M. AND GRUNDMANN, R.T. 2018. *S3-Leitlinie zu Screening, Diagnostik, Therapie und Nachsorge des Bauchortenaneurysmas*. Deutsche Gesellschaft für Gefäßchirurgie und Gefäßmedizin (DGG), AWMF online.
- DERWICH, W., WITTEK, A., BLASE, C. AND SCHMITZ-RIXEN, T. 2017. Dynamische Analyse der biomechanischen Eigenschaften der infrarenalen Aorta. *Gefäßchirurgie* 22, 6, 392–399.
- DERWICH, W., WITTEK, A., PFISTER, K., NELSON, K., BEREITER-HAHN, J., FRITZEN, C.P., BLASE, C. AND SCHMITZ-RIXEN, T. 2016. High Resolution Strain Analysis Comparing Aorta and Abdominal Aortic Aneurysm with Real Time 3D Speckle Tracking Ultrasound. *Eur J Vasc Endovasc Surg* 51, 2, 187–193.
- DÍEZ, J. 2007. Arterial stiffness and extracellular matrix. *Advances in cardiology* 44, 76–95.
- DiMARTINO, E.S., BOHRA, A., VANDE GEEST, JONATHAN P, GUPTA, N., MAKAROUN, M.S. AND VORP, D.A. 2006. Biomechanical properties of ruptured versus electively repaired abdominal aortic aneurysm wall tissue. *J Vasc Surg* 43, 3, 570-6; discussion 576.
- DISSELDORP, E.M.J. van, DRONKELAAR, J.J. van, PLUIM, J.P.W., VOSSE, F.N. van de, SAMBEEK, M.R.H.M. van and LOPATA, R.G.P. 2019a. Ultrasound Based Wall Stress Analysis of Abdominal Aortic Aneurysms using Multiperspective Imaging. *Eur J Vasc Endovasc Surg*.
- DISSELDORP, E.M.J. van, PETERSON, N.J., RUTTEN, M.C.M., VOSSE, F.N. van de, SAMBEEK, M.R.H.M. van and LOPATA, R.G.P. 2016a. Patient Specific Wall Stress Analysis and Mechanical Characterization of Abdominal Aortic Aneurysms Using 4D Ultrasound. *European journal of vascular and endovascular surgery: the official journal of the European Society for Vascular Surgery*.

- DISSELDORP, E.M.J. van, PETERSON, N.J., VOSSE, F.N. van de, SAMBEEK, M.R.H.M. van, LOPATA, R.G.P., VAN DISSELDORP, E.M.J., VAN DE VOSSE, F.N., VAN SAMBEEK, M.R.H.M. AND LOPATA, R.G.P. 2019b. Quantification of aortic stiffness and wall stress in healthy volunteers and abdominal aortic aneurysm patients using time-resolved 3D ultrasound: a comparison study. *Eur Heart J Cardiovascular Imaging* 20, 2, 1–7.
- DISSELDORP, E.M. van, HOBELMAN, K.H., PETERSON, N.J., VOSSE, F.N. van de, van SAMBEEK AND LOPATA, R.G. 2016b. Influence of limited field-of-view on wall stress analysis in abdominal aortic aneurysms. *J Biomech*.
- DUPREY, A., TRABELSI, O., VOLA, M., FAVRE, J.-P. AND AVRIL, S. 2016. Biaxial rupture properties of ascending thoracic aortic aneurysms. *ACTA BIOMATERIALIA*.
- DZAU, V.J., ANTMAN, E.M., BLACK, H.R., HAYES, D.L., MANSON, J.E., PLUTZKY, J., POPMA, J.J. AND STEVENSON, W. 2006a. The cardiovascular disease continuum validated: clinical evidence of improved patient outcomes: part I: Pathophysiology and clinical trial evidence (risk factors through stable coronary artery disease). *Circulation* 114, 25, 2850–2870.
- DZAU, V.J., ANTMAN, E.M., BLACK, H.R., HAYES, D.L., MANSON, J.E., PLUTZKY, J., POPMA, J.J. AND STEVENSON, W. 2006b. The cardiovascular disease continuum validated: clinical evidence of improved patient outcomes: part II: Clinical trial evidence (acute coronary syndromes through renal disease) and future directions. *Circulation* 114, 25, 2871–2891.
- EHRGOTT, M. 2005. *Multicriteria Optimization*. Springer, Berlin, Heidelberg.
- FABER, M. AND MØLLER-HOU, G. 1952. The human aorta. V. Collagen and elastin in the normal and hypertensive aorta. *Acta pathologica et microbiologica Scandinavica* 31, 3, 377–382.
- FAROTTO, D., SEGERS, P., MEURIS, B., VANDER SLOTEN, J. AND FAMAHEY, N. 2018. The role of biomechanics in aortic aneurysm management. Requirements, open problems and future prospects. *J Mech Behav Biomed Mater* 77, 295–307.
- FARZANEH, S., TRABELSI, O. AND AVRIL, S. 2018. Inverse identification of local stiffness across ascending thoracic aortic aneurysms. *Biomechanics and modeling in mechanobiology*.
- FARZANEH, S., TRABELSI, O., CHAVENT, B. AND AVRIL, S. 2019. Identifying Local Arterial Stiffness to Assess the Risk of Rupture of Ascending Thoracic Aortic Aneurysms. *ANNALS OF BIOMEDICAL ENGINEERING*.
- FILLINGER, M., RAGHAVAN, M.L., MARRA, S., CRONENWETT, J. AND KENNEDY, F. 2002. In vivo analysis of mechanical wall stress and abdominal aortic aneurysm rupture risk. *J Vasc Surg* 36, 3, 589–597.
- FILLINGER, M.F., MARRA, S.P., RAGHAVAN, M.L. AND KENNEDY, F.E. 2003. Prediction of rupture risk in abdominal aortic aneurysm during observation: wall stress versus diameter. *J Vasc Surg* 37, 4, 724–732.
- FINLAY, H.M., MCCULLOUGH, L. AND CANHAM, P.B. 1995. Three-dimensional collagen organization of human brain arteries at different transmural pressures. *JOURNAL OF VASCULAR RESEARCH* 32, 5, 301–312.
- FLAMINI, V., DEANDA, A. AND GRIFFITH, B.E. 2015. *Immersed boundary-finite element model of fluid-structure interaction in the aortic root*. arXiv preprint, Cornell University.
- FREESTONE, T., TURNER, R.J., COADY, A., HIGMAN, D.J., GREENHALGH, R.M. AND POWELL, J.T. 1995. Inflammation and matrix metalloproteinases in the enlarging abdominal aortic aneurysm. *Arterioscler Thromb Vasc Biol* 15, 8, 1145–1151.
- FRITZ, T., WIENERS, C., SEEMANN, G., STEEN, H. AND DÖSSEL, O. 2014. Simulation of the contraction of the ventricles in a human heart model including atria and pericardium. *Biomechanics and modeling in mechanobiology* 13, 3, 627–641.
- FRÖMKE, J. 2006. *Standardoperationen in der Gefäßchirurgie*. Steinkopff-Verlag, Darmstadt.
- FUNG, Y.C. 1984. *Biodynamics*. Circulation. Springer New York, New York, NY.
- FUNG, Y.C. 1991. What are the residual stresses doing in our blood vessels? *ANNALS OF BIOMEDICAL ENGINEERING* 19, 3, 237–249.
- FUNG, Y.C., FRONEK, K. AND PATITUCCI, P. 1979. Pseudoelasticity of arteries and the choice of its mathematical expression. *Am J Physiol* 237, 5, H620-H631.
- FUNG, Y.-C. 1993. *Biomechanics. Mechanical properties of living tissues*. Springer, New York, NY, Berlin.
- FUNG, Y.-C. 1997. *Biomechanics. Circulation*. Springer, New York.
- GADE, J.-L., STÄLHAND, J. AND THORE, C.-J. 2019. An in vivo parameter identification method for arteries: numerical validation for the human abdominal aorta. *Computer Methods in Biomechanics and Biomedical Engineering*, 1–16.

- GALLEGO, J.L., DOMINGUEZ, J. AND HOLZAPFEL, G.A. 2015. Influence of Periadventitial Tissues on the Mechanics of the Thoracic Aorta. In *European Solid Mechanics Conference 2015*, J. LLORCA, Ed.
- GARY F. MITCHELL. 2009. Arterial stiffness and wave reflection: Biomarkers of cardiovascular risk. *Artery Research* 3, 2, 56–64.
- GASSER, T.C. 2016. Biomechanical Rupture Risk Assessment. A Consistent and Objective Decision-Making Tool for Abdominal Aortic Aneurysm Patients. *AORTA Journal* 4, 2, 42–60.
- GASSER, T.C., AUER, M., LABRUTO, F., SWEDENBORG, J. AND ROY, J. 2010. Biomechanical rupture risk assessment of abdominal aortic aneurysms: model complexity versus predictability of finite element simulations. *Eur J Vasc Endovasc Surg* 40, 2, 176–185.
- GASSER, T.C., GALLINETTI, S., XING, X., FORSELL, C., SWEDENBORG, J. AND ROY, J. 2012. Spatial orientation of collagen fibers in the abdominal aortic aneurysm's wall and its relation to wall mechanics. *ACTA BIOMATERIALIA* 8, 8, 3091–3103.
- GASSER, T.C., OGDEN, R.W. AND HOLZAPFEL, G.A. 2006. Hyperelastic modelling of arterial layers with distributed collagen fibre orientations. *J R Soc Interface* 3, 6, 15–35.
- GEE, M.W., FÖRSTER, C. AND WALL, W.A. 2010. A computational strategy for prestressing patient-specific biomechanical problems under finite deformation. *Int. J. Numer. Meth. Biomed. Engng.* 26, 52–72.
- GEE, M.W., REEPS, C., ECKSTEIN, H.H. AND WALL, W.A. 2009. Prestressing in finite deformation abdominal aortic aneurysm simulation. *J Biomech* 42, 11, 1732–1739.
- GENOVESE, K., LEE, Y.-U., LEE, A.Y. AND HUMPHREY, J.D. 2013. An improved panoramic digital image correlation method for vascular strain analysis and material characterization. *J Mech Behav Biomed Mater* 27, 132–142.
- GOSS, S.A., JOHNSTON, R.L. AND DUNN, F. 1980. Compilation of empirical ultrasonic properties of mammalian tissues. II. *J Acoust Soc Am* 68, 1, 93–108.
- GREDIAC, M., PIERRON, F., AVRIL, S. AND TOUSSAINT, E. 2006. The virtual fields method for extracting constitutive parameters from full-field measurements: A review. *STRAIN* 42, 4, 233–253.
- GREENHALGH, R.M., BROWN, L.C., KWONG, G P S, POWELL, J.T. AND THOMPSON, S.G. 2004. Comparison of endovascular aneurysm repair with open repair in patients with abdominal aortic aneurysm (EVAR trial 1), 30-day operative mortality results: randomised controlled trial. *Lancet* 364, 9437, 843–848.
- GRIFFITH, B.E. 2012. Immersed boundary model of aortic heart valve dynamics with physiological driving and loading conditions. *International journal for numerical methods in biomedical engineering* 28, 3, 317–345.
- HAN, H.C. AND FUNG, Y.C. 1995. Longitudinal strain of canine and porcine aortas. *J Biomech* 28, 5, 637–641.
- HARTUNG, J., ELPELT, B. AND KLÖSENER, K.-H. 2012. *Statistik. Lehr- und Handbuch der angewandten Statistik*. Oldenbourg, München.
- HE, C.M. AND ROACH, M.R. 1994. The composition and mechanical properties of abdominal aortic aneurysms. *J Vasc Surg* 20, 1, 6–13.
- HEIM, M., RÖMER, L. AND SCHEIBEL, T. 2010. Hierarchical structures made of proteins. The complex architecture of spider webs and their constituent silk proteins. *Chemical Society reviews* 39, 1, 156–164.
- HICKSON, S.S., BUTLIN, M., GRAVES, M., TAVIANI, V., AVOLIO, A.P., MCENIERY, C.M. AND WILKINSON, I.B. 2010. The relationship of age with regional aortic stiffness and diameter. *JACC Cardiovasc Imaging* 3, 12, 1247–1255.
- HINNEN, J.-W., KONING, O.H.J., VISSER, M.J.T. AND VAN BOCKEL, H.J. 2005. Effect of intraluminal thrombus on pressure transmission in the abdominal aortic aneurysm. *J Vasc Surg* 42, 6, 1176–1182.
- HOEGH, A. AND LINDHOLT, J.S. 2009. Basic science review. Vascular distensibility as a predictive tool in the management of small asymptomatic abdominal aortic aneurysms. *Vasc Endovascular Surg* 43, 4, 333–338.
- HOFFMAN, E.A. AND RITMAN, E.L. 1985. Invariant total heart volume in the intact thorax. *Am J Physiol* 249, 4 Pt 2, H883-90.
- HOLZAPFEL, G.A. 2006. Determination of material models for arterial walls from uniaxial extension tests and histological structure. *J Theor Biol* 2, 238, 290–302.

- HOLZAPFEL, G.A. 2008. Collagen in Arterial Walls: Biomechanical Aspects. In *Collagen. Structure and Mechanics*, P. FRATZL, Ed. Springer, Heidelberg, 285–324.
- HOLZAPFEL, G.A. 2009. Arterial Tissue in Health and Disease: Experimental Data, Collagen-based Modeling and Simulation, Including Aortic Dissection. In *Biomechanical Modelling at the Molecular, Cellular and Tissue Levels*, G. A. HOLZAPFEL AND R. W. OGDEN, Eds. Springer Vienna, Vienna, 259–344.
- HOLZAPFEL, G.A. 2010. *Nonlinear solid mechanics. A continuum approach for engineering*. Wiley, Chichester.
- HOLZAPFEL, G.A., GASSER, T.C. AND OGDEN, R.W. 2000. A new constitutive framework for arterial wall mechanics and a comparative study of material models. *J Elasticity* 61, 1-3, 1–48.
- HOLZAPFEL, G.A., GASSER, T.C. AND OGDEN, R.W. 2004. Comparison of a multi-layer structural model for arterial walls with a fung-type model, and issues of material stability. *JOURNAL OF BIOMECHANICAL ENGINEERING-TRANSACTIONS OF THE ASME* 126, 2, 264–275.
- HOLZAPFEL, G.A., NIESTRAWKA, J.A., OGDEN, R.W., REINISCH, A.J. AND SCHRIEFL, A.J. 2015. Modelling non-symmetric collagen fibre dispersion in arterial walls. *J R Soc Interface* 12, 106.
- HOLZAPFEL, G.A. AND OGDEN, R.W. 2009. On planar biaxial tests for anisotropic nonlinearly elastic solids. A continuum mechanical framework. *MATHEMATICS AND MECHANICS OF SOLIDS* 14, 5, 474–489.
- HOLZAPFEL, G.A. AND OGDEN, R.W., Eds. 2017. *Biomechanics: Trends in Modeling and Simulation*. Studies in Mechanobiology, Tissue Engineering and Biomaterials 20. Springer International Publishing, Cham, s.l.
- HOLZAPFEL, G.A., SOMMER, G., AUER, M., REGITNIG, P. AND OGDEN, R.W. 2007. Layer-specific 3D residual deformations of human aortas with non-atherosclerotic intimal thickening. *ANNALS OF BIOMEDICAL ENGINEERING* 35, 4, 530–545.
- HOLZAPFEL, G.A. AND WEIZÄCKER, H.W. 1998. Biomechanical behaviour of the arterial wall and its numerical characterization. *Comput Biol Med* 28, 377–392.
- HORNY, L., ADAMEK, T., GULTOVA, E., ZITNY, R., VESELY, J., CHLUP, H. AND KONVICKOVA, S. 2011. Correlations between age, prestrain, diameter and atherosclerosis in the male abdominal aorta. *J Mech Behav Biomed Mater* 4, 8, 2128–2132.
- HORNY, L., ADAMEK, T. AND KULVAJTOVA, M. 2017. A comparison of age-related changes in axial prestretch in human carotid arteries and in human abdominal aorta. *Biomechanics and modeling in mechanobiology* 16, 1, 375–383.
- HORNY, L., ADAMEK, T., VESELY, J., CHLUP, H., ZITNY, R. AND KONVICKOVA, S. 2012. Age-related distribution of longitudinal pre-strain in abdominal aorta with emphasis on forensic application. *FORENSIC SCIENCE INTERNATIONAL* 214, 1-3, 18–22.
- HORNY, L., ADAMEK, T. AND ZITNY, R. 2013. Age-related changes in longitudinal prestress in human abdominal aorta. *ARCHIVE OF APPLIED MECHANICS* 83, 875–888.
- HORNY, L., KRONEK, J., CHLUP, H., ZITNY, R., VESELY, J. AND HULAN, M. 2010. Orientations of collagen fibers in aortic histological section. *Bulletin of Applied Mechanics* 6, 22, 25–29.
- HORNÝ, L. 2015. *Axial Prestretch and Biomechanics of Abdominal Aorta*. Habilitation, Czech Technical University in Prague.
- HORNÝ, L., NETUSIL, M. AND VONAVKOVÁ, T. 2013. Axial prestretch and circumferential distensibility in biomechanics of abdominal aorta. *Biomech Model Mechanobiol*.
- HORNÝ, L., NETUŠIL, M. AND VOŇAVKOVÁ, T. 2014. Axial prestretch and circumferential distensibility in biomechanics of abdominal aorta. *Biomechanics and modeling in mechanobiology* 13, 4, 783–799.
- HUMPHREY, J.D. 2002. *Cardiovascular solid mechanics. Cells, tissues, and organs*. Springer, New York, NY.
- HUMPHREY, J.D. AND HOLZAPFEL, G.A. 2012. Mechanics, mechanobiology, and modeling of human abdominal aorta and aneurysms. *J Biomech* 45, 5 (2012), 805–814.
- INDRAKUSUMA, R., JALALZADEH, H., PLANKEN, R.N., MARQUERING, H.A., LEGEMATE, D.A., KOELEMAY, M.J.W. AND BALM, R. 2016. Biomechanical Imaging Markers as Predictors of Abdominal Aortic Aneurysm Growth or Rupture: A Systematic Review. *Eur J Vasc Endovasc Surg* 52, 4, 475–486.

- IWAKOSHI, S., HIRAI, T. AND KICHIKAWA, K. 2019. Updates on Ultrasonography Imaging in Abdominal Aortic Aneurysm. *Annals of vascular diseases*.
- JOLDES, G.R., MILLER, K., WITTEK, A. AND DOYLE, B. 2015a. A simple, effective and clinically applicable method to compute abdominal aortic aneurysm wall stress. *J Mech Behav Biomed Mater*.
- JOLDES, G.R., MILLER, K., WITTEK, A., FORSYTHE, R.O., NEWBY, D.E. AND DOYLE, B.J. 2017. BioPARR. A software system for estimating the rupture potential index for abdominal aortic aneurysms. *Scientific reports* 7, 1, 4641.
- JOLDES, G.R., NOBLE, C., POLZER, S., TAYLOR, Z.A., WITTEK, A. AND MILLER, K. 2018. A simple method of incorporating the effect of the Uniform Stress Hypothesis in arterial wall stress computations. *Acta of bioengineering and biomechanics / Wroclaw University of Technology* 20, 4, 59–67.
- JOLDES, G.R., WITTEK, A. AND MILLER, K. 2015b. A Total Lagrangian based method for recovering the un-deformed configuration in finite elasticity. *Applied Mathematical Modelling* 39, 14, 3913–3923.
- JONES, E.M.C., SILBERSTEIN, M.N., WHITE, S.R. AND SOTTOS, N.R. 2014. In situ measurements of strains in composite battery electrodes during electrochemical cycling. *Experimental Mechanics* 54, 6, 971–985.
- KABANIKHIN, S.I. 2008. Definitions and examples of inverse and ill-posed problems. *J. Inv. Ill-Posed Problems* 16, 317–357.
- KALISZEWSKI, I., MIROFORIDIS, J. AND PODKOPAEV, D. 2016. *Multiple Criteria Decision Making by Multiobjective Optimization. A Toolbox*. International Series in Operations Research & Management Science 242. Springer International Publishing, Cham.
- KAPETANAKIS, S., KEARNEY, M.T., SIVA, A., GALL, N., COOKLIN, M. AND MONAGHAN, M.J. 2005. Real-time three-dimensional echocardiography: a novel technique to quantify global left ventricular mechanical dyssynchrony. *Circulation* 112, 7, 992–1000.
- KARATOLIOS, K. *, WITTEK, A. *, NWE, T.H., BIHARI, P., SHELKE, A., JOSEF, D., SCHMITZ-RIXEN, T., GEKS, J., MAISCH, B., BLASE, C., MOOSDORF, R. AND VOGT, S. 2013. Method for Aortic Wall Strain Measurement with Three-Dimensional Ultrasound Speckle Tracking and Fitted Finite Element Analysis. *Ann Thorac Surg* 96, 5, 1664–1671, *equal contribution.
- KARTHIKESALINGAM, A., BAHIA, S.S., PATTERSON, B.O., PEACH, G., VIDAL-DIEZ, A., RAY, K.K., SHARMA, R., HINCHLIFFE, R.J., HOLT, P.J. AND THOMPSON, M.M. 2013. The shortfall in long-term survival of patients with repaired thoracic or abdominal aortic aneurysms: retrospective case-control analysis of hospital episode statistics. *Eur J Vasc Endovasc Surg* 46, 5, 533–541.
- KASSAB, G.S. 2006. Biomechanics of the cardiovascular system: the aorta as an illustratory example. *J R Soc Interface* 3, 11, 719–740.
- KEULENAER, B.L. de, WAELE, J.J. de, POWELL, B. AND MALBRAIN, M.L.N.G. 2009. What is normal intra-abdominal pressure and how is it affected by positioning, body mass and positive end-expiratory pressure? *Intensive Care Med* 35, 6, 969–976.
- KOK, A.M., NGUYEN, V.L., SPEELMAN, L., BRANDS, P.J., SCHURINK, G.-W.H., VAN DE VOSSE, FRANS N AND LOPATA, RICHARD G P. 2015. On the feasibility of wall stress analysis of abdominal aortic aneurysms using three-dimensional ultrasound. *J Vasc Surg*.
- KONTOPODIS, N., METAXA, E., PAPAHRILAOU, Y., TAVLAS, E., TSETIS, D. AND IOANNOU, C. 2015. Advancements in identifying biomechanical determinants for abdominal aortic aneurysm rupture. *Vascular* 23, 1, 65–77.
- KOO, T.K. AND LI, M.Y. 2016. A Guideline of Selecting and Reporting Intraclass Correlation Coefficients for Reliability Research. *Journal of chiropractic medicine* 15, 2, 155–163.
- KOZERKE, S., SCHEIDEGGER, M.B., PEDERSEN, E.M. AND BOESIGER, P. 1999. Heart motion adapted cine phase-contrast flow measurements through the aortic valve. *Magn Reson Med* 42, 5, 970–978.
- KROON, M. 2010. An Efficient Method for Material Characterisation of Hyperelastic Anisotropic Inhomogeneous Membranes Based on Inverse Finite-Element Analysis and an Element Partition Strategy. *The Quarterly Journal of Mechanics and Applied Mathematics* 63, 2, 201–225.

- KROON, M. AND HOLZAPFEL, G.A. 2008. Estimation of the distributions of anisotropic, elastic properties and wall stresses of saccular cerebral aneurysms by inverse analysis. *Proceedings of the Royal Society A: Mathematical, Physical and Engineering Sciences* 464, 2092, 807–825.
- KROON, M. AND HOLZAPFEL, G.A. 2009. Elastic properties of anisotropic vascular membranes examined by inverse analysis. *Computer Methods in Applied Mechanics and Engineering* 198, 45–46, 3622–3632.
- KUGO, H., ZAIMA, N., TANAKA, H., MOURI, Y., YANAGIMOTO, K., HAYAMIZU, K., HASHIMOTO, K., SASAKI, T., SANO, M., YATA, T., URANO, T., SETOU, M., UNNO, N. AND MORIYAMA, T. 2016. Adipocyte in vascular wall can induce the rupture of abdominal aortic aneurysm. *Scientific reports* 6, 31268.
- KÜHNL, A., ERK, A., TRENNER, M., SALVERMOSER, M., SCHMID, V. AND ECKSTEIN, H.-H. 2017. Incidence, Treatment and Mortality in Patients with Abdominal Aortic Aneurysms. *Deutsches Arzteblatt international* 114, 22-23, 391–398.
- LABROSSE, M.R., BELLER, C.J., MESANA, T. AND VEINOT, J.P. 2009. Mechanical behavior of human aortas: Experiments, material constants and 3-D finite element modeling including residual stress. *Journal of Biomechanics* 42, 8, 996–1004.
- LAWTON, R.W. 1954. The thermoelastic behavior of isolated aortic strips of the dog. *Circulation Research* 2, 4, 344–353.
- LEAROYD, B.M. AND TAYLOR, M.G. 1966. Alterations with age in the viscoelastic properties of human arterial walls. *Circulation Research* 18, 3, 278–292.
- LEDERLE, F., WILSON, S., JOHNSON, G., REINKE, D., LITTOOY, F., ACHER, C., BALLARD, D., MESSINA, L., GORDON, I., CHUTE, E., KRUPSKI, W., BUSUTTI, S., BARONE, G., SPARKS, S., GRAHAM, L., RAPP, J., MAKAROUN, M., MONETA, G., CAMBRIA, R., MAKHOUL, R., ETON, D., ANSEL, H., FREISCHLAG, J. AND BANDYK, D. 2002. Immediate repair compared with surveillance of small abdominal aortic aneurysms. *N Engl J Med* 346, 19, 1437–1444.
- LEDERLE, F.A., STROUPE, K.T., KYRIAKIDES, T.C., GE, L. AND FREISCHLAG, J.A. 2016. Long-term Cost-effectiveness in the Veterans Affairs Open vs Endovascular Repair Study of Aortic Abdominal Aneurysm: A Randomized Clinical Trial. *JAMA surgery* 151, 12, 1139–1144.
- LEEMANS, E.L., WILLEMS, T.P., SLUMP, C.H., VAN DER LAAN, M.J. AND ZEEBREGTS, C.J. 2018. Additional value of biomechanical indices based on CTA for rupture risk assessment of abdominal aortic aneurysms. *PloS one* 13, 8, e0202672.
- LEFEVRE, M.L. 2014. Screening for abdominal aortic aneurysm: U.S. Preventive Services Task Force recommendation statement. *Annals of internal medicine* 161, 4, 281–290.
- LESKAUSKAITE, V., IVANOVIENE, L. AND VALANCIŪTE, A. 2003. Programmed cellular death and atherogenesis: from molecular mechanisms to clinical aspects. *Medicina (Kaunas, Lithuania)* 39, 6, 529–534.
- LI, L., ZENG, L., LIN, Z.-J., CAZZELL, M. AND LIU, H. 2015. Tutorial on use of intraclass correlation coefficients for assessing intertest reliability and its application in functional near-infrared spectroscopy-based brain imaging. *J Biomed Opt* 20, 5, 50801.
- LIANG, L., LIU, M., MARTIN, C. AND SUN, W. 2018. A Machine Learning Approach as a Surrogate of Finite Element Analysis-based Inverse Method to Estimate the Zero-pressure Geometry of Human Thoracic Aorta. *International journal for numerical methods in biomedical engineering*, e3103.
- LINDEMAN, J.H.N., ASHCROFT, B.A., BEENAKKER, J.-W.M., VAN ES, M., KOEKOEK, N.B.R., PRINS, F.A., TIELEMANS, J.F., ABDUL-HUSSEIN, H., BANK, R.A. AND OOSTERKAMP, T.H. 2010. Distinct defects in collagen microarchitecture underlie vessel-wall failure in advanced abdominal aneurysms and aneurysms in Marfan syndrome. *Proceedings of the National Academy of Sciences of the United States of America* 107, 2, 862–865.
- LIU, H., CANTON, G., YUAN, C., YANG, C., BILLIAR, K., TENG, Z., HOFFMAN, A.H. AND TANG, D. 2012. Using in vivo Cine and 3D multi-contrast MRI to determine human atherosclerotic carotid artery material properties and circumferential shrinkage rate and their impact on stress/strain predictions. *J Biomech Eng* 134, 1, 11008.
- LIU, M., LIANG, L., LIU, H., ZHANG, M., MARTIN, C. AND SUN, W. 2019a. On the computation of in vivo transmural mean stress of patient-specific aortic wall. *Biomechanics and modeling in mechanobiology* 18, 2, 387–398.

- LIU, M., LIANG, L., SULEJMANI, F., LOU, X., IANNUCCI, G., CHEN, E., LESHOWER, B. AND SUN, W. 2019b. Identification of in vivo nonlinear anisotropic mechanical properties of ascending thoracic aortic aneurysm from patient-specific CT scans. *Sci Rep* 9, 1, 109.
- LIU, M., LIANG, L. AND SUN, W. 2017. A new inverse method for estimation of in vivo mechanical properties of the aortic wall. *J Mech Behav Biomed Mater* 72, 148–158.
- LIU, M., LIANG, L. AND SUN, W. 2018. Estimation of in vivo mechanical properties of the aortic wall: A multi-resolution direct search approach. *J Mech Behav Biomed Mater* 77, 649–659.
- LIU, M., LIANG, L. AND SUN, W. 2019c. Estimation of in vivo constitutive parameters of the aortic wall using a machine learning approach. *Computer Methods in Applied Mechanics and Engineering* 347, 201–217.
- LU, J. AND ZHAO, X. 2009. Pointwise Identification of Elastic Properties in Nonlinear Hyperelastic Membranes—Part I: Theoretical and Computational Developments. *J. Appl. Mech.* 76, 6, 61013.
- LU, J., ZHOU, X. AND RAGHAVAN, M.L. 2007a. Computational method of inverse elastostatics for anisotropic hyperelastic solids. *INTERNATIONAL JOURNAL FOR NUMERICAL METHODS IN ENGINEERING* 69, 6, 1239–1261.
- LU, J., ZHOU, X. AND RAGHAVAN, M.L. 2007b. Inverse elastostatic stress analysis in pre-deformed biological structures: Demonstration using abdominal aortic aneurysms. *J Biomech* 40, 3, 693–696.
- LU, J., ZHOU, X. AND RAGHAVAN, M.L. 2008. Inverse method of stress analysis for cerebral aneurysms. *Biomech Model Mechanobiol* 7, 6, 477–486.
- LUNDBÄCK, S. 1986. Cardiac pumping and function of the ventricular septum. *Acta physiologica Scandinavica. Supplementum* 550, 1–101.
- MAES, L., FEHERVARY, H., VASTMANS, J., MOUSAVI, S.J., AVRIL, S. AND FAMAHEY, N. 2019. Constrained mixture modeling affects material parameter identification from planar biaxial tests. *J Mech Behav Biomed Mater* 95, 124–135.
- MAIER, A., GEE, M.W., REEPS, C., PONGRATZ, J., ECKSTEIN, H.H. AND WALL, W.A. 2010. A comparison of diameter, wall stress, and rupture potential index for abdominal aortic aneurysm rupture risk prediction. *ANNALS OF BIOMEDICAL ENGINEERING* 38, 10, 3124–3134.
- MAKSUTI, E., BJALLMARK, A. AND BROOME, M. 2015. Modelling the heart with the atrioventricular plane as a piston unit. *Med Eng Phys* 37, 1, 87–92.
- MARRA, S.P., KENNEDY, F.E., KINKAID, J.N. AND FILLINGER, M.F. 2006. Elastic and Rupture Properties of Porcine Aortic Tissue Measured Using Inflation Testing. *Cardiovasc Eng* 6, 4, 123–131.
- MARSH, J.N., TAKIUCHI, S., LIN, S.J., LANZA, G.M. AND WICKLINE, S.A. 2004. Ultrasonic delineation of aortic microstructure: the relative contribution of elastin and collagen to aortic elasticity. *J. Acoust. Soc. Am.* 115, 5 Pt 1, 2032–2040.
- MARTIN, C., SUN, W., PRIMIANO, C., MCKAY, R. AND ELEFTERIADES, J. 2013. Age-dependent ascending aorta mechanics assessed through multiphase CT. *Ann Biomed Eng* 41, 12, 2565–2574.
- MARTUFI, G. AND CHRISTIAN GASSER, T. 2013. Review: the role of biomechanical modeling in the rupture risk assessment for abdominal aortic aneurysms. *J Biomech Eng* 135, 2, 21010.
- MARTUFI, G., GASSER, T.C., APPOO, J.J. AND DI MARTINO, E.S. 2014. Mechano-biology in the thoracic aortic aneurysm: a review and case study. *Biomech Model Mechanobiol* 13, 5, 917–928.
- MASSON, I., BOUTOUYRIE, P., LAURENT, S., HUMPHREY, J.D. AND ZIDI, M. 2008. Characterization of arterial wall mechanical behavior and stresses from human clinical data. *J Biomech* 41, 12, 2618–2627.
- MERCER, J.L. 1969. Movement of the aortic annulus. *Br J Radiol* 42, 500, 623–626.
- METAXA, E., KONTOPODIS, N., VAVOURAKIS, V., TZIRAKIS, K., IOANNOU, C.V. AND PAPAHRILAOU, Y. 2015. The influence of intraluminal thrombus on non-invasive abdominal aortic aneurysm wall distensibility measurement. *MEDICAL & BIOLOGICAL ENGINEERING & COMPUTING* 53, 4, 299–308.
- MEUNIER, J. 1998. Tissue motion assessment from 3D echographic speckle tracking. *Phys Med Biol* 43, 5, 1241–1254.
- MEYER, C.A., GUIVIER-CURIEN, C. AND MOORE, J.E. 2010. Trans-thrombus blood pressure effects in abdominal aortic aneurysms. *J Biomech Eng* 132, 7, 71005.

- MITCHELL, G.F., HWANG, S.-J., VASAN, R.S., LARSON, M.G., PENCINA, M.J., HAMBURG, N.M., VITA, J.A., LEVY, D. AND BENJAMIN, E.J. 2010. Arterial stiffness and cardiovascular events: the Framingham Heart Study. *Circulation* 121, 4, 505–511.
- MORRISON, T., CHOI, G., ZARINS, C. AND TAYLOR, C. 2009. Circumferential and longitudinal cyclic strain of the human thoracic aorta: age-related changes. *J Vasc Surg* 49, 4, 1029–1036.
- NELDER, J.A. AND MEAD, R. 1965. A Simplex Method for Function Minimization. *The Computer Journal* 7, 4, 308–313.
- NICHOLS, W.W., O’ROURKE, M.F., VLACHOPOULOS, C. AND McDONALD, D.A. 2011. *McDonald’s blood flow in arteries. Theoretical, experimental and clinical principles*. CRC Press.
- NIESTRAWKA, J.A. 2019. *Experimental and Computational Analyses of Pathological Soft Tissues – Towards a Better Understanding of the Pathogenesis of AAA*. Monographic Series TU Graz 35. Verlag d. Technischen Universität Graz, Graz.
- NIESTRAWKA, J.A., REGITNIG, P., VIERTLER, C., COHNERT, T.U., BABU, A.R. AND HOLZAPFEL, G.A. 2019. The role of tissue remodeling in mechanics and pathogenesis of abdominal aortic aneurysms. *ACTA BIOMATERIALIA* 88, 149–161.
- NIESTRAWKA, J.A., VIERTLER, C., REGITNIG, P., COHNERT, T.U., SOMMER, G. AND HOLZAPFEL, G.A. 2016. Microstructure and mechanics of healthy and aneurysmatic abdominal aortas: experimental analysis and modelling. *J R Soc Interface* 13, 124.
- NOLAN, D.R. AND MCGARRY, J.P. 2016. On the Compressibility of Arterial Tissue. *ANNALS OF BIOMEDICAL ENGINEERING* 44, 4, 993–1007.
- OGDEN, R.W. 1997. *Non-linear elastic deformations*. Dover books on physics. Dover, Mineola, NY.
- OGDEN, R.W. 2009. Anisotropy and Nonlinear Elasticity in Arterial Wall Mechanics. In *Biomechanical Modelling at the Molecular, Cellular and Tissue Levels*, G. A. HOLZAPFEL AND R. W. OGDEN, Eds. Springer Vienna, Vienna, 179–258.
- OISHI, Y., MIZUGUCHI, Y., MIYOSHI, H., IUCHI, A., NAGASE, N. AND OKI, T. 2008. A novel approach to assess aortic stiffness related to changes in aging using a two-dimensional strain imaging. *Echocardiography (Mount Kisco, N.Y.)* 25, 9, 941–945.
- OLLIKAINEN, E., TULAMO, R., LEHTI, S., LEE-RUECKERT, M., HERNESNIEMI, J., NIEMELÄ, M., YLÄ-HERTTUALA, S., KOVANEN, P.T. AND FRÖSEN, J. 2016. Smooth Muscle Cell Foam Cell Formation, Apolipoproteins, and ABCA1 in Intracranial Aneurysms: Implications for Lipid Accumulation as a Promoter of Aneurysm Wall Rupture. *Journal of neuropathology and experimental neurology* 75, 7, 689–699.
- O’ROURKE, M. 1990. Arterial stiffness, systolic blood pressure, and logical treatment of arterial hypertension. *Hypertension* 15, 4, 339–347.
- O’ROURKE, M.F. 2007. Arterial aging: pathophysiological principles. *Vasc Med* 12, 4, 329–341.
- O’ROURKE, M.F., ADJI, A. AND SAFAR, M.E. 2018. Structure and Function of Systemic Arteries. Reflections on the Arterial Pulse. *Am J Hypertens* 31, 8, 934–940.
- O’ROURKE, M.F. AND HASHIMOTO, J. 2007. Mechanical factors in arterial aging: a clinical perspective. *Journal of the American College of Cardiology* 50, 1, 1–13.
- O’ROURKE, M.F., SAFAR, M.E. AND DZAU, V. 2010. The Cardiovascular Continuum extended: aging effects on the aorta and microvasculature. *Vasc Med* 15, 6, 461–468.
- O’ROURKE, M.F., STAESSEN, J.A., VLACHOPOULOS, C., DUPREZ, D. AND PLANTE, G.E. 2002. Clinical applications of arterial stiffness; definitions and reference values. *Am J Hypertens* 15, 5, 426–444.
- PAPE, H., KURTZ, A., SILBERNAGL, S. 2019. *Physiologie*. G. Thieme, Stuttgart.
- PAPPU, S., DARDIK, A., TAGARE, H. AND GUSBERG, R.J. 2008. Beyond fusiform and saccular: a novel quantitative tortuosity index may help classify aneurysm shape and predict aneurysm rupture potential. *Ann Vasc Surg* 22, 1, 88–97.
- PARISCH, H. 2003. *Festkörper-Kontinuumsmechanik. Von den Grundgleichungen zur Lösung mit Finiten Elementen*. Teubner Studienbücher Maschinenbau - Lehrbuch. Teubner, Stuttgart, Leipzig, Wiesbaden, Stuttgart.
- PARK, J.-S., CHOI, Y.-W., SHIN, J.-S., YANG, H.-M., LIM, H.-S., CHOI, B.-J., CHOI, S.-Y., YOON, M.-H., HWANG, G.-S., TAHK, S.-J. AND SHIN, J.-H. 2011. Validation of Three-Dimensional Echocardiography for Quantification of Aortic Root Geometry: Comparison with Multi-Detector Computed Tomography. *J Cardiovasc Ultrasound* 19, 3, 128–133.

- PETERSEN, E., WÄGGER, F. AND ANGQUIST, K.A. 2002. Proteolysis of the abdominal aortic aneurysm wall and the association with rupture. *Eur J Vasc Endovasc Surg* 23, 2, 153–157.
- PETTERSON, N.J., DISSELDORP, M.J. van, SAMBEEK, M.R.H.M. van, VOSSE, F.N. van de, and LOPATA, R.G.P. 2019. Including surrounding tissue improves ultrasound-based 3D mechanical characterization of abdominal aortic aneurysms. *J Biomech* 85, 126–133.
- PIERCE, D.M., FASTL, T.E., RODRIGUEZ-VILA, B., VERBRUGGHE, P., FOURNEAU, I., MALEUX, G., HERIJGERS, P., GOMEZ, E.J. AND HOLZAPFEL, G.A. 2015. A method for incorporating three-dimensional residual stretches/stresses into patient-specific finite element simulations of arteries. *J Mech Behav Biomed Mater* 47, 147–164.
- PIERRON, F. AND GRÉDIAC, M. 2012. *The virtual fields method. Extracting constitutive mechanical parameters from full-field deformation measurements*. Springer, New York.
- POTTIER, T., TOUSSAINT, F. AND VACHER, P. 2011. Contribution of heterogeneous strain field measurements and boundary conditions modelling in inverse identification of material parameters. *EUROPEAN JOURNAL OF MECHANICS A-SOLID* 30, 3, 373–382.
- RAGHAVAN, M., KRATZBERG, J., CASTRO, D., HANAOKA, M., WALKER, P. AND DA, S. 2006. Regional distribution of wall thickness and failure properties of human abdominal aortic aneurysm. *J Biomech* 39, 16, 3010–3016.
- RAGHAVAN, M.L., HANAOKA, M.M., KRATZBERG, J.A., DE LOURDES HIGUCHI, MARIA AND DA SILVA, ERASMO SIMAO. 2011. Biomechanical failure properties and microstructural content of ruptured and unruptured abdominal aortic aneurysms. *J Biomech* 44, 13, 2501–2507.
- RAJAGOPAL, V., CHUNG, J.-H., BULLIVANT, D., NIELSEN, P.M.F. AND NASH, M.P. 2007. Determining the finite elasticity reference state from a loaded configuration. *INTERNATIONAL JOURNAL FOR NUMERICAL METHODS IN ENGINEERING* 72, 12, 1434–1451.
- REDHEUIL, A., YU, W.-C., WU, C.O., MOUSSEAUX, E., CESARE, A. de, YAN, R., KACHENOURA, N., BLUEMKE, D. AND LIMA, J.A.C. 2010. Reduced ascending aortic strain and distensibility. Earliest manifestations of vascular aging in humans. *Hypertension* 55, 2, 319–326.
- REEPS, C., GEE, M., MAIER, A., GURDAN, M., ECKSTEIN, H.-H. AND WALL, W. 2010. The impact of model assumptions on results of computational mechanics in abdominal aortic aneurysm. *J Vasc Surg* 51, 3, 679–688.
- REEPS, C., MAIER, A., PELISEK, J., HARTL, F., GRABHER-MEIER, V., WALL, W.A., ESSLER, M., ECKSTEIN, H.-H. AND GEE, M.W. 2012. Measuring and modeling patient-specific distributions of material properties in abdominal aortic aneurysm wall. *Biomech Model Mechanobiol* 12, 4, 717–733.
- REIMERINK, J.J., HOORNWEG, L.L., VAHL, A.C., WISSELINK, W., VAN DEN BROEK, T.A.A., LEGEMATE, D.A., REEKERS, J.A. AND BALM, R. 2013a. Endovascular repair versus open repair of ruptured abdominal aortic aneurysms: a multicenter randomized controlled trial. *Ann Surg* 258, 2, 248–256.
- REIMERINK, J.J., VAN DER LAAN, M.J., KOELEMAY, M.J., BALM, R. AND LEGEMATE, D.A. 2013b. Systematic review and meta-analysis of population-based mortality from ruptured abdominal aortic aneurysm. *Br J Surg* 100, 11, 1405–1413.
- RENCHER, A.C. AND SCHAALJE, C.B. 2008. *Linear Models in Statistics*. JOHN WILEY & SONS LTD, Hoboken, New Jersey.
- RIBBERS, H., LOPATA, RICHARD G P, HOLEWIJN, S., PASTERKAMP, G., BLANKENSTELJN, J.D. AND DE KORTE, CHRIS L. 2007. Non-invasive two-dimensional strain imaging of arteries: validation in phantoms and preliminary experience in carotid arteries in vivo. *Ultrasound Med Biol* 33, 4, 530–540.
- RIVEROS, F., CHANDRA, S., FINOL, E.A., GASSER, T.C. AND RODRIGUEZ, J.F. 2013. A pull-back algorithm to determine the unloaded vascular geometry in anisotropic hyperelastic AAA passive mechanics. *ANNALS OF BIOMEDICAL ENGINEERING* 41, 4, 694–708.
- ROMO, A., BADEL, P., DUPREY, A., FAVRE, J.-P. AND AVRIL, S. 2014. In vitro analysis of localized aneurysm rupture. *J Biomech* 47, 3, 607–616.
- SASSANI, S.G., KAKISIS, J., TSANGARIS, S. AND SOKOLIS, D.P. 2015. Layer-dependent wall properties of abdominal aortic aneurysms: Experimental study and material characterization. *J Mech Behav Biomed Mater* 49, 141–161.

- SCAIFE, M., GIANNAKOPOULOS, T., AL-KHOURY, G.E., CHAER, R.A. AND AVGERINOS, E.D. 2016. Contemporary Applications of Ultrasound in Abdominal Aortic Aneurysm Management. *Frontiers in surgery* 3, 29.
- SCHLATMANN, T.J. AND BECKER, A.E. 1977. Histologic changes in the normal aging aorta: implications for dissecting aortic aneurysm. *Am. J. Cardiol.* 39, 1, 13–20.
- SCHNEIDER, C.A., RASBAND, W.S. AND ELICEIRI, K.W. 2012. NIH Image to ImageJ: 25 years of image analysis. *Nature methods* 9, 7, 671–675.
- SCHRIEFL, A.J., REINISCH, A.J., SANKARAN, S., PIERCE, D.M. AND HOLZAPFEL, G.A. 2012. Quantitative assessment of collagen fibre orientations from two-dimensional images of soft biological tissues. *J R Soc Interface* 9, 76, 3081–3093.
- SCHULZE-BAUER, C., MORTH, C. AND HOLZAPFEL, G. 2003. Passive biaxial mechanical response of aged human iliac arteries. *J Biomech Eng* 125, 3, 395–406.
- SCHULZE-BAUER, C.A.J. AND HOLZAPFEL, G.A. 2003. Determination of constitutive equations for human arteries from clinical data. *J Biomech* 36, 2, 165–169.
- SCHURINK, G.W., VAN BAALEN, J.M., VISSER, M.J. AND VAN BOCKEL, J.H. 2000. Thrombus within an aortic aneurysm does not reduce pressure on the aneurysmal wall. *J Vasc Surg* 31, 3, 501–506.
- SELLIER, M. 2011. An iterative method for the inverse elasto-static problem. *JOURNAL OF FLUIDS AND STRUCTURES* 27, 8, 1461–1470.
- SENGUPTA, P.P., TAJIK, A.J., CHANDRASEKARAN, K. AND KHANDHERIA, B.K. 2008. Twist Mechanics of the Left Ventricle: Principles and Application. *JACC: Cardiovascular Imaging* 1, 3, 366–376.
- SEO, Y., ISHIZU, T., ENOMOTO, Y., SUGIMORI, H. AND AONUMA, K. 2011. Endocardial surface area tracking for assessment of regional LV wall deformation with 3D speckle tracking imaging. *JACC Cardiovasc Imaging* 4, 4, 358–365.
- SEO, Y., ISHIZU, T., ENOMOTO, Y., SUGIMORI, H., YAMAMOTO, M., MACHINO, T., KAWAMURA, R. AND AONUMA, K. 2009. Validation of 3-dimensional speckle tracking imaging to quantify regional myocardial deformation. *Circulation* 2, 6, 451–459.
- SHROUT, P.E. AND FLEISS, J.L. 1979. Intraclass correlations: uses in assessing rater reliability. *Psychological bulletin* 86, 2, 420–428.
- SHUM, J., DIMARTINO, E.S., GOLDHAMMER, A., GOLDMAN, D.H., ACKER, L.C., PATEL, G., NG, J.H., MARTUFI, G. AND FINOL, E.A. 2010. Semiautomatic vessel wall detection and quantification of wall thickness in computed tomography images of human abdominal aortic aneurysms. *Med. Phys.* 37, 2, 638.
- SILBER, G. AND STEINWENDER, F., Eds. 2005. *Bauteilberechnung und Optimierung mit der FEM. Materialtheorie, Anwendungen, Beispiele ; mit 5 Tabellen und zahlreichen Beispielen.* Teubner, Stuttgart, Leipzig, Wiesbaden.
- SILBER, G. AND THEN, C. 2013. *Preventive biomechanics. Optimizing support systems for the human body in the lying and sitting position.* Springer, Berlin.
- SMOLJKIC, M., VANDER SLOTEN, J., SEGERS, P. AND FAMAHEY, N. 2015. Non-invasive, energy-based assessment of patient-specific material properties of arterial tissue. *Biomech Model Mechanobiol.*
- SOLIMAN, O.I.I., KIRSCHBAUM, S.W., VAN DALEN, B.M., VAN DER ZWAAN, H.B., DELAVARY, B.M., VLETTER, W.B., VAN GEUNS, R.-J.M., TEN CATE, F.J. AND GELEIJNSE, M.L. 2008. Accuracy and Reproducibility of Quantitation of Left Ventricular Function by Real-Time Three-Dimensional Echocardiography Versus Cardiac Magnetic Resonance. *Am J Cardiol* 102, 6, 778–783.
- SOMMER, G., REGITNIG, P., KOLTRINGER, L. AND HOLZAPFEL, G.A. 2010. Biaxial mechanical properties of intact and layer-dissected human carotid arteries at physiological and suprphysiological loadings. *American journal of physiology. Heart and circulatory physiology* 298, 3, H898-912.
- STÄLHAND, J. 2009. Determination of human arterial wall parameters from clinical data. *Biomech Model Mechanobiol* 8, 2, 141–148.
- STÄLHAND, J. AND KLARBRING, A. 2005. Aorta in vivo parameter identification using an axial force constraint. *Biomech Model Mechanobiol* 3, 4, 191–199.

- STÅLHAND, J., KLARBRING, A. AND KARLSSON, M. 2004. Towards in vivo aorta material identification and stress estimation. *Biomech Model Mechanobiol*, 3, 169–186.
- STEDING-EHRENBORG, K., CARLSSON, M., STEPHENSEN, S. AND ARHEDEN, H. 2013. Atrial aspiration from pulmonary and caval veins is caused by ventricular contraction and secures 70% of the total stroke volume independent of resting heart rate and heart size. *Clinical physiology and functional imaging* 33, 3, 233–240.
- STÉPHANE ROUX AND FRANÇOIS HILD. 2018. Optimal procedure for the identification of constitutive parameters from experimentally measured displacement fields. *INTERNATIONAL JOURNAL OF SOLIDS AND STRUCTURES*.
- SWEDENBORG, J. AND ERIKSSON, P. 2006. The intraluminal thrombus as a source of proteolytic activity. *Ann N Y Acad Sci* 1085, 133–138.
- TANAKA, H., ZAIMA, N., SASAKI, T., SANO, M., YAMAMOTO, N., SAITO, T., INUZUKA, K., HAYASAKA, T., GOTO-INOUE, N., SUGIURA, Y., SATO, K., KUGO, H., MORIYAMA, T., KONNO, H., SETOU, M. AND UNNO, N. 2015a. Hypoperfusion of the Adventitial Vasa Vasorum Develops an Abdominal Aortic Aneurysm. *PloS one* 10, 8, e0134386.
- TANAKA, H., ZAIMA, N., SASAKI, T., YAMAMOTO, N., INUZUKA, K., SANO, M., SAITO, T., HAYASAKA, T., GOTO-INOUE, N., SATO, K., KUGO, H., MORIYAMA, T., KONNO, H., SETOU, M. AND UNNO, N. 2015b. Imaging Mass Spectrometry Reveals a Unique Distribution of Triglycerides in the Abdominal Aortic Aneurysmal Wall. *JOURNAL OF VASCULAR RESEARCH* 52, 2, 127–135.
- TAVARES MONTEIRO, J., DA SILVA, E., RAGHAVAN, M., PUECH-LEÃO, P., DE LOURDES HIGUCHI, M. AND OTOCH, J. 2014. Histologic, histochemical, and biomechanical properties of fragments isolated from the anterior wall of abdominal aortic aneurysms. *J Vasc Surg* 59, 5, 1393 - 1401.e2.
- TEIXEIRA, R., VIEIRA, M.J., GONÇALVES, A., CARDIM, N. AND GONÇALVES, L. 2015. Ultrasonographic vascular mechanics to assess arterial stiffness: a review. *Eur Heart J Cardiovasc Imaging*, jev287.
- THOMPSON, S.G., BROWN, L.C., SWEETING, M.J., BOWN, M.J., KIM, L.G., GLOVER, M.J., BUXTON, M.J. AND POWELL, J.T. 2013. Systematic review and meta-analysis of the growth and rupture rates of small abdominal aortic aneurysms: implications for surveillance intervals and their cost-effectiveness. *Health Technol Assess* 17, 41, 1–118.
- THUBRIKAR, M.J., Ed. 2007. *Vascular Mechanics and Pathology*. Springer US, Boston, MA.
- THUBRIKAR, M.J., LABROSSE, M., ROBICSED, F., AL-SOUDI, J. AND FOWLER, B. 2001. Mechanical properties of abdominal aortic aneurysm wall. *Journal of Medical Engineering Technology* 25, 4, 133–142.
- TODD J. ANDERSON. 2006. Arterial stiffness or endothelial dysfunction as a surrogate marker of vascular risk. *Canadian Journal of Cardiology* 22, 0, 72B - 80B.
- TORRENT-GUASP, F. 1957. Anatomia funcional del corazón. *Madrid: Paz Montalvo*, 62–68.
- TRABELSI, O., DUPREY, A., FAVRE, J.-P. AND AVRIL, S. 2015. Predictive Models with Patient Specific Material Properties for the Biomechanical Behavior of Ascending Thoracic Aneurysms. *Ann Biomed Eng* 44, 1, 84–94.
- TRABELSI, O., GUTIERREZ, M., FARZANEH, S., DUPREY, A. AND AVRIL, S. 2017. A non-invasive methodology for ATAA rupture risk estimation. *J Biomech*.
- UK SMALL ANEURYSM TRIAL PARTICIPANTS. 1998. Mortality results for randomised controlled trial of early elective surgery or ultrasonographic surveillance for small abdominal aortic aneurysms. The UK Small Aneurysm Trial Participants. *Lancet* 352, 9141, 1649–1655.
- UK SMALL ANEURYSM TRIAL PARTICIPANTS. 2002. Long-term outcomes of immediate repair compared with surveillance of small abdominal aortic aneurysms. *N Engl J Med* 346, 19, 1445–1452.
- VAISHNAV, R.N. AND VOSSOUGH, J. 1983. ESTIMATION OF RESIDUAL STRAINS IN AORTIC SEGMENTS. In *Biomedical Engineering II*, C. William Hall, Ed. Pergamon, 330–333.
- VAN BORTEL, L.M., LAURENT, S., BOUTOUYRIE, P., CHOWIENCZYK, P., CRUICKSHANK, J.K., BACKER, T. de, FILIPOVSKY, J., HUYBRECHTS, S., MATTACE-RASO, F.U.S., PROTOGEROU, A.D., SCHILLACI, G., SEGERS, P., VERMEERSCH, S. AND WEBER, T. 2012. Expert consensus document on the measurement of aortic stiffness in daily practice using carotid-femoral pulse wave velocity. *J Hypertens* 30, 3, 445–448.

- VAN DER REST, M. AND BRUCKNER, P. 1993. Collagens: diversity at the molecular and supramolecular levels. *Current Opinion in Structural Biology* 3, 3, 430–436.
- VANDE GEEST, J.P., WANG, D.H., WISNIEWSKI, S.R., MAKAROUN, M.S. AND VORP, D.A. 2006. Towards a non-invasive method for determination of patient-specific wall strength distribution in abdominal aortic aneurysms. *ANNALS OF BIO-MEDICAL ENGINEERING* 34, 7, 1098–1106.
- VORP, D.A. 2007. Biomechanics of abdominal aortic aneurysm. *J Biomech* 40, 9, 1887–1902.
- WANHAINEN, A., VERZINI, F., VAN HERZEELE, I., ALLAIRE, E., BOWN, M., COHNERT, T., DICK, F., VAN HERWAARDEN, J., KARKOS, C., KOELEMAY, M., KÖLBEL, T., LOFTUS, I., MANI, K., MELISSANO, G., POWELL, J., SZEBERIN, Z., ESVS, G.C., BORST, G.J. de, CHAKFE, N., DEBUS, S., HINCHLIFFE, R., KAKKOS, S., KONCAR, I., KOLH, P., LINDHOLT, J.S., VEGA, M. de, VERMASSEN, F., DOCUMENT, R., BJÖRCK, M., CHENG, S., DALMAN, R., DAVIDOVIC, L., DONAS, K., EARNSHAW, J., ECKSTEIN, H.-H., GOLLEDGE, J., HAULON, S., MASTRACCI, T., NAYLOR, R., RICCO, J.-B. AND VERHAGEN, H. 2019. European Society for Vascular Surgery (ESVS) 2019 Clinical Practice Guidelines on the Management of Abdominal Aorto-iliac Artery Aneurysms. *Eur J Vasc Endovasc Surg* 57, 1, 8–93.
- WATKINS, M.W. AND LEWINTER, M.M. 1993. Physiologic role of the normal pericardium. *Annual review of medicine* 44, 171–180.
- WEBER, T.F., MULLER, T., BIESDORF, A., WORZ, S., RENGIER, F., HEYE, T., HOLLAND-LETZ, T., ROHR, K., KAUCZOR, H.-U. AND TENGG-KOBLIGK, H. von. 2014. True four-dimensional analysis of thoracic aortic displacement and distension using model-based segmentation of computed tomography angiography. *Int J Cardiovasc Imaging* 30, 1, 185–194.
- WEISBECKER, H., PIERCE, D.M., REGITNIG, P. AND HOLZAPFEL, G.A. 2012. Layer-specific damage experiments and modeling of human thoracic and abdominal aortas with non-atherosclerotic intimal thickening. *J Mech Behav Biomed Mater* 12, 93–106.
- WEIZSÄCKER, H.W., LAMBERT, H. AND PASCALE, K. 1983. Analysis of the passive mechanical properties of rat carotid arteries. *J Biomech* 16, 9, 703–715.
- WESTERHOF, N., LANKHAAR, J.-W. AND WESTERHOF, B.E. 2009. The arterial Windkessel. *MEDICAL & BIOLOGICAL ENGINEERING & COMPUTING* 47, 2, 131–141.
- WHITTAKER, P. AND PRZYKLENK, K. 2009. Fibrin architecture in clots. A quantitative polarized light microscopy analysis. *Blood cells, molecules & diseases* 42, 1, 51–56.
- WILSON, J.S., VIRAG, L., DI ACHILLE, P., KARSJAJ, I. AND HUMPHREY, J.D. 2013. Biochemomechanics of intraluminal thrombus in abdominal aortic aneurysms. *J Biomech Eng* 135, 2, 21011.
- WILSON, K.A., LEE, A.J., HOSKINS, P.R., FOWKES, F GERRY R, RUCKLEY, C.V. AND BRADBURY, A.W. 2003. The relationship between aortic wall distensibility and rupture of infrarenal abdominal aortic aneurysm. *J Vasc Surg* 37, 1, 112–117.
- WITTEK, A., BLASE, C., DERWICH, W., SCHMITZ-RIXEN, T. AND FRITZEN, C.-P. 2017a. Characterization of the mechanical behavior and pathophysiological state of abdominal aortic aneurysms based on 4D ultrasound strain imaging. In *Proc. SPIE 10333, Optical Methods for Inspection, Characterization, and Imaging of Biomaterials III*, P. FERRARO, S. GRILLI, M. RITSCH-MARTE AND C. K. HITZENBERGER, Eds. SPIE, 1033303.
- WITTEK, A., DERWICH, W., FRITZEN, C.-P., SCHMITZ-RIXEN, T. AND BLASE, C. 2017b. VALIDATION OF FULL FIELD MEASUREMENT OF AORTIC WALL MOTION BY 4D-ULTRASOUND. In *CBME17. 5th International Conference on Computational & Mathematical Biomedical Engineering*, P. NITHIARASU AND A. M. ROBERTSON, Eds. Zeta Computational Resources Ltd., Swansea, United Kingdom, 656–659.
- WITTEK, A., DERWICH, W., FRITZEN, C.-P., SCHMITZ-RIXEN, T. AND BLASE, C. 2018. Towards non-invasive in vivo characterization of the pathophysiological state and mechanical wall strength of the individual human AAA wall based on 4D ultrasound measurements. *ZAMM - Journal of Applied Mathematics and Mechanics / Zeitschrift für Angewandte Mathematik und Mechanik* 98, 12 (Special Issue: Mathematical and Computational Modeling in Biomechanics), 2275–2294.

- WITTEK, A., DERWICH, W., KARATOLIOS, K., FRITZEN, C.-P., VOGT, S., SCHMITZ-RIXEN, T. AND BLASE, C. 2016a. A finite element updating approach for identification of the anisotropic hyperelastic properties of normal and diseased aortic walls from 4D ultrasound strain imaging. *J Mech Behav Biomed Mater*, 58, 122–138.
- WITTEK, A., FRITZEN, C.-P., HUB, A. AND BLASE, C. 2019. Inverse Identification of the individual, non-linear and orthotropic material properties of human internal anatomical structures based on non-invasive real-time 3D ultrasound full-field measurements. In *Material Properties in Structure Analysis. Modeling, Calibration, Simulation & Optimization*, NAFEMS, Ed., 129–138.
- WITTEK, A., KARATOLIOS, K., BIHARI, P., SCHMITZ-RIXEN, T., MOOSDORF, R., VOGT, S. AND BLASE, C. 2013. In vivo determination of elastic properties of the human aorta based on 4D ultrasound data. *J Mech Behav Biomed Mater*, 27, 167–183.
- WITTEK, A. *, KARATOLIOS, K. *, FRITZEN, C.-P., BEREITER-HAHN, J., SCHIEFFER, B., MOOSDORF, R., VOGT, S. AND BLASE, C. 2016b. Cyclic three-dimensional wall motion of the human ascending and abdominal aorta characterized by time resolved three-dimensional ultrasound speckle tracking. *Biomech Model Mechanobiol* 15, 5, 1375–1388, *equal contribution.
- WOLINSKY, H. AND GLAGOV, S. 1967a. A lamellar unit of aortic medial structure and function in mammals. *Circulation Research* 20, 1, 99–111.
- WOLINSKY, H. AND GLAGOV, S. 1967b. Nature of species differences in the medial distribution of aortic vasa vasorum in mammals. *Circulation Research* 20, 4, 409–421.
- WUYTS, F.L., VANHUYSE, V.J., LANGEWOUTERS, G.J., DEGRAEMER, W.F., RAMAN, E.R. AND BUYLE, S. 1995. Elastic properties of human aortas in relation to age and atherosclerosis: a structural model. *Phys Med Biol* 40, 10, 1577–1597.
- ZHANG, W., HERRERA, C., ATLURI, S.N. AND KASSAB, G.S. 2005. The Effect of Longitudinal Pre-Stretch and Radial Constraint on the Stress Distribution in the Vessel Wall: A New Hypothesis. *Mechanics & Chemistry of Biosystems Vol. 2*, No. 1, 41–52.
- ZHAO, X., CHEN, X. AND LU, J. 2009. Pointwise Identification of Elastic Properties in Nonlinear Hyperelastic Membranes—Part II: Experimental Validation. *J. Appl. Mech.* 76, 6, 61014.
- ZHAO, X., RAGHAVAN, M.L. AND LU, J. 2011. Identifying heterogeneous anisotropic properties in cerebral aneurysms: a pointwise approach. *Biomech Model Mechanobiol* 10, 2, 177–189.

Appendix

A. Derivatives of the pseudoinvariants

The pseudoinvariants of the right CAUCHY strain tensor \mathbf{C} and one or more preferred directions of anisotropy and their derivatives with regard to \mathbf{C} are given e.g. in Holzapfel [2010], Ogden [2003] and Ogden [2009], however without detailed description of the derivation. Therefore, the derivation is described in detail, here.

The derivative of a scalar valued tensor function with regard to the argument tensor was obtained using the GATEAUX variation δf [cf. Silber and Steinwender 2005]:

$$\delta f(\mathbf{A}, \bar{\mathbf{A}}) = \frac{d}{d\lambda} [f(\mathbf{A} + \lambda\bar{\mathbf{A}})]|_{\lambda=0} = \left(\frac{\partial f}{\partial \mathbf{A}} \right) : \bar{\mathbf{A}} . \quad \text{eq. 8-1}$$

a. 4th pseudoinvariant

$$I_{4\alpha} = \mathbf{C} : \mathbf{a}_{0\alpha} \otimes \mathbf{a}_{0\alpha} = \mathbf{a}_{0\alpha} \cdot \mathbf{C} \cdot \mathbf{a}_{0\alpha} , \quad \text{eq. 8-2}$$

where the vector $\mathbf{a}_{0\alpha} \in \mathbf{R}^3$ indicates the α^{th} preferred direction of anisotropy as determined in the reference configuration and the dyadic product $\mathbf{a}_{0\alpha} \otimes \mathbf{a}_{0\alpha}$ is called *structure tensor*.

$$\begin{aligned}
\delta I_{4\alpha}(\mathbf{C}, \bar{\mathbf{C}}) &= \frac{d}{d\lambda} [(\mathbf{C} + \lambda\bar{\mathbf{C}}): \mathbf{a}_{0\alpha} \otimes \mathbf{a}_{0\alpha}]|_{\lambda=0} = \left(\frac{\partial I_{4\alpha}}{\partial \mathbf{C}}\right): \bar{\mathbf{C}} \\
&\Leftrightarrow \frac{d}{d\lambda} [\mathbf{C}: \mathbf{a}_{0\alpha} \otimes \mathbf{a}_{0\alpha} + \lambda\bar{\mathbf{C}}: \mathbf{a}_{0\alpha} \otimes \mathbf{a}_{0\alpha}]|_{\lambda=0} = \left(\frac{\partial I_{4\alpha}}{\partial \mathbf{C}}\right): \bar{\mathbf{C}} \\
&\Leftrightarrow \bar{\mathbf{C}}: \mathbf{a}_{0\alpha} \otimes \mathbf{a}_{0\alpha} = \left(\frac{\partial I_{4\alpha}}{\partial \mathbf{C}}\right): \bar{\mathbf{C}} \quad \text{eq. 8-3} \\
&\Leftrightarrow \mathbf{a}_{0\alpha} \otimes \mathbf{a}_{0\alpha}: \bar{\mathbf{C}} = \left(\frac{\partial I_{4\alpha}}{\partial \mathbf{C}}\right): \bar{\mathbf{C}} \\
&\Leftrightarrow \underline{\frac{\partial I_{4\alpha}}{\partial \mathbf{C}}} = \mathbf{a}_{0\alpha} \otimes \mathbf{a}_{0\alpha}
\end{aligned}$$

b. 5th Pseudoinvariant

$$I_{5\alpha} = \mathbf{C}^2: \mathbf{a}_{0\alpha} \otimes \mathbf{a}_{0\alpha} = \mathbf{a}_{0\alpha} \cdot \mathbf{C}^2 \cdot \mathbf{a}_{0\alpha}, \quad \text{eq. 8-4}$$

$$\begin{aligned}
\delta I_{5\alpha}(\mathbf{C}, \bar{\mathbf{C}}) &= \frac{d}{d\lambda} [(\mathbf{C} + \lambda\bar{\mathbf{C}})^2: \mathbf{a}_{0\alpha} \otimes \mathbf{a}_{0\alpha}]|_{\lambda=0} = \left(\frac{\partial I_{5\alpha}}{\partial \mathbf{C}}\right): \bar{\mathbf{C}} \\
&\Leftrightarrow \frac{d}{d\lambda} [(\mathbf{C}^2 + \lambda(\mathbf{C} \cdot \bar{\mathbf{C}} + \bar{\mathbf{C}} \cdot \mathbf{C}) + \lambda^2\bar{\mathbf{C}}^2): \mathbf{a}_{0\alpha} \otimes \mathbf{a}_{0\alpha}]|_{\lambda=0} = \left(\frac{\partial I_{5\alpha}}{\partial \mathbf{C}}\right): \bar{\mathbf{C}} \\
&\Leftrightarrow (\mathbf{C} \cdot \bar{\mathbf{C}} + \bar{\mathbf{C}} \cdot \mathbf{C} + 2\lambda\bar{\mathbf{C}}^2): \mathbf{a}_{0\alpha} \otimes \mathbf{a}_{0\alpha}|_{\lambda=0} = \left(\frac{\partial I_{5\alpha}}{\partial \mathbf{C}}\right): \bar{\mathbf{C}} \\
&\Leftrightarrow (\mathbf{C} \cdot \bar{\mathbf{C}} + \bar{\mathbf{C}} \cdot \mathbf{C}): \mathbf{a}_{0\alpha} \otimes \mathbf{a}_{0\alpha} = \left(\frac{\partial I_{5\alpha}}{\partial \mathbf{C}}\right): \bar{\mathbf{C}} \quad \text{eq. 8-5} \\
&\Leftrightarrow (\mathbf{C} \cdot \bar{\mathbf{C}}): \mathbf{a}_{0\alpha} \otimes \mathbf{a}_{0\alpha} + (\bar{\mathbf{C}} \cdot \mathbf{C}): \mathbf{a}_{0\alpha} \otimes \mathbf{a}_{0\alpha} = \left(\frac{\partial I_{5\alpha}}{\partial \mathbf{C}}\right): \bar{\mathbf{C}} \\
&\Leftrightarrow \mathbf{a}_{0\alpha} \otimes \mathbf{a}_{0\alpha}: (\mathbf{C} \cdot \bar{\mathbf{C}}) + \mathbf{a}_{0\alpha} \otimes \mathbf{a}_{0\alpha}: (\bar{\mathbf{C}} \cdot \mathbf{C}) = \left(\frac{\partial I_{5\alpha}}{\partial \mathbf{C}}\right): \bar{\mathbf{C}} \\
&\Leftrightarrow (\mathbf{C}^T \cdot \mathbf{a}_{0\alpha} \otimes \mathbf{a}_{0\alpha}): \bar{\mathbf{C}} + (\mathbf{a}_{0\alpha} \otimes \mathbf{a}_{0\alpha} \cdot \mathbf{C}^T): \bar{\mathbf{C}} = \left(\frac{\partial I_{5\alpha}}{\partial \mathbf{C}}\right): \bar{\mathbf{C}}
\end{aligned}$$

$$\Leftrightarrow (\mathbf{C} \cdot \mathbf{a}_{0\alpha} \otimes \mathbf{a}_{0\alpha} + \mathbf{a}_{0\alpha} \otimes \mathbf{a}_{0\alpha} \cdot \mathbf{C}) : \bar{\mathbf{C}} = \left(\frac{\partial I_{5\alpha}}{\partial \mathbf{C}} \right) : \bar{\mathbf{C}}$$

$$\Leftrightarrow (\mathbf{a}_{0\alpha} \otimes \mathbf{a}_{0\alpha} \cdot \mathbf{C} + \mathbf{C} \cdot \mathbf{a}_{0\alpha} \otimes \mathbf{a}_{0\alpha}) : \bar{\mathbf{C}} = \left(\frac{\partial I_{5\alpha}}{\partial \mathbf{C}} \right) : \bar{\mathbf{C}}$$

$$\Leftrightarrow \underline{\underline{\frac{\partial I_{5\alpha}}{\partial \mathbf{C}} = \mathbf{a}_{0\alpha} \otimes \mathbf{a}_{0\alpha} \cdot \mathbf{C} + \mathbf{C} \cdot \mathbf{a}_{0\alpha} \otimes \mathbf{a}_{0\alpha}}}}$$

c. Pseudoinvariant for the coupling of two preferred directions

In literature this pseudoinvariant is often referred to as 8th invariant I_8 since for two preferred directions (α, β) often the following nomenclature is used: $I_{4\alpha} \equiv I_4$, $I_{4\beta} \equiv I_6$, $I_{5\alpha} \equiv I_5$, $I_{5\beta} \equiv I_7$ and consequently $I_{\alpha\beta} \equiv I_8$.

$$I_{\alpha\beta} = \mathbf{C} : \mathbf{a}_{0\alpha} \otimes \mathbf{a}_{0\beta} = \mathbf{a}_{0\alpha} \cdot \mathbf{C} \cdot \mathbf{a}_{0\beta}, \quad \text{eq. 8-6}$$

$$I_{\alpha\beta}(\mathbf{C}, \bar{\mathbf{C}}) = \frac{d}{d\lambda} [(\mathbf{C} + \lambda \bar{\mathbf{C}}) : \mathbf{a}_{0\alpha} \otimes \mathbf{a}_{0\beta}]|_{\lambda=0} = \left(\frac{\partial I_{\alpha\beta}}{\partial \mathbf{C}} \right) : \bar{\mathbf{C}}$$

$$\Leftrightarrow \frac{d}{d\lambda} [\mathbf{C} : \mathbf{a}_{0\alpha} \otimes \mathbf{a}_{0\beta} + \lambda \bar{\mathbf{C}} : \mathbf{a}_{0\alpha} \otimes \mathbf{a}_{0\beta}]|_{\lambda=0} = \left(\frac{\partial I_{\alpha\beta}}{\partial \mathbf{C}} \right) : \bar{\mathbf{C}}$$

$$\Leftrightarrow \bar{\mathbf{C}} : \left[\frac{1}{2} (\mathbf{a}_{0\alpha} \otimes \mathbf{a}_{0\beta} + (\mathbf{a}_{0\alpha} \otimes \mathbf{a}_{0\beta})^T) + \frac{1}{2} (\mathbf{a}_{0\alpha} \otimes \mathbf{a}_{0\beta} - (\mathbf{a}_{0\alpha} \otimes \mathbf{a}_{0\beta})^T) \right] = \left(\frac{\partial I_{\alpha\beta}}{\partial \mathbf{C}} \right) : \bar{\mathbf{C}}$$

$$\Leftrightarrow \bar{\mathbf{C}} : \frac{1}{2} (\mathbf{a}_{0\alpha} \otimes \mathbf{a}_{0\beta} + (\mathbf{a}_{0\alpha} \otimes \mathbf{a}_{0\beta})^T) + \underbrace{\bar{\mathbf{C}} : \frac{1}{2} (\mathbf{a}_{0\alpha} \otimes \mathbf{a}_{0\beta} - (\mathbf{a}_{0\alpha} \otimes \mathbf{a}_{0\beta})^T)}_0 = \left(\frac{\partial I_{\alpha\beta}}{\partial \mathbf{C}} \right) : \bar{\mathbf{C}}$$

eq. 8-7

$$\Leftrightarrow \frac{1}{2} (\mathbf{a}_{0\alpha} \otimes \mathbf{a}_{0\beta} + \mathbf{a}_{0\beta} \otimes \mathbf{a}_{0\alpha}) : \bar{\mathbf{C}} = \left(\frac{\partial I_{\alpha\beta}}{\partial \mathbf{C}} \right) : \bar{\mathbf{C}}$$

$$\Rightarrow \underline{\underline{\frac{\partial I_{\alpha\beta}}{\partial \mathbf{C}} = \frac{1}{2} (\mathbf{a}_{0\alpha} \otimes \mathbf{a}_{0\beta} + \mathbf{a}_{0\beta} \otimes \mathbf{a}_{0\alpha})}}$$

B. Convergence study for the FE discretization of pressurized aortic segments

A “native” FE discretization was determined by using the measured position vectors $\mathbf{X}_{i,j}$ of discrete material points of the aortic or aneurysmal wall in a chosen, deformed reference configuration as nodes of a mesh of 4-node membrane or shell elements [cf. chapters 3.3.4.1 and 7.6.2]. For the direct computation of local wall strains from reference geometry and measured displacements [cf. chapters 3 and 6], Abaqus 6.12/Standard membrane elements of type M3D4R were used. For this type of strain computation, the mesh was not refined: the obtained strain fields can be regarded as measured data and further refinement would neither provide any additional information, nor increase the accuracy of computation. If, in contrast, strain fields were estimated by a nonlinear FEA as a discrete nonlinear function of reference geometry, boundary conditions and loading and a guess of the unknown constitutive parameters – as was necessary for the constitutive parameter identification that is described in chapter 7 – the degree of discretization affected the accuracy of the analysis results. Therefore, a convergence study was performed in order to determine the appropriate degree of refinement of the “native” mesh providing sufficient accuracy at lowest possible computational costs.

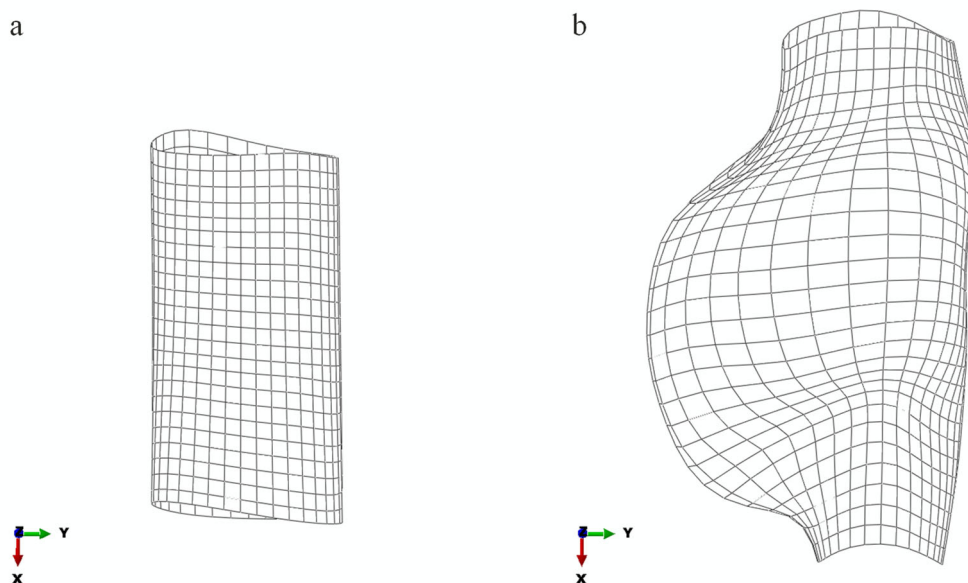


Figure 8-1 Native mesh of the almost cylindrical aortic segment and the geometrically strongly irregular aortic segment as obtained by using the discrete material points \mathbf{X}_{dia}

For the convergence study, 4D ultrasound data of a healthy aortic segment with almost regular cylindrical geometry [Figure 8-1 a] and of a strongly irregular AAA [Figure 8-1 b] were chosen. FE pre-processing was done according to chapter 7.6.2. Dimensions of the imaged segments, characteristic edge length of the “native” mesh and applied pressure load are given in Table 8-1. Since the only purpose of the performed FEAs was to determine the dependency of the analysis results on the degree of discretization, the imaged diastolic configuration was taken as load- and stress-free natural configuration, in this case.

Table 8-1 Reference diameter, length, edge length of shell elements and size of pressure load for the two data sets for which a convergence test was performed.

Geometry	Diameter in mm	Length in mm	Edge length in mm	Pressure in mmHg
Slightly irregular	16.9	32.0	≈ 1.5	120
Strongly irregular	31.8*	53.5	≤ 3.0	120

*In contrast to the geometrically slightly irregular segment, the local maximum diameter of the strongly irregular geometry is given here as the measure that is clinically relevant for AAA.

The same strain energy function for which constitutive parameter identification was performed [cf. chapter 7.4] was used in this convergence study. Reasonable, but arbitrary constitutive parameters were employed. As can be seen immediately, the constitutive parameters that were used with the strongly irregular geometry are the ones that were inversely identified for the AAA sample in chapter 7 [Table 7-4]. For irregular geometries, the convergence study was performed after the *in vivo* parameter identification had been conducted on trial. The results of the convergence study have confirmed that the degree of discretization that had been chosen on the basis of experience was appropriate and then the results of the parameter identification were accepted.

Table 8-2 Constitutive parameters of the Holzapfel-Gasser-Ogden model that were used in the convergence study.

Geometry	μ_1 in MPa	k_1 in MPa	k_2	κ	φ in $^\circ$
Slightly irregular	0.151	0.186	336.27	0.25	21.5
Strongly irregular	0.228	4.736	1960.65	0.21	4.6

Figure 8-2, Figure 8-3 and Figure 8-4 show the results that were obtained for the almost regular cylindrical geometry. Figure 8-2 gives a quantitative comparison of the distributions of local maximum principal in-plane strains that were obtained using the “native” mesh and a 4-fold and 9-fold refinement, i.e. splitting one element of the native mesh into 4 and 9 elements, respectively. The differences between the median as well as the maximum of the distributions that were obtained for the “native” mesh and the 4-fold refinement were < 0.001 . Therefore, the “native” mesh was accepted as sufficient for non-aneurysmal aortae. Figure 8-3 and Figure 8-4 illustrate the good agreement of the spatial in-plane principal strain and stress distributions, respectively.

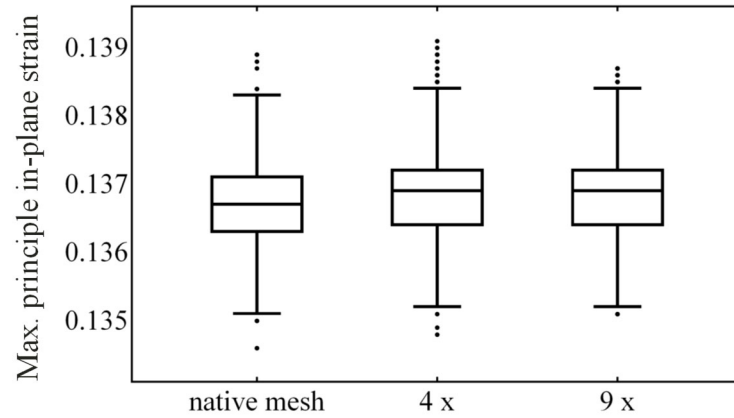


Figure 8-2 Comparison of the distributions of maximum principle in-plane strains obtained for the native mesh and different degrees of mesh refinement of an almost regularly cylindrical tube [cf. Figure 8-1]

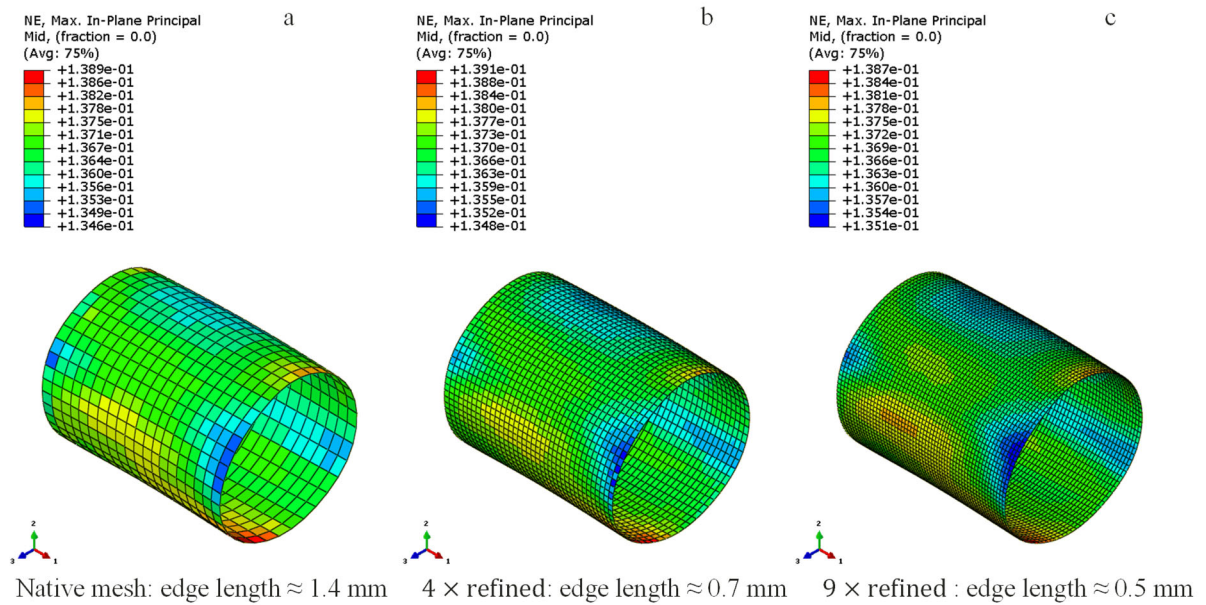


Figure 8-3 Comparison of the spatial distributions of maximum principle in-plane strains obtained for the native mesh and different degrees of mesh refinement of an almost regularly cylindrical tube.

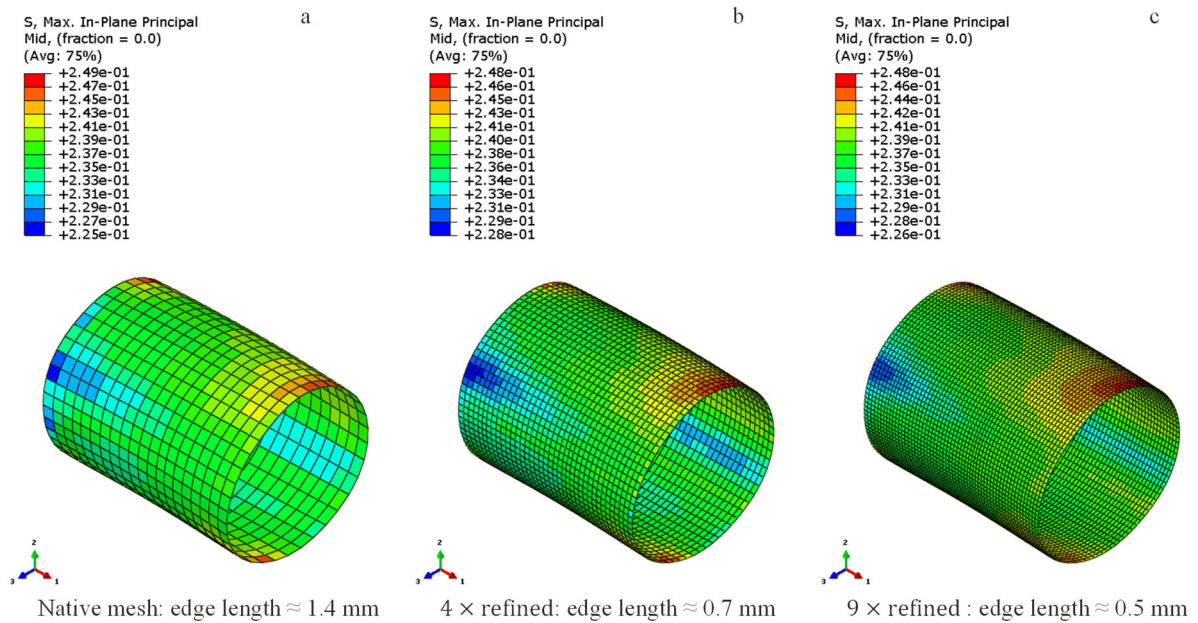


Figure 8-4 Comparison of the spatial distributions of maximum principle in-plane stresses obtained for the native mesh and different degrees of mesh refinement of an almost regularly cylindrical tube.

The results for the strongly irregular aneurysmal geometry are given in Figure 8-5, Figure 8-6 and Figure 8-7. Figure 8-5 gives a quantitative comparison of the distributions of local maximum principal in-plane strains obtained for the “native” mesh and 4-fold, 9-fold, 16-fold, 25-fold and 36-fold refinement. A considerable difference was found between the native mesh and the 4-fold refinement. In contrast, only negligible differences were observed between the median value obtained using the 4-fold refined mesh and the median values obtained for all further refinements. Though a steady increase of the local maximum value was observed, this difference was < 0.01 and affected far outliers of the distribution of local strains, only. Figure 8-6 and Figure 8-7 illustrate the good qualitative agreement of the spatial in-plane principal strain and stress distributions, respectively. Note, in particular, that the locations and areas of local peak strains and local peak stresses agree very well. Based on these results, a 4-fold refinement of the “native” mesh was accepted for aneurysmal geometries.

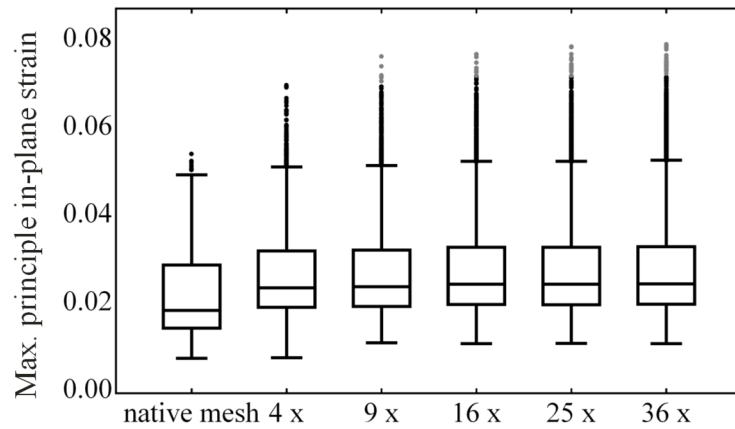


Figure 8-5 Comparison of the distributions of maximum principle in-plane strains obtained for the native mesh and different degrees of mesh refinement of a strongly irregular geometry (cf. Figure 8-1)

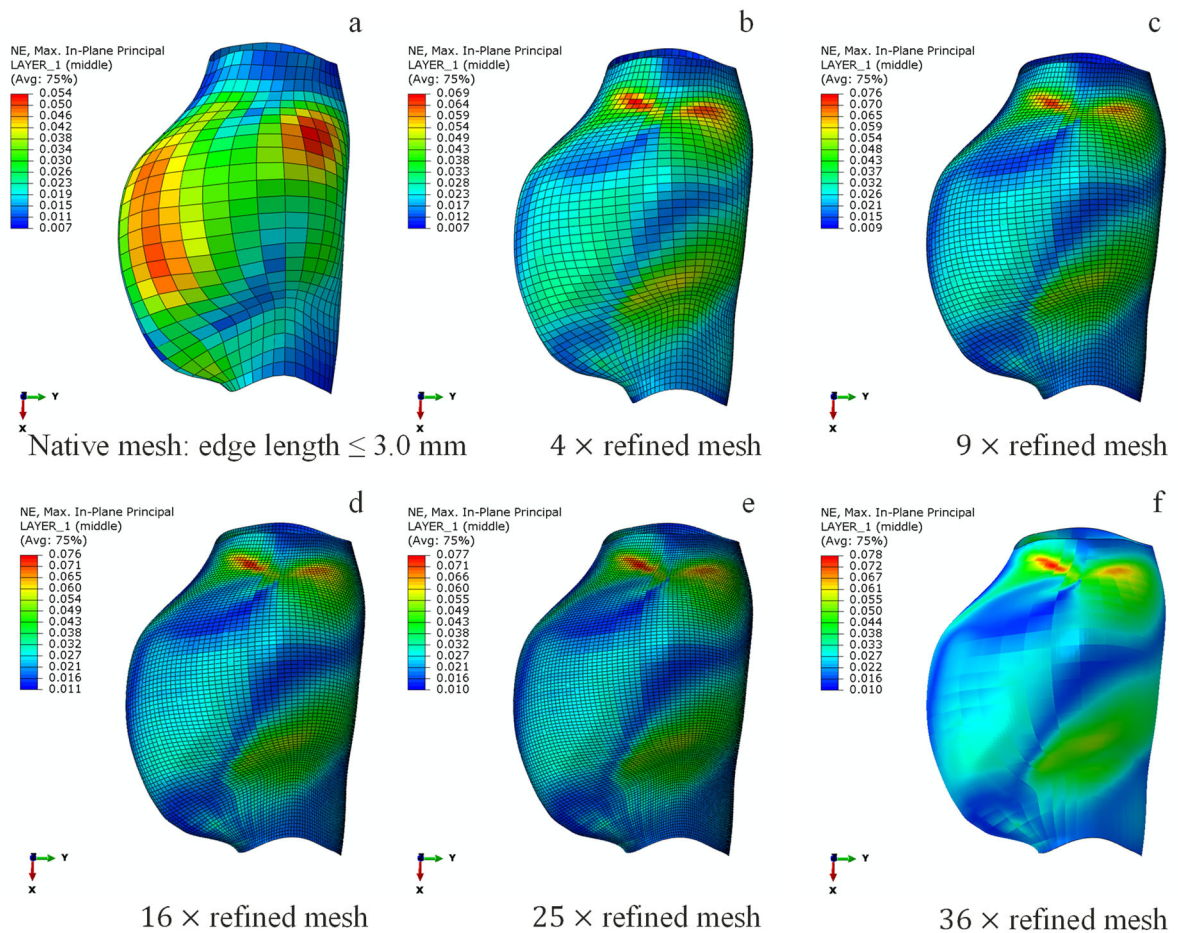


Figure 8-6 Comparison of the spatial distributions of maximum principle in-plane strains obtained for the native mesh and different degrees of mesh refinement of a strongly irregular AAA geometry.

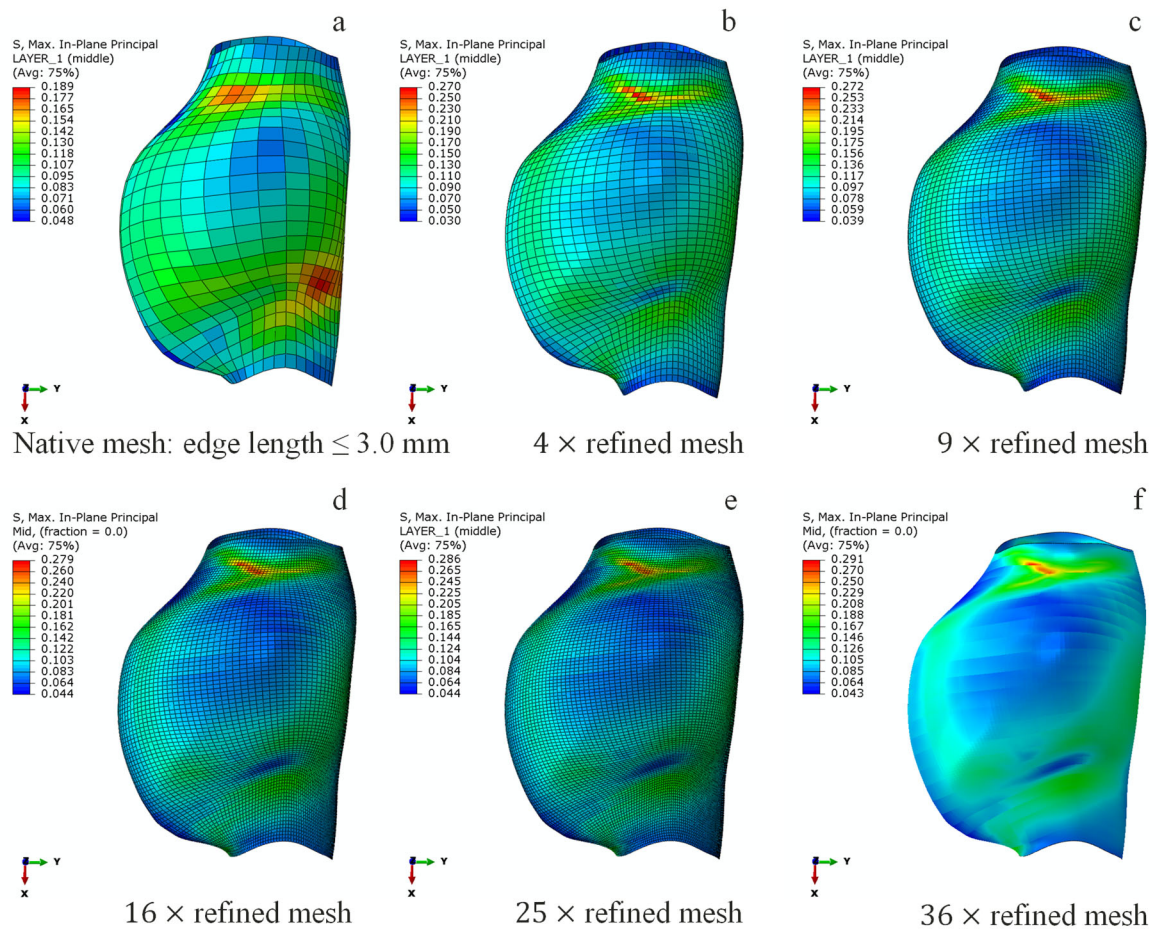


Figure 8-7 Comparison of the spatial distributions of maximum principle in-plane stresses obtained for the native mesh and different degrees of mesh refinement of a strongly irregular AAA geometry.

C. First approach to a Finite Element Model Updating workflow

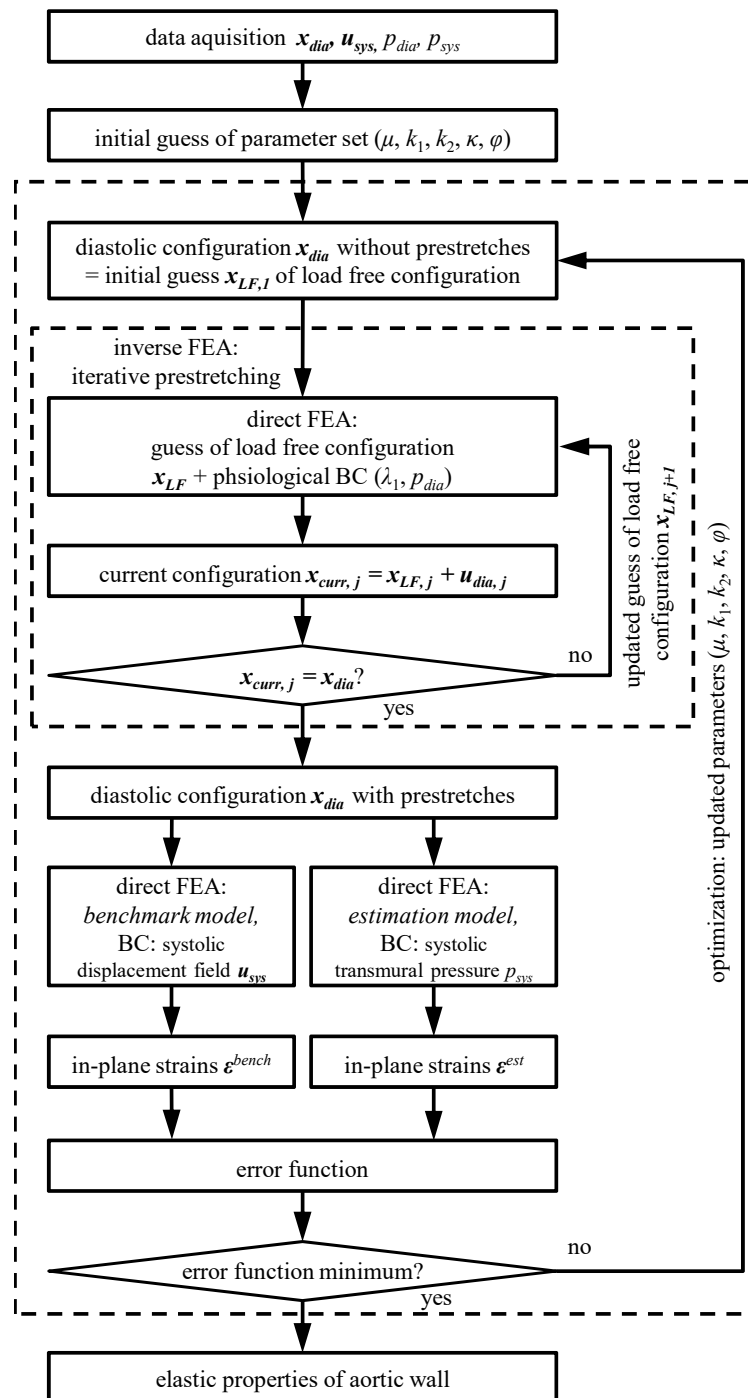


Figure 8-8 Flow chart of the 2013 version of the Finite Element Model Updating method (FEMU) to determine individual elastic properties of the aortic wall based on non-invasively in vivo acquired 4D-US data. [Reprinted from Wittek et al. 2013 with permission from Elsevier]

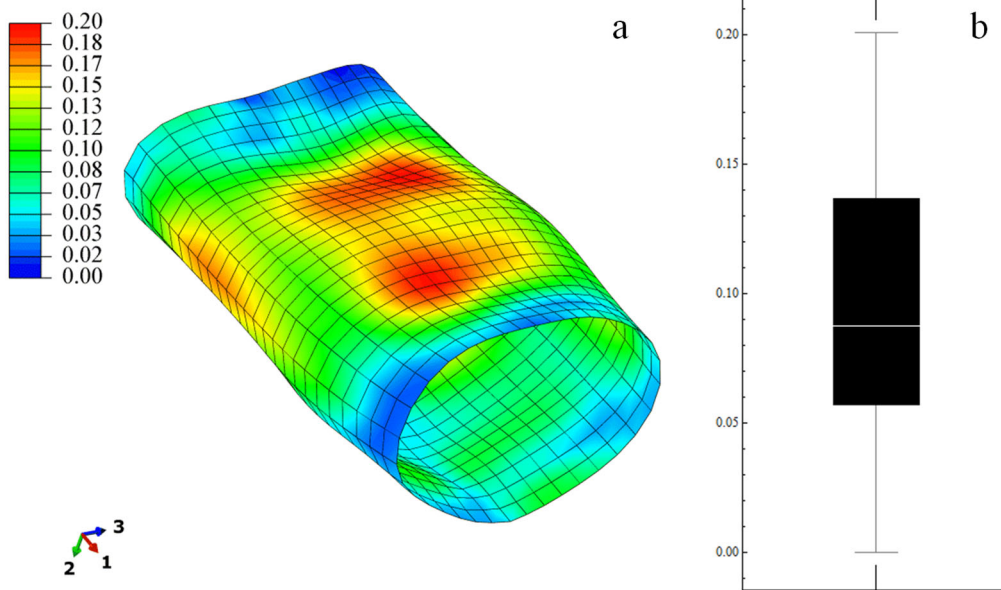


Figure 8-9 Recovery of the load-free configuration that was achieved in the numerical verification experiment using the 2013 FEMU workflow according to Figure 8-8: Comparison of the load-free geometry given by the master model and the geometry of the estimation model (EM) determined by the iterative optimal design algorithm depending on the identified constitutive parameter set. a) Load-free configuration of the master model. The geometrical differences to the load-free configuration of the EM are indicated (scale in mm). b) Quantitative distribution of the geometrical differences indicating a median difference of 0.09 mm and a Hausdorff distance of 0.20 mm. [Reprinted from Wittek et al. 2013 with permission from Elsevier]

D. List of first author publications that were used in this thesis

a. Peer reviewed journal articles

- KARATOLIOS, K. *, WITTEK, A. *, NWE, T.H., BIHARI, P., SHELKE, A., JOSEF, D., SCHMITZ-RIXEN, T., GEKS, J., MAISCH, B., BLASE, C., MOOSDORF, R. AND VOGT, S. 2013. Method for Aortic Wall Strain Measurement with Three-Dimensional Ultrasound Speckle Tracking and Fitted Finite Element Analysis. *Ann Thorac Surg* 96, 5, 1664–1671, *equal contribution.
- WITTEK, A., KARATOLIOS, K., BIHARI, P., SCHMITZ-RIXEN, T., MOOSDORF, R., VOGT, S. AND BLASE, C. 2013. In vivo determination of elastic properties of the human aorta based on 4D ultrasound data. *J Mech Behav Biomed Mater*, 27, 167–183.
- WITTEK, A., DERWICH, W., KARATOLIOS, K., FRITZEN, C.P., VOGT, S., SCHMITZ-RIXEN, T. AND BLASE, C. 2016a. A finite element updating approach for identification of the anisotropic hyperelastic properties of normal and diseased aortic walls from 4D ultrasound strain imaging. *J Mech Behav Biomed Mater*, 58, 122–138.
- WITTEK, A. *, KARATOLIOS, K. *, FRITZEN, C.-P., BEREITER-HAHN, J., SCHIEFFER, B., MOOSDORF, R., VOGT, S. AND BLASE, C. 2016b. Cyclic three-dimensional wall motion of the human ascending and abdominal aorta characterized by time resolved three-dimensional ultrasound speckle tracking. *Biomech Model Mechanobiol* 15, 5, 1375–1388, *equal contribution.
- WITTEK, A., DERWICH, W., FRITZEN, C.-P., SCHMITZ-RIXEN, T. AND BLASE, C. 2018. Towards non-invasive in vivo characterization of the pathophysiological state and mechanical wall strength of the individual human AAA wall based on 4D ultrasound measurements. *ZAMM - Journal of Applied Mathematics and Mechanics / Zeitschrift für Angewandte Mathematik und Mechanik* 98, 12 (Special Issue: Mathematical and Computational Modeling in Biomechanics), 2275–2294.

b. Peer reviewed contributions to conference proceedings

- WITTEK, A., BLASE, C., DERWICH, W., SCHMITZ-RIXEN, T. AND FRITZEN, C.-P. 2017a. Characterization of the mechanical behavior and pathophysiological state of abdominal aortic aneurysms based on 4D ultrasound strain imaging. In *Proc. SPIE 10333, Optical Methods for Inspection, Characterization, and Imaging of Biomaterials III*, P. FERRARO, S. GRILLI, M. RITSCH-MARTE AND C. K. HITZENBERGER, Eds. SPIE, 1033303.
- WITTEK, A., DERWICH, W., FRITZEN, C.-P., SCHMITZ-RIXEN, T. AND BLASE, C. 2017b. Validation of full field measurement of aortic wall motion by 4D-ultrasound. In *CBME17. 5th International Conference on Computational & Mathematical Biomedical Engineering*, P. NITHIARASU AND A. M. ROBERTSON, Eds. Zeta Computational Resources Ltd., Swansea, United Kingdom, 656–659.
- WITTEK, A., FRITZEN, C.-P., HUB, A. AND BLASE, C. 2019. Inverse Identification of the individual, non-linear and orthotropic material properties of human internal anatomical structures based on non-invasive real-time 3D ultrasound full-field measurements. In *Material Properties in Structure Analysis. Modeling, Calibration, Simulation & Optimization*, NAFEMS, Ed., 129–138